The evolution and formation of the SDC13 Infrared Dark Cloud hub filament system

Gwenllian Mair Williams

A Thesis submitted to
Cardiff University
for the degree of
Doctor of Philosophy

January 2018

I Mamgu a Dadcu.
Dyma chi, sêr y nôs.

ACKNOWLEDGEMENTS

Today, I packed up my desk and left office N/3.25. This day felt so distant when I started my PhD over 3 years ago. Cardiff has been my home for more than 7 years now, and upon reflecting on my time here there are many people that I want to thank for helping me get to this point.

First and foremost, I would like to thank my wonderful supervisor Dr Nicolas Peretto. Thanks for giving me the opportunity to do this research, and for your guidance, support, patience and friendship over the last 3.5 years. Your door was always open to me, whether it was to ask for help even with the simplest of things, to ask a stupid question, or just if I wanted to run down and show you something cool. I look forward to keep working with you in the future.

My thanks go to Prof Haley Gomez for inspiring me during my undergraduate years to pursue a PhD, and for helping me believe in myself a little. Thanks to Dr Sarah Ragan and Dr Steve Longmore for being friendly examiners, and for putting me at ease as much as possible during the Viva. Thanks to my secondary school Physics teacher Mr Jonathan Williams for nurturing my enthusiasm for science.

The Star Formation Group have been the most welcoming and wonderful bunch of people to work with for the past 3.5 years. There is no doubt that I have made friends for life here, and I would in particular like to thank Seamus Clarke, Sarah Jaffa, Camilo Peñaloza and Rachael Spowage, with whom I have shared this entire PhD journey. Seamus: thanks for introducing me to K-pop and BTS, and for talking science with me. Sarah: thanks for your persistence in always asking if I want to go get tea even though I pretty much always said no, and for introducing me to Rummy. Camilo: thanks for always messing with my office chair (I guess...), and for being my cinema buddy and introducing me to the Odeon snackies. Rachael: thanks for watching dog videos with me from day one, and for never failing to remind me in my moments of need that my floof is soff. My special thanks also go to Paul Clark, Emily Drabek-Maunder, Ana Duarte-Cabral, Jane Greaves, Alex Howard, Zeinab Khorrami, Oliver Lomax, Andrew Rigby, Elizabeth Watkins and Anthony Whitworth. I thank you all for making this such a happy working environment, I really am going to miss it dearly. Thanks to all at The Rest Frame coffee breaks for the chit-chat, thanks to Cake Thursday bakers for giving me a much needed tasty sugar boost, and to the Flute and Tankard for stocking Punk IPA for me to consume most Fridays.

Most importantly, I would like to thank my family. / Yn bennaf ôll, hoffwn rhoi diolch i fy nheulu. Mam, Dad a Megan: gallen i byth a fod wedi gwneud hwn heb eich cariad a chefnogaeth. Chi yw'r pobol sydd wastod wedi credu yn fi, hyd yn oed pan o'n i ddim yn credu yn fy hunan. Rwyf yn ddiolchgar iawn eich bod chi wastod wedi fy ngwthio i gyflawni fy ngobeithion a breuddwydion. Diolch am bod yna i fwynhau yr uchelbwyntiau gyda fi, ond yn bennaf ôll helpu fi trwyddo pob un iselbwynt trwy gydol fy mywyd, yn enwedig dros y 7 mlynedd diwethaf. Fi'n gwbod bydde chi wastod yn fy nghefnogi i beth bynnag rwy'n dewis i gwneud gyda fy mywyd, ac am hynny, diolch. Caru chi.

Finally, I dedicate this work to my grandparents. / Rhoddaf y gwaith hwn i Mamgu a Dadcu. Mae hiraeth arnaf, achos galla i ddim dweud wrthoch chi bod fi wedi neud e. Bod eich Gwenllian fach chi wedi gorffen y doethuriaeth o'r diwedd ar sêr y nôs. Mae amser maith wedi carlamu heibio ers i fi eistedd yn eich côl chi ar y stepyn drws yn edrych i fynny ar y sêr mewn syndod. Fi'n gweld eisiau chi'n ofnadwy bob dydd. Fi'n gwbod byddech chi'n andros o falch. Mae hwn i chi. Caru chi.

ABSTRACT

It is now widely accepted that interstellar filaments represent a key intermediate stage in the star formation process. The vast majority of cores, the direct progenitors of stars, sit on top of the densest filaments. Yet a number of questions remain regarding the physics that govern their evolution and fragmentation. Only the detailed study of the early stages of cloud evolution can help shed light on the exact role of filaments in the star formation process. This is the purpose of this thesis.

I present a study of the SDC13 infrared dark cloud hub filament system. SDC13 resides 3.6 ± 0.4 kpc away in the galactic plane, and has a remarkable morphology, containing 4 parsec-long filaments that spatially converge on a central hub region. Containing $1000\mathrm{M}_{\odot}$ of material, it is classed as an intermediate to high mass star forming region. Overall, SDC13 is an ideal target to study how filaments form, fragment and dynamically interact with each other.

The evolution of SDC13 was studied by probing the dense NH_3 gas in the system down to small spatial scales of 0.07 pc by combining data from the Jansky Very Large Array (JVLA) and the Green Bank Telescope (GBT). The mass-per-unit-lengths of all four hub filaments are thermally supercritical, consistent with the presence of tens of gravitationally bound cores along them. These cores exhibit a regular separation of $\sim 0.37 \pm 0.16$ pc suggesting that gravitational instabilities running along these super-critical filaments are responsible for their fragmentation. The dense gas velocity dispersion towards starless cores is observed to increase locally in two-thirds of the population compared to the surrounding filament, believed to be a consequence of such a fragmentation process. Using energy conservation arguments, I estimate that the gravitational to kinetic energy conversion efficiency in these peaked cores is $\sim 40\%$. Furthermore, the velocity gradient also peaks towards $\sim 63\%$ of the cores, as one would expect during the early stages of filament fragmentation. The largest acceleration gradients in SDC13 were found to be near the hub centre, where the velocity dispersion is largest and directly correlating with the location of the massive cores at the hub-filament junctions. This is suggested to be a direct result of the hub morphology itself.

In order to constrain the formation mechanism of the SDC13 filaments, an initial study of $C^{18}O(1\text{–}0)$ and $^{13}CO(1\text{–}0)$ emission at larger spatial scales of 0.4 pc with the IRAM 30 m telescope was conducted. In recent years, velocity-coherent sub-filaments (termed fibres) have been suggested to represent a specific turbulence-dominated mode of filament formation. In studying position-velocity slices along the filaments, fibres are not identified in SDC13. In conjunction with conclusions drawn from the NH_3 data, it is suggested that the dominance of gravity in the system as a

direct result of the hub-morphology itself suppresses the formation of fibres, which in both observations and simulations are thought to be products of turbulence (Tafalla & Hacar 2015; Smith et al. 2016). On the other hand, it is a possibility that the presence of fibres in Taurus shown by Tafalla & Hacar (2015) is unique, and that fibres are not typical constituents of the ISM. Following the fitting of multiple velocity components of the $C^{18}O(1–0)$ emission, we find that the velocity dispersion decreases towards the filament in comparison to the surrounding environment. Coherent velocity structures resembling shells corresponding to a more diffuse cloud to the North of SDC13 are found to evolve with velocity. To investigate whether turbulence could produce such shells, I conducted the same analysis on an MHD, cloud-cloud collision simulation, post-processed using RADMC-3D to create $^{13}CO(1–0)$ synthetic observations (Clark et al. in prep). Initial analysis seems to suggest such shells may be present in the simulation, but this is certainly a work-in-progress at this stage. Whether such structures are indicative of the turbulent beginnings of SDC13 will be investigated in the near future.

Overall, I propose a scenario for the evolution of the SDC13 hub in which filaments first form as post-shock structures in a supersonic turbulent flow. As a result of the turbulent energy dissipation in the shock, the dense gas within the filaments is initially mostly sub-sonic. Then gravity takes over and starts shaping the evolution of the hub, suppressing fibre formation, fragmenting filaments and pulling the gas towards the centre of the gravitational well. By doing so, gravitational energy is converted into kinetic energy in both local (cores) and global (hub centre) potential well minima, generating more massive cores at the hub centre as a result of larger acceleration gradients.

CONTENTS

List of Tables

LIST OF FIGURES

CHAPTER 1

AN INTRODUCTION TO STAR FORMATION

Nuclear burning, compact balls of gas called stars are traditionally separated by their mass into three groups: low mass stars with masses of few tenths to a few solar mass ($M_\odot$), intermediate mass stars with masses $\sim$2–8$M_\odot$, and high-mass stars with masses $> 8M_\odot$. Low-mass stars are the most common, dominating the mass in stars of a Galaxy. High-mass stars are far rarer, and instead dominate the luminosity in stars of a Galaxy.

The evolution of these groups of star is known to be very different, with low-mass stars living for billions of years, whilst high-mass stars live fast and die young, enriching the interstellar medium with heavy elements as they explode as a supernova at the end of their lives. It is not clear however if such a clear distinction exists in their formation mechanisms. Through the study of cold and dense molecular cloud environments that harbour the earliest stages of star formation, a complete picture of the process is on the horizon. Such an understanding is essential in our knowledge of planet formation, a natural bi-product of the star formation process, and of galaxy evolution over cosmic time, dependent on the physics of the interstellar medium.

1.1 The Interstellar Medium

The Interstellar Medium (ISM) represents all of the gas and dust that resides in the space between stars in a galaxy, constituting $\sim$ 10% of the visible mass in the Milky Way (Stahler & Palla 2005). The largest portion of the ISM belongs to the gas phase, and predominantly consists of Hydrogen (atomic, molecular and ionized), then Helium and traces of metals. The remaining percent or so of the ISM is made of interstellar dust. The gaseous ISM is multi-phase, with a distribution of density-temperature regimes that transition to each other. A three phase ISM was proposed by McKee & Ostriker (1977). In their model, the first phase is the Hot Ionized Medium (HIM) with typical temperature and density of 10^6 K and $0.001\,\mathrm{cm}^{-3}$. The second phase is the warm phase, today split into two separate phases called the Warm Ionized Medium (WIM, e.g. Hill et al. 2015) predominantly made up of ionized hydrogen with $\mathrm{T} < 1000\,\mathrm{K}$, and the Warm Neutral Medium (WNM) predominantly made from neutral atomic hydrogen with $300 < \mathrm{T} < 400\,\mathrm{K}$. The final phase is the cold phase, today sub-divided into the Cold Neutral Medium (CNM) predominantly made of neutral atomic Hydrogen and with $\mathrm{T} < 300\,\mathrm{K}$, and the Molecular Medium (MM) made up of molecular hydrogen with $\mathrm{T} < 30\,\mathrm{K}$ and $n > 1000\,\mathrm{cm}^{-3}$.

Gas constantly transitions between the phases of the ISM through a wide variety of heating and cooling processes. At one end, the HIM typically reaches its 10^6 K temperatures due to supernova shocks. At the other extreme, high column density regions shield their molecular interiors from heating, protecting the molecules from photodissociation by UV radiation. This in turn allows for cooling of molecular clouds by molecular and dust emission, predominantly done through collisional excitation followed by radiative decay. Due to the high energies required for the collisional excitation of Hydrogen or Helium from their ground states, cooling in the ISM is dominated by the metal lines. This type of cooling is most efficient in an optically thin gas, where the radiated photon has less chance of being re-absorbed, causing heating.

Nowadays, complex numerical simulations attempt to model the multi-phase ISM. One such collaboration is the SILCC project (Walch et al. 2015; Girichidis et al. 2016; Gatto et al. 2017; Peters et al. 2017) who include the essential physics such as heating, cooling, chemistry, gravity and magnetic fields. By studying the changes in the ISM under different physical conditions (such as supernova explosions for example) their goal is to understand the full life-cycle of molecular clouds.

1.2 MOLECULAR CLOUDS

Molecular Clouds (MCs) are cold and dense regions of atomic and molecular gas that are known to condense out of the warm ISM. For this to happen, the WNM must be cooled down appropriately by two orders of magnitude to the MM regime.

Most of the mass in the ISM is contained within Giant Molecular Clouds (GMCs), constituting typically 30% in mass but only 0.05% in volume (Stahler & Palla 2005). MCs have a wide range of masses, the extremes being from 10^2 to $10^7\,\mathrm{M}_\odot$, but typically lying between 10^4–$10^5\,\mathrm{M}_\odot$, with typical sizes of a few parsec to $\sim$200 pc, and typical densities of a few hundred particles per cubic centimetre. Most GMCs have a HI envelope that dominate their mass. Further to shielding, molecules and dust radiate away energy, facilitating the cooling of MCs down to a typical of temperature of 10–30 K.

MCs are thought to typically form from supersonic gas compression. The origin of such compression can be varied, such as turbulence, an HII region, wind bubbles or supernova remnant shells expanding through the gas, for example, which can easily accumulate $10^4\mathrm{M}_\odot$ of mass, enough to form typically sized MCs (e.g. Hartmann et al. 2001). To form more massive MCs out of smaller clouds, Inutsuka et al. (2015) proposed that continuous cloud compression is required. They call this sequential molecular cloud formation, and this proceeds by repeated compressions of a network of overlapping dense shells. Such a repeated event can come in the form of supernova events due to the clustered nature of massive star formation. These multiple supernova shells cause continuous shock compression of the surrounding molecular gas. Further collisions of the formed MCs themselves can occur at the edges of the dense HII shell network, again increasing the mass of MCs able to be formed (e.g. Dobbs et al. 2011).

MCs are not very long-lived structures, only surviving a few free-fall times. Long thought to be gravitationally bound, studies such as Clark & Bonnell (2004) show that this is not necessarily the case. Given their cold temperature, the lack of thermal support enhances fragmentation by gravitational instabilities, which is further promoted by turbulence (e.g. Clark & Bonnell 2005). Resulting over-dense sub-structures then themselves collapse locally, facilitating the formation of the direct progenitors of stars.

1.3 PRESTELLAR CORES

Gravitationally bound condensations of dense gas ranging in size from 0.01 pc to 0.1 pc represent the smallest constituent of the star formation process (e.g. Andre et al. 2000; Lomax et al. 2013). Termed cores, these are the direct progenitors of stars and can have masses from $0.1\,\mathrm{M}_\odot$ to tens of solar masses. As they are far denser than their parent molecular cloud with typical H_2 central densities exceeding $10^5\,\mathrm{cm}^{-3}$ (e.g. Keto & Caselli 2008), they are shielded from being heated by external radiation hence have cold temperature of typically 10 K achieved by radiative cooling. Cores are typically sub-divided into starless and protostellar cores, the key difference being that protostellar cores contain a Young Stellar Object (YSOs) whilst starless cores do not and represent the earliest core phase. Starless cores themselves are also subdivided into prestellar, gravitationally bound cores, and those which are unbound. A fraction of starless cores will become prestellar, while the remaining population will disperse back into the parent molecular cloud.

The Jeans mass is used to distinguish prestellar cores from unbound cores. For a spherically symmetric core with mean density ρ to collapse, its mass must be greater than the Jeans mass given by (Jeans 1928),

$$M_J = \left(\frac{4\pi}{3}\right)\frac{a_o^3}{G^{3/2}\rho^{1/2}}\,, \tag{1.1}$$

where G is the gravitational constant and a_o is the isothermal sound speed of the gas given by,

$$a_o = \left(\frac{k_B T}{\bar{m}}\right)^{1/2}\,, \tag{1.2}$$

where k_B is the Boltzmann constant, T is the temperature of the gas, and $\bar{m}$ is the mean mass of a gas particle. If we assume that the gas is isothermal, optically thin, that there is no source of support against gravity, and that the core mass exceeds M_J, during the initial stages of the collapse gravitational potential energy will be radiated away quickly and efficiently, occurring in a few free-fall times, t_{ff} given by,

$$t_{ff} = \left(\frac{3\pi}{32G\rho}\right)^{1/2}\,. \tag{1.3}$$

On the other hand, if we consider a core mass that fails to exceed M_J, without any external containing pressure the core will disperse in a time t_d given by,

$$t_d \simeq \frac{R}{\sigma}\,, \tag{1.4}$$

where R is the core radius, and σ is the internal velocity dispersion (e.g. Ward-Thompson & Whitworth 2015).

Whilst low-mass prestellar cores are routinely observed, dominating the observed core mass function (CMF) in star forming regions (e.g. Motte et al. 1998), their massive counterparts (of order a few hundreds of $M_{\odot}$) remain elusive. Truly starless cores are central to core accretion models of massive star formation (see Section 1.7) yet they are in particular notoriously elusive and often evade observation. Sanhueza et al. (2017) studied the fragmentation of a massive infrared dark clump, revealing that its cores (even though on the low-mass side, containing only $\sim$15$M_\odot$ within $0.01 - 0.1$ pc) appear to be starless from the lack of molecular outflow signatures. Cyganowski et al. (2014) find an excellent candidate for a massive prestellar core in G11.92-0.61. The core is devoid of maser and outflow emission, both classic telltale signs of embedded star formation. Bizarrely, it is also devoid of sub-millimetre molecular line emission despite it being an incredibly strong millimetre dust continuum source. Following chemical modelling, severe gas depletion due to freeze-out onto dust grains was found to be a plausible explanation given the extreme core physical conditions. The fitting of an SED revealed these core conditions to include 30 $M_\odot$ of gas within a small 1000 AU radius, implying a very large H_2 column density exceeding 10^{25} cm^{-2} if one assumes spherical symmetry.

1.4 Filaments

Filaments are elongated, over-dense structures of gas and dust, and are prevalent on a wide variety of size scales in the Universe, the importance of which in the interstellar context already recognised for decades (Schneider & Elmegreen 1979). Observed on the scales of tens of parsecs (Beuther et al. 2015; Kainulainen et al. 2016), filaments are seen to dominate the mass budget of GMCs at high densities (Schisano et al. 2014; Könyves et al. 2015). Some of the longest filaments have been observed to be as large as $\sim$100 pc in length (e.g. Wang et al. 2015, 2016). One such filament is the $\sim$80 pc long “Nessie” filament (Jackson et al. 2010; Goodman et al. 2014) observed to coincide with the Scutum-Centaurus galactic spiral arm. A sample of 7 velocity-coherent, $\sim$100 pc long filaments (named Giant Molecular Filaments) with masses ranging 10^4–$10^5$$M_\odot$ observed by Ragan et al. (2014) were all identified to be galactic inter-arm clouds, possibly corresponding to spurs that extend from the spiral arm as it rotates around the galactic centre.

On the scales of a few parsec, observations of the Galactic interstellar medium with the Herschel Space Observatory have revealed that filaments are a key intermediate stage towards the formation of stars (André et al. 2010; Molinari et al. 2010; Arzoumanian et al. 2011). As shown by the Herschel Gould Belt survey (HGBS) (André et al. 2010), the majority of prestellar and protostellar cores (the direct progenitors of stars) are embedded in the densest of filaments (Polychroni et al. 2013; Könyves et al. 2015; Marsh et al. 2016) whose mass-per-unit-length ($M_{\rm line}$) is larger than the theoretical upper limit for an isothermal, infinitely long cylinder to maintain hydrostatic equilibrium (Ostriker 1964) i.e. thermally supercritical in nature (see Figure 1.1). For an isothermal, self-gravitating cylinder of gas, this is given by,

$$M_{\rm line,crit} = \frac{2a_o^2}{G}\,, \tag{1.5}$$

where G is the gravitational constant, and a_o is the isothermal sound speed of the gas, given by equation 1.2. Taking typical values of 10K and solar metallicity, $M_{\rm line,crit} \sim 16.7\,{\rm M_\odot pc^{-1}}$. Understanding the connection between filament evolution and core formation has become one of the main goals of star formation research over the past decade.

Herschel observations seem to suggest that filaments that reside within molecular clouds have a near universal width of 0.1 pc regardless of the central density (Arzoumanian et al. 2011), a result that according to more recent work (André et al. 2016) prevails in much higher mass filaments outside of the Gould Belt. This is contradicted by Panopoulou et al. (2017), who do not find a characteristic scale in their spatial Fourier analysis of the data. Also, by observing the dense gas of the L1495 region of Taurus, Hacar et al. (2013) show that a number of velocity-coherent subfilaments (termed fibers) constitute filaments. This was further observed by Henshaw et al. (2017), who using ALMA resolve narrow structures in the previously known hub-filaments of the G35.28 IRDC with widths of typically 0.028±0.005 pc.

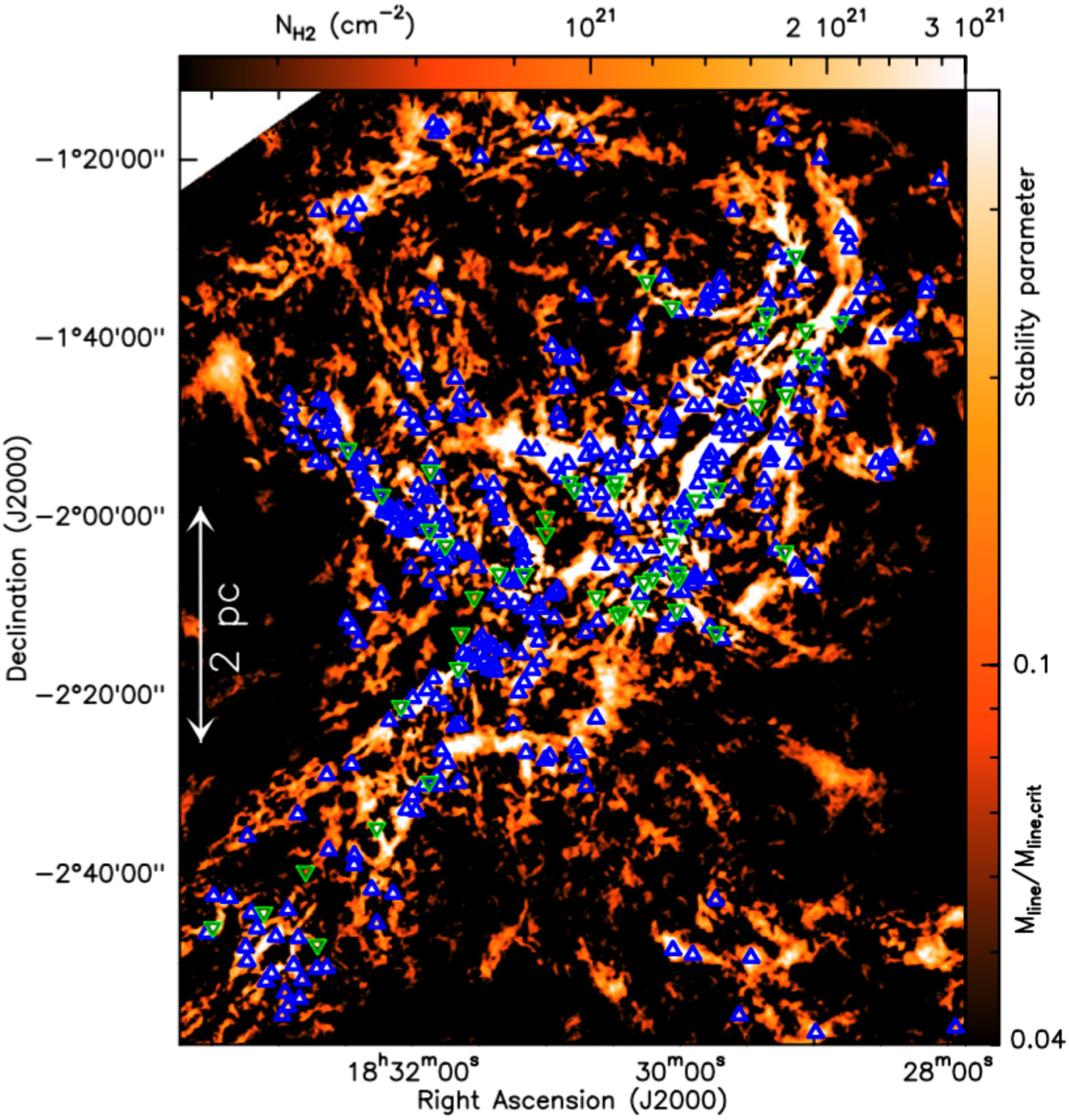

Figure 1.1 H_2 column density map of the Aquila region taken from Könyves et al. (2015), where the colour scale also corresponds to the stability of the filament assuming a constant filament width of 0.1 pc and the isothermal mass per unit length. White regions on the map correspond to supercritical filaments. Triangles mark the positions of prestellar and protostellar cores, in blue and green respectively. 90% of cores lie along the most supercritical filaments in the region, where the line mass $M_{line} \geq 15\,M_\odot$/pc, extinction $A_v \sim 7$ and surface density $\Sigma \sim 150\,M_\odot/pc^2$.

1.4.1 Formation

A cloud that is not perfectly spherical will naturally begin large scale collapse along its shortest axis. Numerically, the formation of filamentary structures has been shown to be a natural occurrence in the turbulent ISM (e.g. Federrath et al. 2010; Hennebelle et al. 2008; Smith et al. 2016), and can be simplified down to two main causes: the compression of an object, or the extension of an object. In the former case, such a process has been shown to be the collisions of shocked sheets of gas, generating stagnation points in the molecular cloud where turbulent energy is dissipated (e.g. Padoan et al. 2001; Klessen et al. 2005; Federrath et al. 2016), or converging flows of gas (e.g. Hennebelle et al. 2008; Gong & Ostriker 2015). The presence of magnetic fields promotes the formation of ever larger aspect ratio structures due to the extra support it provides against fragmentation (Hennebelle 2013). In the latter case, shear can be the formation mechanism (e.g. Hennebelle 2013), where two opposing flows of turbulent gas causes the pulling and extending of an object. This shear is especially felt by extended objects on galactic scales as they rotate around the galactic centre (Dobbs et al. 2015; Duarte-Cabral & Dobbs 2017).

Gravitational instabilities in a self-gravitating sheet has been shown to cause fragmentation (Miyama et al. 1987; Whitworth 2016). Perturbations of order a few times the thickness of the sheet cause the sheet to be unstable to fragmentation. The aspect ratio of the unstable mode increases over time, eventually lending itself to the formation of elongated filament structures. Hub-filament systems (networks of spatially converging filaments) are suggested to form in this gravity dominated way (Myers 2009).

Palmeirim et al. (2013) observe striations perpendicular to filaments in the L1495 region of Taurus which align parallel to the magnetic field direction. This suggests that these striations may represent funnels through which material flows along magnetic field lines onto filaments to be accreted. How much of a role this may play in the formation of the filament itself remains unclear.

1.4.2 FRAGMENTATION

Due to their geometry, filaments are prone to fragmentation. Inutsuka & Miyama (1992) and Miyama et al. (1994) showed that filaments in hydrostatic equilibrium fragment under density perturbations where the wavelength of the fastest growing mode is equal to four times the filament diameter. Further investigated by Clarke et al. (2016) who study the perturbations of an accreting filament, the fastest growing mode is found to be,

$$\lambda_{core} = 2\tau_{crit} a_o \,, \tag{1.6}$$

where a_o is the isothermal sound speed and τ_{crit} is the time it takes to build-up a critical filament through accretion, hence the time at which the filament becomes radially unstable. By measuring the separation of the periodic fragments along a filament, and rearranging equation 1.6 for τ_{crit}, one can calculate the lower limit on the age of the filament when it becomes supercritical. Naturally, the average accretion rate of the filament can also be calculated, using

$$\dot{M} = \frac{M_{\rm line,crit}}{\tau_{crit}} = \frac{2a_o M_{\rm line,crit}}{\lambda_{core}} \,, \tag{1.7}$$

where $\dot{M}$ is the mass accretion rate, and λ_{core} is the core spacing. However, it is unlikely that filaments settle down to equilibrium after ceasing accretion, and then proceed to fragment. Clarke et al. (2017) extend the work to include filaments that are accreting from a turbulent medium. To account for the turbulent medium, this alters the above equations by substituting the isothermal sound speed (a_o) for the effective sound speed, $a_{eff} = \sqrt{a_o^2 + \sigma_{1D}^2}$, where σ_{1D} is the one-dimensional velocity dispersion.

Hacar et al. (2013) find the presence of velocity-coherent fibers within larger-scale interstellar filaments. Smith et al. (2016) propose a *"fragment and gather"* scenario, where fibers fragment due to turbulence in the ISM and are gathered together by gravitational collapse into bundles of filaments in a larger, higher column density filament structure. Tafalla & Hacar (2015) instead propose the hierarchical *"fray and fragment"* scenario, where filaments (that first formed from colliding flows) further fragment into fibers, which in turn fragment into cores. Hierarchical fragmentation of filaments into cores is a popular mechanism, often interpreted in observation (e.g. Takahashi et al. 2013; Friesen et al. 2016; Henshaw et al. 2016a). However, Gong & Ostriker (2015) on the other hand find that in their numerical simulations (where they focussed on regions where supersonic turbulent gas flows converge) that filaments and cores form simultaneously instead of hierarchically.

Much remains unclear about filament formation and fragmentation, and they are both key areas of star formation research. While a lot of effort has focused on the properties of individual filaments in nearby star-forming regions (Arzoumanian et al. 2011; Peretto et al. 2012; Palmeirim et al. 2013; Panopoulou et al. 2014; Salji et al. 2015), this thesis focusses on hub filament systems (HFS), i.e. a small network of spatially converging interstellar filaments (Myers 2009). The converging nature of such systems is suggestive of the role played by gravity in shaping them. Follow-up observations have shown that hubs are likely collapsing on parsec scales, gathering matter at their centre as a result of the collapse (e.g. Peretto et al. 2013, 2014; Liu et al. 2013; Henshaw et al. 2016a). Kirk et al. (2013) in particular showed that for the filaments in the Serpens South cloud of Aquila that accretion flows govern the evolution of the hub-filament system, providing the material for YSOs to form towards its centre.

Schneider et al. (2012) showed that stellar protoclusters in the Rosette molecular cloud tend to form at the junction of high-column density filamentary structures. One of the most massive prestellar cores ever observed in the Galaxy was found lying at the centre of a hub-filament system called SDC335 with a staggering $545(\pm^{770}_{385})\,M_{\odot}$ of gas within an 0.05 pc radius (Peretto et al. 2013; Avison et al. 2015), indicating that such hubs may play a key role in the formation of massive stars. As can be seen in the three-colour composite image of SDC335 in Figure 1.2, the filaments appear dark at the *Spitzer* mid-infrared wavelengths, classifying this cloud as an infrared dark cloud (IRDC).

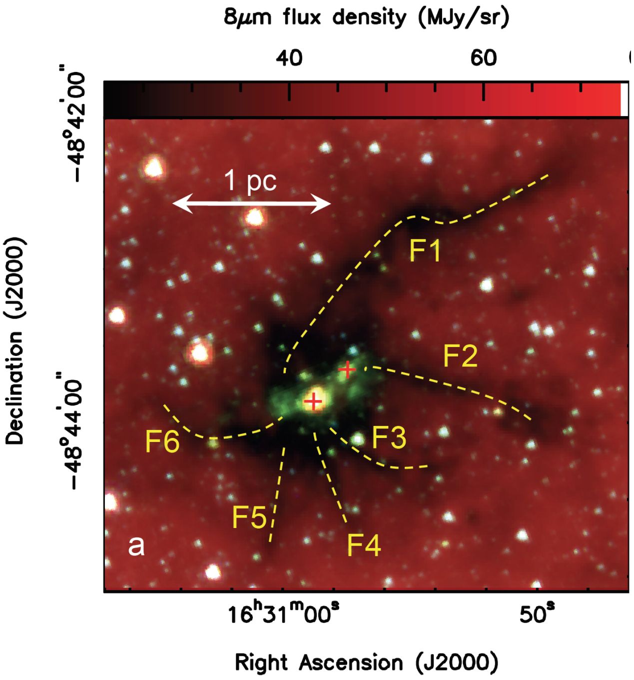

Figure 1.2 Composite image of the SDC335 hub-filament system, using *Spitzer* mid-infrared wavelengths, where R, G and B bands correspond to 8μm, 4.5μm and 3.6μm emission, taken from Peretto et al. (2013).

1.5 Infrared Dark Clouds

IRDCs are cold ($T < 20K$) and dense ($n > 10^3\,cm^{-3}$) reservoirs of gas seen in extinction against the bright mid-infrared emission of the Galactic plane background (Perault et al. 1996; Egan et al. 1998; Simon et al. 2006; Peretto & Fuller 2009; Butler & Tan 2009; Peretto et al. 2010). They are considered to be mostly undisturbed by stellar feedback due to the lack of a significant embedded population of stars, hence preserving the pristine fingerprints of the cloud initial conditions prior to the onset of star formation. IRDCs exhibit a wide range of morphologies, masses, and sizes (Peretto et al. 2010), the most massive of which are thought to contain the initial conditions required for the formation of massive stars (Rathborne et al. 2006; Pillai et al. 2006; Beuther & Steinacker 2007). Millimeter continuum studies of IRDCs show that they are fragmented into a number of cores. While most are quiescent, some cores show signatures of active star formation, including water maser emission or a bright 24μm compact source for example (e.g. Wang et al. 2006; Ragan et al. 2011), and high mass protostars (e.g. Beuther et al. 2005; Pillai et al. 2006). Avison et al. (2015) identify the presence of three hyper-compact Hii regions at the heart of the SDC335 infrared dark hub-filament system, two of them residing in the $\sim 500\,\mathrm{M}_\odot$ protostellar core identified by Peretto et al. (2013). Hyper-compact Hii regions are by nature small ($r < 0.03\,\mathrm{pc}$) and dense ($n > 10^6\,,\mathrm{cm}^{-3}$), hence are associated with the earliest stages of massive star formation (Kurtz 2005; Sánchez-Monge et al. 2011).

Understanding how hub-filament systems form and evolve can tell us what physical mechanisms are behind the fragmentation of filaments and how their interaction influence the formation of more massive objects. High-angular resolution observations of infrared dark clouds in particular provides us with the opportunity for such studies very early on in their evolutionary stage. Such a study is the focus of this thesis, which uses molecular line emission to constrain the kinematics and fragmentation of an infrared dark hub.

1.6 Molecular tracers

Even though the largest constituent of molecular clouds is molecular hydrogen, H_2 is a symmetric molecule meaning it does not have a permanent dipole moment. Molecular clouds must therefore be traced indirectly using other molecules. The detectability of such molecules has some dependence on its critical density, which is defined as the density at which the spontaneous and collisional de-excitation of a photon from the upper energy level are equal, and can be written as,

$$n_{crit} \equiv \frac{A_{u,l}}{C_{u,l}} \, , \tag{1.8}$$

where $A_{u,l}$ and $C_{u,l}$ are the Einstein coefficients for spontaneous and collisional de-excitation respectively. Gas with density larger than n_{crit} is said to be thermally excited, while gas with density lower than n_{crit} is sub-thermally excited. In the context of this PhD, I have analysed CO and NH_3 molecular line emission to study the star formation in an IRDC called SDC13. The rest of this section discusses these two tracers.

1.6.1 CARBON MONOXIDE (CO)

Carbon Monoxide (CO) is a asymmetric molecule, and has a charge differential over the two ends of the molecule, meaning it has a strong permanent dipole moment. At the high column densities of molecular clouds and IRDCs, CO self-shields itself from destruction by external radiation (e.g. Visser et al. 2009; Glover & Clark 2012) allowing it to become the second most abundant molecule after H_2. As a result, its rotational transitions are easily excited in the cold interiors of molecular clouds.

The most abundant CO isotope is $^{12}C^{16}O$ (hereafter ^{12}CO), which due to its low critical density (see Table 1.1) is excited in the diffuse, low density regions of molecular clouds. In particular, the $^{12}CO(1\text{–}0)$ rotational transition is generally optically thick and thermally excited, making it a good tracer of the gas kinetic temperature, but a poor tracer of the inner regions of cores for example. The second most abundant CO isotope is $^{13}C^{16}O$ (hereafter ^{13}CO) with an abundance of 1/61 compared to ^{12}CO (Wilson & Rood 1994). Given its low optical depth it is able to trace denser regions than ^{12}CO. $^{12}C^{18}O$ (hereafter $C^{18}O$) is even more optically thin and is incredibly rare with an abundance of 1/500 compared to ^{12}CO (Wilson

Table 1.1 The critical densities of the J = 1–0 transitions of three CO isotopologues, and of the (J,K) = (1,1) and (2,2) NH_3 transitions. The Einstein $A_{u,l}$ coefficients and the rest frequency ν were taken from LAMDA (Schöier et al. 2005). The Einstein $C_{u,l}$ coefficients for the CO isotopologues were taken from Yang et al. (2010) (at a temperature of 20 K), whilst those for NH_3 were taken from Danby et al. (1988) (at a temperature of 15 K).

Molecule	$A_{u,l}$ (s^{-1})	$C_{u,l}$ ($cm^{-3}s^{-1}$)	n_{crit} (cm^{-3})	ν (GHz)
$^{12}CO(1\text{–}0)$	7.2×10^{-8}	3.3×10^{-11}	2.3×10^{3}	115.271
$^{13}CO(1\text{–}0)$	6.3×10^{-8}	3.3×10^{-11}	1.9×10^{3}	110.201
$C^{18}O(1\text{–}0)$	6.3×10^{-8}	3.3×10^{-11}	1.9×10^{3}	109.782
$NH_3(1,1)$	1.7×10^{-7}	8.6×10^{-11}	1.9×10^{3}	23.694
$NH_3(2,2)$	2.3×10^{-7}	1.1×10^{-10}	2.1×10^{3}	23.723

& Rood 1994). Therefore, $C^{18}O$ traces the densest gas of these three isotopologues. The Einstein $A_{u,l}$ and $C_{u,l}$ coefficients, critical densities and rest frequencies of these three CO isotopologues are tabulated in Table 1.1.

CO surveys are particularly used for the identification of molecular clouds, such as the entire Milky Way in $^{12}CO(1\text{–}0)$ (Dame et al. 1987, 2001), the ^{12}CO High-Resolution Survey of the Galactic Plane (COHRS, Dempsey et al. 2013) in $^{12}CO(3\text{–}2)$, and the CO Heterodyne Inner Milky Way Plane Survey (CHIMPS, Rigby et al. 2016) in $^{13}CO(3\text{–}2)$ and $C^{18}O(3\text{–}2)$.

The cloud conditions traced by the ratio (called $R_{2,1/1,0}$) of the two lowest rotational transitions of ^{12}CO (the $J = 2 - 1$ and $J = 1 - 0$ transitions) have been studied (e.g. Sakamoto et al. 1994; Nishimura et al. 2015). It is found that towards the centre of the Orion GMC for example, $R_{2,1/1,0} \sim 1$, however it decreases outwardly to ~ 0.5, attributed to density variations under an isothermal assumption. More recently, Peñaloza et al. (2017) show that the ratio in their synthetic clouds is in fact bimodal, peaking at 0.7 and 0.3 representing the tracing of two distinct cloud conditions: firstly, the high mean density and low mean temperature regime, and secondly the low mean density and high mean temperature regime. Such a bimodal behaviour of $R_{2,1/1,0}$ is attributed to the fact that when $R_{2,1/1,0} \sim 0.3$, both $J = 2 - 1$ and $J = 1 - 0$ lines are sub-thermally excited, whilst when $R_{2,1/1,0} \sim 0.7$, the $J = 1 - 0$ is thermalised whilst $J = 2 - 1$ remains sub-thermal. This results in a bimodal instead of a continuous population, as CO becomes optically thick very quickly once thermalised, hence its emission becomes saturated. This analysis suggests that were a molecular cloud observed with both these transitions, evaluating whether its $\mathrm{R}_{2,1/1,0}$ ratio is found within the high or low peak of the bimodal distribution places constraints on the cloud conditions, ultimately allowing the probing of different regimes observationally within molecular clouds.

1.6.2 AMMONIA (NH_3)

The Ammonia molecule (NH_3) has a trigonal-pyramid arrangement of its three Hydrogen (H) atoms at the base of the pyramid, and a single Nitrogen (N) atom at the tip of the pyramid (Figure 1.3). Two species of NH_3 exist depending on the orientation of the Hydrogen atom spins: ortho-NH_3 for parallel Hydrogen spins, and para-NH_3 for non-parallel spins (Ho & Townes 1983). Each of the labelled axes in Figure 1.3 (A, B and C) denote the three principle axes of rotation, which have associated moment of inertia components I_A, I_B and I_C and total angular momentum ($\mathbf{J}$) components of J_A, J_B and J_C. As a result, the kinetic energy may be calculated following,

$$E_{\mathrm{rot}} = \frac{J_A^2}{2I_A} + \frac{J_B^2}{2I_B} + \frac{J_C^2}{2I_C}\,. \tag{1.9}$$

NH_3 is a symmetric top molecule, meaning that it has two degenerate axes of rotation (axes B and C) with identical moment of inertia components, and one unique axis of rotation (axis A). In particular, NH_3 is a prolate molecule (where its shape resembles a rugby ball), meaning that axis A has a lower I component than axes B and C i.e. $I_A < I_B = I_C$. If the molecule were to be oblate (with a shape resembling a disk), I_A would be greater than I_B and I_C.

The projection of the total angular momentum vector $\mathbf{J}$ onto the principal axis

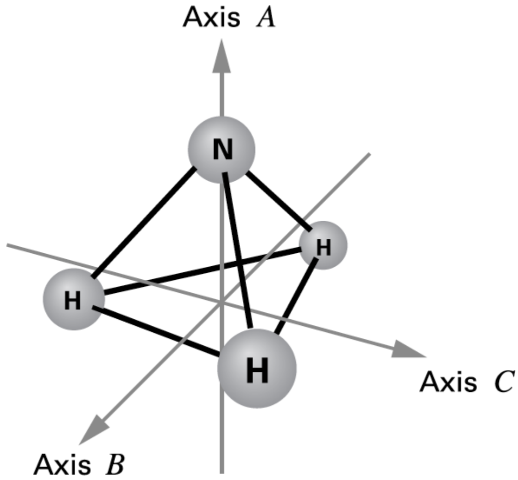

Figure 1.3 A schematic of the trigonal-pyramid arrangement of the NH_3 molecular (Stahler & Palla 2005).

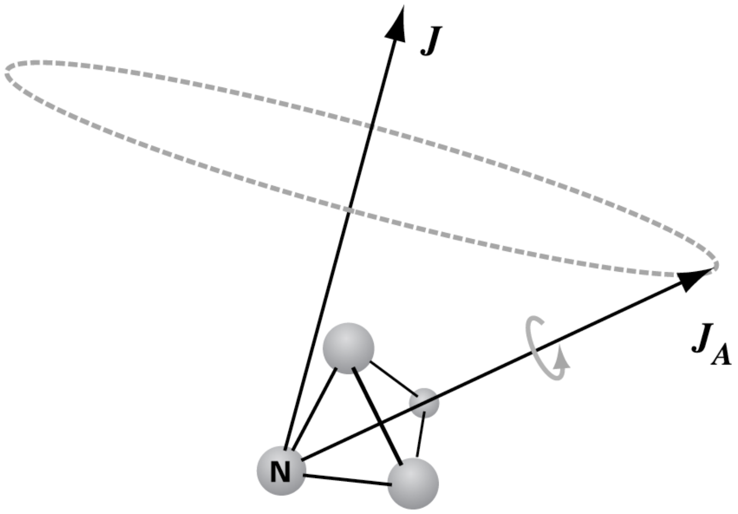

Figure 1.4 A schematic denoting the multiple axes of rotation of the NH_3 molecule's rotation inversion transition (Stahler & Palla 2005).

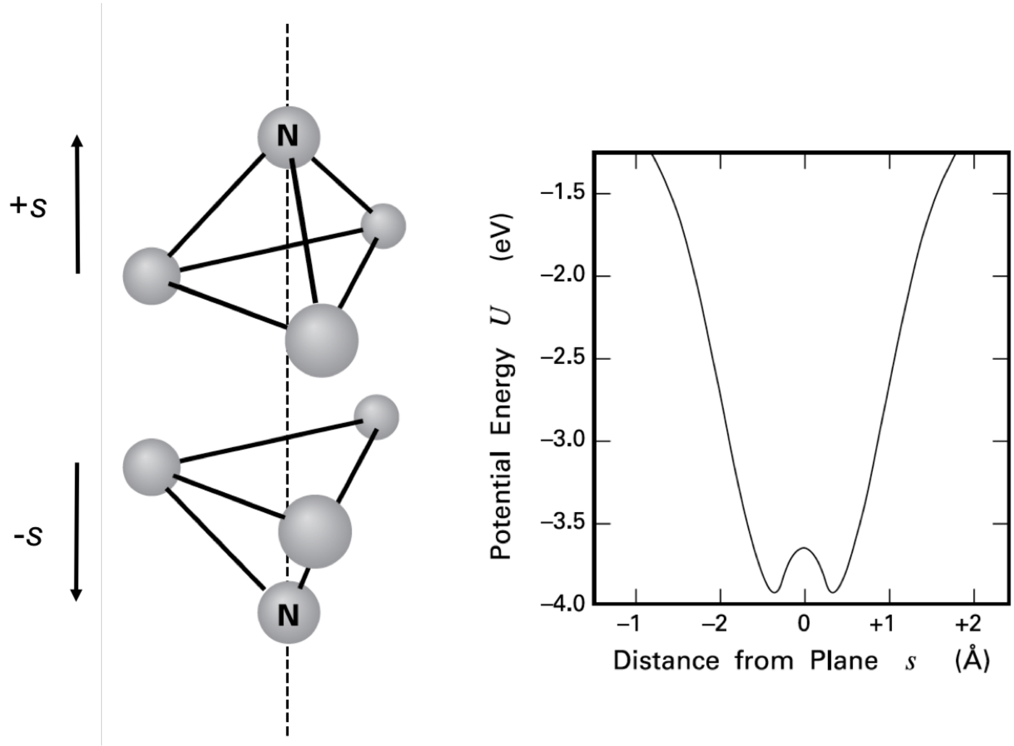

Figure 1.5 *Left*: Schematic of the inversion transition of NH_3, slightly adapted from Stahler & Palla (2005). The distance of the Nitrogen atom from the plane of Hydrogen atoms is denoted by s. The positive s direction denotes when N is above the plane, while negative s denotes when the N atom has tunneled through the plane. *Right*: the potential energy of NH_3 as a function of s. The Nitrogen atom can oscillate through the energy barrier at the Hydrogen plane ($s \sim 0$).

is labelled by K. NH_3 emission is described following the (J,K) notation. Selection rules state that no radiative transitions between K values are allowed, hence NH_3 emission is considered as independent "K-ladders". As such, the J transitions within a K-ladder are greatly collisionally dependent, therefore reflecting the thermal properties of the emitting gas. The upper states in a K-ladder (where J is much greater than K) are called *nonmetastable* states as they can rapidly decay their J values by $\Delta J = 1$. However the lower states (approaching J = K at the bottom of the K-ladder) are called *metastable* states as they are far longer lived, making them excellent tracers of gas thermal properties.

In particular, the (J,K) = (1,1) transition of NH_3 is classed as a rotation inversion transition. Figure 1.4 shows the multiple modes of rotation of the entire NH_3 molecule. Not only does it rotate about the principle axis perpendicular to the Hydrogen plane (axis A), but it also precesses about the axis aligned with the total angular momentum vector, **J**. Furthermore, as shown in Figure 1.5, the Nitrogen atom inverts its trigonal-pyramid structure, as it tunnels through the energy barrier of the double-potential well at the Hydrogen atom plane. Usually, the Nitrogen atom is trapped in a single potential well as it does not have enough energy to pass the barrier. However, quantum theory states that the Nitrogen atom can tunnel through the energy barrier. This leads to transitions called inversion doublets with a main line wavelength (denoted by the transition labelled ν_{22} in Figure 1.6) of 1.3 cm. These inversion doublet transitions split again due to hyperfine interactions, mostly due to the interaction of the electric quadrupole moment of the Nitrogen nucleus (due to the non-spherical charge distribution) and the electric field of the electrons. The basic quadrupole splitting transitions further split due to weak magnetic interactions between the nuclei spins. In total, this leads to 18 hyperfine transitions for the (J,K) = (1,1) rotation inversion transition (shown in Figure 1.6), and 21 hyperfine transitions for the (J,K) = (2,2) rotation inversion transition (Townes & Schawlow 1955; Kukolich 1967). Of the 18 and 21 hyperfine transitions, 5 and 3 groups of lines respectively are typically resolved in astronomical observations with the current best spectral set-up. The rest frequencies of $NH_3(1,1)$ and $NH_3(2,2)$ are 23.6944955 GHz and 23.7226336 GHz respectively (Ho & Townes 1983), and examples of their synthetic spectra are shown in Figure 1.7.

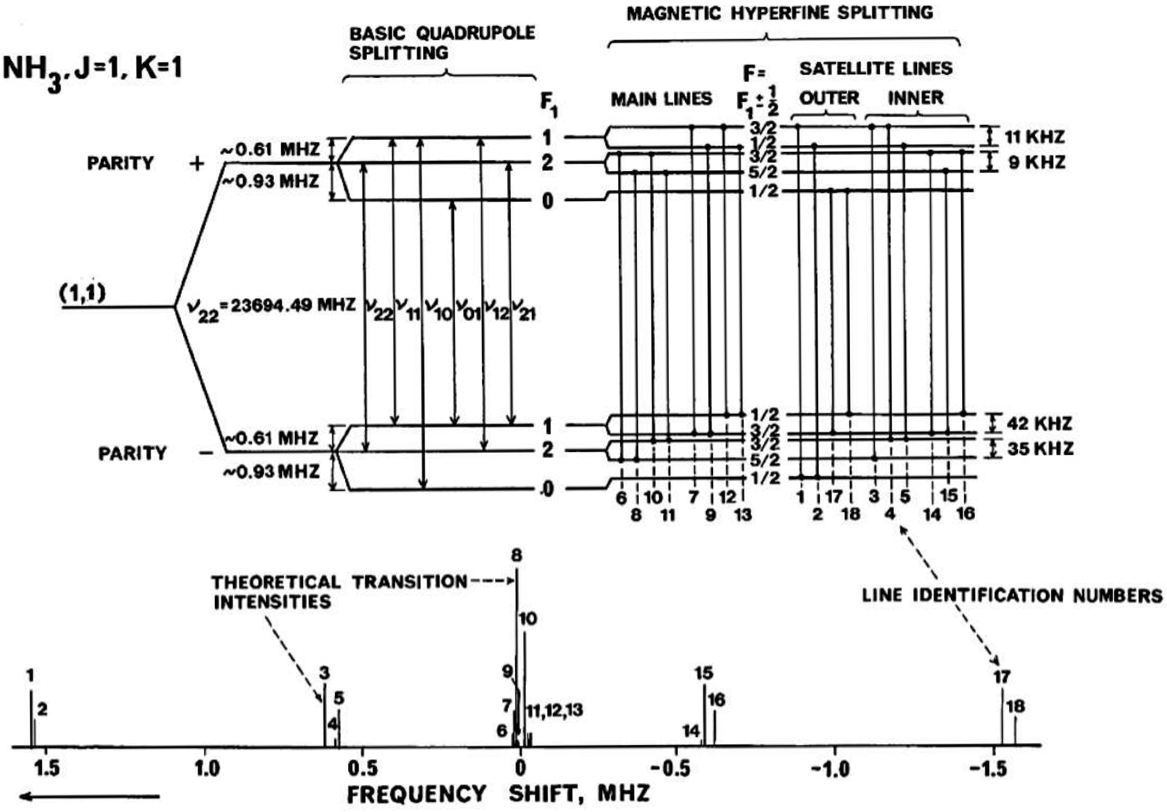

Figure 1.6 Schematic taken from Rydbeck et al. (1977), indicating all allowed hyperfine transitions of the $NH_3(1,1)$ rotation inversion transition with an arrow.

NH_3 as a dense gas tracer in the interstellar medium

The discovery of NH_3 towards the Galactic centre by Cheung et al. (1968) was pivotal in the realization that the interstellar medium (ISM) is denser than previously thought. NH_3 has a critical density of $n \simeq 10^3\,\mathrm{cm}^{-3}$, however given the hyperfine splitting, the emission from the (J,K)=(1,1) line is spread over a large $40\,\mathrm{kms}^{-1}$ for example, increasing the effective column density of the line to $n \geq 10^5\,\mathrm{cm}^{-3}$. For this reason, as well as the long-lived nature of the J = K levels previously discussed, the

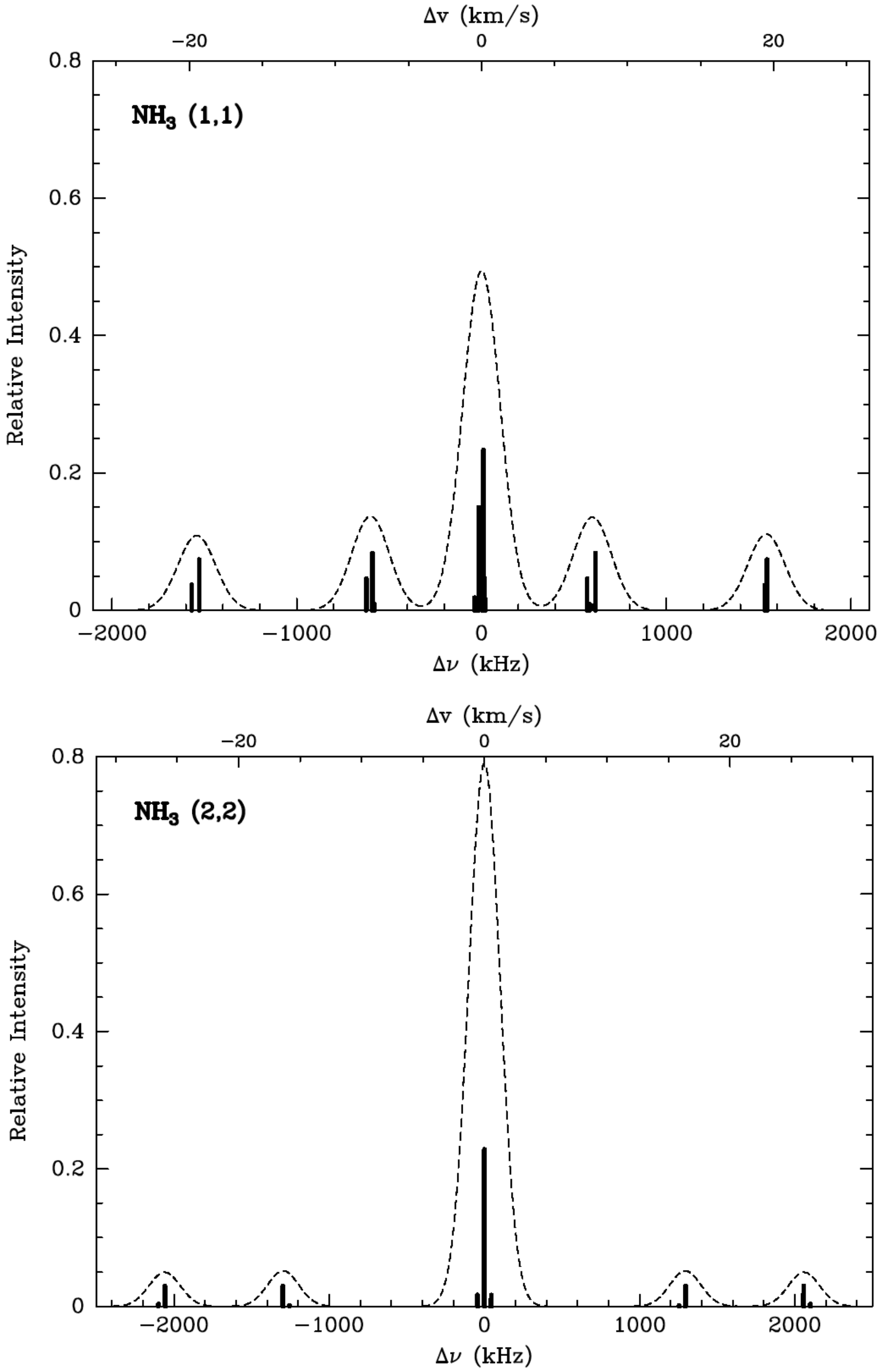

Figure 1.7 Synthetic spectra taken from Mangum & Shirley (2015) of the NH_3(1,1) (top) and NH_3(2,2) (bottom) spectra. Each solid black line indicates the hyperfine structure transitions and their relative intensities. Frequencies on the x-axis are relative to the rest frequencies of the lines. The overplotted dashed line is a result of a Gaussian convolution, and shows the overall shape one can expect from their resolvable astronomical spectra.

(J,K) = (1,1) and (2,2) rotation inversion transitions are particularly good tracers of the cold ($< 20\,\mathrm{K}$) and dense ($n \geq 10^3\,\mathrm{cm}^{-3}$) gas of early stage star formation in molecular clouds and IRDCs. Additionally, NH_3 has been shown to not be depleted in core environments, such as L1498 for example studied by Tafalla et al. (2004), where $C^{18}O$ was in contrast strongly depleted.

Using the 22 metre Mopra radio telescope, the H_2O Galactic Plane Survey (HOPS, Walsh et al. 2008; Purcell et al. 2012) simultaneously mapped 100 square degrees of the Galactic plane in NH_3, maser and radio recombination line (RRL) emission. Longmore et al. (2013) collated data from HOPS, and compared the NH_3 emission distribution to the location of star formation tracers, such as the location of HII regions and water or methanol maser emission. They find that even though 80% of the NH_3(1,1) integrated emission is concentrated within the first few degrees of the Galaxy's central molecular zone (CMZ), the concentration of star formation tracers do not seem to correspond remarkably, with a typically even distribution across the plane, suggesting that star formation around the Galactic centre is less efficient.

NH_3 is often termed the thermometer of molecular clouds. Unlike other common tracers such as CO or N_2H^+ for example, the temperature of the gas can be directly calculated from the ratio of the intensities of the NH_3 (J,K) = (1,1) and (2,2) rotation inversion transitions. For conducting such a calculation, one must begin with the opacity of the gas.

Opacity

The opacity (τ) of a gas defines its optical thickness. Being inversely proportional to the photon mean free path, τ describes how long before an emitted photon is reabsorbed. Typically, an optically thin gas (where $\tau < 1$) allows the photon to travel further than in an optically thick gas (where $\tau \geq 1$). The opacity is found by solving the following numerically, (Barrett et al. 1977),

$$\frac{\Delta T_a(1,1,m)}{\Delta T_a(1,1,s)} = \frac{1 - e^{-\tau(1,1,m)}}{1 - e^{-a\tau(1,1,m)}} \,, \tag{1.10}$$

where the parameters $\Delta T_a(1,1,m)$ and $\Delta T_a(1,1,s)$ refer to the observed peak spectra of the NH_3(1,1) main (denoted by the m) and satellite (denoted by the s) components. The expected relative intensities between the main and inner satellite lines is denoted by a. The opacity of the main NH_3(1,1) line is denoted by $\tau(1,1,m)$. This opacity is converted to the total opacity of all components $\tau(1,1,t)$ (denoted by the t) by dividing by the relative strength of the remaining component to the main component, of 0.502 (Li et al. 2003).

The opacity of NH_3(2,2) is calculated similarly (Barrett et al. 1977),

$$\frac{\Delta T_a(1,1,m)}{\Delta T_a(2,2,m)} = \frac{1 - e^{-\tau(1,1,m)}}{1 - e^{-\tau(2,2,m)}} \,, \tag{1.11}$$

where $\Delta T_a(2,2,m)$ and $\tau(2,2,m)$ are the observed peak of the spectra and the opacity of the NH_3(2,2) main component, respectively. This opacity is converted to the total opacity, $\tau(2,2,t)$ of NH_3(2,2) by dividing by the relative strength of 0.796 (Li et al. 2003).

Temperature

If a gas is in thermal equilibrium with its surroundings, the number of molecules at a given rotational energy in an ensemble is described by the Boltzmann distribution,

$$\frac{n_J}{n_o} = \frac{g_J}{g_o} \exp\left(\frac{-(E_J - E_o)}{k_B T_{ex}}\right) \,, \tag{1.12}$$

where subscript o and J denote the lowest rotational state (at $J = 0$) and the J^{th} energy state respectively, n is the number of density of molecules, g is the statistical weight. T_{ex} is the excitation temperature of the gas, defined as the temperature that will reproduce the observed ratio of the zeroth and the J^{th} energy states. When the conditions are in Local Thermodynamic Equilibrium (LTE), T_{ex} is also equal to the kinetic temperature T_k, which is the temperature at which the Maxwell-Boltzmann distribution (see equation 1.20) of particle motions is reproduced, hence characterises the random gas velocities.

In LTE, the total number density of molecules, n, is given by,

$$n = \sum_{i=0}^{\infty} n_i \, . \tag{1.13}$$

Assuming the molecule's level populations can be described by a Boltzmann distribution, n may be evaluated from the population of a single energy level. Substituting equations 1.12 and 1.13 gives,

$$n = \frac{n_o}{g_o} \exp\left(\frac{E_o}{k_B T}\right) Q(T_{ex}) \, , \tag{1.14}$$

where Q(T) is the rotational partition function given by $Q(T_{ex}) = \sum\limits_i g_i \exp\left(\frac{-E_i}{k_B T_{ex}}\right)$. The rotational temperature (T_{rot}) describes the relative populations of the NH_3(1,1) and NH_3(2,2) levels, and can be found from integrating n over a path length, and the Boltzmann distribution by,

$$\frac{N_{2,2}}{N_{1,1}} = \frac{g_{2,2}}{g_{1,1}} \exp\left(-\frac{E_{2,2} - E_{1,1}}{k_B T_{rot}}\right) \, , \tag{1.15}$$

where $N_{J,K}$, $E_{J,K}$ and $g_{J,K}$ are the column densities, energies, and statistical weights of the $(J, K) = (1, 1)$ and $(2, 2)$ transitions. The statistical weights of the two transitions are 3 and 5 respectively, whilst $T_o = (E_{2,2} - E_{1,1})/k_B = 41\,\mathrm{K}$. From assuming optically thin transitions, it is known that the column density of a state can be expressed as $N_{J,K} \propto \tau(J, K, t)\Delta v_{J,K}/A_{J,K}$, where $\tau(J, K, t)$, $\Delta v(J, K)$ and $A_{J,K}$ are the total optical depths, velocity width, and Einstein coefficients for spontaneous de-excitation of the $(J, K) = (1, 1)$ and $(2, 2)$ transitions. Rearranging equation 1.15 for T_{rot} and substituting for $N_{J,K}$ and the constants yields the expression,

$$T_{rot} = -41\mathrm{K}/\ln\left(\frac{9}{20}\frac{\tau(2,2,t)}{\tau(1,1,t)}\left[\frac{\Delta v_{2,2}}{\Delta v_{1,1}}\right]\right) . \tag{1.16}$$

If one were to assume that the NH_3(1,1) and NH_3(2,2) emission are excited in the same volume of gas, one could simplify this equation by assuming that both velocity widths are equal. This means that the rotational temperature of the gas may be evaluated from the ratio of the emission line intensities only.

Column density

With opacity and temperature, the total column density of NH_3 and H_2 can be calculated. Firstly, the column density of the NH_3(1,1) upper level only can be evaluated by (Goldsmith & Langer 1999),

$$N[\mathrm{NH_3}(1,1)] = \frac{8\mathrm{k}\pi\nu_{1,1}^2}{\mathrm{A}_{1,1}\mathrm{hc}^3}\int_{-\infty}^{\infty}\mathrm{T_b dv}\left(\frac{\tau(1,1,\mathrm{t})}{1-\mathrm{e}^{-\tau(1,1,\mathrm{t})}}\right) , \tag{1.17}$$

where k is the Boltzmann's constant, $\nu_{1,1}$ is the rest frequency of the NH_3(1,1) line, $A_{1,1}$ is the Einstein Coefficient for spontaneous emission, h is the Planck constant, c is the speed of light, $\tau(1,1,t)$ is the total opacity of the NH_3(1,1) line, and $\int_{-\infty}^{\infty} T_b \mathrm{dv}$ is the integrated intensity of NH_3(1,1) emission. Beam information can be ignored under the assumption that the source fills the beam. In the case of extended sources, this is a fair assumption.

Assuming local thermodynamic equilibrium (LTE), where the rotational temperature is assumed to equal the excitation temperature, $N[\mathrm{NH_3}(1,1)]$ was converted into the total column density of Ammonia, $N(\mathrm{NH_3})$ (Goldsmith & Langer 1999),

$$N(\mathrm{NH_3}) = \frac{N[\mathrm{NH_3}(1,1)]}{g_{1,1}} e^{E_{1,1}/\mathrm{k}T_{rot}} Q(T_{rot}) , \tag{1.18}$$

where $g_{1,1}$ is the statistical weight, $E_{1,1}$ is the energy of the NH_3(1,1) line, T_{rot} is the rotational temperature, and $Q(T_{rot})$ is the partition function. Expanding the partition function, $Q(T_{rot}) = \sum_i g_i e^{-E_i/kT_{rot}}$ over J and K energy levels, where J and K are the transition quantum numbers (Ungerechts et al. 1986),

$$N(\mathrm{NH_3}) = N[\mathrm{NH_3}(1,1)] \left[\frac{1}{3} \mathrm{e}^{+23.26/\mathrm{T_{rot}}} + 1 + \frac{5}{3} \mathrm{e}^{-41.18/\mathrm{T_{rot}}} \cdots \right], \tag{1.19}$$

where T_{rot} is the rotational temperature, and $N[\mathrm{NH_3}(1,1)]$ follows from Equation 1.17. The H_2 column density is calculated by assuming an abundance of NH_3 to H_2 of $[\mathrm{NH_3}]/[\mathrm{H_2}] \sim 3 \times 10^{-8}$ (Harju et al. 1993).

The NH_3(2,2) transition is a weaker emitter than NH_3(1,1), and is separated from the energy of the (1,1) line by 41 K. This means that the coverage of the final column density map is limited to the regions of the NH_3(2,2) emission. This was discussed at length by Morgan et al. (2013) who show how much coverage can be recovered if one makes a global assumption on the temperature, without introducing significant changes to the common areas of coverage.

1.6.3 LINE BROADENING

Molecular lines are most commonly used to trace the kinematics of gas in molecular clouds. Emission lines are broadened by a variety of processes, the study of such broadening giving us information about the internal motion of the gas. The most fundamental line broadening process is natural line broadening (or intrinsic line broadening) as a consequence of the Heisenberg uncertainty principle, $\Delta E_i \Delta t_i \sim \hbar$. This arises as the energy (ΔE_i) of an excited state i cannot be precisely measured because of its finite lifetime (Δt_i), resulting in a superposition of possible states spread across the energy E_i. However, this is not a significant process in the ISM.

Thermal broadening

Thermal (or Doppler) broadening occurs due to a distribution of individual atom or molecule random motions. The distribution of these velocities can be found by the one-dimensional Maxwell-Boltzmann distribution,

$$dN(V_{los}) = N\left(\frac{m}{2\pi k_B T}\right)^{1/2} \exp\left(-\frac{mV_{los}^2}{2k_B T}\right) dV_{los}\,, \tag{1.20}$$

where V_{los} is the atom velocity component along the line of sight, m is the mass of the atom which is assumed to be in thermal equilibrium at temperature T, and N gives the number of atoms with a given velocity.

According to the Doppler effect, if an atom with velocity component $V_{los} << c$ emits a photon with a frequency ν_o, it is detected at a different frequency ν given by:

$$\frac{\nu_o - \nu}{c} = \frac{V_{los}}{c}\,. \tag{1.21}$$

Therefore the one-dimensional velocity of the atom is related to frequency. Combining equations 1.21 and 1.20 gives a profile function of the emitted radiation in terms of frequency,

$$\phi_D(\nu) = \frac{c}{\Delta\nu_D}\left(\frac{m}{2\pi k_B T}\right)^{1/2} \exp\left(-\frac{mc^2}{2k_B T}\frac{(\nu-\nu_o)^2}{\Delta\nu_D^2}\right)\,, \tag{1.22}$$

the morphology of such a profile being of Gaussian shape. This profile function yields the Doppler width $\Delta\nu_D$ defined as,

$$\Delta\nu_D = \frac{\nu_o}{c}\left(\frac{2k_B T}{m}\right)^{1/2}\,. \tag{1.23}$$

In radio astronomy, the full width half maximum (FWHM) of a line is found by solving equation 1.22 at half intensity,

$$\exp\left(-\frac{mc^2}{2k_BT}\frac{\Delta\nu^2}{4\nu_o^2}\right)=\frac{1}{2}\,, \tag{1.24}$$

giving a FWHM line width of a purely thermally broadened line of,

$$\Delta\nu=\left(\frac{8\ln 2k_BT}{mc^2}\right)^{1/2}\nu_o\,, \tag{1.25}$$

where $\Delta\nu$ is the FWHM line width, or written in terms of velocity as,

$$\Delta V_{FWHM}(\text{therm})=\left(\frac{8\ln 2k_BT}{m}\right)^{1/2}\,. \tag{1.26}$$

This can also be re-written in terms of the one-dimensional velocity dispersion $\sigma_{\rm 1D}(\text{therm})$ as,

$$\Delta V_{FWHM}(\text{therm})=2(\ln 2)^{1/2}\left(\frac{\Delta\nu_D}{\nu_o}\right)c\,, \tag{1.27}$$

where $\sigma_{\rm 1D}(\text{therm})=\frac{\Delta\nu_D}{\nu_o}c$.

Turbulent broadening

The total velocity dispersion is defined as the sum in quadrature of both thermal and non-thermal contributions. These non-thermal motions are what contribute to turbulent broadening of an emission line, given by (Myers 1983),

$$\sigma_{NT,1D}=\sqrt{\frac{\Delta V^2_{FWHM}(\text{therm})}{8\ln 2}-\frac{k_BT}{m}}\,, \tag{1.28}$$

where $\sigma_{NT,1D}$ is the non-thermal one-dimensional velocity dispersion. Such non-thermal motions may be due to turbulent random fluid motions, infalling material accreting onto a core, rotation, or shocks propagating through the medium.

Kolmogorov (1941) presented a theory of how turbulent energy is conserved and cascaded down from large, unstable eddies of turbulent motion that break up into smaller eddies, deriving a characteristic relation between the velocity dispersion σ and size L of an eddy,

$$\sigma \propto L^{1/3} \, . \tag{1.29}$$

This conserved-cascade of energy to successively smaller eddies continues until a stable eddy is reached, where the energy is then dissipated on small-scales supersonic shocks, shown numerically to occur in a free-fall time (e.g. Padoan et al. 2001).

Turbulence dissipation in prestellar cores has been observed (e.g. Fuller & Myers 1992; Goodman et al. 1998; Caselli et al. 2002; Pineda et al. 2010, 2015), where distinct decreases in the non-thermal velocity dispersion at the positions of prestellar cores compared to the surrounding gas were observed. The term "transition to coherence" was coined for this behaviour, suggesting that cores have sizes that are intimately linked to the turbulent properties. More recently, this transition to coherence has also been observed towards entire parsec-long filaments (Hacar & Tafalla 2011; Hacar et al. 2016). Such transonic cores and filaments are expected to form in the turbulent ISM where supersonic shocks generate stagnation regions where the turbulent energy is dissipated (Padoan et al. 2001; Klessen et al. 2005; Federrath et al. 2016).

1.7 MASSIVE STAR FORMATION

Having discussed each aspect of the ISM individually, I shall now combine them and discuss them in terms of massive star formation theories. There are two main theories of massive star formation that I will focus on that one could class as the front-runners of current active research, and those are Core Accretion and Competitive Accretion.

Competitive Accretion (Bonnell et al. 2001) begins with the global, free-fall collapse of a sub-virial molecular cloud, which then fragments into cores due to the

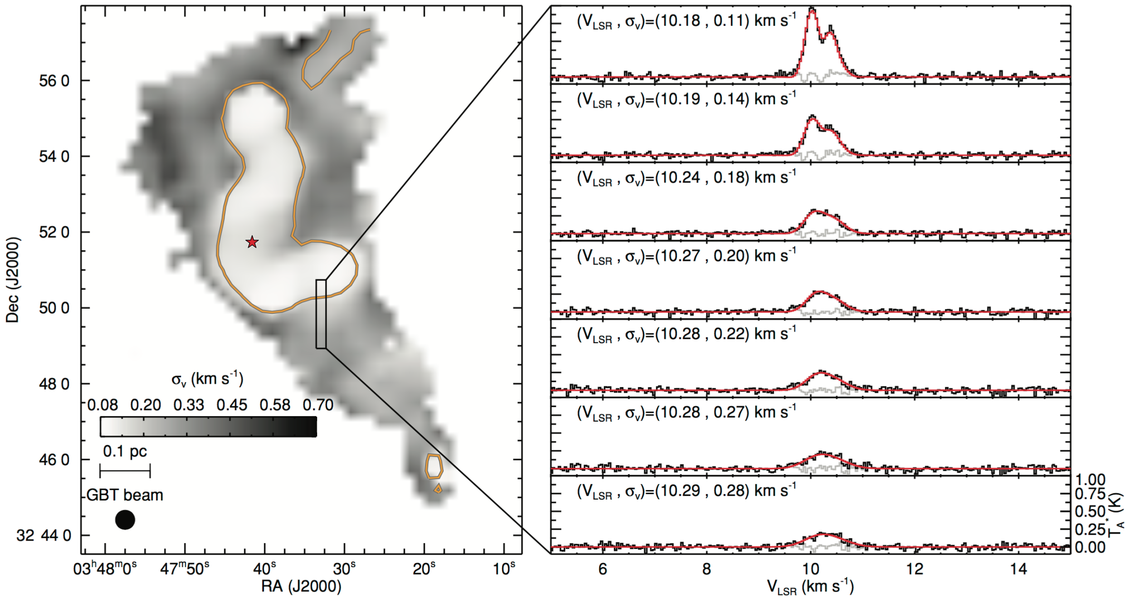

Figure 1.8 Velocity dispersion map of the B5 region of Perseus, taken from Pineda et al. (2010). Example spectra are shown from within the core and crossing the core boundary. The transition to coherence is clearly seen, as the velocity width of the shown spectra narrows within the core boundary compared to the surroundings.

effects of turbulence. Cores jostle for position, competing with other cores for the material to accrete. Protostellar seeds are formed of typically less than a stellar mass, which continually accrete unbound gas from the rest of the cloud. The high mass stars form as a direct result of the gravitational potential of the gas mass, which funnels the gas down to the gravitational potential well minimum at the centre of the cloud to be accreted. Massive protostellar cores have the advantage by winning most of the material whilst also forming near the centre of the forming cluster where the most mass falls, making the formation of high-mass stars a natural consequence of the system. Simulations by Smith et al. (2009) show that the constituent material of a massive star when traced back in time were originally randomly distributed within the parent molecular cloud. Essentially, material is accreted from anywhere and everywhere.

Core Accretion (McKee & Tan 2002), often termed Monolithic Collapse, describes an ordered collapse and can be considered an extension of the low-mass star formation theory presented by Shu et al. (1987). Similarly to competitive accretion, core accretion begins with the fragmentation of a molecular cloud into cores. However, one distinct departure from competitive accretion is that the are truly starless in nature, and once the fragmentation into cores stops and the cores become bound and in virial equilibrium with the surroundings, they are isolated from the parent molecular cloud and never gain any more mass. As it collapses, this provides a closed reservoir of material for the eventual central protostar to accrete from its envelope. This theory was extended by McKee & Tan (2003) into the Turbulent Core model. In equilibrium, the self-gravity of a core is balanced by the gradient of its internal pressure. However, given the shear amount of mass needed for high-mass star formation, the internal pressure is instead provided by the non-thermal mechanisms of turbulence and magnetic fields.

1.8 AIM OF THIS THESIS

There are many outstanding questions regarding the formation of filaments, and their fragmentation into cores. What is clear in hub-filament systems in particular is that accretion flows along the filaments towards the hub centre plays an important role in the evolution of the system. Understanding this process is one of the main aims of this work, utilising both high, and low angular resolution data from the Jansky Very Large Array (JVLA), the Green Bank Telescope (GBT) and the IRAM 30 m telescope to achieve this. I focus on the properties of a particular infrared dark cloud hub-filament system called SDC13. SDC13 lies 3.6 ±0.4 kpc away in the Galactic plane, and contains 1000 $M_\odot$ of material, classing it an intermediate to high-mass star forming region. I characterise its fragmentation and kinematics with high resolution observations of $NH_3(1,1)$ and $NH_3(2,2)$ rotation inversion transitions. With lower resolution observations of $^{13}CO(1–0)$ and $C^{18}O(1–0)$, I study the larger scale kinematics of the dense gas, looking for tell-tale signs of filament formation.

1.8.1 THESIS PLAN

In Chapter 2, I outline the radio astronomy techniques implemented in single-dish observations and interferometry. In Chapter 3, I give an overview of previous observations of the SDC13 infrared dark cloud and their results. Here, I also present the new data that was obtained and used for the work carried out in this thesis. In Chapter 4, I discuss the analysis of high angular resolution Jansky Very Large Array (JVLA), combined with the Green Bank Telescope (GBT) observations of the cold and dense gas tracer Ammonia in SDC13. In Chapter 5, I discuss the initial analysis of the lower angular resolution IRAM 30m telescope data probing both the ^{13}CO(1–0) and C^{18}O(1–0) molecular line emission, a work in-progress. In Chapter 6, I summarise the main conclusions of this work and outline my plans for future work on SDC13.

CHAPTER 2

RADIO OBSERVATIONS

This chapter outlines the basics of radio observations. After a brief discussion of single-dish telescopes, I present the radio interferometer and its advantages over single-dish observations. I go on to discuss the main interferometry techniques such as aperture synthesis and synthesis imaging, and the key stages of the data reduction and calibration process.

2.1 THE BASICS

Light is attenuated as it travels through the Earth's atmosphere. A narrow window is available for optical light to travel through unimpeded at wavelengths of a typically 0.5 to a few microns. Another far larger window also exists where radio wavelengths between $\lambda \sim 0.5\,\mathrm{mm} - 20\,\mathrm{m}$ are free to reach the ground.

Radio telescopes are commonly parabolic dishes made of many smaller metal panels. The dish makes a detection of an incoming electromagnetic wave by reflecting it from the main dish area to a receiver box, where an amplifier boosts the weak signal. The amplifier is cooled as much as possible to limit the introduction of interference to the signal due to thermal noise. The flux density S_ν measured from a given direction is proportional to the rate at which energy is incident to it over its area, and is spread across the frequency band of the receiving antenna. This means the total observed flux is the integral over the frequency bandwidth:

$$S = \int S_\nu \mathrm{d}\nu \,. \tag{2.1}$$

Astronomical sources however subtend a finite angular size, meaning their flux is instead measured per unit solid angle, called the brightness B(θ, ϕ). The total flux is then rewritten as the integral of the brightness per unit solid angle per bandwidth:

$$S = \int B(\theta, \phi) \mathrm{d}\Omega \mathrm{d}\nu \,. \tag{2.2}$$

This yields the flux of the source, with SI units of $\mathrm{W\,m^{-2}}$.As radio astronomy deals with small fluxes, the flux density is more conveniently substituted by the *Jansky* (Jy) where $1\mathrm{Jy} = 10^{-26}\,\mathrm{W\,m^{-2}\,Hz^{-1}}$.

The brightness temperature is a measure in radio astronomy of the intensity an antenna receives. The *specific intensity* of radiation from a blackbody is given by Planck's law, which at low-frequencies can be simplified to:

$$I(\nu) = \frac{2h\nu^2 T_B}{c^2} \,, \tag{2.3}$$

where h is the Planck constant, ν is the frequency and c is the speed of light. The brightness temperature, T_B, is defined as the temperature required of a blackbody in thermal equilibrium with its surroundings to reproduce the specific intensity of an object. The antenna temperature, T_A, is similarly defined as the temperature of the blackbody that would result in the equivalent amount of power being received by the telescope, and can be written as:

$$P = kT_A \Delta\nu \,, \tag{2.4}$$

where $\Delta\nu$ denotes the frequency bandwidth that the power was collected over. This antenna temperature may be corrected for atmospheric attenuation by measure of the zenith opacity, and is termed T'_A.

Antennas that are directional i.e. measure radiation from a specific direction, have a power pattern of lobes of radiation it receives. The largest of these lobes, called the main beam, will be in the direction of the source, whilst unwanted radiation from other directions manifest as weaker side-lobes. This is shown in Figure 2.1. Telescope quality is often determined by how much of the power is concentrated within the main beam, as determining the direction of a source of interest is made more difficult if a significant fraction of the power is received by the side-lobes. As such, there are many efficiency terms that are defined to quantify the antenna performance. In the case of sources that are larger than the main beam, it is useful to consider the efficiency of the antenna over the main beam only, termed the main beam efficiency (η_{mb}). This is then subsequently used to define the beam-averaged temperature of an extended astronomical source over the solid angle of the main beam, called the main beam brightness temperature (T_{mb}), as $T_A = \eta_{mb} T_{mb}$. By only considering the 2π steradians in the forward direction of the antenna, a correction can be made for the rear-sidelobes of the power pattern. This is termed the T^*_A temperature scale, and is what is measured at the IRAM 30 m telescope. One can convert the measured T^*_A into T_{mb}, by the following:

$$T_{mb} = \frac{F_{eff}}{B_{eff}} T^*_A \,, \tag{2.5}$$

where F_{eff} is the fraction of the power in the forward 2π steradians to the full 4π steradians (called the forward efficiency), whilst B_{eff} is the fraction of the power in the main beam solid angle to the full 4π steradians (called the beam efficiency). These efficiencies are measured and tabulated by the telescope, typically by observing a bright point source such as Mars in the case of B_{eff}, and by performing sky dips for the measuring of F_{eff}.

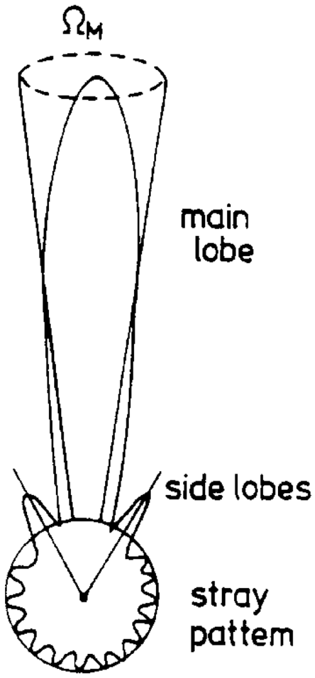

Figure 2.1 The power pattern of a directional antenna, taken from Rohlfs & Wilson (2000). Ω_M denotes the solid angle of the main beam.

This thesis makes use of observations of $C^{18}O(1\text{–}0)$ and $^{13}CO(1\text{–}0)$ emission from the IRAM 30 m telescope, and $NH_3(1,1)$ and $NH_3(2,2)$ molecular line emission from the Robert C. Byrd Green Bank Telescope, both single-dish radio telescopes.

2.1.1 The IRAM 30 m telescope

The IRAM 30 m telescope resides on Pico Veleta in the Sierra Nevada in Spain. At an elevation of 2850 m, the telescope site is cold and dry, meaning precipitable water vapour (pwv) is low. EMIR (Eight MIxer Receiver, Carter et al. 2012) is the multi-band, mm-wave, heterodyne receiver on the IRAM 30 m telescope. It operates in four frequency bands, covering 83–360 GHz (excluding between 174–200 GHz). Heterodyne receivers work by mixing the weak incoming signal with the known frequency of a pure sinusoid signal produced by a local oscillator in the system. This shifts the original signal to an intermediate frequency while preserving the phase of the wave. The Fast Fourier Transform Spectrometer (FTS) backend is often used in conjunction with EMIR, and can have a spectral resolution of either 50 kHz or 200 kHz.

2.1.2 THE GREEN BANK TELESCOPE

The Robert C. Byrd Green Bank Telescope (GBT) is a 100 m diameter dish is West Virginia USA, and is the largest man-made steerable structure in the world. The dish itself has an active surface, meaning it can compensate for dish distortions. The GBT operates in a vast number of different frequency bands between $\nu = 0.1 - 116\,\mathrm{GHz}$, and has low radio frequency interference (RFI) given its location in the National Radio Quiet Zone. The K-band Focal Plane Array (KFPA) for example is a heterodyne receiver for the 18–27.5 GHz band specfically. There are two continuum backends (called DCR and CCB), and one spectral line backend called VEGAS (the VErsatile GBT Astronomical Spectrometer). VEGAS is often used in conjunction with the KFPA receiver, and has a range of spectral window setups with wide bandwidths (1000-1500 MHz), making simultaneous observation of molecular lines feasible.

2.2 RADIO INTERFEROMETRY

Single-dish telescopes have a resolution defined by the diffraction limit equation:

$$\theta = \frac{1.22\lambda}{D}, \tag{2.6}$$

where θ is the resolution in radians, and λ and D are the wavelength and dish diameter in metres. For example, the Hubble space telescope with its 2.4 m dish at 1 μm optical wavelengths has a resolution of $\sim 0.13''$. However, to probe this resolution in the radio regime of the spectrum ($\lambda \sim 1$mm), one would need to construct a dish 2 km in diameter. This is an impossible task. Therefore, vast arrays of smaller dishes are constructed, called interferometers. The resolution achievable with such a system is equivalent to a single-dish telescope with the diameter of the largest dish separation in the interferometer array. This allows a whole new resolution regime to be probed. For instance, the Jansky Very Large Array (JVLA) interferometer, in a configurations with a maximum baseline length of 1 km, would have a resolution an order of magnitude better than the 100 m diameter, single-dish Green Bank Telescope.

2.2.1 Two-element interferometer

The simplest way to consider an interferometer is the two-element Michelson interferometer. Consider two antennas (labelled x and y, as shown in Figure 2.2) separated by a distance $\mathbf{b}$ (known as the baseline) receiving a signal from a monochromatic point source with direction vector $\mathbf{S}$ and frequency ν.

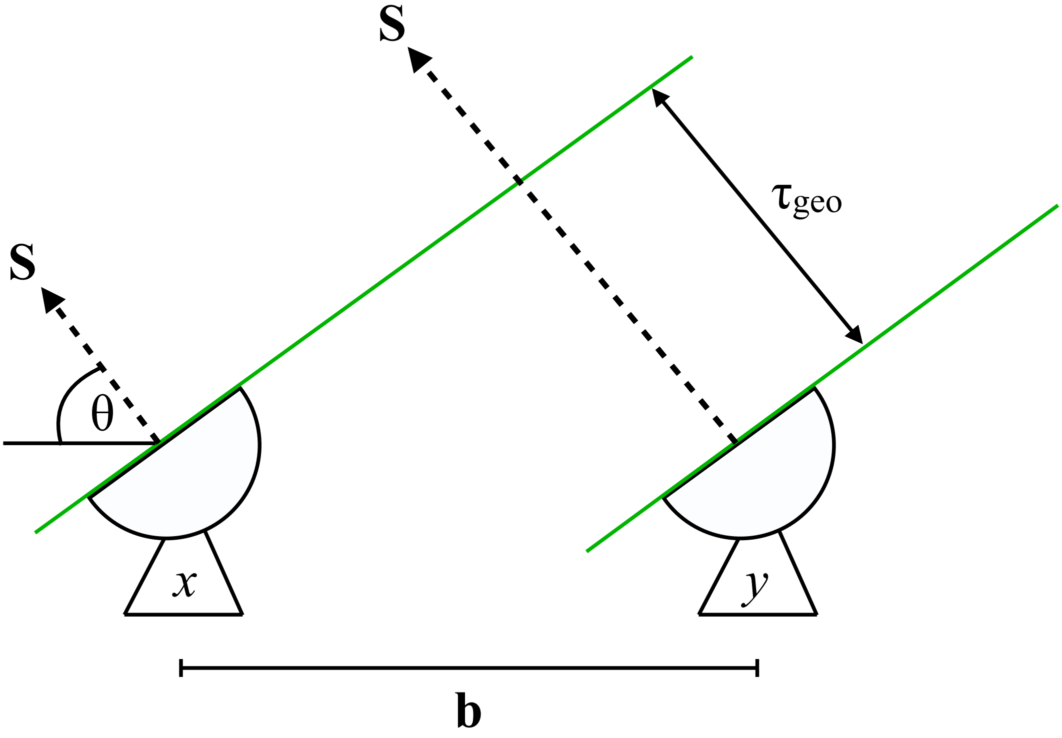

Figure 2.2 A simplified schematic of the two-element Michelson interferometer. The two antennas are labelled x and y, and are separated by a distance $\mathbf{b}$. There is a time delay (τ_{geo}) in the incoming signal (green lines, of direction vector $\mathbf{S}$ and incident angle θ) reaching antenna y. This schematic was inspired by those presented by Rohlfs & Wilson (2000), Burke & Graham-Smith (2014) and Thompson et al. (2017).

An incoming signal reaches the first antenna at a time t_x, however reaches the second antenna at a later time $t_y = t_x + \tau_{\text{geo}}$, where τ_{geo} is the geometric time delay given by:

$$\tau_{geo} = \frac{\mathbf{b} \cdot \mathbf{S}}{\mathrm{c}}\,, \tag{2.7}$$

where c is the speed of light. A substitution can be made by measuring the baseline distance in the number of wavelengths, $\mathbf{b} = \lambda \mathbf{b}_\lambda$:

$$\tau_{geo} = \frac{\lambda \mathbf{b}_\lambda \cdot \mathbf{S}}{\mathrm{c}} = \frac{b_\lambda S \cos\theta}{\nu_o}\,, \tag{2.8}$$

where ν_o is the reference frequency and θ the incident angle of the emission. This time delay is counter-acted by adding an instrumental time τ_i to t_x such that $\tau_{\text{geo}} - \tau_i = 0$.

The signal received by both antennas is passed to a voltage multiplier, where each output as a function of time is given by (Burke & Graham-Smith 2014):

$$x(t) = \mathrm{v}_x \cos(2\pi\nu_o t_x) \qquad \text{and} \qquad y\,(t) = \mathrm{v}_y \cos(2\pi\nu_o(t_x + \tau_{\text{geo}}))\,, \tag{2.9}$$

where v_x and v_y are the voltage outputs. These two signals are combined when passed to the correlator, which contains a voltage multiplier (among other technical intricacies), and so the two signals are correlated by the time-averaged multiplication of the two antenna outputs,

$$R_{x,y}(\tau_{geo}) = \langle x(t) y(t) \rangle\ . \tag{2.10}$$

This expression is called the *cross-correlation* function, and given it has the dimensions of power is often also called the *cross-power product* (Burke & Graham-Smith 2014). Following substitution, this equals:

$$R_{x,y}(\tau_{\text{geo}}) = \frac{\mathrm{v}_x \mathrm{v}_y}{2} \cos(2\pi\nu_o \tau_{\text{geo}})\,. \tag{2.11}$$

Relating this back to the physical properties of the observed source, the voltages are proportional to the source brightness $I\,(\mathbf{S})$, and the power pattern of the antenna A($\mathbf{S}$) over a solid angle dΩ within a frequency bandwidth $\Delta\nu$, and is normalized to unity (Thompson 1989). The assumption is made that the signal received from two points within the source on the sky are not correlated i.e. spatially incoherent (Thompson 1989). Following substitution:

$$R_{x,y}(\mathbf{S}) = \Delta\nu \int A(\mathbf{S}) I(\mathbf{S}) \cos(2\pi \mathbf{b}_\lambda \cdot \mathbf{S}) \mathrm{d}\Omega \,. \tag{2.12}$$

where the integral is evaluated over all 4π steradian of the sky. In constructing images from the incoming signals, and given that the two antennas can track the source on the sky, one needs to define a reference position called the *phase tracking centre*, given by the direction in which the time delay was cancelled. This is so the synthesised field of view can be centred, is denoted the vector $\mathbf{S}_0$, and is expressed as a vector offset $\boldsymbol{\sigma}$ from $\mathbf{S}$ such that $\mathbf{S} = \mathbf{S}_0 + \boldsymbol{\sigma}$ (Thompson 1989) (as shown in Figure 2.3). Substituting into equation 2.12 and using the standard $\cos(\alpha+\beta) = \cos(\alpha)\cos(\beta) - \sin(\alpha)\sin(\beta)$ trigonometric identity, one obtains:

$$\begin{aligned} R_{x,y}(\boldsymbol{\sigma}) = \Delta\nu \cos(2\pi\nu \mathbf{b}_\lambda \cdot \mathbf{S}_0) \int A(\boldsymbol{\sigma}) I(\boldsymbol{\sigma}) \cos(2\pi \mathbf{b}_\lambda \cdot \boldsymbol{\sigma}) \mathrm{d}\Omega \\ - \Delta\nu \sin(2\pi\nu \mathbf{b}_\lambda \cdot \mathbf{S}_0) \int A(\boldsymbol{\sigma}) I(\boldsymbol{\sigma}) \sin(2\pi \mathbf{b}_\lambda \cdot \boldsymbol{\sigma}) \mathrm{d}\Omega \,. \end{aligned} \tag{2.13}$$

The *complex visibility* is subsequently defined from this expression as:

$$V \equiv |V|\, e^{i\phi_V} = \int A(\boldsymbol{\sigma}) I(\boldsymbol{\sigma}) e^{-2\pi i \mathbf{b}_\lambda \cdot \boldsymbol{\sigma}} \mathrm{d}\Omega \,, \tag{2.14}$$

where ϕ_V is the phase of the visibility (Thompson 1989). This expression has units of spectral power flux density ($\mathrm{W\,m^{-2}\,Hz^{-1}}$) and measures the coherence of the electric field generated by the incoming signal from the source in the interferometer. With

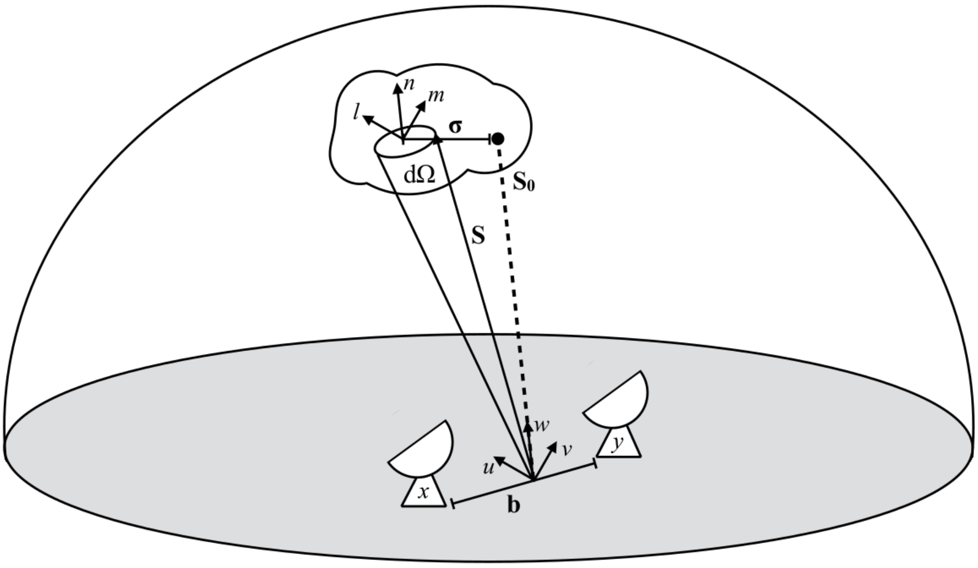

Figure 2.3 A simplified schematic of the projection of the vectors $\mathbf{S}$, $\mathbf{S}_0$ and $\boldsymbol{\sigma}$ on the sky, as well as the projection of the uv-plane (discussed in Section 2.2.3), and their on-sky parallel counterparts l and m. w denotes a direction along the vector $\mathbf{S}_0$. The phase tracking centre is shown by the black circle. The source is represented by the wavy outline on the sky. This schematic was inspired by those presented by Burke & Graham-Smith (2014) and Thompson et al. (2017).

the separation of equation 2.14 into its real and imaginary parts, and by substitution into 2.13 we get a final expression for the output of the correlator as:

$$R_{x,y} = A_0 \Delta\nu \, |V| \cos(2\pi \mathbf{b}_\lambda \cdot \mathbf{S}_0 - \phi_V) \, . \tag{2.15}$$

This is the fundamental principal behind interferometry, that from the correlator measureables $|V|$ and ϕ_V, one can solve for the intensity distribution of the source.

2.2.2 THE u,v–PLANE

The u,v–plane is the name for the rectilinear coordinate system where the baseline vector $\mathbf{b}_\lambda$ resides. u denotes the east-west direction, v denotes the north-south direction, whilst w is at a right angle to u and v and denotes the direction of the vector $\mathbf{S}_0$ (see Figure 2.3). Following this convention, it follows that the source lies perpendicular to the u,v–plane, whilst the offset vector $\boldsymbol{\sigma}$ lies parallel to it (Burke &

Graham-Smith 2014). l and m are the direction cosines of the vector $\mathbf{S}$ with respect to the u,v–plane, and are parallel to u and v respectively on the sky. It is therefore possible to re-write equation 2.14 in terms of these coordinates:

$$V(u,v,w) = \int\int \boldsymbol{A}(l,m)I(l,m)e^{-2\pi i(ul+vm+wn)}\frac{\mathrm{d}l\mathrm{d}m}{\sqrt{1-l^2-m^2}}\,, \tag{2.16}$$

where $\mathrm{d}\Omega = \frac{\mathrm{d}l\mathrm{d}m}{\sqrt{1-l^2-m^2}}$. Since $\mathbf{S}_0$ is perpendicular to the u,v–plane, w is zero. It follows that this equation is simply a two-dimensional Fourier transform. The *van Cittert-Zernike* theorem states that following an inverse Fourier transform, the brightness distribution is recoverable from the visibility $V(u,v)$ as:

$$\boldsymbol{A}(l,m)I(l,m) = \int\int V(u,v)e^{2\pi i(ul+vm)}\mathrm{d}u\mathrm{d}v\,. \tag{2.17}$$

Given that the angular size of the source will often be far smaller than the antenna beam, the l and m direction cosines (where $l = \sin x$ and $m = \sin y$) will also be small, and may be replaced under this small angle approximation by the x and y angular offsets, which are equivalent to the actual celestial coordinates of the target source (Burke & Graham-Smith 2014). Equation 2.16 may then be re-written as:

$$V(u,v) = \int\int \boldsymbol{A}I(x,y)e^{-2\pi i(ux+vy)}\mathrm{d}x\mathrm{d}y\,. \tag{2.18}$$

This means that the Fourier transform of the source brightness distribution is measured directly by the interferometer in the u,v–plane.

2.2.3 APERTURE SYNTHESIS

Thus far, a simplified case has been considered that only includes two antennas in the interferometer set-up. As this only corresponds to one baseline, this would yield the measurement of just the one Fourier component in the u,v–plane. Aperture synthesis is the technique of expanding this to multiple baselines in a full array of antennae. For an array containing N telescopes, the number of visibilities sampled in the u, v–plane increases to $N(N-1)/2$ per time integration (Burke & Graham-Smith 2014). However, if the target source is a complex, extended source for example, the u, v–plane may still not be sampled with enough Fourier components to fill the u, v–plane. The number of measured visibilities can be drastically increased when using the Earth's rotation as an advantage. As the Earth rotates, the position of an antenna relative to the target source changes, hence increasing the effective number of baselines and hence the Fourier sampling of the u, v–space. For the Atacama Sub-millimetre Array (ALMA), with the large number of antennas the Earth's rotation is not necessary to well fill the u, v-plane. This is demonstrated in Figure 2.4 (made using the *Pynterferometer* tool, Avison & George 2013), which shows the different coverage sampled in u, v–space by different number of antennae in an array. It can be seen that the u, v–plane is almost entirely filled in the case where 30 antennae are arranged in the array configuration and the Earth's rotation is implemented.

2.2.4 Data reduction and calibration

Each pair of antennas in the interferometer array will measure an amplitude and phase visibility. The goal of data calibration is to produce corrections on these measureables for any effects such as atmospheric or instrumental, by producing models that the observations will fit. These corrections are then applied to the target source, therefore good data reduction and calibration is essential if one is to produce good, reliable science. Without appropriate calibration, the data is essentially meaningless.

Flagging

The first steps of data reduction predominantly include inspecting the data, and removing any erroneous data points and bad data. Removing data is predominantly done by a process called *flagging*. Common examples of reasons to flag data include: an antenna dropping out, radio frequency interference (RFI), and the antenna still

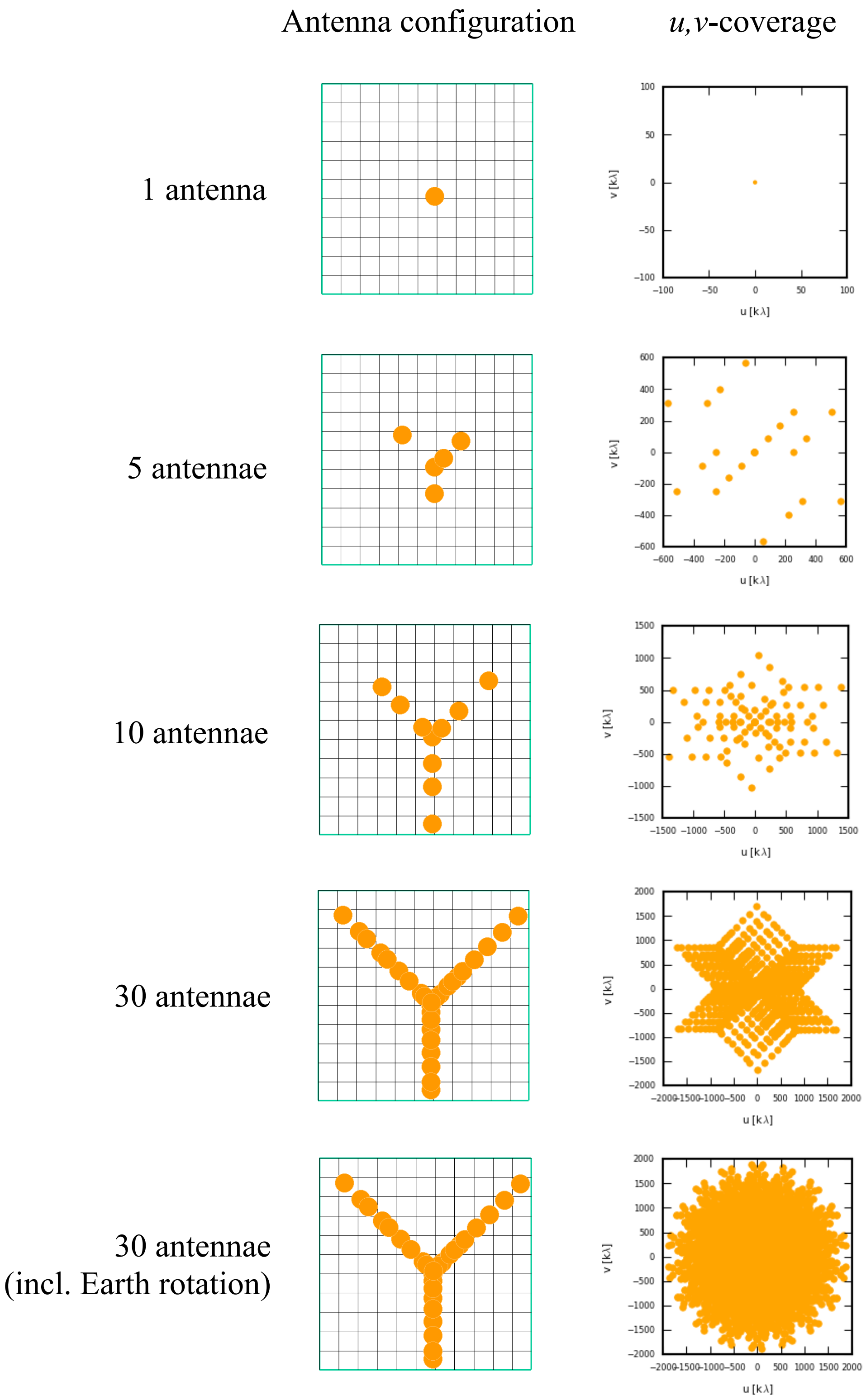

Figure 2.4 A collection of plots demonstrating the sampling of the u, v–plane (right column) with varying number of antennae in an array configuration (left column). This plot was made using the *Pynterferometer* tool (Avison & George 2013). The array was set-up in a 'Y' shape, and the final example includes the effects of the Earth's rotation.

slewing to the source at the beginning of its scan. Once the data is thought to only contain the good information, one can proceed to calibrate it, following the three key procedures below.

Flux calibration

This is required to set the right scale for the measured flux of the target source. To achieve this, observation of a well-known astronomical object, with a non-varying flux is ideal. Each telescope tends to have a catalogue of standard sources they commonly use. Common sources will be regularly monitored, and calibration tables of their flux maintained.

Phase calibration

This is required to correctly set the phase of the target source. To achieve this, observations of the position of a well-known, point source astronomical object is required. Observation of a phase calibrator is required at regular intervals throughout an observing session, as atmospheric changes can introduce errors in the phase. This means that for the best, consistent calibration, one needs to choose a phase calibrator as close to the target source as possible so that similar atmospheric conditions affect them both.

Bandpass and gain calibration

Bandpass calibration determines the variations of phase and amplitude with respect to the frequency (i.e. per channel), whilst gain calibration determines variation of phase and amplitude with respect to time (i.e. per integration). These variations can be due to change in weather conditions or elevation of the source during observing. The calibrator to correct for these variations needs to be a high signal-to-noise point source, therefore is often chosen to be the same as the flux calibrator, such as a bright quasar relatively near to the science target.

2.2.5 Synthesis imaging

Once reduction and calibration is complete, simply taking a Fourier transform of the visibilities produces an image called the *dirty map*, $I^D(l,m)$. The point spread function of the dirty map is known as the *dirty beam*, $D(l,m)$, which is itself the inverse Fourier transform of the sampling of the u,v–plane. The convolution theorem states that the dirty map is none other than the convolution of the dirty beam with the true brightness distribution of the source:

$$I^D(l,m) = I(l,m) * D(l,m)\,. \tag{2.19}$$

Hence, a deconvolution algorithm is needed to recover the true source brightness distribution. The CLEAN algorithm does just this, and was first introduced by Högbom (1974). The dirty beam in reality is a poor point spread function (PSF), with many unwanted sidelobe features. The CLEAN algorithm first finds the position of the brightest emission in the dirty map, and subtracts the dirty beam from it. This removes any spurious emission in the dirty beam at this position, and reveals any weaker emission hidden beneath. This process is iterative, and is implemented for each successively bright source in the dirty map. A map is then reconstructed by convolving with an idealized PSF (usually a Gaussian) called the *clean beam*. The process should only be stopped when the residual map resembles noise, meaning that all of the source emission was recovered. CLEAN is a Fast Fourier Transform (FFT) technique of recovering $I(l,m)$. A stipulation on the use of FFT techniques is that the data must be uniformly spaced in the u,v–plane. This is not a condition often met by extended array configurations, hence the resampling of the $V(u,v)$ data onto a regular grid before CLEANing is necessary.

2.2.6 Limitation

In a given configuration, interferometers are only sensitive to a given range of scales, defined by both the resolution and the largest angular scale. The resolution is defined by largest distance between antennas in the array and defines the smallest probable scales. The largest angular scale is defined by the smallest distance between antennas in the array. This unavoidable gap in the u, v–coverage between the two closest antennas means that any interferometer cannot probe resolutions larger than this largest angular scale. As a consequence, interferometers cannot be sensitive to the total flux of a source. Naturally, given that a single-dish telescope is a single, coherent structure with no gaps between elements, it is indeed able to recover the total flux of a source. A common technique currently in use is the combination of interferometer data with single-dish data. This allows one to probe the fine angular resolution with interferometers, whilst recovering the total flux of a source with the single-dish, simultaneously. I discuss this combination process in more detail in Chapter 3.

2.2.7 The *Karl G. Jansky Very Large Array* (JVLA)

This thesis makes use of $NH_3(1,1)$ and $NH_3(2,2)$ molecular line emission from the JVLA. The JVLA is a radio interferometer in New Mexico, USA, and contains an array of 27 antennas, each with a diameter of 25 m. There are four main configurations, from A through D, the largest being the A configuration reaching a maximum baseline of 36.4 km. There are also three “hybrid” configurations named DnC, CnB and BnA that tend to be half-way houses between the main configurations. With its 27 antennas arranged in a ‘Y’ configuration, the JVLA has 351 baselines. This means the JVLA has great sensitivity with its dense sampling of the u, v–plane.

CHAPTER 3

OBSERVATIONS OF SDC13 *

My PhD focusses on one specific infrared dark cloud hub-filament system called SDC13. In this chapter, an overview of previous observations of the SDC13 is given. The observations used within this thesis are also detailed, including their acquisition, reduction and calibration.

3.1 PREVIOUS OBSERVATIONS

SDC13 (Figure 3.1, where SDC stands for *Spitzer Dark Cloud*) is a remarkable IRDC hub-filament system that lies 3.6 ± 0.4 kpc away in the Galactic plane. Each of its four well-defined parsec-long filaments (including SDC13.174-0.07, SDC13.158-0.073 and SDC13.194-0.073, Peretto & Fuller 2009) converges on a central hub, and contains a total mass of $\sim 1000\,\mathrm{M}_{\odot}$ (Peretto et al. 2014). SDC13 has been the subject of two previously published works.

3.1.1 GAS FLOWS ALONG FILAMENTS

The analysis of 1.2 mm dust continuum data from the MAMBO bolometer array on the IRAM 30m telescope (at $12''$ resolution) led Peretto et al. (2014) to

---

[*] The new data presented here is published in Williams, Peretto et al. 2018 A&A in press.

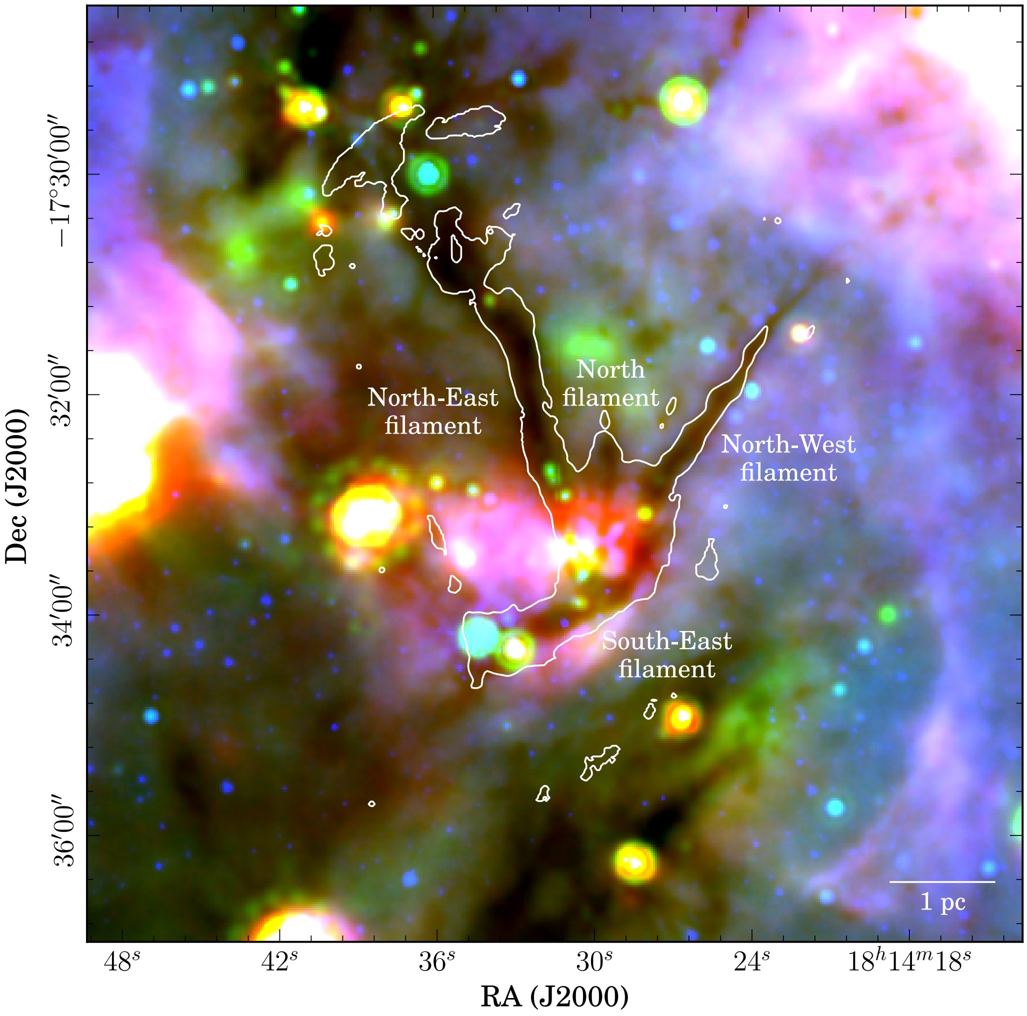

Figure 3.1 Three colour image of SDC13. R, G and B bands correspond to 70μm HIGAL (Molinari et al. 2010), 24μm Spitzer MIPSGAL (Carey et al. 2009) and 8μm Spitzer GLIMPSE (Churchwell et al. 2009) maps respectively. The overplotted contour is from the H_2 column density map at $2 \times 10^{22}\,\mathrm{cm}^{-2}$ (see Section 4.1.4 and the middle panel of Figure 4.7). A 1 pc scale bar is plotted in the bottom right corner. The filament names are labelled following those used by Peretto et al. (2014).

extract 18 compact sources, and identify their starless or protostellar nature from their association with *Spitzer* 8 μm and 24 μm sources. The two most massive cores (named MM1 and MM2) are located right at the junction of the hub filaments (see Figure 3.2). Tracing the dense gas in N_2H^+(1–0) with the IRAM 30m telescope (at 27″ resolution), they also identified organised velocity gradients along each of the filamentary arms of SDC13 which anti-correlate with a gradient in velocity dispersion that reaches its maximum at the centre of the hub. Given these organised velocity

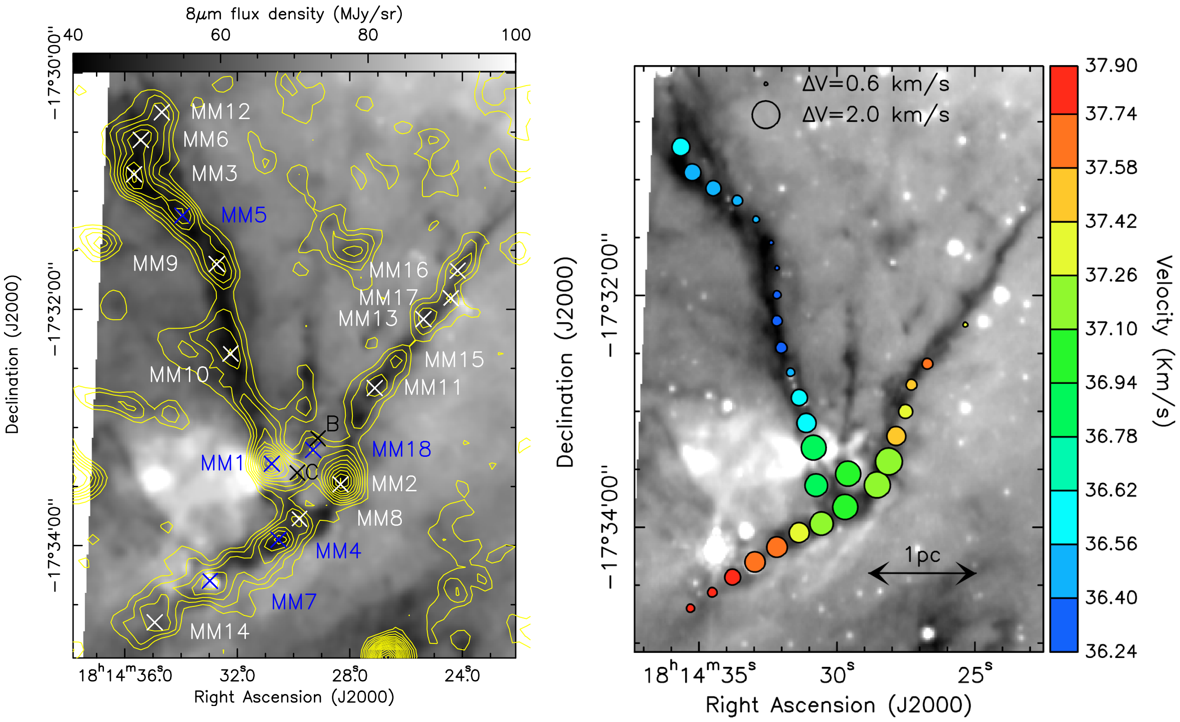

Figure 3.2 *Left*: Spitzer 8 μm flux density in units of MJy/sr, overlaid with IRAM 30m MAMBO 1.2mm dust continuum contours in steps of 5mJy/beam, from 3mJy/beam to 88mJy/beam. Crosses denote the positions of identified 1.2mm MAMBO compact sources (white for starless and blue for protostellar, Peretto et al. 2014) and two 1.3mm SMA continuum sources (in black crosses, McGuire et al. 2016, discussed in Section 3.1.2). *Right*: Spitzer 8 μm flux density overplotted by the $N_2H^+(1–0)$ pointings from the IRAM 30m telescope (Peretto et al. 2014). Symbol colours denote the velocity of the gas, following the colour bar to the right. The size of the symbols represent the FWHM velocity width of the gas, following the key at the top of the figure. This figure was taken from Peretto et al. (2014).

gradients and the presence of protostellar sources along the filaments, they suggest that both local and global longitudinal collapse is under way in SDC13. This collapse of the gas along the filaments would generate an increase of kinetic pressure (hence turbulent support) at the centre of the hub, implying that hub-filament systems such as SDC13 provide the necessary conditions for the formation of super-Jeans cores, i.e. cores with masses that are several times larger than the local Jeans mass. The presence of the super Jeans cores MM1 and MM2 at the junction of the filaments is likely the consequence of such a process.

3.1.2 RESOLVED CORE SUBSTRUCTURE

As identified by Peretto et al. (2014), the two largest cores in the SDC13 system lie at the hub-filament junction. Their substructure was studied using high resolution ($< 3''$) 1.3 mm *Submillimeter Array* (SMA) dust continuum emission by McGuire et al. (2016), as shown in Figure 3.3. MM1 was found to contain two sub-fragments (labelled A and C), whilst MM2 was resolved to contain just one (labelled D). Fragment A (the centremost of the two coincident with MM1) was found to be brighter than the MM2 fragment. Given that MM2 is starless, this strongly suggests that it is at an earlier evolutionary stage than MM1. Therefore, this dimmed brightness of fragment D was attributed to filtering of extended emission at 1.3 mm wavelengths, a conclusion strengthened by the precedent set by studies of Cygnus-X that also find that a $100\,\mathrm{M}_\odot$ core detected in 1.2 mm emission using the IRAM 30 m telescope (Motte et al. 2007) is barely detected at all at 1.3 mm using the Plateau de Bureau Interferometer (PdBI, Bontemps et al. 2010; Duarte-Cabral et al. 2013). Modelling the cores with RADMC-3D, McGuire et al. (2016) reveal that MM2 requires a steeper density profile than MM1, suggesting that it may be most likely to form a single massive central object (Girichidis et al. 2011). The fragment labelled B does not coincide directly with any significant 1.2 mm dust continuum emission. After investigation, B was not found to correlate with the position of any AGB star nor coincident with a radio source in the VLA CORNISH survey, therefore cannot be explained by free-free emission from a HII region either. The most likely explanation for B is that it is a runaway object that was ejected from MM1, with the 1.3 mm continuum emission arising due to a circumstellar disk. Calculated escape velocities based on its distance from MM1 and time since it was formed (estimated as $\sim 10^5$ years for massive pre/protostellar objects) was found to be consistent with literature.

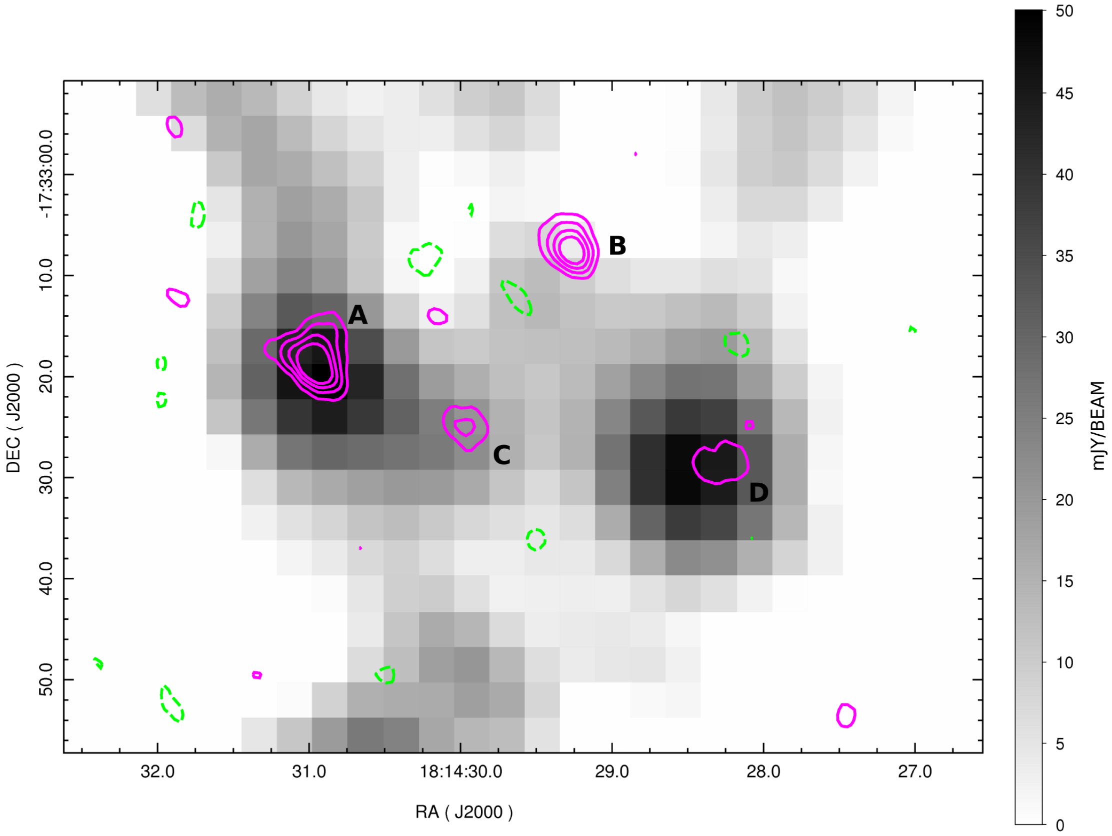

Figure 3.3 A zoomed in view of the centre of the SDC13 hub-filament system. SMA 1.3 mm dust continuum contours (McGuire et al. 2016) are overplotted on the MAMBO 1.2 mm dust continuum map (Peretto et al. 2014), taken directly from McGuire et al. (2016). The contours are placed at -3, 3, 5, 7 and 9 mJy/beam. Positive contours are in magenta, whilst negative contours are in dashed green. Four sub-fragments are identified, and are labelled A, B, C and D. The A and D subfragments are coincident with the MM1 and MM2 cores respectively.

3.2 New observations

The observations presented by Peretto et al. (2014), with their resolution of $27''$ is not sufficient for studying the link between the cores and their parent filament. This is a regime of interest to probe since much is unknown about which is the dominant fragmentation mechanism of filaments into cores in the first place. The cold and dense gas tracer Ammonia (NH_3) was observed at the position of SDC13 with both the *Karl. G. Jasnky Very Large Array* (JVLA) and the *Green Bank Telescope* (GBT), with the aim of probing this core-filament regime.

3.2.1 JVLA observations

The NH_3(1,1), NH_3(2,2) and NH_3(3,3) transitions were observed at the position of the SDC13 infrared dark cloud (J2000 18:14:30.0 -17:32:50.0) at 23.7GHz using the JVLA in the DnC configuration. The angular resolution achieved of $3.3''$ is an 8-fold improvement on the $27''$ resolution of the N_2H^+(1–0) molecular line IRAM 30m data (Peretto et al. 2014). This new data probes 0.07 pc spatial scales, ideal for studying filament fragmentation, offering a brand new view point on the system. A mosaic across the full $5' \times 5'$ extent of the cloud was performed in eight, half-beam spaced pointings, collected over 8 observing sessions between 18th and 20th of May 2013, each with a 90 minute integration time. Further information on these data are provided in Table 3.1. The NH_3(3,3) transition was not significantly detected. In terms of cloud conditions this is interesting in itself, given the higher temperature required for NH_3(3,3) to be thermally excited compared to NH_3(1,1) and NH_3(2,2).

Data reduction and calibration

Data reduction and calibration was completed using the *Common Astronomy Software Applications* CASA[†] (McMullin et al. 1992). CASA was developed for the specific job of reducing next-generation interferometer data, replacing the old AIPS[‡] data reduction software. Phase and flux calibration was completed using the two bright quasars J1832-1035 and 3C286, respectively. The phase calibrator was chosen to sit within 6 degrees of the target position on the sky to ensure similar atmospheric conditions. Bandpass calibration was completed with the J1743-0350 quasar. Figure 3.4 shows the phase versus time of the phase calibrator before and after calibration, whilst Figures 3.5 and 3.6 shows the phase versus frequency and amplitude versus frequency respectively of the bandpass calibrator, following phase and amplitude calibration respectively.

[†] `http://casa.nrao.edu`

[‡] `http://aips.nrao.edu`

I flagged any bad data using the `flagcmd()` and `flagdata()` tasks within CASA. The most common flagging method required in this data was the *'quack'* mode of `flagcmd()`. This allows you to trim data off the beginning or end of a scan by specifying a time interval. Figure 3.4b shows an example of data that required quacking. It is clear that even after phase calibration, there is a portion of data at the beginning of the first scan of the phase calibrator that cannot be calibrated correctly. This is likely due to the telescope still slewing to the source even though it had already began taking data. To deal with this, I inspected the data to find exactly what combination of antenna, spectral window and scan was causing the bad data, and over what time interval it occurred. After quacking, the calibration was re-done and checked, as many times as needed until all the data looked well-calibrated.

Imaging

I imaged all three transitions using the `clean()` task in CASA. One of the modes within `clean()` that determines the quality of the final image is the *weighting* mode. Three of the most common weighting modes are *Natural*, *Uniform* and *Briggs*. Each different weighting mode affects the dirty beam used in deconvolution differently, by convolving the weighting parameter with the dirty beam in the u, v–plane before the inverse Fourier Transform:

$$D(l,m) = \mathcal{F}^{-1}\left\{W(u,v) \times D(u,v)\right\} \,, \tag{3.1}$$

where $W(u,v)$ is the weighting parameter. Natural weighting takes a weighting parameter of the form:

$$W(u,v) = \frac{1}{\sigma^2(u,v)} \,, \tag{3.2}$$

where σ^2 is the noise variance of the u, v sample. This results in more weighting being applied to short baselines, therefore emphasising large scale structure in the intensity distribution. This degrades resolution slightly, but sensitivity is not compromised.

(a) Before phase calibration

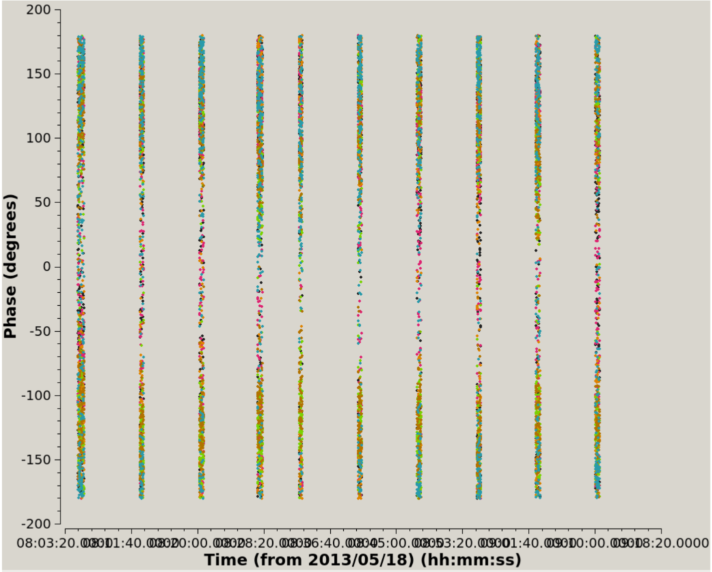

(b) After phase calibration

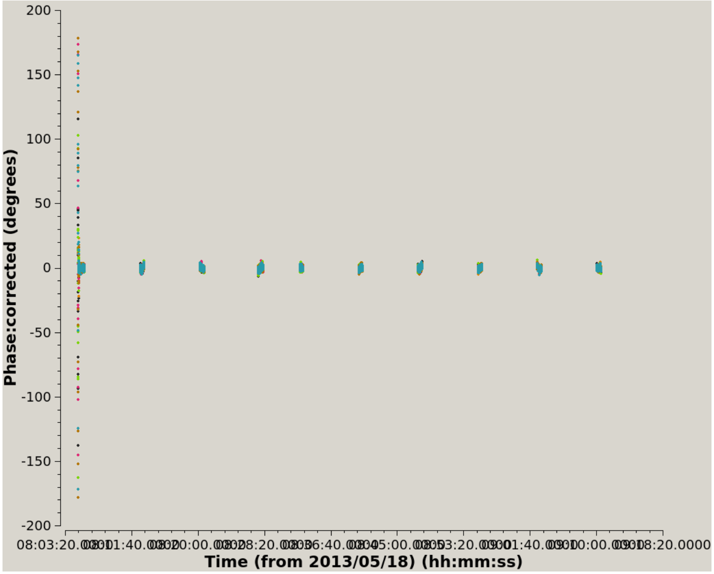

Figure 3.4 Screenshots taken from the CASA `plotms()` window of the phase versus time of J1832-1035 (the phase calibrator) (a) before calibration, and (b) after calibration. This plots one 90-minute observing session out of the eight conducted. It is clear that J1832-1035 was observed regularly throughout the run, enabling good monitoring of phase changes with altering weather/atmospheric conditions. The phase before calibration can be seen to vary through the entirety of the ±180° scale. After application of the source model, the phase improves to within ±10°. Data that should be flagged is obviously present in the first scan of the calibrator. Each different colour plotted represents a different spectral window. The data was averaged for ease of plotting over 128 channels, and all baselines.

(a) Before bandpass (phase) calibration

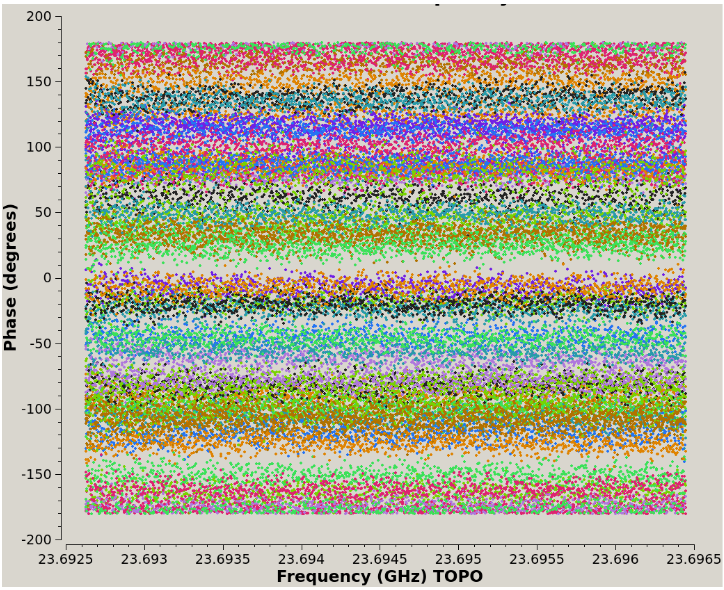

(b) After bandpass (phase) calibration

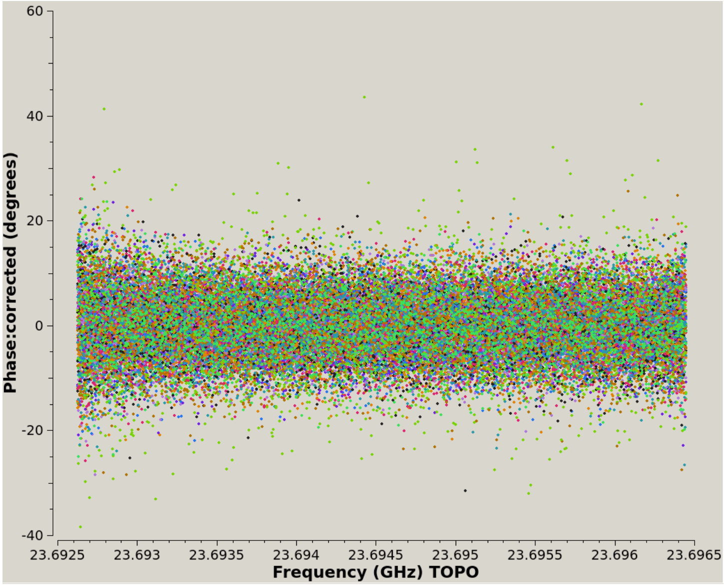

Figure 3.5 Screenshots taken from the CASA `plotms()` window of the phase versus frequency of J1743-0350 (the bandpass calibrator) (a) before calibration of the phase, and (b) after calibration of the phase. This plots one 90-minute observing session out of the eight conducted. Each of the coloured bands plotted represents a single baseline to a single antenna in the array configuration. The phase before calibration can be seen to vary through the entirety of the ±180° scale. After application of the source model the phase improves to within ±20°. The data was averaged for ease of plotting over time.

(a) Before bandpass (amp) calibration

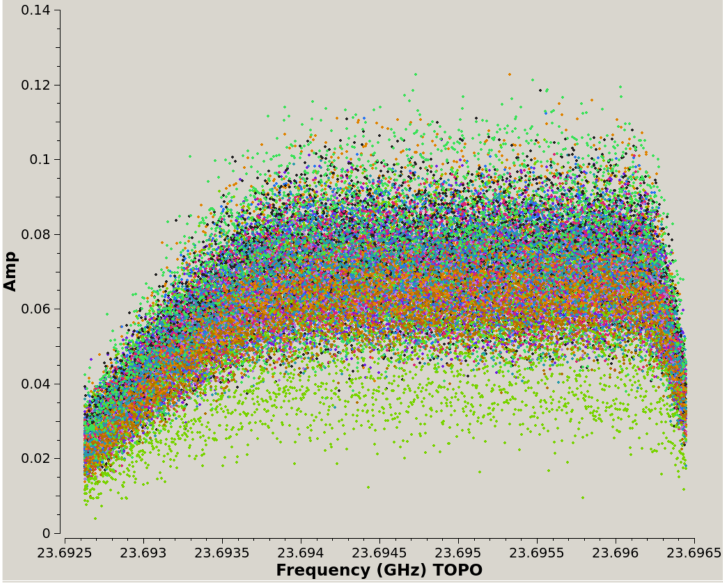

(b) After bandpass (amp) calibration

Figure 3.6 Screenshots taken from the CASA `plotms()` window of the amplitude versus frequency of J1743-0350 (the bandpass calibrator) (a) before calibration of the amplitude, and (b) after calibration of the amplitude. This plots one 90-minute observing session out of the eight conducted. Each of the coloured bands plotted represents a single baseline to a single antenna in the array configuration. It is clear that before calibration, the amplitude showed an arced morphology, which becomes nice and flat after calibration. The data was averaged for ease of plotting over time.

Uniform weighting is initially a scheme identical to the natural weighting scheme. However, it then departs from this by regridding the u, v–plane to a number of uniformly distributed cells (given as two over the field of view of the image). Each cell is then given an equal weight, meaning that both low and high u, v baselines have the same weight during CLEANing. This improves the resolution compared to the natural weighting, and reduces the side-lobes of the dirty beam, however increases the RMS noise of the image.

The Briggs weighting scheme is an adjustable one, that can be changed between emphasising large scale and small scale structure, combining the best features from the Natural and Uniform weighting schemes. The *robust* parameter defines how close to each scheme the Briggs weighting resembles, from -2 (closest to Uniform weighting) to +2 (closest to Natural weighting), with the default value being 0.5. The Briggs weighting was the first port-of-call in the imaging tests, and resulted in the integrated intensity map shown in Figure 3.7. It is clear in this iteration that not enough cleaning was done, since the South-East filament is not detected. However, the most striking feature of the map is the small scale, regular striped pattern from left to right in the intensity distribution. Initially, one would assume that this is due to poor calibration of the phase of the source, since it is the phase that determines how the spatial distribution of flux is mapped. However, following revision of the phase calibration, there was no significant improvement. The u, v–coverage of the data is plotted in Figure 3.8, representing the Fourier footprint of the JVLA. At the time of observation, SDC13 was quite low in the sky, peaking at just 37°. This low elevation stretches the u, v–coverage from being circular (the ideal) towards being elliptical (not ideal). As the dirty beam used in the CLEAN deconvolution is the Fourier transform of the u, v–coverage itself, this also results in an elliptical beam, hence also stretching the flux distribution of the map. Given that these stripes manifest as small scale structure in the maps, Uniform weighting would not be suitable to correct for this as it applies equal weighting to both low and high u, v baselines.

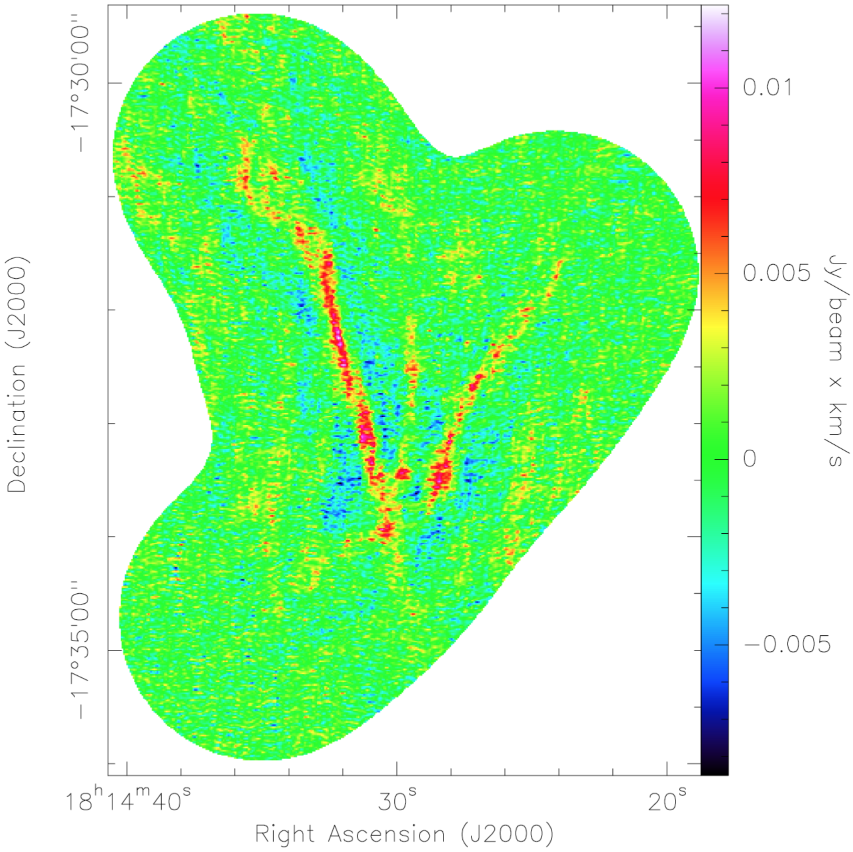

Figure 3.7 The integrated intensity map of SDC13 resulting from the first CLEAN test which used the Briggs weighting scheme, with a *robust* parameter of 0.5. It exhibits an unsightly striped pattern in intensity, which is clearly an artefact.

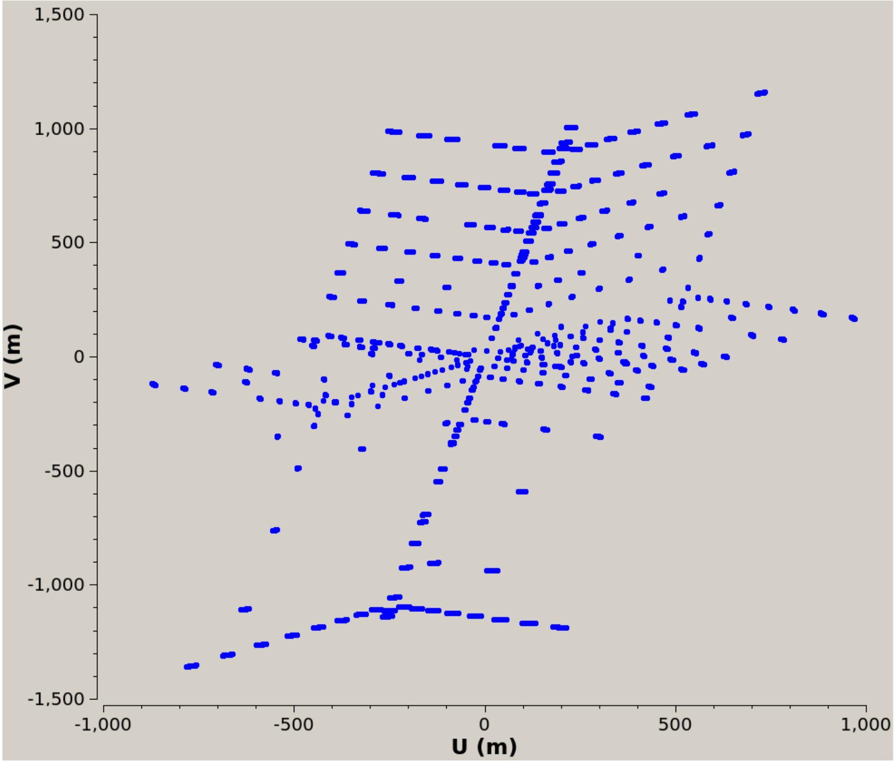

Figure 3.8 A plot of the u, v–coverage of one session out of the eight observed, for one of the source target fields. This plots all baselines.

Natural weighting however puts less emphasis on the largest u, v–plane baselines (i.e. smallest scale structure) by definition. Even though Natural weighting does degrade the resolution slightly due to the way it modifies the dirty beam in equation 3.1, it is a satisfactory compromise to recover a better quality intensity distribution. The final integrated intensity map is shown in the middle panel of Figure 3.13.

The sampling theorem states that to aid deconvolution, one must have at least 3 to 5 pixels within the main lobe of the dirty beam. Any more pixels and one risks over-sampling the data and introduce artefacts. Too little, and one risks not sampling enough and lose information. This is set by the `cellsize` parameter in the `clean()` task. I satisfied the sampling theorem by having 3 pixels within the beam area equivalent to $1.2''$ in size each. A well-cleaned image is one where the residual image looks to contain the least amount of structure and resembles noise features only. This can be achieved by using the optimal values for the `threshold` and `niter` parameters. CLEANing is stopped when either the intensity threshold has been reached, or the number or CLEAN iterations has been reached. In CLEANing the $NH_3(1,1)$ and $NH_3(2,2)$ maps, the `threshold/niter` parameters were 10 mJy/10,000 and 10mJy/3000 respectively. The number of iterations was always set rather high to allow CLEAN to first reach the intensity threshold, which is a more meaningful stopping criteria. As can be seen in Table 3.1, the threshold value was not set below the RMS noise values, ensuring that it was real signal being CLEANed as much as possible and not noise. Finally, primary beam correction must be applied to the final cleaned image. This accounts for the centre of a beam being less affected by noise than the edges of a beam. This is why the observations were designed as half-beam spaced pointings, to maximise the signal-to-noise towards the source where the beam edges overlap.

For regions of the u, v–plane that are un-sampled (for example due to the largest angular scale of the interferometer), `clean()` can extrapolate the visibilities $V(u, v)$ during deconvolution to find a sensible result for the source brightness distribution $I(l, m)$ that is compatible with the data. A single dish antenna on the other hand does probe short u, v distances by recovering all spatial frequencies up to the dish diameter. If one had access to both single dish and interferometer, this extrapolation of the u, v–plane in cleaning would not be necessary, as one could in effect replace the shortest u, v–coverage of the interferometer with that of the single dish. For best result, data with some amount of overlap in the recovered spatial frequencies is required. For the JVLA, this is satisfied by the 100 m dish of the GBT.

3.2.2 GBT observations

We used the 7-beam K-band Focal Plane Array at the GBT with the VEGAS (*VErsatile GBT Astronomical Spectrometer*) backend to observe the $NH_3(1,1)$ and (2,2) transitions employing a position switched scheme, where the Off source reference position (18:13:59.3 -17:35:02.0) was devoid of NH_3 emission. Two maps were scanned in right ascension, while another two were scanned in declination so as to mitigate any artefacts that could arise during imaging had only one mapping scheme been used. All four maps were observed on 14th Nov 2015, each with an integration time of 17.9 minutes (see Table 3.1 for data properties).

Data reduction and calibration

The GBT pipeline (Masters et al. 2011) was implemented on each map scan separately to calibrate, reduce and subtract the continuum emission. All scans were then combined and imaged in AIPS using the aipspy ParselTongue scripts included with the pipeline. Possible issues with the noise diode voltages at the time of observation skewed our flux calibration but had no effect on the quality of the data. Figure 3.9 shows the observed antenna temperature of the flux calibrator, J1833-2103 (a quasar). From the height of the peak (from the baseline to the peak) the measured antenna temperature is 2.357 K. Looking in the published calibration tables, the flux should be 4 Jy. This published flux was converted to antenna temperature by:

$$T_a = \frac{2.85 S_\nu \eta_a}{\exp\left(\frac{\tau_0}{\sin el}\right)} , \tag{3.3}$$

taken from the GBT Observing Manual[§] where S_ν is the flux, η_a is the aperture efficiency, τ_0 is the zenith opacity and el is the elevation of the source (~30°). The zenith opacity at the time of observation is shown in Figure 3.10, and was taken to be 0.04 at the rest frequency of NH_3(1,1). The aperture efficiency itself is calculated following:

$$\eta_a = 0.71 \times \exp\left[-\left(\frac{4\pi\epsilon\nu}{c}\right)^2\right] , \tag{3.4}$$

called the Ruze equation (taken from the GBTIDL Calibration Guide[¶]) where ϵ is the surface accuracy. The surface accuracy varies with the distortion of the surface

---

[§] `https://science.nrao.edu/facilities/gbt/observing/GBTog.pdf`

[¶] `http://www.gb.nrao.edu/GBT/DA/gbtidl/gbtidl_calibration.pdf`

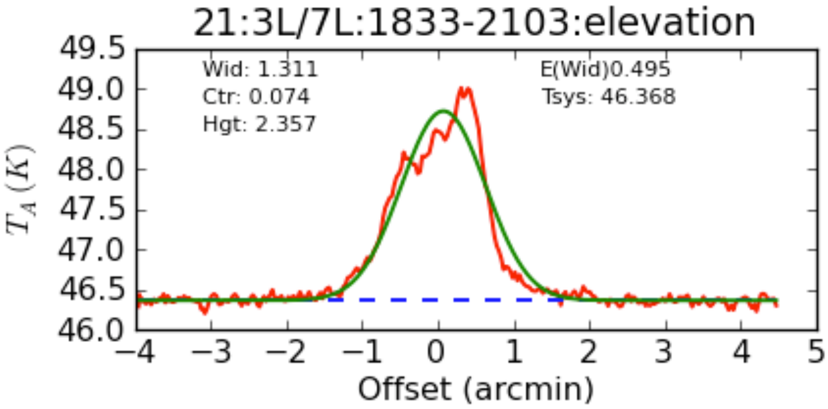

Figure 3.9 Screenshot taken from ASTRID (Astronomer's Integrated Desktop), the all-in-one GBT observation software. This shows a scan in elevation of the flux calibrator. The red line is the observation, whilst the green line is a fit. The blue dashed line shows the baseline. The difference between the baseline and the peak gives the observed brightness temperature of the calibrator, which in this case is 2.357 K. Comparing this to the standard tables, this is 3 times lower than that published. This is the basis of the calibration factor we applied to the data.

of the dish due to thermal gradients, which themselves vary with the time of day and weather conditions, for example. Typical values for this range between 220–360 μm, with 220 μm being a good efficiency and 360 μm being poor. These poor ϵ values were taken as typical back in 2009, and current values are much improved to the good end of the scale between 220–260 μm. Taking a value of $\epsilon = 240\,\mu$m gives an $\eta_a = 0.67$, consistent with predicted values at the NH_3(1,1) frequency in the calibration guide. Converting the known 4 Jy flux into an antenna temperature, this corresponds to 7 K. This is three times larger than the measured antenna temperature. After investigation, this is best explained by problems with the system noise diode temperatures, T_{cal}, at the time of observation (as hinted at in Figure 3.11). If the noise diode input voltages were not set correctly on-site, this would result in the output power of the noise diode being stronger or weaker than known laboratory values, meaning measured antenna temperatures of sources would be weaker or stronger than expected respectively. This should have been checked in real time during observation

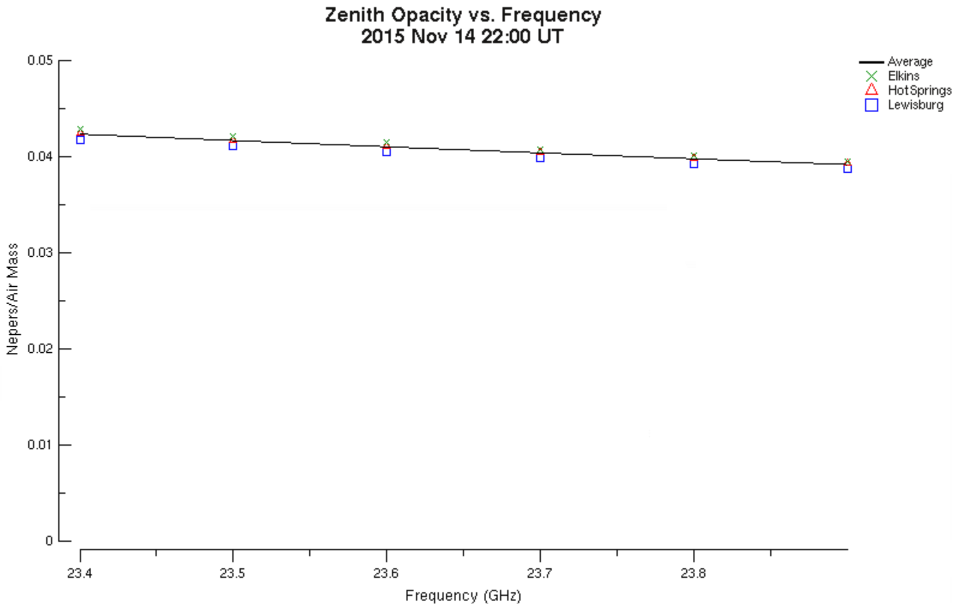

Figure 3.10 Screenshot of the CLEO software available at the GBT showing the zenith opacity plot as a function of frequency at the time of the observation at the GBT. Each measurement was taken by a different weather station in the area (following the key in the top right), and the fit in the black line is the average.

by doing the conversion already done above using equation 3.3. Therefore, as this issue only affects the flux scale of the data, I retrospectively corrected for this discrepancy by applying a calibration factor to the GBT data equal to the ratio of the expected to the measured antenna temperature, of three.

3.2.3 Combination of JVLA and GBT data

Interferometers only probe a limited range of spatial frequencies of the source brightness spatial distribution, the largest frequency being determined by the shortest distance between any pair of the interferometer antennas. As a consequence, interferometers filter out extended emission. Single-dish antennae on the other hand recover all spatial frequencies up to the dish diameter. In order to recover this large-scale emission, and therefore be able to analyse the source structure on all spatial scales, one needs to combine interferometer data with single dish data. Hence, we combined our JVLA data with the GBT observations.

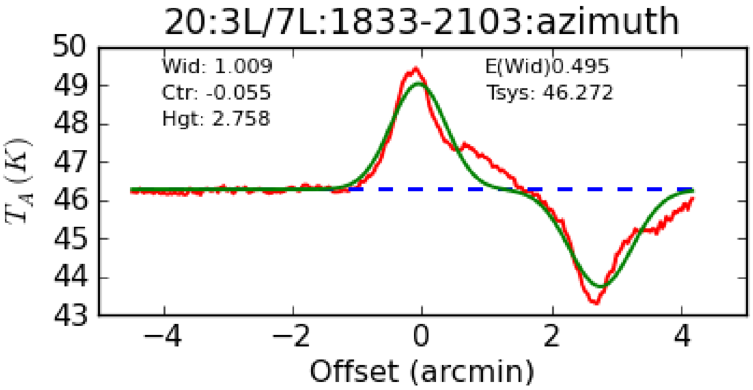

Figure 3.11 Screenshot taken from ASTRID (Astronomer's Integrated Desktop), the all-in-one GBT observation software. This shows a scan in azimuth of the flux calibrator. The red line is the observation, whilst the green line is a fit. The blue dashed line shows the baseline. The noise in the data and poor fit hints at this being a very poor observation, either due to weather conditions, problems with the noise diode temperature values, or a combination of both.

As a preliminary combination step, we re-clean our JVLA visibilities in the same way as described in Section 3.2.1, whilst using the GBT cube as a starting model (Dirienzo et al. 2015). This method assists in initializing the clean algorithm by using the GBT primary beam to determine the flux scale. Moreover, as the JVLA is missing information at the shortest baselines, this approach allows the clean algorithm to extrapolate the GBT data and converge on a better solution in this *u*-*v* regime. Note that this is not the same as performing a joint deconvolution.

Combination is achieved with the use of the CASA task, `feather`. With the high and low resolution images as inputs, `feather` Fourier transforms the two cubes, applies a low-pass filter to the low resolution data and a high-pass filter to the high resolution data, sums the two Fourier and filtered cubes in *u*-*v* space, and reconvolves the final combined cube. The low and high pass filters (weights calculated from the input clean beams) are applied to recover the larger scale emission of the GBT data at low *u*-*v* distances which the JVLA naturally filters out, whilst retaining the fine scale structure probed by the JVLA at larger *u*-*v* distances which the GBT cannot be sensitive to. The primary beam response of the JVLA was applied to the GBT data prior to feathering, so that only emission within the JVLA mosaic area was considered.

The `casafeather` visual interface provides the tools to inspect slices of the u-v plane of both the original and weighted deconvolved input images. This is especially useful while setting the `sdfactor` parameter, which applies a flux scaling factor to the low resolution image. For the conservation of flux, one would expect the fluxes of the weighted deconvolved high and low resolution images to be roughly equal. Therefore, if one were to plot one against the other in `casafeather`, one would expect the combined data to fall on a straight line following $x = y$. One can achieve this flux conservation by altering the `sdfactor` until the casafeather plots demonstrate this equality. Figure 3.12 shows such plots of the combination process. Given the uncertainty in the flux calibration of the GBT, an `sdfactor` was expected to be required, however, with the default `sdfactor` of 1 the combined data (dark blue points) seem to lie along the solid black line, indicating good flux conservation. This demonstrates that the calibration factor applied to the GBT data in the first instance during calibration was sound and appropriate.

Figure 3.13 shows a comparison of the GBT, JVLA and combined integrated intensity maps of $NH_3(1,1)$. It is clear that the combined data recovers more extended flux than the JVLA only, resulting in a doubling of the JVLA flux on the whole, whilst retaining the small scale detail and RMS noise of the interferometer. We can clearly see that the negative bowl features, a consequence of missing flux, that surrounds the cloud structure in the JVLA only map are mostly eradicated in the combined map and filled by the recovered extended emission. A check was made on the conservation of flux, performed by smoothing the feathered image to the resolution of the GBT, converting the units to Jy per GBT beam, and dividing by the original GBT map. In doing this, we find that flux is conserved. In the filament regions, we find a ratio of unity on the whole, whilst in the regions of significant emission such as the hub the combined flux is typically ∼20% less than the GBT map (a similar result to that

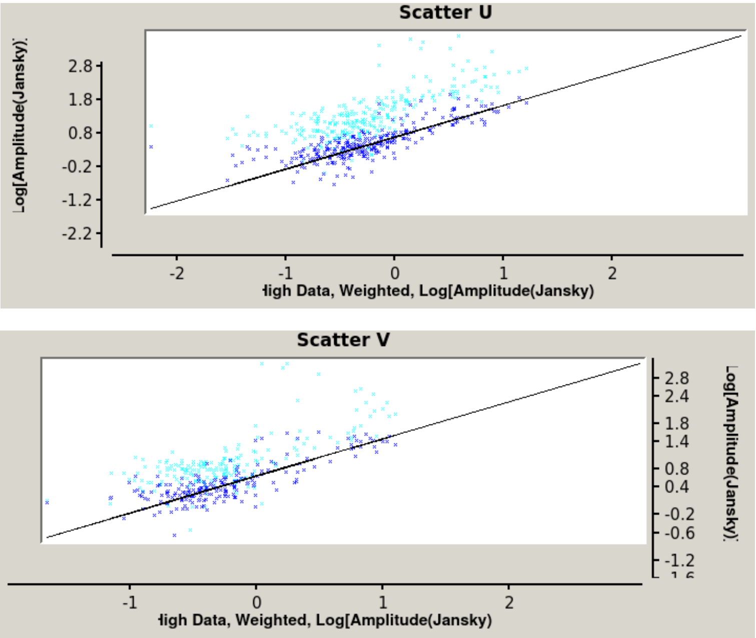

Figure 3.12 Screenshots of the `casafeather` window. The high-resolution data weighted by the high-pass filter is plotted on the x axis, whilst the low-resolution data weighted by the low-pass filter is plotted on the y axis. The original, low-resolution data is plotted in cyan, whilst the combined data is plotted in dark blue. The solid black line denotes the $x = y$ relation. The combined data can be seen to fall on the straight line, which is what one expects for flux conservation.

reported by Dirienzo et al. 2015).

In order to gain in signal to noise ratio we convolved the combined datacube with a Gaussian kernel of 2.4″, degrading the angular resolution to $\sim 4''$.

3.2.4 IRAM 30m observations

The $C^{18}O$(1–0) and ^{13}CO(1–0) molecular lines were observed by the IRAM 30 m telescope towards SDC13 between 26th June to 4th July 2013, with an integration time of 36 hours (including overheads). Position switching was employed during on-the-fly mapping of a $6' \times 6'$ area, where the Off source reference position was chosen to be devoid of ^{13}CO and $C^{18}O$ emission (identified with the help of low-column density Herschel emission). Note the map size is extended by $1'$ in comparison to the JVLA mosaiced area. Each line, with rest frequencies of 109.8 GHz and 110.2 GHz respectively were simultaneously observed by the EMIR receiver (Carter et al. 2012) in the B1 frequency band (83–117 GHz), achieving an angular resolution of $\sim$23.6″, probing spatial scales of $\sim$0.4 pc at the distance of SDC13. Using the FTS backend (Fast Fourier transform Spectrometer), the spectral resolution achieved of 0.15 kms^{-1} ($\sim$50 kHz) results in an RMS noise per channel of $\sim$0.16 K. Standard data reduction procedures were followed using the CLASS[‖] package of the Gildas software, using Mars as the primary calibrator. Temperature was measured on the T_A^* scale. Tabulated values of the forward and beam efficiencies (F_{eff} and B_{eff}) are 0.94 and 0.78 respectively, for the conversion of temperature to T_{mb}.

[‖] The fitting procedure of hyperfine structure is described at: https://www.iram.fr/IRAMFR/GILDAS/doc/pdf/class.pdf

Table 3.1 A table summarising the observational properties of the JVLA, GBT and combined data. For the purposes of hyperfine structure fitting, velocity resolutions were smoothed to 0.098km/s for the JVLA, and 0.072km/s for the GBT. RMS noise was estimated from emission free areas. The combined data were smoothed by a Gaussian kernel of 2.4″, and have the same spectral resolution as the smoothed JVLA data. RMS noise of the IRAM 30 m data was converted to T_{mb}.

Telescope	JVLA		GBT		Combined data		IRAM 30 m	
Parameters	NH_3(1,1)	NH_3(2,2)	NH_3(1,1)	NH_3(2,2)	NH_3(1,1)	NH_3(2,2)	$C^{18}O$(1–0)	^{13}CO(1–0)
Channel width (kHz)	3.906	3.906	2.86	2.86	7.812	7.812	50.0	50.0
Velocity resolution (km/s)	0.049	0.049	0.036	0.036	0.098	0.098	0.13	0.13
RMS noise (K)	2.5	2.5	12.5	13.2	2.6	2.7	0.2	0.2
Beam major axis (″)	3.87	3.77	31.32	31.32	4.35	4.30	23.6	23.5
Beam minor axis (″)	2.81	2.87	31.32	31.32	3.44	3.48	23.6	23.5
Position angle (°)	30.95	30.56	0.0	0.0	30.95	30.56	0.0	0.0

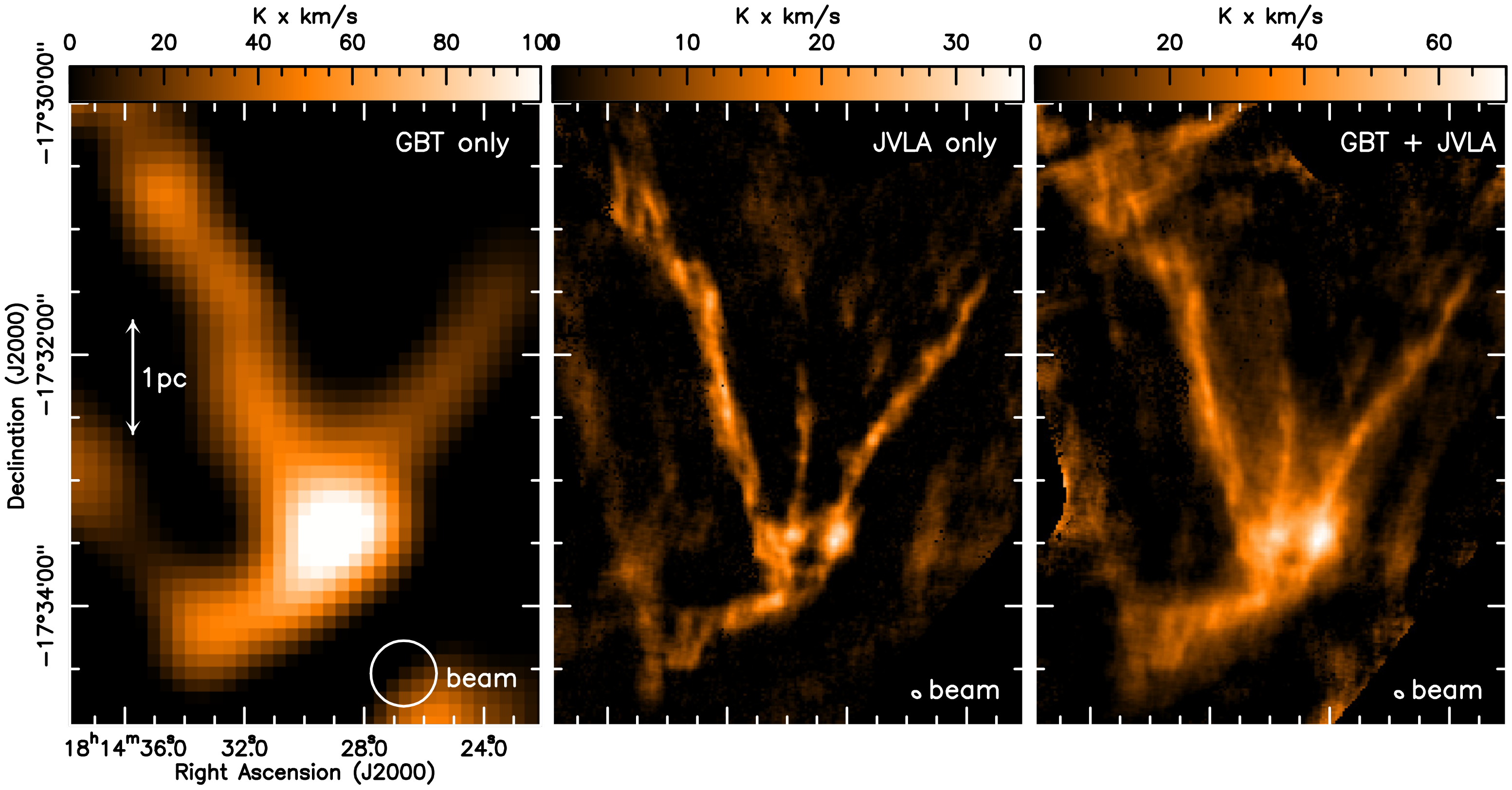

Figure 3.13 Plot showing a comparison between the integrated intensity maps of the NH_3(1,1) emission from the GBT (left), the JVLA (middle) and the combined GBT and JVLA (right) data sets. The GBT map displayed here has already had the calibration factor applied (see Section 3.2.2). The beam sizes are plotted in the bottom right corner of each panel. A parsec scale at the distance of the cloud is plotted in the first panel.

CHAPTER 4

RESOLVING FILAMENT EVOLUTION ON SMALL SPATIAL SCALES WITH NH_3 *

This section presents the kinematic and density structure of the SDC13 infrared dark hub at high angular resolution, with the goal of determining what drives its evolution and fragmentation. I discuss: the process of fitting the hyperfine structure emission of NH_3*; the kinematics of the gas; the derived* H_2 *column density map; and the extracted core and filament structures.*

4.1 LINE FITTING

Hyperfine structure fitting of the combined JVLA and GBT data was performed using the NH_3(1,1) and NH_3(2,2) fitting schemes within the CLASS† software, where the spectra are fitted at every pixel over all channels. The NH_3 fitting methods contain the velocity offset and relative intensity information of all the hyperfine components of the lines. The fitting procedure assumes Local Thermodynamic Equilibrium (LTE), where the excitation temperature of all N hyperfine components are

---

*The work presented here is published in Williams, Peretto et al. 2018 A&A in press.

†The fitting procedure of hyperfine structure is described at: https://www.iram.fr/IRAMFR/GILDAS/doc/pdf/class.pdf

the same. Gaussian line profiles are assumed for the opacity of the lines as a function of velocity v, where the total opacity is the sum of N profiles, such that:

$$\tau(v) = \tau_{\text{main}} \sum_{i=1}^{N} r_i \exp\left[- \left(\frac{v - v_{0,i}}{\alpha \Delta v} \right)^2 \right] , \tag{4.1}$$

where r_i is the intensity of the i^{th} component as a fraction of the total intensity, $v_{0,i}$ is the central velocity of the i^{th} component, τ_{main} is the opacity of the main central group of lines in the emission, Δv is the FWHM width of the line, and $\alpha = \frac{1}{2\sqrt{\ln 2}}$ is the Gaussian profile normalisation factor.

The CLASS fitting procedure makes the assumption that all hyperfine components are well separated, and do not overlap. This means that the central velocity of each i component can be written as $v_{0,i} = v_i + v_{ref}$, where v_i is the relative velocity of the i^{th} component with respect to the velocity of a reference component, v_{ref}. The reference component by convention is the main central component of the emission, meaning that by definition, the reference component velocity is the centroid line of sight velocity of the line. The centroid line of sight velocity is kept by CLASS as a free parameter in the fitting procedure. Another assumption made by CLASS is that the velocity dispersion of every component is the same. Hence, Δv gives the FWHM velocity width of the gas, which is also a free parameter in the line fitting procedure.

For velocities at the centre of the components, $v_i' = v_i + v_{ref}$, and assuming that all components are well separated, equation 4.1 is rewritten as:

$$\tau(v_i') = \tau(v_i + v_{ref}) = \tau_{\text{main}} \sum_{i=1}^{N} r_i \, , \tag{4.2}$$

which when r_i is normalised to unity is just equal to τ_{main}. The main group opacity is kept by CLASS as a free parameter in the fitting procedure.

To understand the final free parameter in the CLASS fitting procedure, one must briefly consider radiative transfer. The standard radiative transfer equation, taking into account both absorption and emission is given by:

$$\frac{\mathrm{d}I_\nu}{\mathrm{d}s} = -\kappa_\nu I_\nu + \epsilon_\nu \,, \tag{4.3}$$

where I_ν is the specific intensity of the source radiation, ds is the thickness of a thin slab the emission from a source passes through on the way to the detector, κ_ν is the absorption coefficient of that emission by the slab, and ϵ_ν is the emissivity of the emitting medium.

The radiative transfer equation may be expressed in terms of optical depth, $\mathrm{d}\tau_\nu = -\kappa_\nu \mathrm{ds}$, and is written as:

$$\frac{\mathrm{d}I_\nu}{\mathrm{d}\tau_\nu} = I_\nu - \frac{\epsilon_\nu}{\kappa_\nu} = I_\nu - S_\nu \,, \tag{4.4}$$

where $S_\nu = \epsilon_\nu / \kappa_\nu$ is the *source function*, and describes both absorption and emission of the source. Solving this equation gives the general solution to the radiative transfer equation for an isothermal and homogeneous medium:

$$I_\nu = I_{\nu,0} e^{-\tau_\nu} + S_\nu (1 - e^{-\tau_\nu}) \,, \tag{4.5}$$

where $I_{\nu,0}$ is the background intensity. If a source is assumed to be a blackbody, it may be described by the Planck function, which at low frequencies of emission such as NH_3 is approximated by the Rayleigh-Jeans law:

$$B_\nu(T) = \frac{2k_B \nu^2 T}{c^2} \,, \tag{4.6}$$

which is equal to S_ν in LTE, and where T is the temperature. Hence, the observed brightness temperature T_B of emission may be defined as:

$$T_b = \frac{c^2}{2k_B \nu^2} B_\nu(T) = \frac{h\nu}{k} J_\nu(T) \,, \tag{4.7}$$

where $J_\nu(T) = [\exp((E_u - E_l)/kT) - 1]^{-1}$. Hence, equation 4.5 can be written in terms of the brightness temperature as:

$$T_b = \frac{h\nu}{k} \left[J_\nu(T_{ex}) - J_\nu(T_{bg})\right] \left(1 - e^{-\tau_\nu}\right), \tag{4.8}$$

$$T_b(v) \approx (T_{ex} - T_{bg})(1 - e^{-\tau(v)}), \tag{4.9}$$

under the assumption that the temperature of the background is T_{bg}, and T_{ex} is the excitation temperature of the source. This is often called the *detection equation*. For reasons that later become apparent, multiplying equation 4.9 by $\tau_{\rm main}/\tau_{\rm main}$ gives:

$$T_b(v) = \frac{\tau_{\rm main}(T_{ex} - T_{bg})}{\tau_{\rm main}}(1 - e^{-\tau(v)}). \tag{4.10}$$

Similar to the simplification made in equation 4.2, rewriting equation 4.10 in terms of $v' = v_i + v_{ref}$ gives:

$$T_b(v_i') = \frac{\tau_{\rm main}(T_{ex} - T_{bg})}{\tau_{\rm main}}(1 - e^{-\tau_{\rm main} r_i}). \tag{4.11}$$

CLASS assumes that the opacity of each hyperfine component is optically thin, which simplifies this expression to $T_b(v_i') = \tau_{\rm main}(T_{ex} - T_{bg})r_i$. When r_i is normalised to unity, this means that the $\tau_{\rm main}(T_{ex} - T_{bg})$ simply gives the peak intensity of the component. This is the final parameter kept by CLASS as a free parameter in the fitting procedure.

Figure 4.1 shows examples of ten spectra and their model hyperfine structure fits at positions distributed across the cloud. After visual inspection, we do not find multiple velocity components, even at the filament junctions in the hub centre. Therefore we proceed to follow the above fitting procedure for a single velocity component everywhere. Using the `result` command, a model fit to the data was created, where the opacity-corrected Gaussian profiles are fitted to each hyperfine transition. The channel maps of the resulting cubes are shown in Figures 4.2 and 4.3. We use these model fit cubes for all analysis conducted in the rest of this work.

Due to a miss-alignment of the centre of the bandwidth with respect to the main hyperfine component at the cloud velocity ($V_{sys} = 37\,\mathrm{km\,s^{-1}}$) we do not detect the fifth hyperfine satellite group of the NH_3(1,1) line at $57\,\mathrm{km\,s^{-1}}$. To correct for this missing flux, in the construction of integrated intensity maps we assumed that the missing component's intensity was identical to that of its symmetric pair at $17\,\mathrm{km\,s^{-1}}$. Using the GBT data, which does cover all hyperfine components, we estimate that this correction leads to an uncertainty on the total integrated intensity of $\leq 5\%$.

4.1.1 Integrated intensity

Figure 4.4 (left) shows the integrated intensity of the NH_3(1,1) (top) and NH_3(2,2) (bottom) hyperfine structure lines. The structures in both maps are very similar even though, being typically 6 times weaker, the NH_3(2,2) emission is less extended and noisier than the NH_3(1,1) emission. When comparing the integrated intensity maps (or column density map - see Section 4.1.4) to both the 1.2mm dust continuum and $8\,\mu$m maps (see Figure 4.7) we find excellent agreement between the structures seen in the different images. All four filamentary arms seen in dust extinction/emission are well resolved in our NH_3 maps. This demonstrates that ammonia is an excellent tracer of cold dense gas as numerous previous works had already theoretically (Bergin & Langer 1997) or observationally (Lu et al. 2014) shown. There is, however, one exception to this excellent match between ammonia and dust emission. Indeed, we do not detect MM1 ($74.8 \pm 27.1\mathrm{M}_\odot$ within 0.26pc, Peretto et al. 2014, labelled in Figure 4.7), the largest protostellar source detected in the 1.2mm dust continuum map. This is a rather striking result since ammonia has consistently shown to be a good tracer of both cold and warm dense gas in star-forming clouds (Pillai et al. 2011; Ragan et al. 2011). Because of the protostellar nature of MM1, the lack of ammonia in the gas phase points towards a destruction mechanism rather

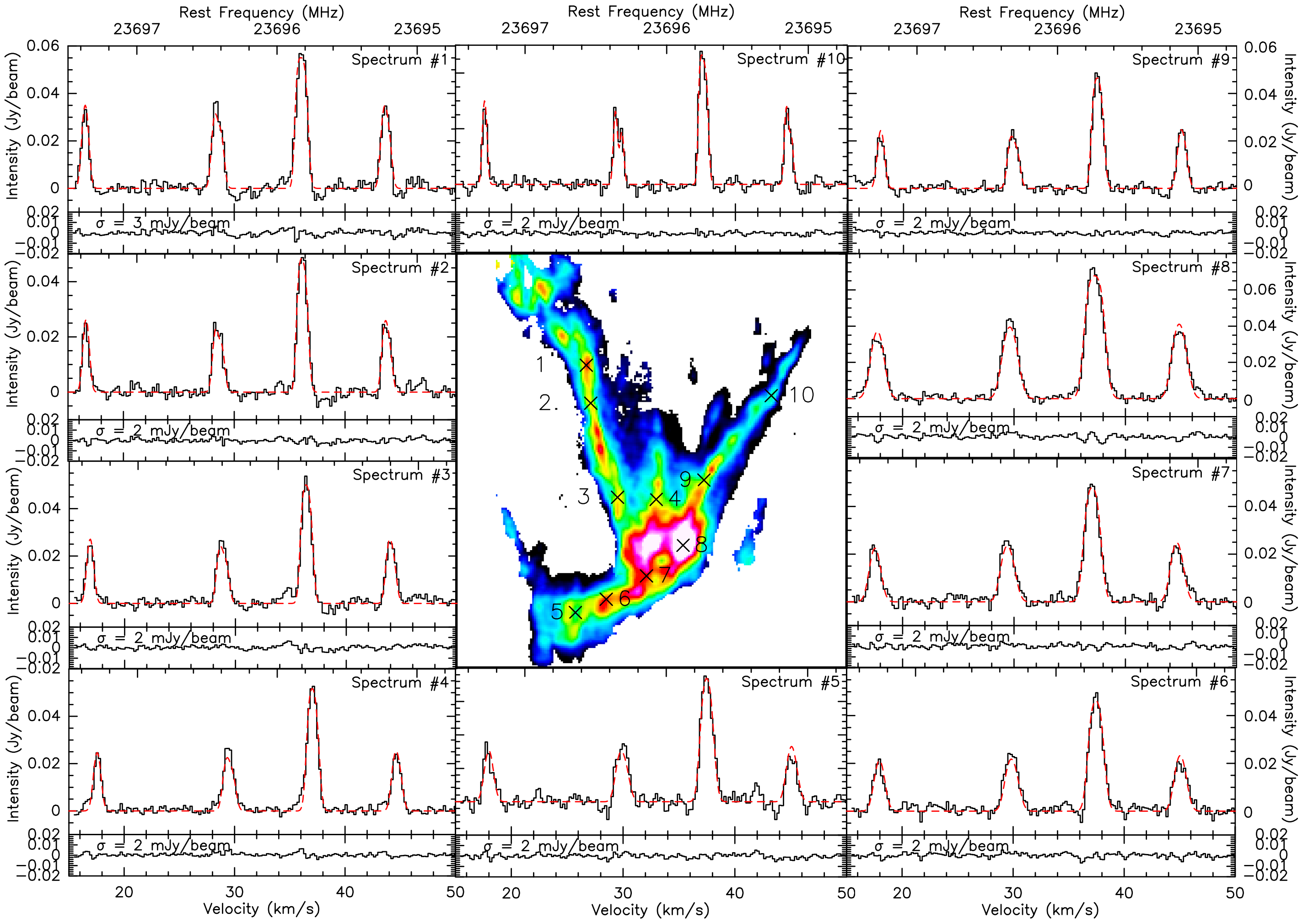

Figure 4.1 Examples of NH_3(1,1) spectra at ten positions in the cloud, plotted surrounding the H_2 column density derived from the NH_3 emission (discussed later in Section 4.1.4). The model fit is plotted over each spectrum in red, whilst the residual of the two is plotted in the bottom panel with the standard deviation quoted in mJy/beam. Regions of specific interest include those where the velocity width is seen to increase (spectra 1 and 6), positions where the centroid velocity changes as a filament meets the central hub (spectra 3, 4 and 7) and the large starless core MM2 (spectrum 8). It is clear that there is only a single velocity component everywhere in the cloud, with some lines being narrow enough to start resolving further hyperfine components (spectrum 10), and some showing the tell-tale signs of the cloud identified by Peretto et al. (2014) at a $V_{sys} = 54\,\mathrm{kms}^{-1}$ that likely overlaps in projection with the North-East filament (spectrum 1 and 2).

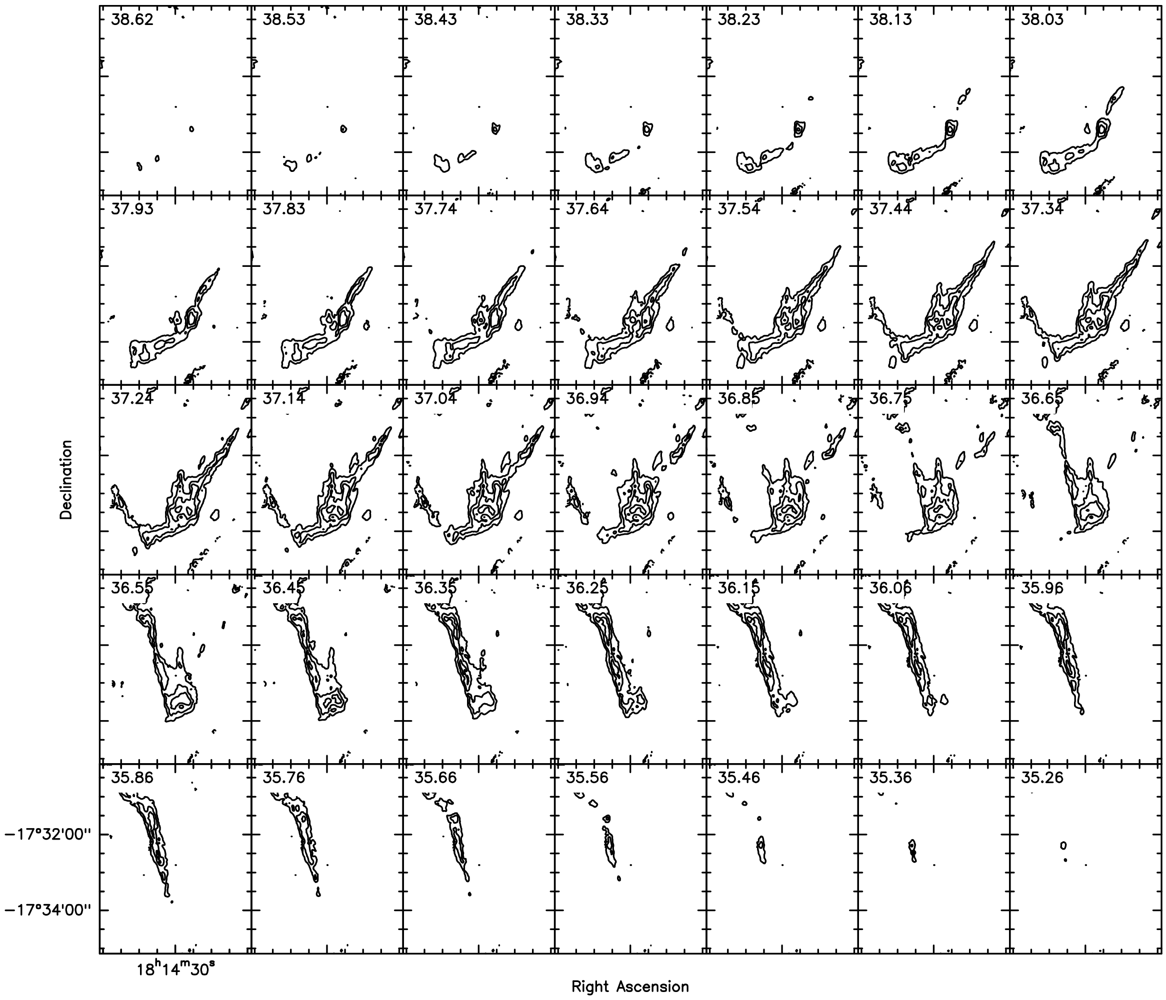

Figure 4.2 Channel map of the main transition of $NH_3(1,1)$ in the model combined data cube. Contour levels are placed at 0.015 Jy/beam steps, from 0.02 Jy/beam to 0.095 Jy/beam. The channel velocity is plotted in the top left corner of each panel.

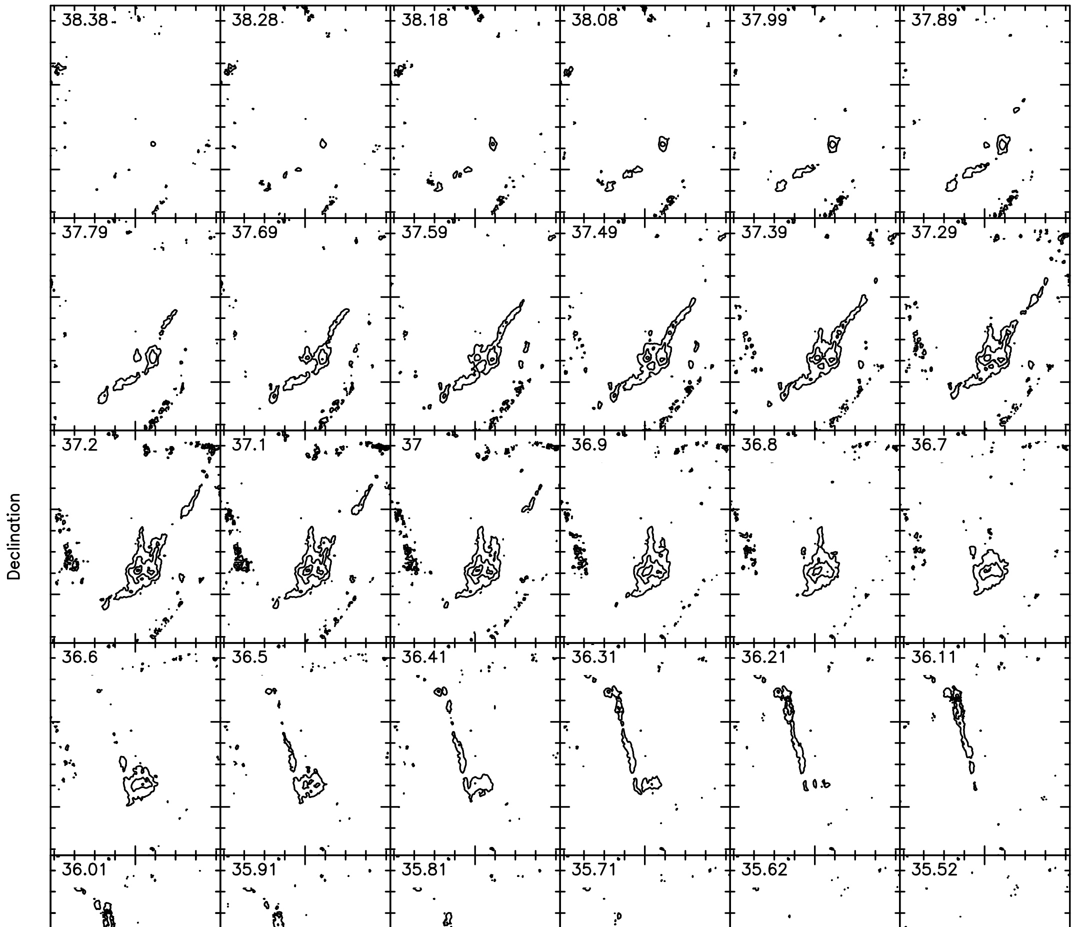

Figure 4.3 Channel map of the main transition of $NH_3(2,2)$ in the model combined data cube. Contour levels are placed at 0.008 Jy/beam steps, from 0.01 Jy/beam to 0.04 Jy/beam. The channel velocity is plotted in the top left corner of each panel.

than depletion. Chemical modelling of MM1 would be necessary to better constrain the physical origin of the lack of ammonia, but this goes beyond the scope of this work. Also, the cavity in column density (centred on 18:14:29.3 -17:33:37.4) is also seen in the 8 μm *Spitzer* data as diffuse emission, with no evidence of any related compact source that may have caused clearing of surrounding material.

4.1.2 CENTROID VELOCITY

The channel map of the main NH_3(1,1) transition in this model cube is shown in Figure 4.2. It shows large-scale velocity structures, with filaments appearing at different velocities, with a total velocity span of $\sim$ 7 km/s, consistent with the global velocity structure observed in N_2H^+(1-0) by Peretto et al. (2014). Figure 4.4 (middle columns) display the line of sight centroid velocity from both the NH_3(1,1) and (2,2) transitions. As a result of the increased angular resolution (almost by an order of magnitude), we observe a far more complex velocity field in SDC13 than previously revealed by the IRAM 30m data. In particular, we resolve both longitudinal and radial velocity gradients across all filaments (where filaments are named following the same convention as Peretto et al. 2014, and their extraction is discussed in Section 4.2.2). This is most evident across the bottom half of the North-East oriented filament, and across the entire South-East oriented filament (labelled in Figures 4.4 and 4.7). At face value, it is not clear that our ammonia velocity map is consistent with the N_2H^+(1-0) data published by Peretto et al. (2014). In order to check for consistency, we fitted the hyperfine components of the NH_3(1,1) and NH_3(2,2) emission from the GBT data only (see Figure 4.5), at a similar angular resolution to the IRAM 30m data. The GBT velocity map (the middle panel of Figure 4.5) reveals gradients along each and every filamentary arm towards the centre of the system, identical to those observed in the N_2H^+(1–0) IRAM 30m data. The large number of NH_3(1,1) hyperfine components makes the best fit centroid velocity and velocity width both very accurate. We estimate that the related uncertainty is less than half a channel width, i.e. $\sim 0.05\,\mathrm{km\,s^{-1}}$.

4.1.3 VELOCITY WIDTH

Figures 4.4 and 4.5 (right column) shows the FWHM velocity width of the dense gas of the JVLA&GBT combined data, and GBT only data respectively. We report an increased velocity width at the filament hub junction, peaking at $\sim$ 1.6 km/s and $\sim$ 3.0 km/s in each respectively, consistent with the broadening reported by Peretto et al. (2014). Interestingly, we also observe local increases of the velocity width sprinkled along each filamentary arms. As discussed later in Section 4.2, these are correlated to peaks in the H_2 column density. Note that opacity broadening is accounted for as a consequence of the fitting procedure used. However, because of the relatively large peak NH_3(1,1) main line opacity of 4.7, we independently performed a Gaussian fit of the optically thinner of the hyperfine components. By doing so, we observe the same increase of the line width. We conclude that the line widths plotted in Figure 4.4 represent the true velocity dispersion of the dense gas. Furthermore, we also notice the velocity width increases around some localised regions at the edges of filaments, most evident on the Eastern edge of the lower portion of the North-East filament, and the Western edge of the lower portion of the North-West filament.

4.1.4 H_2 COLUMN DENSITY MAP

Ammonia is often called the thermometer of molecular clouds (e.g. Maret et al. 2009), as the temperature of the gas can be directly calculated from the ratio of the intensities of the two main lower metastable transitions, NH_3(1,1) and NH_3(2,2). In turn, the ammonia column density map can be calculated using the temperature, opacity, and brightness temperature maps. The derivations of each of these quantities can be found in Section 1.6.2. Using a constant abundance of ammonia with respect to H_2 of 3×10^{-8} (Harju et al. 1993) one can then compute the H_2 column density map of

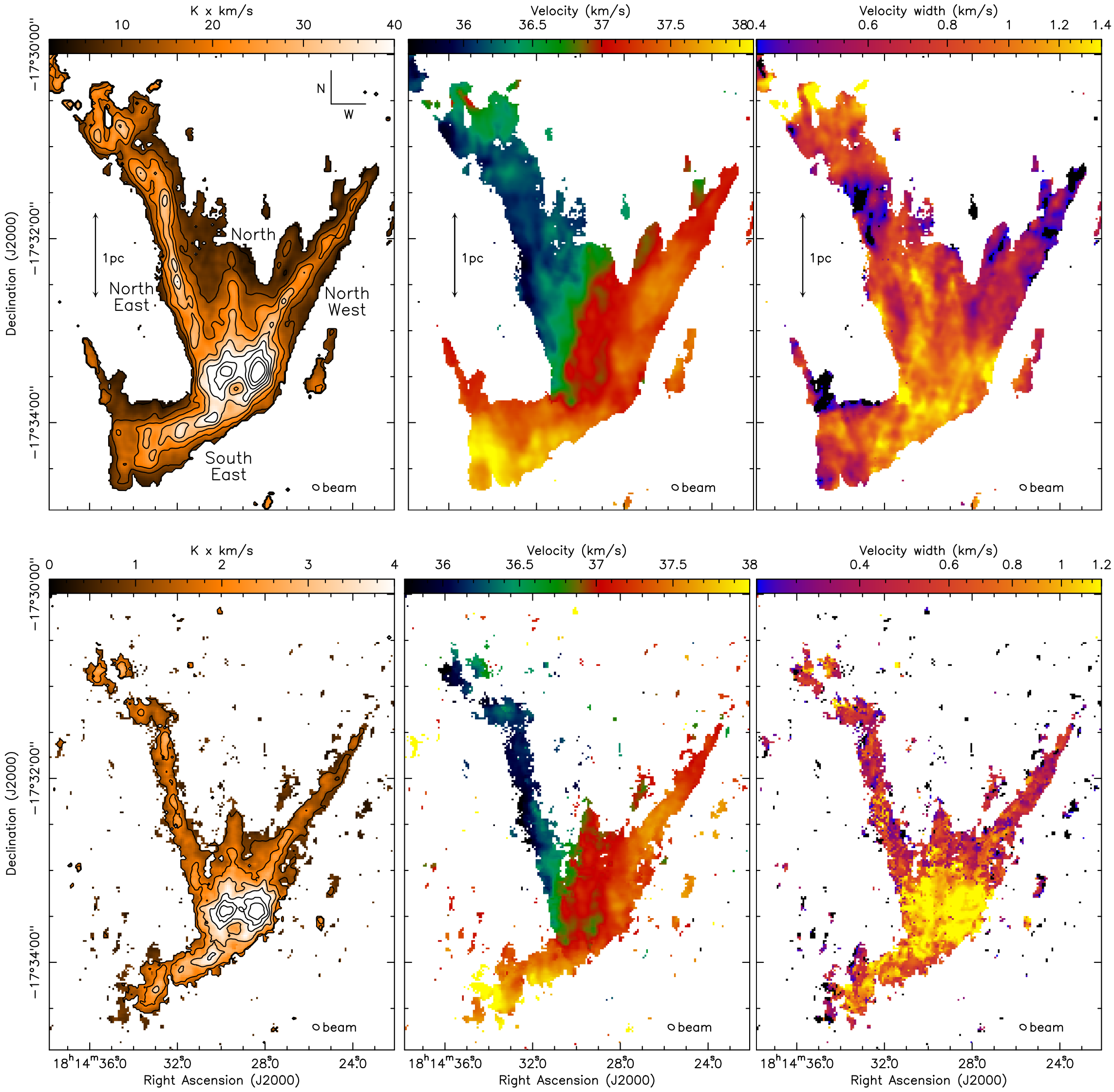

Figure 4.4 Integrated intensity (first column), centroid velocity (middle column) and velocity width (right column) of the $NH_3(1,1)$ transition (top row) and $NH_3(2,2)$ transition (bottom row) of the JVLA+GBT combined data. The $NH_3(1,1)$ data was masked to $5\,\sigma$, while the weaker $NH_3(2,2)$ data was masked to $3\,\sigma$. Filaments are named in the top left panel. Contours in the top left panel are in steps of $7\,\mathrm{K} \times \mathrm{km/s}$, from $5\,\mathrm{K} \times \mathrm{km/s}$ to $61\,\mathrm{K} \times \mathrm{km/s}$, while contours in the bottom left panel are in steps of $1\,\mathrm{K} \times \mathrm{km/s}$, from $1\,\mathrm{K} \times \mathrm{km/s}$ to $6\,\mathrm{K} \times \mathrm{km/s}$. Beam information is plotted in the bottom right corner of each panel, while the scale of 1pc is plotted in each panel of the top row.

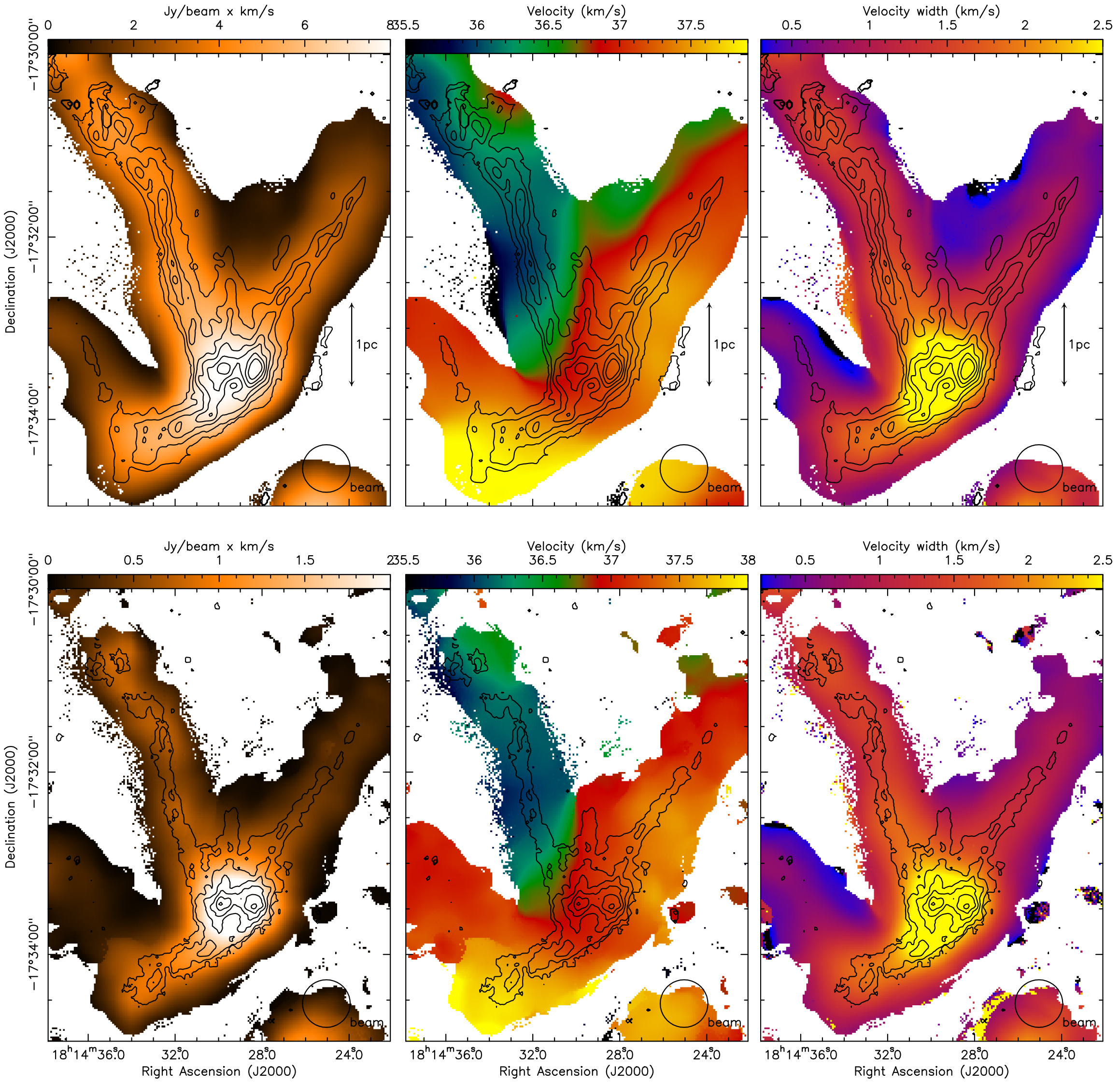

Figure 4.5 Integrated intensity (first column), centroid velocity (middle column) and velocity dispersion (right column) of the NH$_3$(1,1) transition (top row) and NH$_3$(2,2) transition (bottom row) of the GBT data. The data has been regridded to the JVLA pixel size. The NH$_3$(1,1) data was masked to 3σ, while the weaker NH$_3$(2,2) data was masked to 2σ. Contours in the top row correspond to the integrated intensity of the combined JVLA and GBT NH$_3$(1,1) data in steps of 0.04 Jy/beam × km/s, from 0.05 Jy/beam × km/s to 0.29 Jy/beam × km/s, while contours in the bottom row correspond to the integrated intensity of the combined NH$_3$(2,2) data in steps of 0.008 Jy/beam × km/s, from 0.008 Jy/beam × km/s to 0.096 Jy/beam × km/s. Beam information is plotted in the bottom right corner of each panel, while the scale of 1 pc is plotted in each panel of the top row.

SDC13. This calculation is however limited by the weaker emission of the NH_3(2,2) transition, which in our case traces 42% less of the cloud area than the NH_3(1,1) transition. To overcome this, we take a median value of the temperature across the cloud of 12.7 K. The full temperature map and histogram are shown in Figure 4.6. The corresponding column density map is displayed in Figure 4.7. Comparing this column density map to that calculated with a non-uniform temperature, we are satisfied that assuming a constant temperature across the entire cloud does not introduce any significant changes to the morphology of features in the map, whilst extending the coverage of the map (a result also reported by Morgan et al. 2013). Increasing the temperature by a standard deviation (1.8 K) decreases the column density by 12%. It is important to note that given our non-detection of the MM1 protostellar core, our assumption of constant abundance across the entire cloud (whilst a fair assumption given the excellent correlation between the NH_3(1,1) integrated intensity and the 8μm Spitzer emission) does not hold entirely for such portions of the cloud as the MM1 region.

Abundance of NH_3 to H_2

In this work, a standard abundance of NH_3 to H_2 column density was used, taken from the work of Harju et al. (1993) on nearby star forming regions. However, it is clear from works such as Benson & Myers (1983) that the abundance is not constant from source to source. The abundance in their sample of 19 dark clouds varies between 3×10^{-8} and 2×10^{-7} in TMC-1C and L1498 for example respectively. Given access to dust continuum emission, one can calculate a H_2 column density by rearranging the following:

$$I_\nu = N_{H_2} \mu_{H_2} m_H \kappa_0 \left(\frac{\nu}{\nu_0} \right)^\beta B_\nu(T_d) \,, \tag{4.12}$$

derived from equation 4.5 for LTE and optically thin conditions, where ν is the frequency, I_ν is the specific intensity of the dust continuum emission (in units of

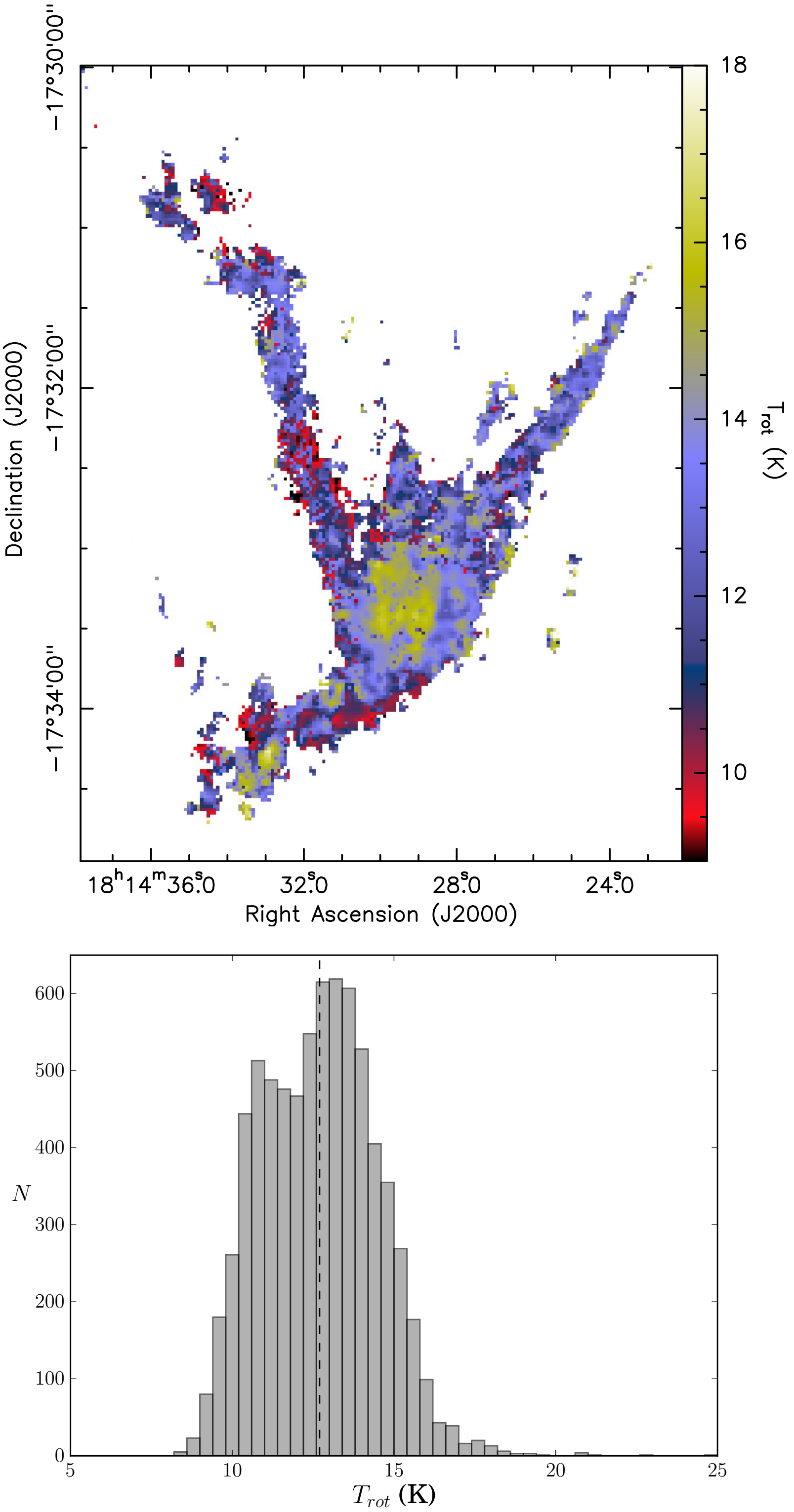

Figure 4.6 *Top*: Map of the rotational temperature calculated using equation 1.16. It is clear that the coverage of the image is limited to that of the weaker NH_3(2,2) line. No correlation is found between temperature and core position. *Bottom*: Histogram of the T_{rot} map in the top panel. Vertical dashed line indicates the median value of 12.7 K. The standard deviation is 1.8 K.

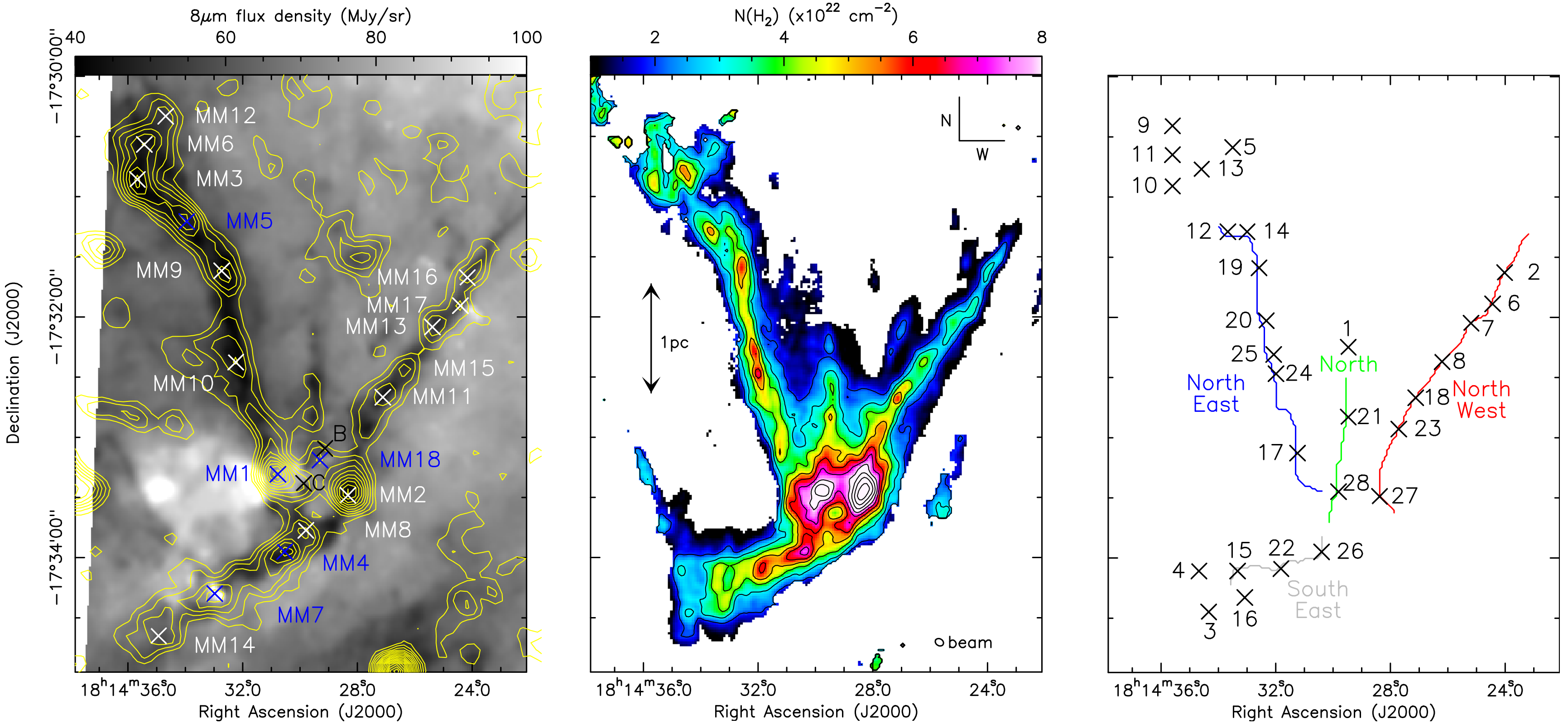

Figure 4.7 *Left*: Spitzer 8 μm flux density in units of MJy/sr, overlaid with IRAM 30m MAMBO 1.2mm dust continuum contours in steps of 5mJy/beam, from 3mJy/beam to 88mJy/beam. Crosses denote the positions of identified 1.2mm MAMBO compact sources (white for starless and blue for protostellar, Peretto et al. 2014) and two 1.3mm SMA continuum sources (in black crosses, McGuire et al. 2016). *Middle*: H_2 column density map in units of $10^{22}\,\mathrm{cm}^{-2}$, derived from the NH_3 integrated intensity. Overlaid contours are placed in $1 \times 10^{22}\,\mathrm{cm}^{-2}$ steps, from $2 \times 10^{22}\,\mathrm{cm}^{-2}$ to $12 \times 10^{22}\,\mathrm{cm}^{-2}$. *Right*: Plot showing the extracted cores (black crosses, numbered according to Table 4.1) and filaments (labelled coloured lines). The extraction of these structures are discussed in Section 4.2. Extra cores at the outskirts of the North-East and South-East arms are in the more diffuse regions of the cloud where the spines did not extend through. Spine colours match those in subsequent figures.

Jy/sr), μ_{H_2} is the mean molecular weight (taken as 2.8), m_H is the mass of a hydrogen atom, κ_0 is the specific dust opacity at the reference frequency ν_0 of 1.2 THz, β is the dust emissivity index (taken as 1.8, Planck Collaboration et al. 2011) normalised such that $\kappa = 0.12\,\mathrm{cm}^2\,\mathrm{g}^{-1}$ assuming a dust to gas mass ratio of 1%, and T_d is the dust temperature. $B_\nu(T_d)$ is the Planck function given by,

$$B_\nu(T_d) = \frac{2h\nu^3}{c^2}\frac{1}{\exp^{\frac{h\nu}{k_B T_d}} -1}\,, \tag{4.13}$$

where h is the Planck constant, c is the speed of light and k_B is Boltzmann's constant. The only assumption required is on the dust temperature, which can reasonably be set equal to the gas temperature if we assume that the dust and gas is well coupled at the high densities of IRDCs.

In using the 1.2 mm dust continuum emission (Peretto et al. 2014) from the MAMBO bolometer array on the IRAM 30m telescope at 11″ resolution, a comparison is made between this dust-based H_2 column density and the NH_3 column density in Figure 4.8. Fitting a straight line through all the points revels a gradient of $(3.3 \pm 0.1) \times 10^{-8}$, a consistent value to the 3×10^{-8} used to construct the H_2 column density map of Figure 4.7. On first impression, it appears bizarre that the fit would have a low standard deviation equivalent to only $\sim 3\%$, given that the distribution appears to have a large spread of values. The density of the points were plotted (in colour on Figure 4.8) by constructing a Gaussian Kernel Density Estimation on a regular grid of 300 bins within the data extent. From doing this it is clear that the fit is dominated by the clustering of the highest concentration of points at low column, hence the low standard deviation on the fit. As a result, we conclude the dominant error source on the H_2 column density is the assumption on the temperature (12% when increasing the temperature by a standard deviation as mentioned previously in this section). Overall, we take a conservative estimate of the uncertainty on the H_2 column density of 20%.

Two low concentration departures can be seen in the distribution of Figure 4.8, one at large NH_3 column and large H_2 column, the other at low NH_3 column and large H_2 column. These two regions are identified to correspond to the MM2 and MM1 cores respectively, showing clearly the depletion of NH_3 towards MM1. As mentioned in Section 4.1.1, chemical modelling would be required to properly understand the nature of the depletion. However, a simple way to make a ball-park estimate on the level of depletion would be to fit the data excluding the MM2 and MM1 core in turn separately, and compare the resulting abundances. This is shown by the dashed lines in Figure 4.9. Excluding MM1 results in a marginally steeper gradient, hence larger abundance of $(3.7 \pm 0.1) \times 10^{-8}$. Excluding the MM2 core results in a significantly shallower gradient, hence lower abundance of $(2.0 \pm 0.1) \times 10^{-8}$. If one were to assume that perhaps the steepest gradient were more representative of the abundance in SDC13, and worked backwards to determine the mean NH_3 column density from the H_2 column density, this still does not bring the NH_3 column density of MM1 back in-line with what one might expect were there no depletion. It is clear this simple and crude approach is not sufficient to understand the depletion, and is a very interesting outstanding question that needs to be looked into in more detail. This is discussed more in Chapter 6.

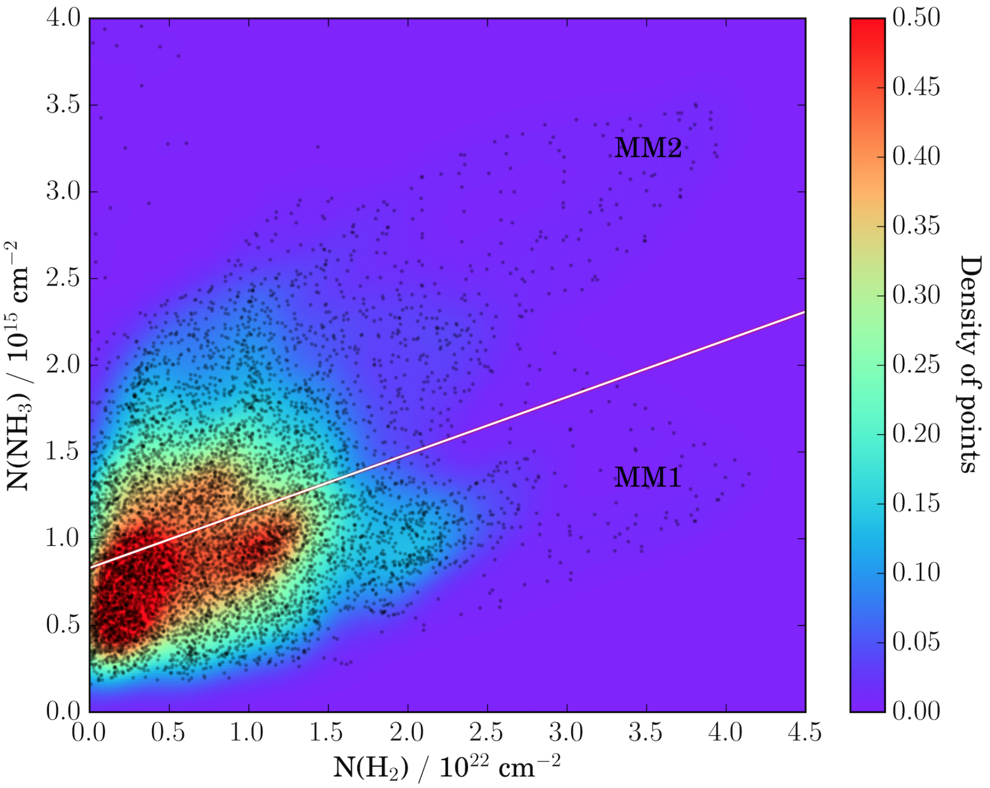

Figure 4.8 Plot of the H_2 column density calculated from dust continuum emission against the NH_3 emission from the JVLA and GBT combined data set. The colour scale plots the density of the scatter points. The white line indicates a best-fit straight line through the points, with a gradient of 3.3×10^{-8}, with a 1σ error plotted in red (but can hardly see it) corresponding to $\pm 3\%$. The points corresponding to the MM1 and MM2 cores are labelled.

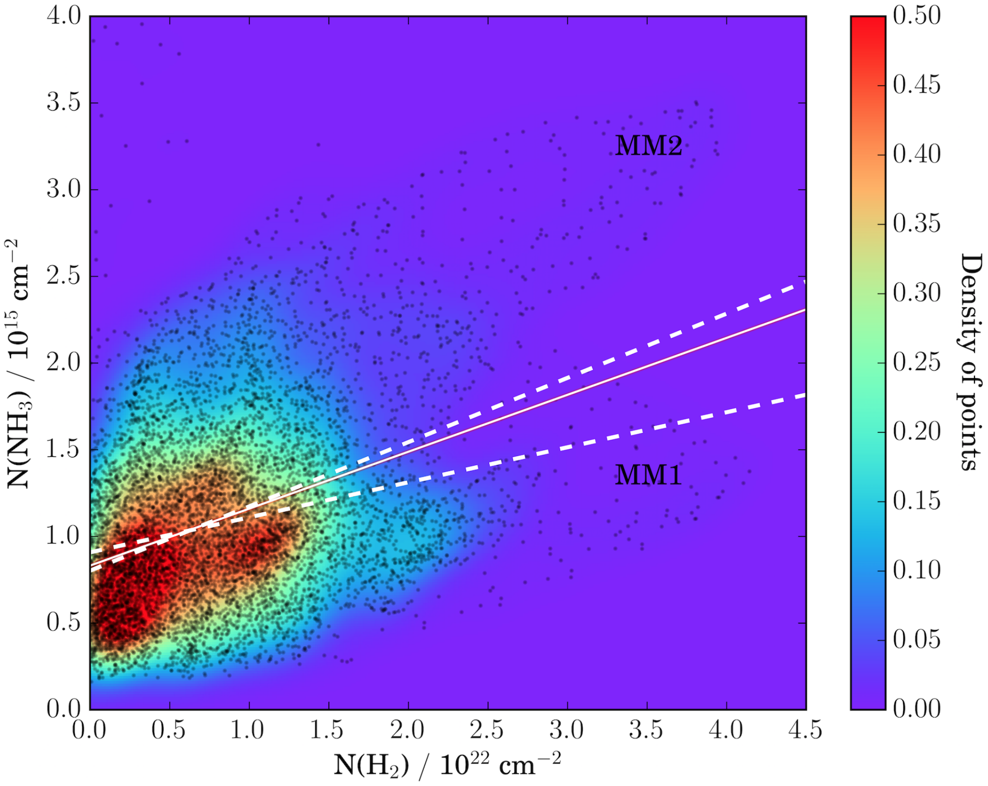

Figure 4.9 Same as Figure 4.8, however showing straight line fits whilst excluding the MM1 and MM2 cores separately (dashed lines). The steepest gradient of $(3.7 \pm 0.1) \times 10^{-8}$ was found excluding the MM1 core, and the shallowest gradient of $(2.0 \pm 0.1) \times 10^{-8}$ was found whilst excluding the MM2 core. Errors are the standard deviation.

4.2 Analysis: Structure extraction

In this section, I discuss the identification of cores and filaments within SDC13.

4.2.1 Cores

Dendrograms are a useful tool for the understanding of hierarchical structure, and are invaluable for understanding the fragmentation of molecular clouds (e.g. Rosolowsky et al. 2008). We used the dendrogram code developed by Peretto & Fuller (2009) to extract all clumps from the NH_3 derived H_2 column density map at regular isocontours. A minimum isocontour value is set at $N(H_2) = 1 \times 10^{22}\,cm^{-2}$ defining the "trunk" of the dendrogram tree, with a regular isocontour spacings at $1\,\sigma$ of $0.04 \times 10^{22}\,cm^{-2}$ throughout, and a $5\,\sigma$ detection threshold. A pixel limit of 7 defines the smallest size of structure considered resolved, as it roughly matches the beam shape. Cores were identified as the highest levels in the dendrogram hierarchy (termed "leaves") meaning that they contain only themselves and no other sub-structures. All observed core properties are listed in Table 4.1, such as the central core coordinates, major and minor axes, position angle, aspect ratio, radius and mean H_2 column density. Core radii were calculated by considering each isocontour core boundary a disc with an equivalent area. The smallest deconvolved core radius can be seen to match half of the beam width, a direct effect of matching the pixel limit of the extraction code to the beam.

We identified 28 cores, of which seven lie along each of the North-West and North-East filaments, three lie along the South-East filament and two along the North filament (plotted in the right panel of Figure 4.7). The remaining cores mostly lie at the end of the North-East filament. Their starless (or protostellar) nature was identified by the lack (or presence) of Spitzer 8μm and 24μm sources (Peretto et al. 2014). Only three protostellar sources were detected, which were already identified by Peretto et al. (2014) (listed in Table 4.1), two of which (MM5 and MM7) appear in the 70μm Herschel sources catalogue of Molinari et al. (2016). The previously unidentified core 28 which resides in the hub centre also corresponds to a 70μm source. Core masses were calculated by taking the mean H_2 column density (middle panel of Figure 4.7, calculated from the NH_3 column density) within the core boundary, and setting the average molecular weight, $\mu = 2.8$. Two mass estimates were calculated for each core, one excluding the outer column density shell (effectively excluding the "background", equivalent to the *clipping* scheme of Rosolowsky et al. 2008) regarded as the lower limit of the mass, and one that incorporates the background column density (equivalent to the *bijection* scheme of Rosolowsky et al. 2008) regarded an upper limit of the mass. Small column density peaks on top of a large background column density will generate very different mass estimates. The cores we identify here range from low- to high-mass, with the most massive ones being located near the filament junctions (core IDs 26, 27 and 28 - See Figure 4.7). Both mass ranges, as well as the virial ratio (see Section 4.3.5) are listed in Table 4.1. The association of the newly identified cores with those published in Peretto et al. (2014) is also provided in the table. The dominant source of uncertainties in the estimate of core properties are the distance (11%), the abundance (within a factor of 2), and the way cores are defined (bijection versus clipping - see Table 2). Note that uncertainties related to distance and abundance are systematic and therefore will not change observed trends.

As already mentioned in Section 4.1.3, we do observe a correlation between the increase of velocity width and the presence of cores. In order to quantify the number of cores displaying such behaviour, we systematically computed the average velocity width within the extracted core area at its position in the dendrogram tree where it is first identified as a leaf (ΔV_{core}). Doing so we find that 73% of the cores show an increase in their mean velocity width of $\geq 10\%$ when compared to the velocity width of the underlying "branch" structure of the dendrogram tree (ΔV_{branch}, as shown in Figure 4.10). Furthermore, 87.5% of these belong to the starless core population (according to the lack of mid-infrared point source).

Table 4.1 Observed and calculated properties of extracted cores. Column 1: core ID number; Cols. 2 and 3: right ascension and declination of the core peak emission; Cols. 4 and 5: core major and minor axes; Col. 6; position angle; Col. 7: major-to-minor axes ratio; Col. 8: mean value of H_2 column density within core boundary; Col. 9: deconvolved core radius in arcseconds; Col. 10: deconvolved core radius in parsec; Col. 11: lower limit on the mass; Col. 12: upper limit on mass; Col. 13: Virial ratio, calculated using equation 4.20 where the upper limit on the mass was used; Col. 14: Core associations to the MM identifications of previous work (Peretto et al. 2014). The detected protostellar sources are MM4, MM5 and MM7. Systematic error from the kinematical distance to SDC13 (3.6 ± 0.4 kpc) is associated to all size parameters. Uncertainty on the column density and masses originate from the assumption of constant $[NH_3]/[H_2] \sim 3 \times 10^{-8}$ abundance (Harju et al. 1993) and temperature (12.7 K) in the cloud. Increasing the temperature by 1.8 K (equivalent to a standard deviation) decreases $N(H_2)$ by 12%.

ID	RA (J2000)	Dec (J2000)	Min. ($''$)	Maj. ($''$)	P.A. ($_\circ$)	Aspect ratio	$N(H_2)$ (10^{22}cm^{-2})	Radius ($''$)	Radius (pc)	Mass$_{low}$ ($M_\odot$)	Mass$_{up}$ ($M_\odot$)	α_{vir}	MM assoc.
1	18:14:29.5	-17:32:14.9	2.3	5.0	10.3	2.2	2.22	3.0	0.07	0.5	5.4	1.47	–
2	18:14:24.0	-17:31:37.7	2.6	9.9	-32.6	3.8	2.90	4.5	0.09	1.9	14.4	0.54	MM16
3	18:14:34.3	-17:34:26.9	3.0	3.7	8.4	1.2	2.95	3.0	0.07	0.5	7.2	1.43	–
4	18:14:34.7	-17:34:06.5	3.5	6.5	-7.2	1.8	2.94	3.7	0.08	0.6	10.3	1.49	–
5	18:14:33.5	-17:30:35.3	2.7	5.7	-35.3	2.1	3.02	3.4	0.08	0.7	9.1	2.00	–
6	18:14:24.4	-17:31:53.3	1.7	5.7	-26.5	3.3	3.30	2.7	0.07	0.4	7.1	0.56	MM17
7	18:14:25.2	-17:32:02.9	2.9	8.8	-26.8	3.0	3.37	4.4	0.09	1.2	15.8	0.54	MM13
8	18:14:26.2	-17:32:22.1	2.8	6.6	-25.7	2.3	3.84	4.0	0.08	1.1	15.0	0.65	MM15
9	18:14:35.6	-17:30:24.5	1.9	2.8	-85.3	1.5	3.80	1.5	0.05	0.2	4.1	4.15	–
10	18:14:35.6	-17:30:54.5	3.7	6.8	5.3	1.8	4.22	4.6	0.10	2.6	21.8	0.61	MM3
11	18:14:35.6	-17:30:38.9	1.6	3.3	17.9	2.1	3.87	1.7	0.05	0.2	4.5	1.50	–
12	18:14:33.7	-17:31:17.3	3.9	7.4	33.4	1.9	4.35	5.0	0.10	3.5	25.9	0.45	MM5
13	18:14:34.6	-17:30:46.1	4.7	6.9	28.1	1.5	4.64	5.3	0.11	4.2	30.8	0.64	–
14	18:14:33.0	-17:31:17.3	1.2	4.9	34.5	4.1	4.20	1.7	0.05	0.1	4.9	0.84	–
15	18:14:33.3	-17:34:06.5	2.4	7.8	-5.5	3.2	4.43	3.9	0.08	0.9	16.9	0.87	–
16	18:14:33.1	-17:34:19.7	2.2	4.4	-18.6	2.0	4.35	2.6	0.07	0.3	8.9	0.88	MM7
17	18:14:31.2	-17:33:07.7	2.7	11.9	0.7	4.4	4.59	5.2	0.11	2.2	29.6	0.43	–
18	18:14:27.1	-17:32:40.1	2.7	7.8	-32.9	2.9	4.86	4.2	0.09	2.3	20.9	0.47	MM11
19	18:14:32.6	-17:31:35.3	3.0	11.7	1.3	3.9	5.05	5.5	0.11	3.5	36.0	0.25	MM9
20	18:14:32.3	-17:32:01.7	1.1	6.5	21.2	5.9	4.73	1.8	0.06	0.1	6.0	0.73	–
21	18:14:29.5	-17:32:49.7	1.7	6.3	-4.4	3.8	4.83	2.4	0.06	0.3	9.0	0.92	–
22	18:14:31.8	-17:34:05.3	3.7	6.8	-38.4	1.8	5.68	4.6	0.10	2.0	29.4	0.83	–
23	18:14:27.7	-17:32:55.7	1.6	2.3	-7.1	1.5	5.44	1.0	0.05	0.1	4.2	1.05	–
24	18:14:32.0	-17:32:28.1	2.2	4.7	10.9	2.2	5.87	2.7	0.07	1.0	12.6	0.75	MM10
25	18:14:32.1	-17:32:18.5	1.5	4.5	13.2	2.9	5.71	2.0	0.06	0.5	8.4	0.94	–
26	18:14:30.4	-17:33:56.9	4.6	8.6	-41.9	1.9	6.48	5.4	0.11	3.5	44.3	0.85	MM4
27	18:14:28.4	-17:33:29.3	8.1	12.6	-7.4	1.6	9.11	9.9	0.18	36.7	195.7	0.28	MM2
28	18:14:29.8	-17:33:26.9	6.4	11.4	-37.6	1.8	8.20	8.1	0.15	11.6	119.2	0.30	–

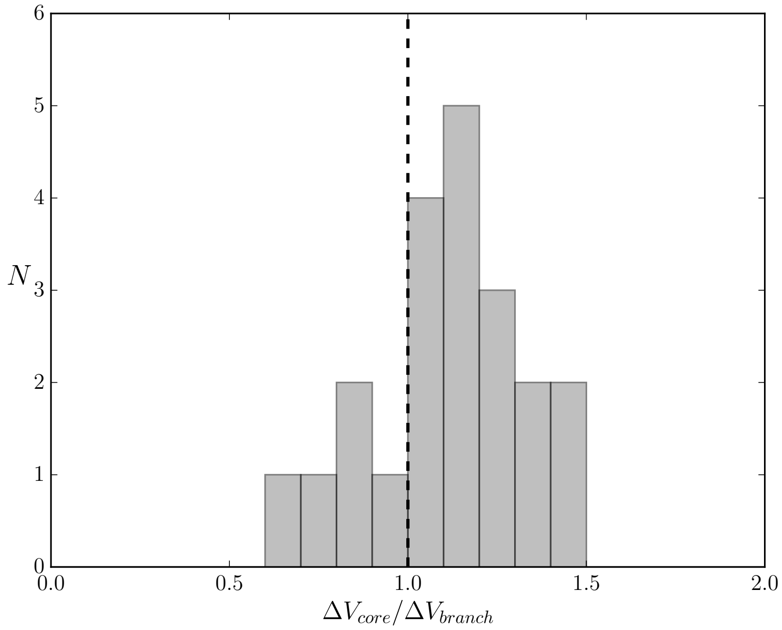

Figure 4.10 Histogram of the ratio of the average velocity width within a core region (ΔV_{core}) to that of the underlying branch structure (ΔV_{branch}) in the dendrogram tree. The vertical dashed line indicates where $\Delta V_{core} = \Delta V_{branch}$.

To visually demonstrate this increase even further, we split the cores into two sub-samples. The first contains cores with $\Delta V_{core}/\Delta V_{branch} > 1$, whilst the second contains cores with $\Delta V_{core}/\Delta V_{branch} \leq 1$. In Figure 4.11 we stack each of the sub-samples separately and take the mean velocity width (for starless cores only). The overplotted contours are of the average H_2 column density. As the inclination angles of the cores in Table 4.1 align with the natal filament, and the majority of the cores included in the stack reside in the North-West and North-East filaments (with mean inclination angles of $-25°$ and $+18°$ respectively, see Table 4.2), the orientation of the mean column density contours (dominated by the largest column density cores) are seen to align to the North direction on average. This figure clearly shows that the velocity dispersion is increased over the entire extent of the cores, with a peak towards their centres.

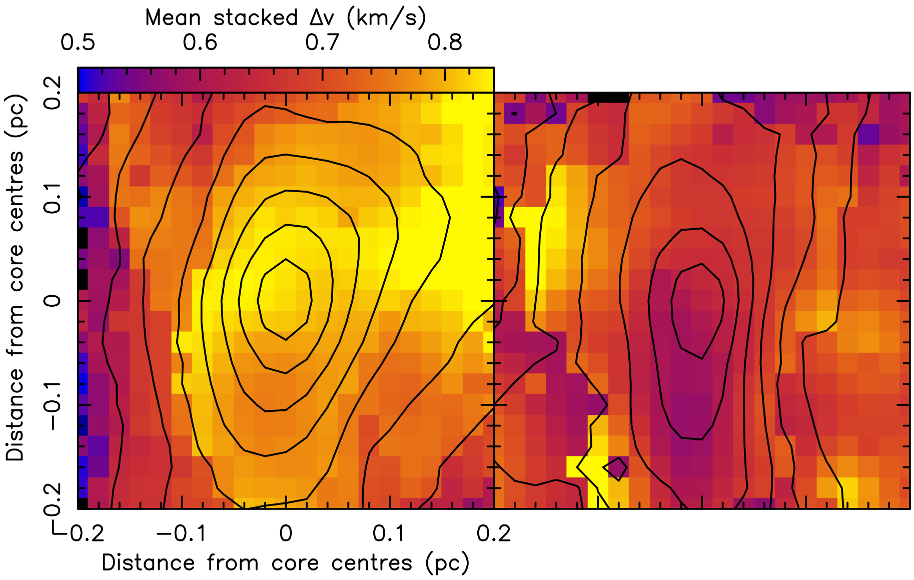

Figure 4.11 The average stacked velocity width of cores identified with $\Delta V_{core}/\Delta V_{branch} > 1$ (left) and those with $\Delta V_{core}/\Delta V_{branch} < 1$ (right). Included in the construction of the left and right panels are 12 and 5 cores respectively. Only starless cores within the filamentary arms are included, excluding both protostellar and central hub region sources. Contours are of the respective average stacked column density in $0.5\times10^{22}\,\mathrm{cm}^{-2}$ steps from 0 to $6\times10^{22}\,\mathrm{cm}^{-2}$ on the left, and in $0.4\times10^{22}\,\mathrm{cm}^{-2}$ steps from 0.2 to $3.8\times10^{22}\,\mathrm{cm}^{-2}$ on the right.

4.2.2 FILAMENTS

The orientation and morphology of all filamentary structures were constrained by identifying the spines of the filaments. As the name suggests, the spine is considered the backbone of a filament, tracing the pixels where the column density exhibits a local maximum in at least one direction. This was quantified by computing the 2$^{\mathrm{nd}}$ derivative matrix (e.g. Schisano et al. 2014), i.e., the Hessian matrix, for each pixel in the column density map. Then, by diagonalising the matrix, and selecting areas where at least one of the eigenvalues is negative, we can identify the filament areas. To reduce this to a spine, we used the `THIN` IDL function. The local orientation of the filaments at each pixel along the spine is provided by the angle of the first eigenvector and the x axis of the image. Figure 4.7 shows the spines of each of the four identified filaments, and Table 4.2 compiles their properties. The masses of all filaments (including the portions of the spines that intersect the central hub) total to

$\sim 1000\,\mathrm{M}_{\odot}$, equal the mass quoted by Peretto et al. (2014). Separating the central hub region from the filaments places half the total mass in the hub region and half in the filaments.

Longitudinal filament profiles

We first study the filaments along their spines. Figure 4.12 plots the line profiles of all four filaments in H_2 column density (first row), velocity width (second row) and absolute centroid line-of-sight velocity (third row) where the origin of the filaments was defined to reside at the centre of the hub. Filaments show variations in all quantities, and on a range of spatial scales. First, we notice that these variations are correlated in all three quantities, being particularly obvious for the North-East and North-West filaments. More specifically, core positions (marked by shaded regions on all panels) correlate with the velocity width, but also in centroid velocity where local velocity gradients are developed. This is shown in the fourth row of Figure 4.12 where we plot the absolute velocity gradient along the spine, evaluated over the mean core size of 0.1 pc. We note that a significant fraction of the cores (~63%) are located at a peak of velocity gradient. In the bottom row of Figure 4.12 we plot the rotational temperature derived from the NH_3 emission. Although quite variable along the length of the filament, we do not find a correlation between the temperature and core positions, nor the kinematic properties. We conduct Spearman's rank correlation coefficient test on these correlations for all four filament separately. We find a definite correlation between the column density and velocity width peaks in every filament (as shown in Figure 4.13) with vanishingly small p-values in every filament with coefficients ranging from 0.24 in the North-East filament (indicating a moderate correlation), to 0.74–0.91 in the other three filaments (indicating a strong correlation). We find similarly small p-values in the column density and centroid velocity correlations, showing to us a definite link between all three of these properties. Furthermore, we notice that there are other common features to all filaments, such as the strongest column

Table 4.2 Summary of filament properties. Column 1: Filament name. Col. 2: The length of the filament spine in parsec. Col. 3: The mean orientations from the minimisation of the eigenvalues of the Hessian matrices, in degrees. The origin at 0° was defined by the North direction, and the positive values are anticlockwise. Col. 4: median core separation, excluding hub cores, quoted with their standard deviation. Given we have excluded hub centre cores, this leaves only one core in the North filament.. Column 5: Mean filament width in parsec (from 2.35 times the standard deviation of each radial column density) evaluated from the regions of the filament outside the hub centre only. Col. 6: Mass per unit length, evaluated from the integration of radial column density profiles outside the cloud hub. Col. 7: the total mass of the filament, including the regions that pass through the cloud hub centre. Col. 8: The lower limit on the age of the filament (equation 4.14) (in-evaluable for the North filament given its single core.). Col. 9: The accretion rate of material onto the filament during its formation. Col. 10: the time elapsed since the filament became critical. Col. 11: mean radial velocity gradient across the inner 0.2 pc filament width. Systematic errors from the kinematical distance to SDC13 (3.6 ± 0.4 kpc) and unknown filament inclination are associated to the filament lengths and mean core separations. Inclination angle affects the timescales quoted, as discussed in Section 4.3.2.

Filament	Length (pc)	Orientation (°)	λ_{core} (pc)	Width (pc)	M$_{line}$ (M$_{\odot}$/pc)	M$_{\text{fil}}$ (M$_{\odot}$)	τ_{crit} (Myr)	$\dot{M}$ (M$_{\odot}$/pc/Myr)	τ_{age} (Myr)	$\lvert\nabla V_r\rvert$ (km/s/pc)
North (N)	1.32	-8.1	–	0.27	270	259	–	–	–	0.3
North-West (NW)	3.06	-25.6	0.34 ± 0.06	0.16	147	393	0.64	48.9	3.0	0.2
South-East (SE)	1.17	+145.2	0.41 ± 0.02	0.37	374	223	0.78	40.0	9.4	1.1
North-East (NE)	2.89	+18.0	0.33 ± 0.21	0.25	264	401	0.62	50.5	5.3	1.5

density and velocity dispersion peaks located at the origin of the filaments. Note that this is not true for the North-East filament, but would likely be true if the abundance of ammonia towards the MM1 protostellar core (Peretto et al. 2014, labelled in the left panel of Figure 4.7) were not decreased (see Section 4.1.1).

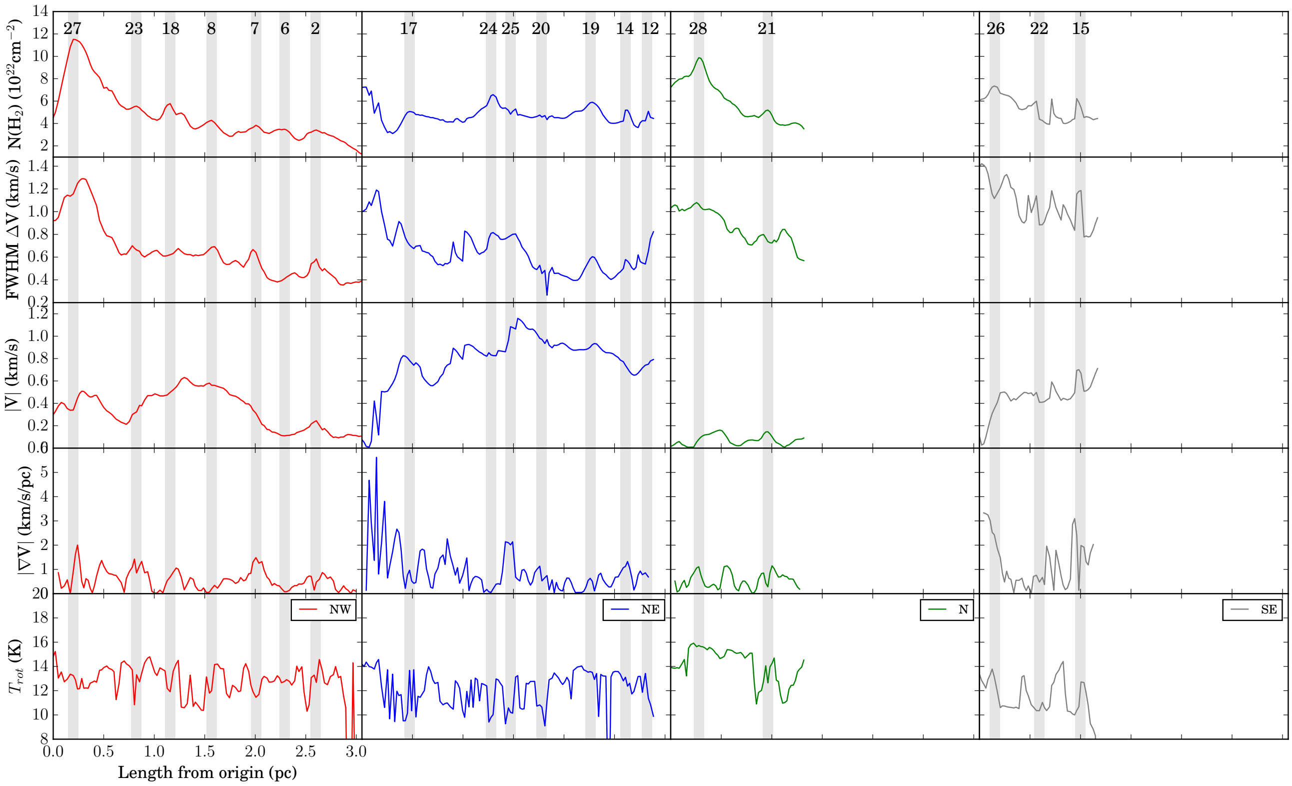

Figure 4.12 Profiles along the spines, where each column denotes a different filament (North-West in red, North-East in blue, North in green and South-East in grey). The origin of each spine was centred at the hub region. The first row plots the column density of H_2 calculated from the fitted NH_3 integrated intensity. The second row plots the FWHM velocity width, while the third row plots the absolute centroid line-of-sight velocity (offset from the cloud systemic velocity of 37 km s^{-1}), both also from the hyperfine structure fitting. The fourth row plots the absolute velocity gradient evaluated over the mean core size of ∼0.1 pc. The fifth row plots the rotational temperature derived from the NH_3 emission, which has a standard deviation of 1.8 K. The drops of temperature below 8 K are artificial and due to missing NH_3(2,2) detections at these particular locations. The vertical shaded regions in each panel correspond to the peak N(H_2) positions of the cores along the spine, and are ∼0.1 pc wide.

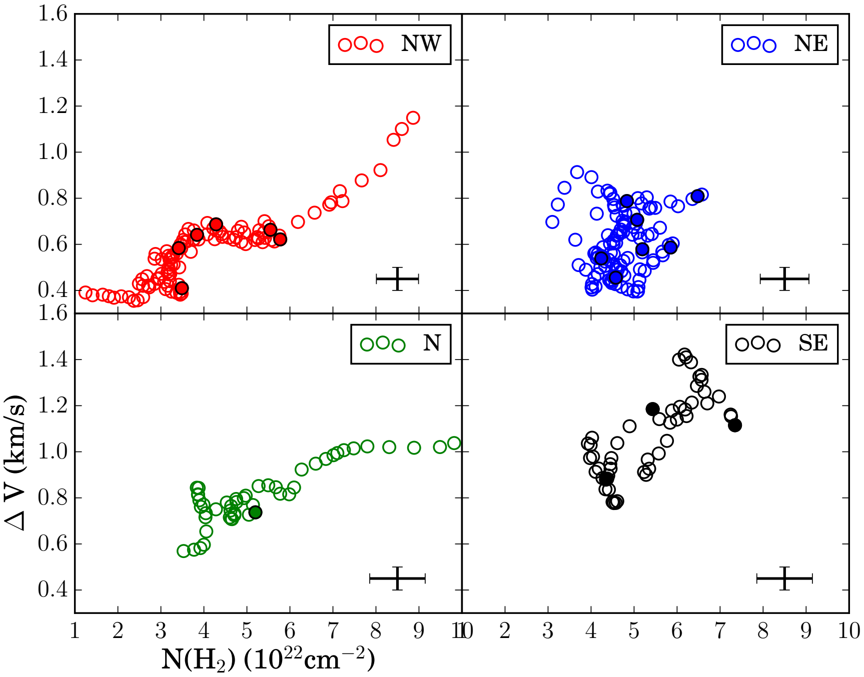

Figure 4.13 The correlations of velocity width to H_2 column density along the filament spine directions for the North-West (top left) North-East (top right), North (bottom left) and South-East (bottom right) filaments, excluding the portion of the spines that intersect the central hub regions (identified as where the filament can no longer be distinguished from the hub). Filled circles denote the spinal pixel position of the identified cores along the filaments. A mean error is plotted in the bottom right of each panel, equal to ±20% on the mean H_2 column density, and $\pm 0.05\,\mathrm{km\,s^{-1}}$ on ΔV.

Radial filament profiles

To construct a radial view of the filaments, we interpolate along an 0.4pc slice perpendicularly oriented to each spinal pixel using a Taylor expansion method (where the interpolation step is equivalent to half a pixel). Every slice is used to construct radial position-velocity (PV) profiles from the NH_3 hyperfine structure fitted cube. Any prevailing velocity gradient oriented parallel to the filaments however causes each radial PV slice to be centred differently in velocity, effectively smearing the mean radial PV profile. This was corrected by aligning each PV slice to the central velocity of the slice.

It is clear from the on-axis concentric nature of the highest intensity emission in the North and North-West filaments in Figure 4.14 that any radial velocity gradient does not dominate the velocity field. The intensity-weighted mean of these profiles does appear flat at their centremost regions around the spinal pixel, with radial velocity gradients of only $0.3\,\mathrm{km\,s^{-1}\,pc^{-1}}$ and $0.2\,\mathrm{km\,s^{-1}\,pc^{-1}}$ respectively. In contrast, the South-East and North-East filaments have mean radial velocity components across their entire width an order of magnitude larger than this, corresponding to $1.1\,\mathrm{km\,s^{-1}\,pc^{-1}}$ and $1.5\,\mathrm{km\,s^{-1}\,pc^{-1}}$ respectively. Although significant in this context, these gradients are not as strong as others observed by Fernández-López et al. (2014) or Beuther et al. (2015) for example, who observe radial gradients an order of magnitude larger than longitudinal velocity gradients in Serpens South and IRDC 18223, respectively.

The radial variations of the velocity width are plotted in the bottom panels of Figure 4.14. These profiles show that the longitudinally averaged velocity dispersion varies across all filaments, with, in some cases, local minima along the filament spine, and local maxima at the edges. However, as discussed in Section 5, these trends result from the average of a number of different processes that are mixed-up together in such profiles.

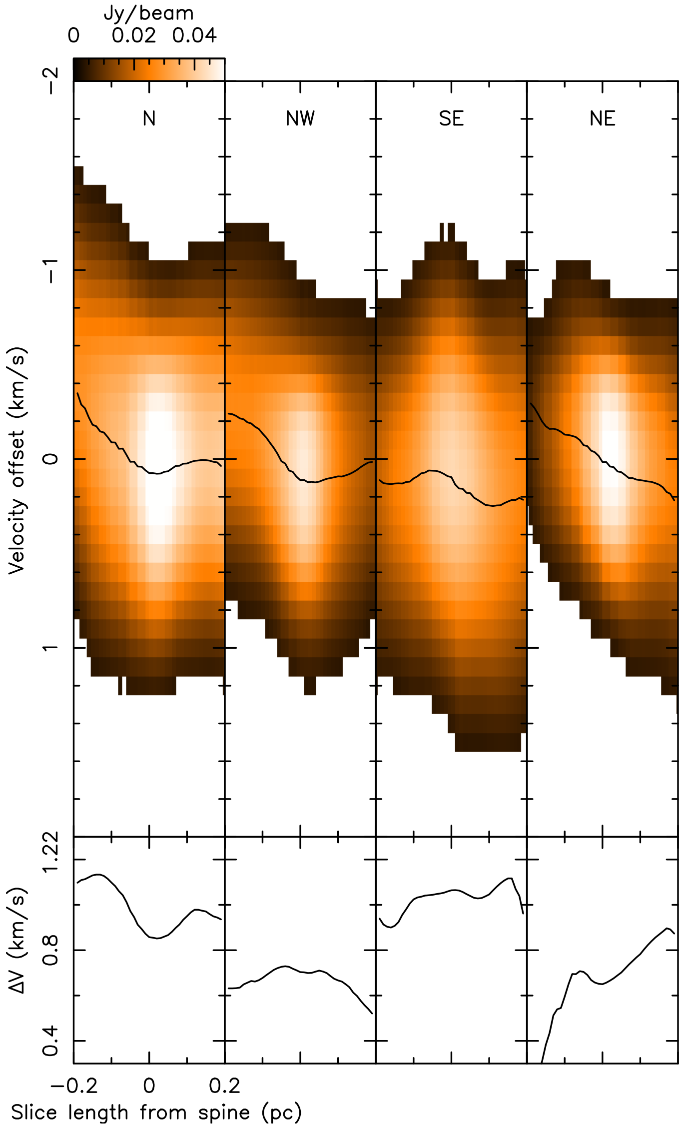

Figure 4.14 *Top*: The mean position-velocity diagrams across the North, North-West, South-East and North-East filaments (from left to right), where position denotes the length of a perpendicular slice relative to the central spine pixel in parsec, and the velocity are relative to the peak velocity of each slice. The overplotted black line shows the trend of the intensity-weighted mean offset velocity at each position along the radial slice. Mean radial gradients were computed within the inner 0.2pc width around the spinal pixel. *Bottom*: The mean variation in the velocity width in the radial direction, in km/s.

4.2.3 JVLA/GBT COMBINED VERSUS JVLA–ONLY DATASETS

In previous sections, results obtained from the combined JVLA/GBT dataset were presented. As already mentioned in Section 3.2.3, such a combined dataset is optimal to recover emission at all spatial scales. However, when trying to characterise the gas properties of the densest parts of the filaments (i.e. cores and filament spines) as we have done above, results can be affected by the contamination of the larger scale, more diffuse, foreground/background emission. The effect of this contamination would be to dilute the observational signatures one is trying to identify. For that reason we redid some of the analysis presented in earlier sections using the JVLA–only dataset, which traces only the most compact/densest regions of the cloud. We particularly focus on the velocity dispersion variations along the filament spines and towards the cores. By fitting the hyperfine components of the JVLA–only NH_3 emission, we find that the increase of the velocity width at the core positions is even larger than in the combined data set. This is illustrated in Figures 4.15 and 4.16, reproductions of Figures 4.11 and 4.12 but of the JVLA data only. From these figures, one can see that the JVLA velocity width towards the core centres is 1.5–2 times larger than that of the surroundings, compared to a 1.1–1.4 factor in the JVLA & GBT combined data. We also notice that in the JVLA–only data the remaining starless cores also display an increase of velocity width. This analysis strengthens our conclusions about the local increase of velocity dispersion towards the SDC13 starless cores.

4.3 DISCUSSION

In this section, we discuss the various observational properties of the filaments in SDC13 in terms of filament evolution theories. To facilitate the visualisation of the filament properties, the radial interpolation carried out in Section 4.2.2 was carried out on the column density, centroid velocity, velocity width and Spitzer 8 μm opacity for all filaments. Aligning each slice to the pixel that lies along the filament spines

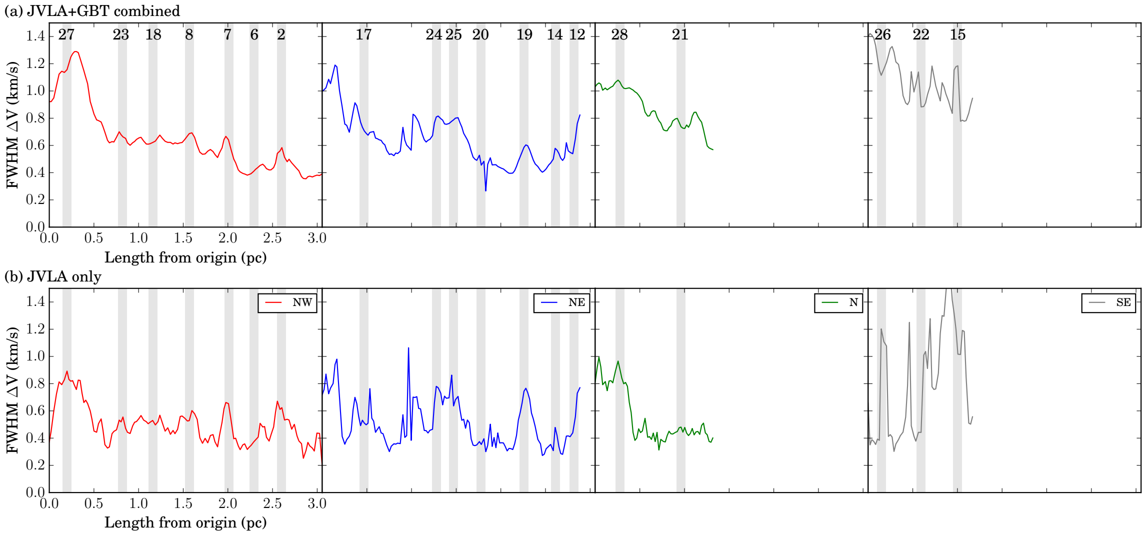

Figure 4.15 The velocity width profiles of the North-West (red), North-East (blue), North (green) and South-East (grey) filaments in the combined data (top row, as presented in the second row of Figure 4.12) and the JVLA–only data (bottom row), evaluated over the same filament spines as identified in Section 4.2.2.

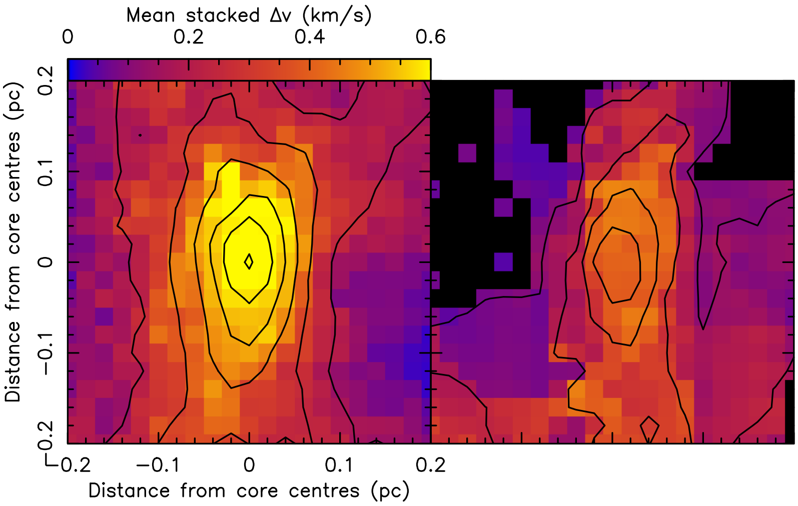

Figure 4.16 A reproduction of Figure 4.11, but for the JVLA–only data. The average stacked velocity width of cores identified with velocity width peaks (left) and those without peaks (right). Included in the construction of the left and right panels are 13 and 4 cores respectively. Plot details are the same as those detailed in the caption of Figure 4.11.

gives us a unique deprojected perspective of the filaments (the North-West and North-East filaments in Figure 4.17, and the South-East and North filaments in Figure 4.18) i.e. a view of the filament independent of their on-sky projection, making some of the filament features discussed below stand out.

4.3.1 SUPERCRITICAL FILAMENTS

One important parameter of interstellar filaments regarding their stability is their mass-per-unit-length, $M_{\rm line}$. The first step towards measuring this quantity is to determine their radial column density profiles, by fitting each radial column density slice (found in Figures 4.17 and 4.18) with Gaussian or Plummer (Whitworth & Ward-Thompson 2001) functions. Examples of such fits are shown in Figure 4.19. Looking at the mean profiles of the North-East and North-West filaments (the fourth panels of Figure 4.19), it is clear that they are not well described by Plummer nor Gaussian fits. This trend continues when considering individual column density slices along the filaments (shown in the first three panels of Figure 4.19). Although a Plummer may reasonably well describe slice 50 in the North-West filament (and perhaps even the centre-most portion of slice 54 in the North-East filament) the extended emission in the majority of slices renders fitting them with Gaussian or Plummer profiles inappropriate as they do not accurately reflect the complexity of the radial column density slices (unlike Arzoumanian et al. 2011, for example). We have evaluated further the impact of constraining the Gaussian fit parameters on the goodness of the fit itself. While setting the peak position of the Gaussian profiles to lie on the spine (i.e. $x = 0$) does not improve the produced fits, restricting the fitting to the inner portion of the filaments does result in better Gaussian fits of the central portion of the filament. However, filament properties (width and line mass) derived from such fits are very much dependent on the exact fitting range used. Such properties calculated from Trapezoidal integration of the asymmetrical profiles (as shown in Table 4.2 and Figure 4.20) are less affected by such restrictions, and therefore more robust.

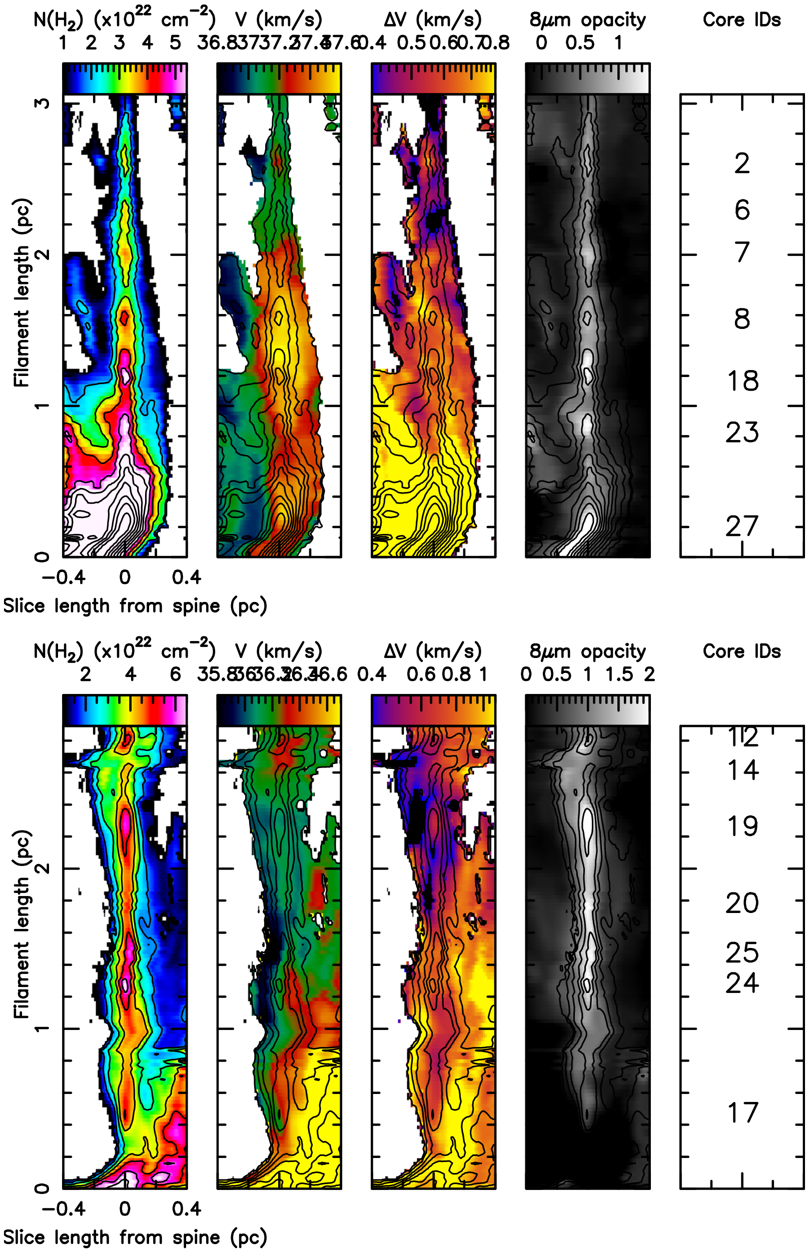

Figure 4.17 Deprojected views of the North-West (top) and North-East (bottom) filaments. The filament length is plotted on the y-axis, while the length of the radial slices from the central spine pixel is plotted on the x-axis. In both sub-figures, the panels show (from left to right) the H_2 column density derived from the NH_3 emission, the line-of-sight velocity, the velocity width, the opacity derived from the 8μm Spitzer emission, and finally the core ID as listed in Table 4.1. Contours in the first four panels are of the column density, from $1 \times 10^{22}\,\mathrm{cm}^{-2}$ to $11 \times 10^{22}\,\mathrm{cm}^{-2}$, spaced by $1 \times 10^{22}\,\mathrm{cm}^{-2}$.

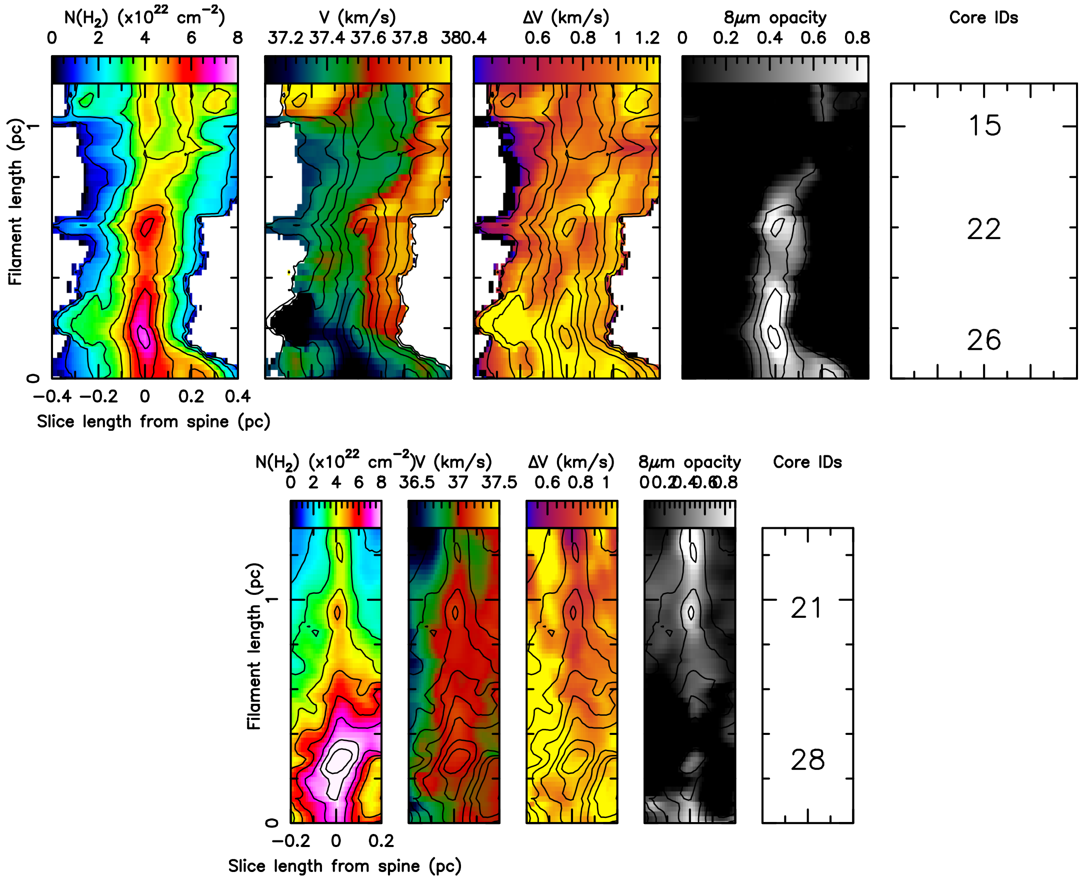

Figure 4.18 Deprojected views of the South-East (top) and North (bottom) filaments. The North filament was restricted to 0.2 pc either side of the spine due to contamination from the North-West and North-East filaments. Figure details are same as listed in the Figure 4.17 caption.

(a) North-East filament

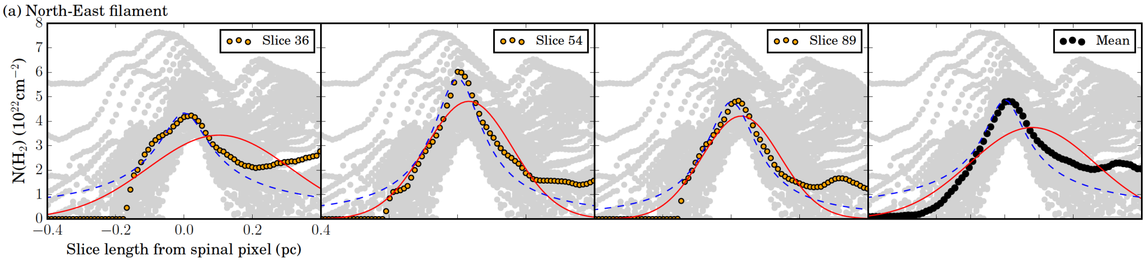

(b) North-West filament

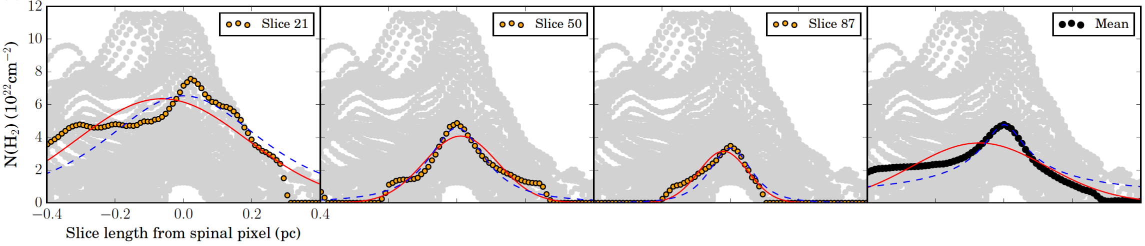

Figure 4.19 Plots showing the results of fitting Gaussian (red line) and Plummer (blue dashed line) profiles to *individual* radial column density slices (orange circles in the first, second and third panels of each row) and the *mean* radial column density profile (black circles in the fourth panel of each row) of (a) the North-East filament (top row) and (b) the North-West filament (bottom row). The grey points in the background of each panel plots all of the radial column density slices simultaneously. Plummer profiles may on occasion well describe the inner regions of the filaments only, whilst Gaussian profiles fail to fit any of the distributions.

Characterising filaments is fraught with difficulty, and caution must be observed whilst deriving global properties from their mean profiles (e.g. Panopoulou et al. 2017).

Therefore, we instead integrate all radial column density distributions using the Trapezoidal rule at every position along the filaments spines to calculate the mass per unit length. A rough estimation of the filament widths were obtained by taking $\sqrt{8 \ln 2}$ times the standard deviation of the radial column density profiles. In calculating the mean M$_{\rm line}$ and filament widths (listed in Table 4.2), we excluded the regions that intersected the cloud hub, (identified as belonging to the radial column density slices where the extended nature of the hub emission makes the determination of the width impractical). Figure 4.20 plots the evolution of the filament width and M$_{\rm line}$ along the filament lengths respectively.

The critical mass per unit length, $M_{\rm line,crit} = 2a_0^2/G$ (where a_0 is the isothermal

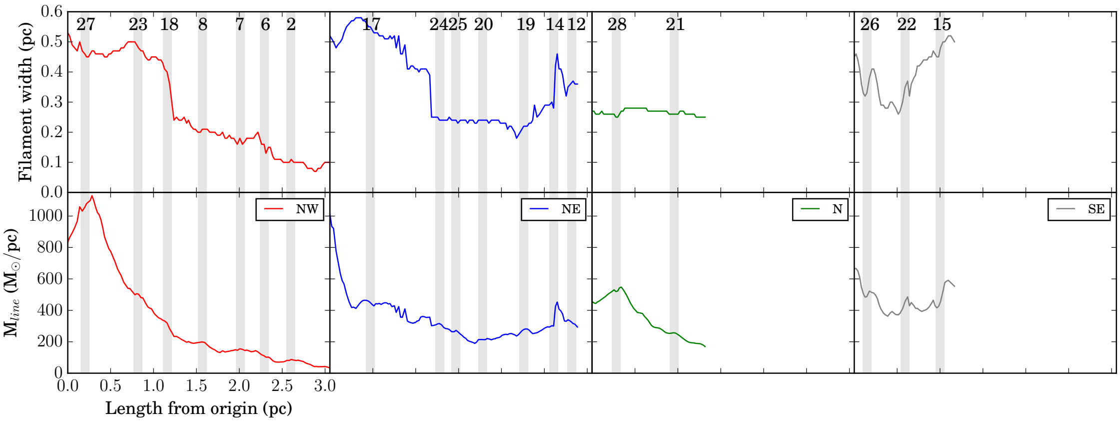

Figure 4.20 Caption as for Figure 4.12. The first row plots the filament width calculated from 2.35 times the standard deviation of the radial column density distributions. The jump in width seen at roughly 1.2 pc in the North-West and North-East filaments is due to the exit of the filament spine from the hub. The mean filament width was evaluated beyond this point. The second row plots the mass per unit length, evaluated from conducting a Trapezoidal integration under all radial column density distributions.

sound speed and G is the Gravitational constant) is the critical value above which an interstellar filament becomes gravitationally unstable to radial contraction and fragmentation (Ostriker 1964). For a typical 10 K filament, $M_{\rm line,crit} = 16\,{\rm M_\odot\,pc^{-1}}[\frac{T}{10K}]$. At the mean rotational temperature of SDC13 of 12.7 K, $a_0 = 0.21\,{\rm km\,s^{-1}}$ and the critical mass per unit length is $20.4\,{\rm M_\odot\,pc^{-1}}$. All SDC13 filaments can be classed as thermally supercritical (see Table 4.2) therefore prone to radial gravitational contraction and fragmentation along their lengths. When considering the effective sound speed, $a_{eff,0} = \sqrt{a_o^2 + \sigma_{NT,0}^2} = 0.26 \pm 0.02\,{\rm km\,s^{-1}}$ (where $\sigma_{NT,0} = 0.15\,{\rm km\,s^{-1}}$, taken from Figure 4.23 as the most representative value of the filament dense gas prior to fragmentation - see Section 4.3.4) the critical mass per unit length becomes $31.3\,{\rm M_\odot\,pc^{-1}}$, a factor of 1.5 larger than the previously calculated thermal M$_{\rm line,crit}$, but still a factor of 4 to 10 lower than the measured filament line masses.

4.3.2 Core separation and age estimates

The separation of cores along filaments can provide clues regarding the physical mechanism driving the fragmentation. The top panel of Figure 4.21 shows the Gaussian Kernel Density Estimation (KDE) plot of core separations in all filaments (excluding hub cores). When plotting a histogram, the choice of bin size can sometimes have a great effect on data visualisation. Producing a density estimation rids us of this dependence, by instead considering the density of points as a whole and not the number of points that fall into a bin. When considering each point as a Gaussian, the only dependence is on the bandwidth of the Gaussian used, which is less biased than bin size. In Figure 4.21 the two plotted distributions each use a different bandwidth Gaussian, one that matches the beam size of 0.07 pc (dashed blue) and the other the mean core size of 0.1 pc (black line). The core separations were calculated on the original on-sky projected filament spines, and not from the deprojected plots in Fig. 4.17, although both provide identical results. There is clearly a peak in each distribution in both distributions at a core separation $\lambda_{core} \simeq 0.37 \pm 0.16$ pc. Regular spacings in IRDCs with core separation ranging between ~ 0.2 to 0.4 pc have already been reported (Beuther et al. 2015; Henshaw et al. 2016a; Zhang et al. 2009). For comparison, we simulated the four filaments by randomly placing the same number of cores as observed along each of the four filament lengths and calculated the separation of each consecutive core pair (e.g. Teixeira et al. 2016), and repeated the process 100,000 times. In doing this, we stipulated that the smallest core separation in these random core distributions must exceed the beam size, equivalent to 0.07 pc spatial scale. We can clearly see that the observed cumulative histogram (black) is steeper than the simulated cumulative histogram (red) in the bottom panel of Figure 4.21. To quantify these differences, we used the Kolmogorov-Smirnov test to estimate the probability that these two histograms originate from the same parent distribution. We find that there is a 15% chance that this is the case, exceeding the significant test

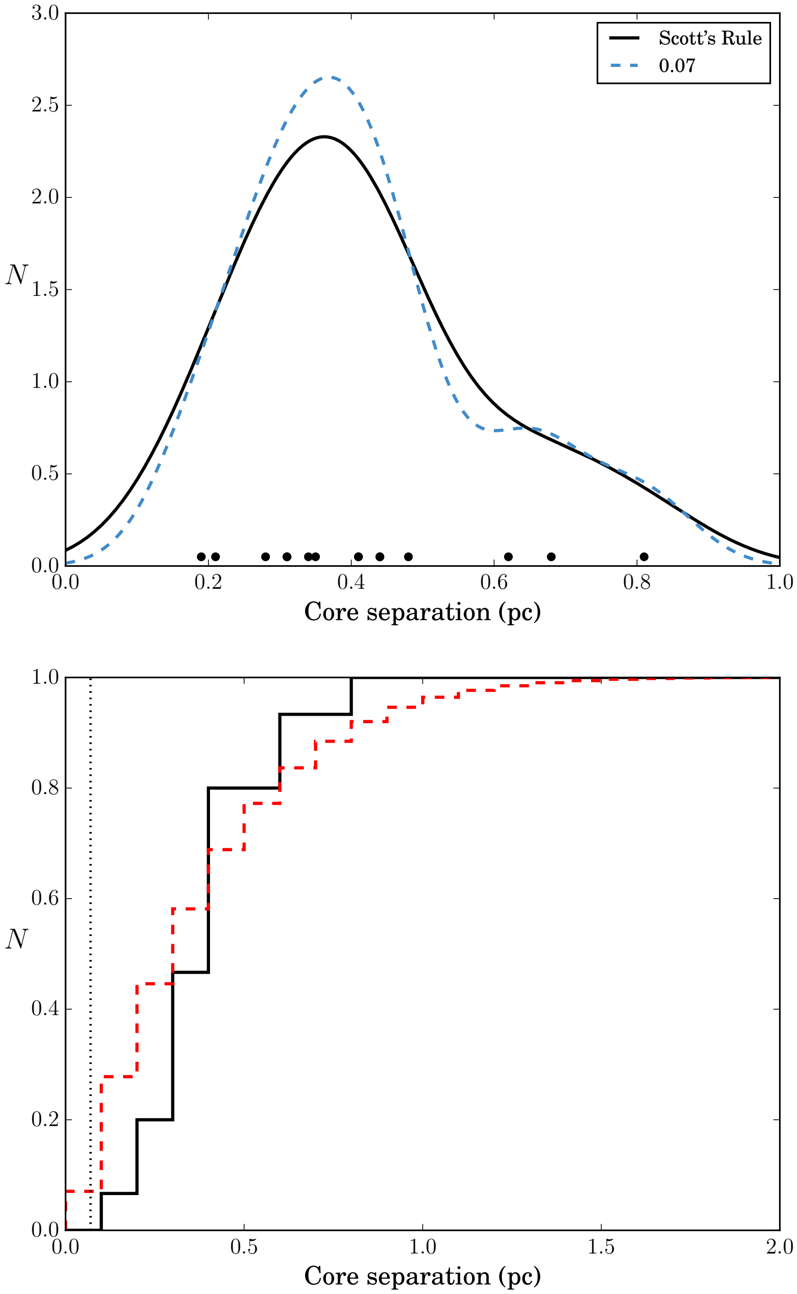

Figure 4.21 *Top*: A Gaussian Kernel Density Estimation (KDE) plot of the separation of each consecutive core pair in each of the four filaments. Each line denotes a different bandwidth Gaussian, 0.07 pc (equivalent to the beam size, in dashed blue) and 0.1 pc (derived by the standard Scott's Rule, and equivalent to the mean core radius, in black). Black circles at $N = 0.05$ are overplotted to show the positions of the individual spacings in the sample. The standard deviation is 0.16 pc. *Bottom*: Normalised, cumulative distribution of the observed core separation (black line) and the 100,000 simulated core separations (dashed red line). The bin size in both plots was set to be slightly larger than the beam at 0.1 pc in size. The vertical dotted line in both denotes the data spatial resolution of 0.07 pc, used as a cut-off of the allowed simulated spacings.

limit of 5%. However, coupled with the relatively large K-S statistic of 0.28 (suggesting a large maximum distance between the two cumulative distributions), we reject the null hypothesis and consider that these two histograms are significantly different, demonstrating that the core spacing in the SDC13 filaments are not randomly distributed. The median value of λ_{core} in each filament is given in Table 4.2. Note that looking at the deprojected view of the filaments in Figure 4.17, the spacing of the North-West filament seems to be more regular than the others. This is supported by the lower core spacing standard deviation of the North-West filament, i.e. 0.06 pc (whilst excluding core number 27 in the hub centre) versus 0.21 pc for the North-East filament.

Inutsuka & Miyama (1992) and Miyama et al. (1994) showed that filaments in hydrostatic equilibrium fragment under density perturbations where the wavelength of the fastest growing mode is four times the filament diameter. Looking at the relevant values given in Table 4.2 we see that the ratio between the core separation of the SDC13 filaments and their widths varies between 1.1 to 2.1 which, given the unknown inclination, is compatible with a ratio of 4. However, in a turbulent medium, filaments in equilibrium are likely to be rare objects. Interestingly, Clarke et al. (2016, 2017) studied the fragmentation of non-equilibrium, accreting filaments and showed that the fastest growing mode of density perturbations in such systems, λ_{core}, is a function of the time it takes to build-up a critical filament through accretion, τ_{crit}, and the effective sound speed, $a_{eff,0}$:

$$\lambda_{core} = 2a_{eff,0}\tau_{crit} \, , \tag{4.14}$$

By measuring the core separation and the gas temperature, it then becomes possible to derive τ_{crit}. One can also relate τ_{crit} to the accretion rate onto the filament $\dot{M}$ by:

$$\tau_{crit} = \frac{M_{\rm line,crit}}{\dot{M}} \tag{4.15}$$

where $\mathrm{M_{line,crit}}$ is the critical mass per unit length. Values for τ_{crit} and $\dot{M}$ (derived using the previously calculated $a_{eff,0} = 0.26 \pm 0.02\,\mathrm{km\,s^{-1}}$ and $\mathrm{M_{line,crit}} = 31.3\,\mathrm{M_\odot\,pc^{-1}}$) are given in Table 4.2 for each filament. According to this model, we see that it takes on average ~ 0.68 Myrs to form the SDC13 filaments up to the critical mass per unit length, with an average accretion rate $\sim 46.5\,\mathrm{M_\odot\,pc^{-1}Myr^{-1}}$. Interestingly, assuming that the derived accretion rate remained constant over the entire filament lifetime, one can derive the age, τ_{age}, through:

$$\tau_{age} = \frac{M_{line}}{\dot{M}} \tag{4.16}$$

As shown in Table 4.2 we obtain an average value of $\tau_{age} \sim 5.9$ Myr, which implies that the elapsed time since the filaments became critical is ~ 5.2 Myr. Based on the observed longitudinal velocity gradients and assuming that the gas is free-falling, Peretto et al. (2014) estimated that the SDC13 filaments had been collapsing for $\sim$ 1 to 4 Myr. This is consistent with the estimate based on the Clarke et al. (2016, 2017) model. However, in the calculation of τ_{crit} we have not taken into account projection effects in the estimate of λ_{core}. Doing so will increase τ_{crit} by a factor $1/\cos(\theta)$ where θ is the angle between the direction of the main axis of the filament and the plane of the sky, which for an average angle of 67° (Peretto et al. 2014) is equal to 1.7 Myr. This brings the estimated age of the filament to 15.1 Myr, more than a factor of 3 larger than the dynamical timescale estimated by Peretto et al. (2014).

The derived τ_{crit} values are relatively fast timescales in the context of star formation. Reflecting upon the theories of massive star formation discussed in Chapter 1, the core accretion model of McKee & Tan (2002) and turbulent core accretion model of McKee & Tan (2003) is a slow and quasi-static process. On the other hand, the competitive accretion model of Bonnell et al. (2001) is a fast and dynamic process, converting gas into stars in only a few free fall times. Given the mean filament density of $4.8 \times 10^{-17}\,\mathrm{kg\,m^{-3}}$ (derived from the mean filament width and line masses later in Section 4.3.6), the free-fall collapse time $t_{ff} = 0.3\,\mathrm{Myrs}$. With τ_{crit} being only two times larger than t_{ff}, this is consistent with the dynamic process proposed by competitive accretion.

4.3.3 COLLAPSE TIMESCALES

With all the hierarchical structure in SDC13 extracted using the dendrogram method, we calculate their radii, aspect ratios and mean densities. As the free-fall collapse time of a structure depends only on the density, we calculate t_{ff} for all extracted structures, from the base of the dendrogram tree up to the leaves using:

$$t_{ff} = \left(\frac{3\pi}{32\mathrm{G}\rho}\right)^{1/2}, \tag{4.17}$$

where G is the gravitational constant, and ρ is the density of the core (for which we use the upper limit on the mass in column 12 of Table 4.1). However, this is not an appropriate approach for non-spherical objects like the high-aspect ratio filamentary structures within SDC13 (Pon et al. 2012; Toalá et al. 2012). Clarke & Whitworth (2015) derive a collapse timescale (t_{col}) valid for both filamentary and near spherical structures:

$$t_{col} = (0.49 + 0.26\mathrm{A_o})(\mathrm{G}\rho)^{-1/2}, \tag{4.18}$$

where $\mathrm{A_o}$ is the aspect ratio, valid down to values of $\mathrm{A}_o \gtrsim 2$. The filamentary nature of SDC13 from large to small scale (i.e. 61% of cores having $A_0 > 2$ - Table 4.1) justifies the need to use equation 4.18. Figure 4.22 shows the collapse time t_{col} for all identified structures in the SDC13 dendrogram. Overall we see a decrease of the collapse time, from $\sim 0.7\,\mathrm{Myr}$ to $0.1\,\mathrm{Myr}$ as we go from large to small structures as a result of the structures' decreasing aspect ratios and increasing densities. A consequence of this hierarchical collapse time is that cores will collapse well before the filaments. This is the basic idea behind the hierarchical star formation models of Vázquez-Semadeni et al. (2009, 2017). On the same figure, we see one structure in the North-East filament that departs from the rest of the SDC13 structures, with a longer collapse time than the structure in which it is embedded in. This is due to the particularly long aspect ratio of that particular structure. We also notice that the same structure exhibits the strongest radial velocity gradient (see Section 5.2) and the smallest core separation (see Table 4.2). As speculated later in this chapter, we argue that this is a direct consequence of the compression of the pre-existing filament by the feedback of a nearby star formation event.

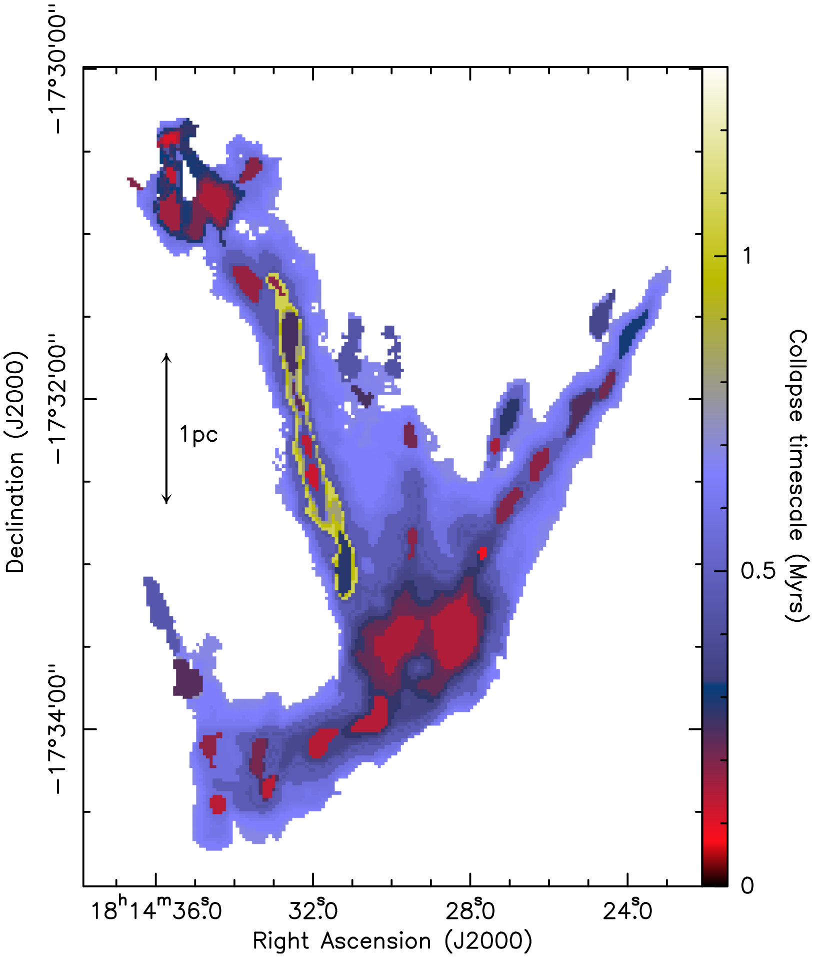

Figure 4.22 Map where the outline of all extracted structures are coloured by their collapse timescale t_{col} in Myrs.

4.3.4 LINEWIDTH AS A PROBE OF INFALL

The increase of velocity width within the cores can be quantitatively compared to the velocity dispersion within the filaments. In that respect, we calculated the non-thermal contribution of each pixel within SDC13 following (Myers 1983):

$$\sigma_{NT} = \sqrt{\frac{\Delta V_{obs}^2}{8\ln 2} - \frac{\mathrm{k_b T}}{m_{\mathrm{NH_3}}}} \tag{4.19}$$

where ΔV_{obs} is the fitted FWHM velocity width, k_b is the Boltzmann constant, and $m_{\mathrm{NH_3}}$ is the mass of an $\mathrm{NH_3}$ molecule. To determine whether the filaments are sub-sonic or supersonic in nature, we compare this non-thermal sigma velocity dispersion to the isothermal sound speed a_0 at 12.7 K of $0.21\,\mathrm{km\,s^{-1}}$. Figure 4.23 shows the histograms of σ_{NT}/a_0 for all four filaments, where pixels within core regions only are overplotted in white. Overplotted in black are the corresponding distributions taken from the JVLA–only data. We see that in all filaments the gas in the combined data is predominantly supersonic, however, the North-West and North-East filaments also peaks significantly in the sub/transonic regime. This second peak is coincident with that of the JVLA data which only exhibits a minor supersonic tail in its distribution whilst peaking sub/transonically.

Barranco & Goodman (1998) and Goodman et al. (1998) find that σ_{NT} remains constant across core regions, and increases once outside the core boundary. They call this behaviour velocity "coherence", suggesting that cores have sizes that are intimately linked to the turbulence properties. We observe a different behaviour, with 88% of pixels within core regions have $\sigma_{NT}/a_0 \geq 1$. This is consistent with our systematic identification of 73% of cores exhibiting a peak in velocity width. However, 87% of pixels within the surrounding filament also have $\sigma_{NT}/a_0 \geq 1$. Despite this similarity in the core and filament pixel distributions, conducting a Kolmogorov-Smirnov test of the two show vanishingly small p-values with moderate coefficient values (between 0.2 and 0.3), indicating they are significantly different. In the JVLA

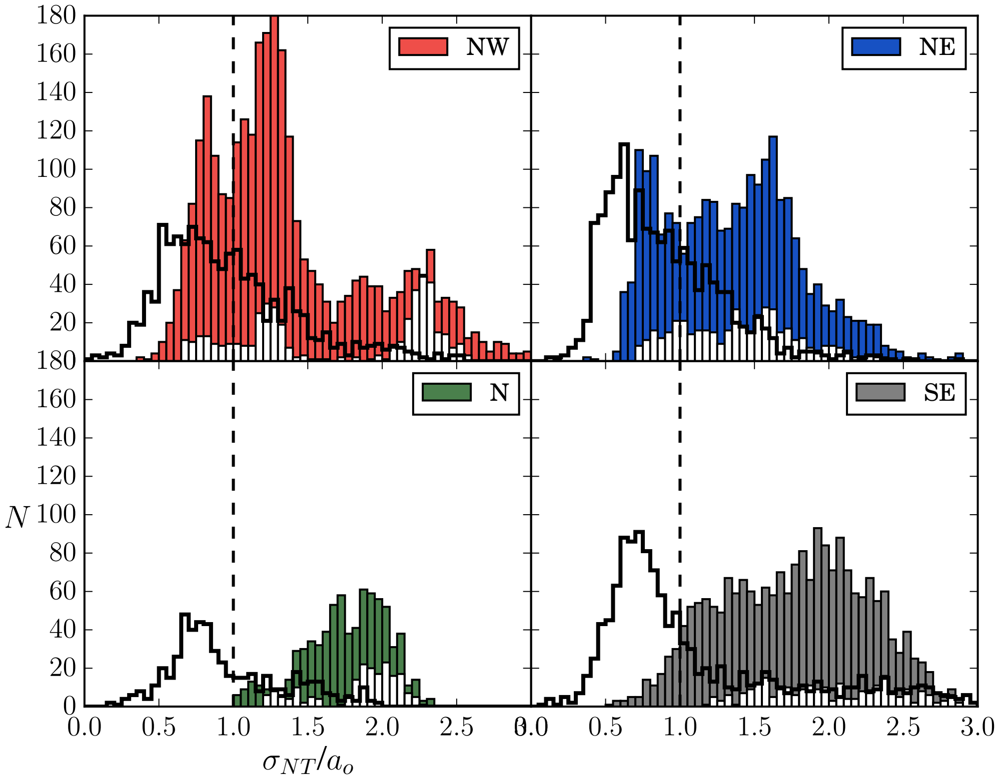

Figure 4.23 Histogram of the non-thermal contribution to the velocity dispersions, divided by the isothermal sound speed at the temperature of the NH_3 gas of 12.7 K i.e. the Mach number. The red histogram is the North-West filament, blue is the North-East, green is the North while grey is the South-East. The vertical dashed line denotes the transition from subsonic to supersonic motions. Overplotted in white in each panel is the Mach number of the core regions only from the combined data. The overplotted black line is the distribution of the JVLA–only velocity dispersion results.

data however, 55% of pixels within core regions peak supersonically compared to only 36% of filament pixels. This further demonstrates that with the addition of the extended background emission in the combined data, the kinematics of the cores have become diluted and similar to that of the surrounding filament. Probing the densest gas with the JVLA–only shows that the kinematics of the cores are more distinct from the surrounding filament.

A decrease of velocity dispersion towards low-mass prestellar cores has been previously observed (Fuller & Myers 1992; Goodman et al. 1998; Caselli et al. 2002; Pineda et al. 2010, 2015). More recently, this transition to coherence has also been observed towards entire, parsec-long filaments (Hacar & Tafalla 2011; Hacar et al. 2016). Transonic cores and filaments are expected to form in a turbulent ISM where supersonic shocks generate stagnation regions where turbulent energy has been dissipated (Padoan et al. 2001; Klessen et al. 2005; Federrath et al. 2016). Turbulence dissipates on a crossing time (see equation 1.4). In SDC13, for a mean filament width of 0.26 pc (from Table 4.2) and mean filament velocity width of 0.6 kms^{-1}, we calculate that turbulence should dissipate across the filaments on timescales of $\sim$ 0.42 Myrs. This is in agreement with both the free-fall collapse time ($t_{ff} = 0.3\,\text{Myrs}$) and critical timescale ($\tau_{crit} = 0.68\,\text{Myrs}$, calculated in Section 4.3.2). With mostly transonic velocity dispersion (where both the combined and JVLA data sets peak in Figure 4.23, hence best representing the dense gas of the system), everything indicates that the filaments of SDC13 do indeed represent such post-shock regions, the increase of the dispersion in some localised region at the edge of the filament being reminiscent of what Klessen et al. (2005) sees in their turbulent simulation of core formation. In this context, the velocity dispersion increase towards the core would be then purely generated by gravity (e.g. Ballesteros-Paredes et al. 2017, submitted).

Another possible explanation for a local increase of velocity dispersion towards the cores could be the presence of embedded protostellar sources. Even though we do not see any mid-infrared sources toward them, such protostars could be embedded enough to remain undetectable with both *Spitzer* and *Herschel*. These protostars could have associated outflows which disrupt the surrounding gas, contributing to a local increase in the velocity dispersion (Duarte-Cabral et al. 2012). ALMA observations of SDC13 cores at sub-arcsecond resolution could settle this issue.

4.3.5 EVOLUTION OF THE VIRIAL RATIO FROM LARGE TO SMALL SCALE

Using the dendrogram tree, we can estimate the virial ratio for all extracted structures. Following Bertoldi & McKee (1992), the virial ratio of a uniform density sphere is given by:

$$\alpha_{vir} = \frac{5a_{eff}^2 R}{\mathrm{G}M}\,, \tag{4.20}$$

where R is the radius and M is the mass of the cores found by the extraction code respectively, and a_{eff} is the total velocity dispersion considering both thermal and non-thermal contributions from all molecules. We use the upper limit on the mass as it matches the amount of gas responsible for the observed velocity dispersion. In the absence of significant magnetic energy density, structures with $\alpha_{vir} < 2$ are thought to be gravitationally bound, those with $\alpha_{vir} \sim 1$ are compatible with hydrostatic equilibrium, those with $\alpha_{vir} < 1$ are likely to be gravitationally unstable, while structures with $\alpha_{vir} > 2$ are unbound and either dispersing or held together by external pressure. Figure 4.24 shows the map of virial ratios for all SDC13 structures. Based on this map, it is clear that as we go from large to small scale, the virial ratio increases from $\alpha_{vir} \sim 0.1$ towards 1. Such low-values suggest that SDC13 is gravitationally unstable on all scales, and that the transfer of gravitational to kinetic energy could be the process responsible for the increase of the virial ratios on small scales.

Such an evolution of the virial ratio can be analytically described. Consider a uniform density filament fragmenting at the length scale equal to the separation of a core, λ_{core}. In an idealised scenario, energy is conserved during collapse whilst

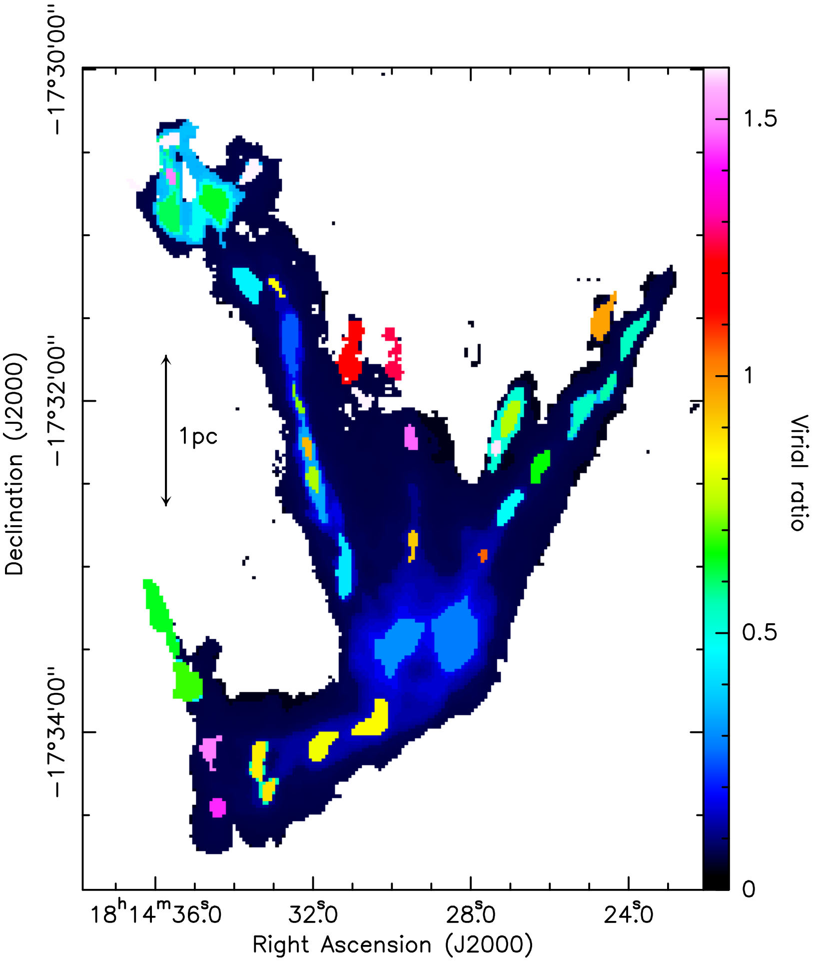

Figure 4.24 Virial ratio map of all identified dendrogram structures.

fragmentation is happening. However, there is a fraction of energy converted from gravitational potential energy (E_g) into kinetic energy (E_k) at the time the filament fragmentation starts. This conversion may be expressed in the virial equation as an efficiency ϵ, where if no energy is converted, $\epsilon = 0$. If energy conversion does occur, this can be expressed as a fractional increase in E_k, expressed as $E_k = E_{k,0} + \Delta E_k$, where $E_{k,0}$ is the initial kinetic energy of the fragmenting core before collapse. This fractional increase in kinetic energy can be expressed as $\Delta E_k = \epsilon\,(E_g - E_{g,0})$, where $E_{g,0}$ is the initial gravitational potential energy. Substitution into the standard virial ratio of $\alpha_{vir} = 2E_k/E_g$ gives:

$$\alpha_{vir} = \frac{2E_{k,0} + 2\epsilon\,(E_{g,0} - E_g)}{E_g}\,, \tag{4.21}$$

and simplifying gives:

$$\alpha_{vir} = 2\frac{E_{k,0}}{|E_g|} + 2\epsilon\left(1 - \frac{|E_{g,0}|}{|E_g|}\right) \tag{4.22}$$

Note that as $|E_g|$ becomes increasingly larger during the collapse, $\epsilon = 1$ translates into $\alpha_{vir} \rightarrow 2$, which is expected if all the gravitational energy were to be converted into kinetic energy. By estimating each energy term of equation 4.22 for every core showing an increase of velocity dispersion one can determine which value of ϵ is required to reproduce the observed α_{vir} value. The energy terms may be expressed as:

$$E_{k,0} = \frac{3}{2}Ma_{eff,0}^2\,, \tag{4.23}$$

where $a_{eff,0}$ is the 1D velocity dispersion, and:

$$E_g = -\beta\frac{GM^2}{R}\,, \tag{4.24}$$

where $\beta = \frac{3-k_\rho}{5-2k_\rho}$ is a factor depending on the power law index k_ρ of the density profile of collapsing cores, and:

$$E_{g,0} = -\beta_0 \frac{GM^2}{R_0} , \tag{4.25}$$

is the initial gravitational potential energy, and β_0 and R_0 are the initial values of β and R respectively. Making these substitutions gives:

$$\alpha_{vir} = \frac{3}{\beta G} \frac{R a_{eff,0}^2}{M} + 2\epsilon \left(1 - \frac{\beta_0}{\beta} \frac{R}{R_0} \right) . \tag{4.26}$$

One may rewrite R_o as $\lambda_{core}/2$ under the assumption that all cores are initially their separation in size, and $\beta_0 = 3/5$ under the assumption that the filament is initially uniform in density (i.e. $k_\rho = 0$) before the onset of collapse. Making these assumptions simplifies the equation to:

$$\alpha_{vir} = \frac{3}{\beta G} \frac{R a_{eff,0}^2}{M} + 2\epsilon \left(1 - \frac{6}{5\beta} \frac{R}{\lambda_{core}} \right) . \tag{4.27}$$

A mean $a_{eff,0} \sim 0.26 \pm 0.02\,\mathrm{km\,s^{-1}}$ is evaluated from Figure 4.23. For simplicity, we assumed an initially flat density profile before the onset of collapse (i.e. $\beta_0 = 3/5$), and $k_\rho = 2$ at the time we observe (i.e. $\beta = 1$). Figure 4.25 plots the energy conversion efficiency ϵ against the virial ratio for every core for both the combined JVLA/GBT data and JVLA–only data. On this plot, only starless cores are included, as protostellar cores, or cores at filament junctions are subject to extra energy sources that will affect the estimate of ϵ. One can see that a conversion efficiency between 20–50% can explain most of the observed velocity dispersion increases towards starless cores. The JVLA–only data points (orange circles), believed to be less contaminated by foreground/background emission to the cores, are clustered around a median efficiency of 43%.

Klessen & Hennebelle (2010) proposed a theory according to which accretion is capable of driving turbulent motions in galaxies on all scales, finding an ϵ value of a few percent when considering both galaxy and molecular cloud sized structures. Clarke

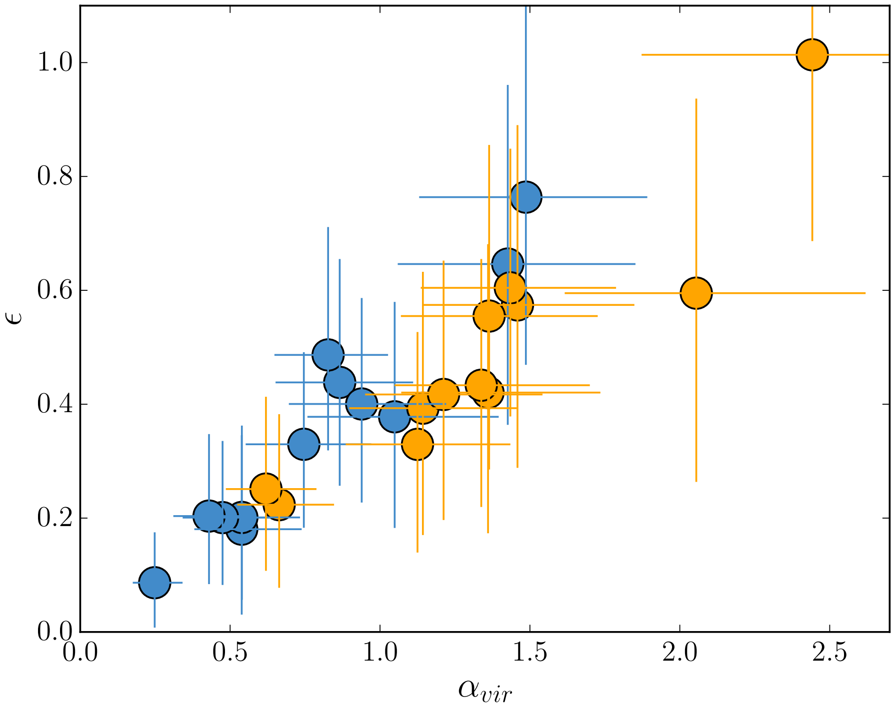

Figure 4.25 Observed virial ratio plotted against the energy conversion efficiency of gravitational energy into kinetic energy for the combined JVLA+GBT data (in blue), and the JVLA–only data (in orange). Only starless cores along the filaments are plotted, as protostellar or hub centre cores are subject to extra energy source that will effect the estimate of ϵ. Errors were propagated using a Monte Carlo error propagation method.

et al. (2017) evaluate the efficiency required to reproduce a given velocity dispersion due to accretion driven turbulence in filament structures. They find an $\epsilon = 5-10\,\%$ is sufficient to drive a $\sigma_{\rm 1D} \sim 0.23\,{\rm km\,s^{-1}}$, a consistent efficiency to that found by Heitsch (2013). While these are theoretical estimates, our observationally derived value of $\sim 40\%$ is somewhat larger. This could point towards an even more important role of gravity-driven turbulence than previously thought (see also Traficante et al. 2018; Ballesteros-Paredes et al. 2017, submitted).

4.3.6 ORIGIN OF THE RADIAL VELOCITY GRADIENTS

Two of the four SDC13 filaments exhibit strong radial velocity gradients, the largest of which in the combined data set reaches $1.5\,{\rm km\,s^{-1}\,pc^{-1}}$, an order of magnitude larger than in the remaining two filaments. In the JVLA–only data, although the morphology of the centroid line-of-sight velocity is the same as in the combined data, the magnitude of the radial velocity gradients double, approaching $\sim 3\,{\rm km\,s^{-1}\,pc^{-1}}$ in both the North-East and South-East filaments. The physical origin of such gradients is unclear as they could be the result of accretion/compression, rotation, shear, or a combination of these. It is important to realise that, given the measured velocity gradients (up to $1.5\,{\rm km\,s^{-1}\,pc^{-1}}$), the crossing time of the filaments is $\sim 0.3-0.4\,{\rm Myr}$, which is a factor of ~ 3 lower than the estimated age of the filaments. This implies that, whatever the origin of the gradient is, it cannot be of disruptive nature or the filaments would already have dispersed. This therefore excludes shear motions as a possible origin. Here, we are going to investigate if the magnitude of the gradients are compatible with gravity and/or rotation.

For gravity to be responsible for radial velocity gradients in filaments, large-scale accretion into a plane is the only option as axisymmetric accretion would not produce any velocity gradients. Assuming that the filaments are infinitely long, then one can estimate the acceleration of a piece of gas at a radius r (Palmeirim et al. 2013), as:

$$\mathrm{v_r} = 2\sqrt{\mathrm{GM_{line}} \ln\left(\frac{\mathrm{r_{initial}}}{\mathrm{r}}\right)}\,. \tag{4.28}$$

Substituting for the mean observed M_{line} of SDC13 we may calculate the $r_{initial}$ that would produce the observed velocity (~ 0.3 km/s) at a distance of 0.20 pc from the spine of the filament. By doing so we obtain $r_{initial} \simeq 0.21\,\mathrm{pc}$. The associated dynamical timescale is 3.3×10^4 yr, nearly two orders of magnitude shorter than our age estimates for the filaments. This suggests that gravity alone is not the origin of the observed radial velocity gradients in SDC13. As proposed by Arzoumanian et al. (2013), turbulence generated by the accretion of matter onto filaments can provide an additional kinetic pressure that can eventually counteract the pull of gravity, and slow down the filament radial contraction, even though such a process might not be efficient enough (Seifried & Walch 2015). Magnetic fields can also contribute to slow down radial contraction, either when they run parallel to the main axis of filaments (Seifried & Walch 2015), or when in a helical configuration (Fiege & Pudritz 2000). However, B fields are often observed to be perpendicular to the main axis of the star-forming filaments (e.g. Palmeirim et al. 2013; Cox et al. 2016), therefore leaving the radial contraction unaffected.

We now investigate whether rotation could explain these observed gradients. Recchi et al. (2014) simulate the rotation about the main axis of filaments in equilibrium. They predict the radial velocity gradient required for rotation to stabilize filaments with varying $\mathrm{M_{line}}$ and temperature profiles against gravitational instabilities. Following their calculations for a mean SDC13 filament mass of $319\,\mathrm{M_\odot}$, mean filament length and width of 2.11 pc and 0.26 pc respectively (hence central density of $4.8 \times 10^{-17}\,\mathrm{kg/m^3}$), and uniform temperature profile (given we assume a constant temperature everywhere), a radial velocity gradient of $1.42\,\mathrm{km\,s^{-1}pc^{-1}}$ is required for rotation to halt the fragmentation of SDC13. Despite this being larger than the mean radial velocity gradient across the South-East filament (and less than that across the

North-East filament) it is clear from the core extraction that there is indeed fragmentation along both filaments. Hence, we conclude that the observed radial velocity gradient cannot be solely due to rotation as the fragmentation was not halted. The model also only considers equilibrium filaments, which seems to be an unrealistic assumption to make for such a dynamic system as SDC13.

Therefore, we believe that the most likely origin for the observed radial velocity gradients is compression. We speculate that an external site of active star formation, clearly seen in Figure 3.1 within 1 pc proximity to the North-East filament on the sky (centred on 18:14:33.5 -17:33:30.0) may be compressing the North-East and South-East filaments of SDC13, influencing the radial velocity field and their density structures. The WISE catalog of HII region sources (Anderson et al. 2014) reveals a HII region they term as being radio-quiet (called G013.170-00.097) coinciding with this external star formation site, however there is no kinematic information available. Further to this, large scale ^{13}CO(1–0) and C^{18}O(1–0) emission from the IRAM 30m telescope seem to show a cavity in emission corresponding to this region (Williams et al. in preparation; discussed in Chapter 5), consistent with the clearing of material due to feedback effects. We find no maser emission such as water (Walsh et al. 2008; Purcell et al. 2012) nor methanol (Breen et al. 2012) around the position of the HII region. Other works have shown the influence of external feedback on the density structure of star-forming filaments (Peretto et al. 2012; Tremblin et al. 2014).

4.3.7 Origin of the longitudinal velocity gradients

As mentioned in Section 4.2.2, the SDC13 filaments exhibit a complex oscillating longitudinal velocity profile which is at least partially correlated to their column density structure. In their simulations of turbulent cloud evolution, Smith et al. (2016) find very similar looking filament velocity profiles (see their Figure 6). However, they argue that they do not see any clear correlation between the velocity fluctuations and the location of density peaks, concluding that the velocity fluctuations are the result of transient motions generated by the turbulent field in which the filaments are immersed. While we might be partly witnessing such effect in some of the SDC13 filaments, we do observe that ∼63% of the SDC13 cores are located at a peak of velocity gradient as expected for cores accreting from their parent filaments.

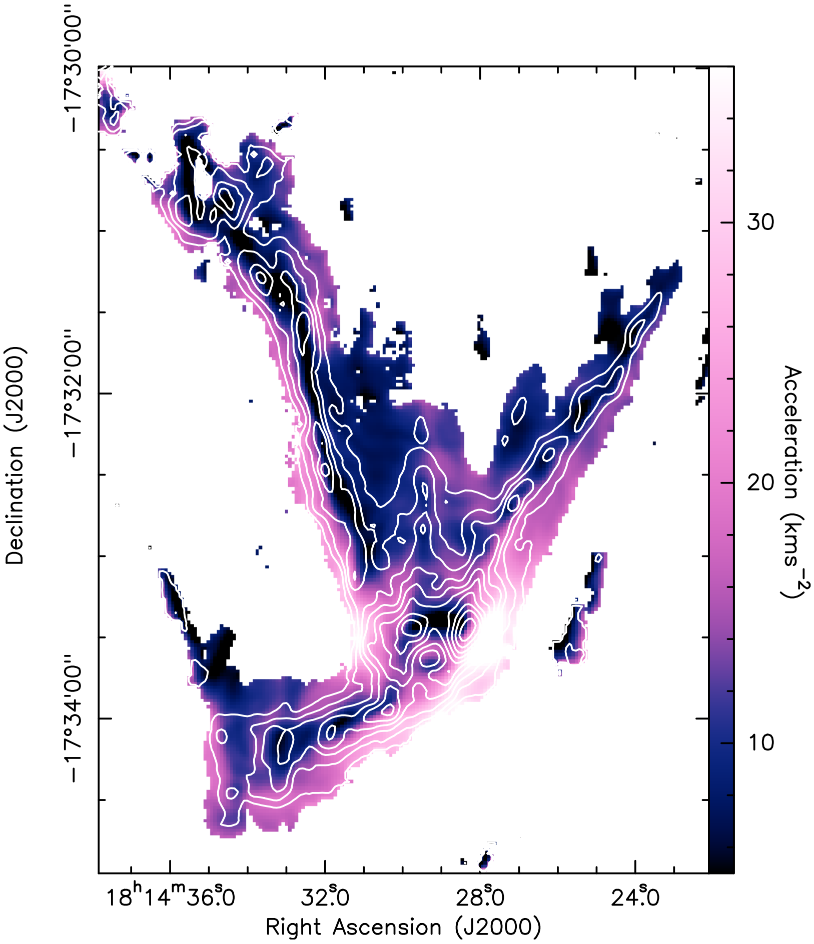

Figure 4.26 Map of gravitational acceleration in SDC13 in units of $1 \times 10^{-12}\,\mathrm{km\,s^{-2}}$. Mass was calculated from the H_2 column density map in the middle panel of Figure 4.7. Contours are of the H_2 column density in Figure 4.7, plotted in $1 \times 10^{22}\,\mathrm{cm^{-2}}$ steps, from $2 \times 10^{22}\,\mathrm{cm^{-2}}$ to $12 \times 10^{22}\,\mathrm{cm^{-2}}$.

One specificity of SDC13 is its hub morphology, suggestive of converging gravity-driven flows towards the filament junction. In order to evaluate if the hub morphology has an impact on the density and velocity profiles of SDC13, for each position we computed the amplitude of the acceleration following:

$$|\vec{a_j}| = \left| - \sum_{i \neq j} \frac{G m_i}{r_{i,j}^3} \vec{r_{i,j}} \right| \tag{4.29}$$

where indices i and j correspond to given pixels in our SDC13 column density map, m_i is the gas mass at pixel i, and $r_{i,j}$ is the distance between pixels i and j. Observationally, one only has access to the 2D projected quantities, and acceleration estimated that way can only provide trend indications and order of magnitude estimates. Figure 4.26 shows the acceleration map obtained from the SDC13 H_2 column density map. As expected, the accelerations along the filament spine are at a minimum due to the axisymmetric nature of gravity in such systems. The acceleration appears to peak around the filament hub junctions and the edges of some filaments, reminiscent of the behaviour seen in the velocity dispersion map in Figure 4.4. More interestingly, we have constructed acceleration profiles along each filament. These are shown in the first row of Figure 4.27. We observe oscillations of the acceleration and an increase of the acceleration towards the hub centre which are reminiscent of the velocity structure. In order to check if this behaviour is due to the presence of cores or to the hub morphology, we constructed another acceleration map with uniform column density, effectively removing the presence of density fluctuations. The second row of Figure 4.27 shows such profiles. One can see that, for the two main filaments (North-East and North-West), the acceleration profiles remain mostly unchanged, demonstrating that the hub morphology is the main driver of the acceleration fluctuation we observed, and therefore the driver of the SDC13 kinematics as a whole. Another interesting point is given by the last row of Figure 4.27 where the gradients of the acceleration is provided. We notice here that the strongest acceleration gradient peak is associated with the most massive core within SDC13. Gradients of acceleration represent accumulation points and are therefore privileged locations for the formation of massive cores. The systematic presence of massive cores near the hub centre could therefore be a direct consequence of large acceleration gradients generated by the hub morphology.

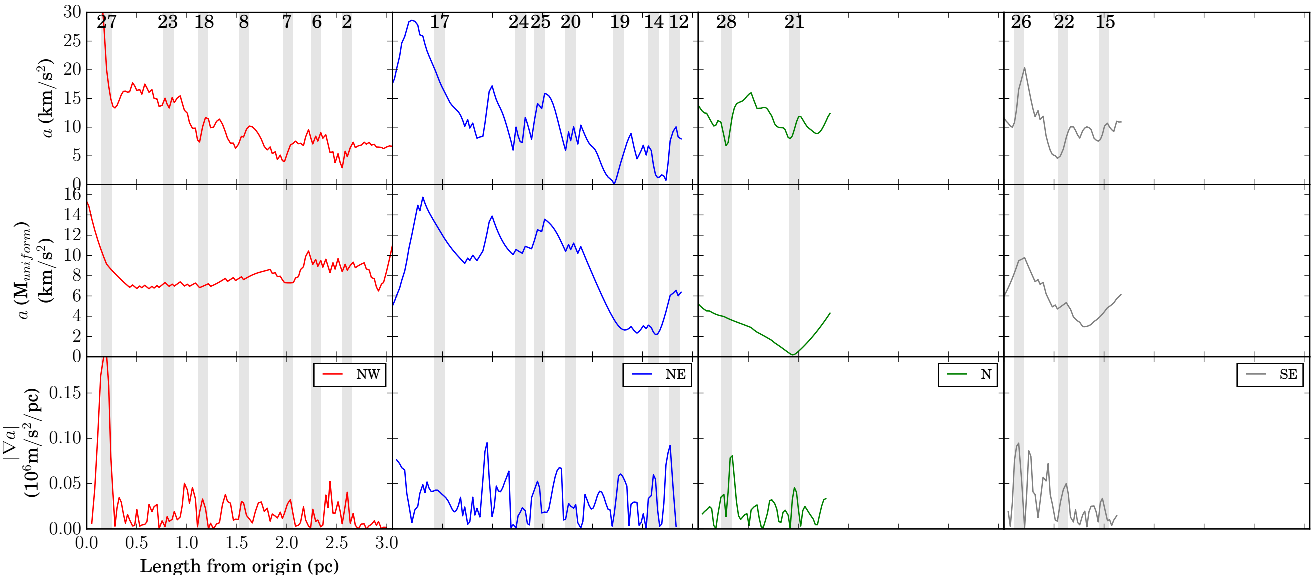

Figure 4.27 Profiles along the spines, where each column denotes a different filamentary arm, as labelled (North-West in red, North-East in blue, North in green and South-East in grey). The origin of each of the spines was defined to begin at the heart of the hub. The first row plots the acceleration due to gravity in SDC13 where the mass was calculated using the H_2 column density map, while a uniform, mean cloud mass was used for the acceleration in the second row. The third row plots the absolute gradient of the acceleration from row three evaluated at each position over the mean core size of ~0.1 pc. The vertical shaded regions correspond to the positions of the cores along each of the filaments, are ~0.1 pc wide and overplotted by the core ID number in Table 4.1.

4.4 SUMMARY AND CONCLUSIONS

We have conducted a study of the SDC13 infrared dark hub filament system using the rotation inversion transition of $NH_3(1,1)$ and $NH_3(2,2)$. The fitting of the hyperfine structure of these lines allowed the construction of centroid velocity, velocity dispersion, and H_2 column density maps. These maps were used to identify both core structures and filament spines, allowing us to characterise their kinematics. We find that all filaments are supercritical, with an average transonic non-thermal velocity dispersion, and that core spacing is typically regular along them ($\sim 0.37 \pm 0.16\,\mathrm{pc}$). Using semi-analytical models of non-equilibrium filaments (Clarke et al. 2016, 2017) we determine that the filaments are a few Myrs old, consistent with the SDC13 dynamical timescale derived by Peretto et al. (2014). We find that the large radial velocity gradients across two of the four filament cannot be due to gravity nor rotation, but most likely due to the compression caused by a nearby HII region. We also find that the velocity dispersion increases towards 73% of the identified cores, which we interpret as the result of the accumulation of matter due to the filament fragmentation process itself. We derive an average gravitational to kinetic energy conversion efficiency within these cores of $\epsilon \simeq 40\,\%$, larger than theoretical values published in the literature. Finally, we propose that the presence of massive cores near the filament junction is due to the large acceleration gradients produced by the hub morphology.

All elements put together, we propose a scenario for the evolution of the SDC13 hub-filament system in which filaments first form as post-shock structures in a supersonic turbulent flow. As a result of the turbulent energy dissipation in the shock, the dense gas within the filaments is initially mostly sub-sonic. Then gravity takes over and starts shaping the evolution of the hub, both fragmenting filaments and pulling the gas towards the centre of the gravitational well. By doing so, gravitational energy is converted into kinetic energy in both local (cores) and global (hub centre) potential well minima, generating more massive cores at the hub centre as a result of larger acceleration gradients.

CHAPTER 5

RESOLVING FILAMENT FORMATION ON LARGE SPATIAL SCALES WITH $C^{18}O$ AND ^{13}CO [*]

*In this chapter, I present $C^{18}O(1–0)$ and $^{13}CO(1–0)$ data from the IRAM 30m telescope. The aim is to look at the large scale kinematics of the SDC13 infrared dark cloud, and investigate to see if any signatures of the filament formation process can be identified from more diffuse gas properties. I discuss the presence of fibres in the cloud, the procedure used to fit multiple velocity components, how a number of clouds along the line-of-sight were separated and extracted, and the impact of a nearby H*II *region.*

5.1 ANALYSIS

The SDC13 filaments discussed in Chapter 4 have average densities of 10^4 cm^{-3}. One possible filament formation mechanism is from the accumulation of lower density material in the parent molecular cloud. If such a process did prevail, we would

---

[*] The work presented here is to be presented in Williams, Peretto et al. in preparation.

expect its signatures to be imprinted in the lower effective critical density gas, like that traced by CO isotopologues. Key questions that we aim to answer include the following: Did the filaments form from the accumulation of lower density material? Are the filaments made from velocity-coherent sub-filaments termed fibres? Were the filaments formed at the fronts of post-shock regions? Are the postulated impacts of the identified HII region on the NH_3 dense gas kinematics and filament evolution (discussed in Chapter 4) also seen in the less dense gas? We aim to answer such questions using $C^{18}O(1–0)$ (hereafter $C^{18}O$) and $^{13}CO(1–0)$ (hereafter ^{13}CO) data observed with the IRAM 30 m telescope.

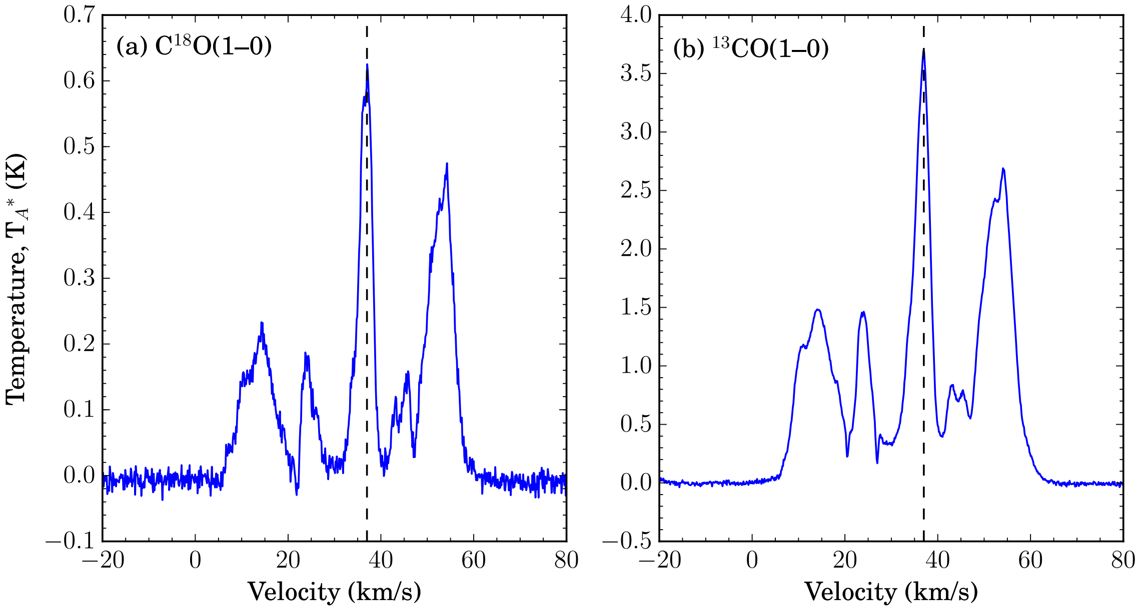

Figure 5.1 The mean spectrum of (a) the $C^{18}O(1–0)$ emission and (b) $^{13}CO(1–0)$ emission, as a function of velocity. The systemic cloud velocity of $37 kms^{-1}$ is denoted by the vertical dashed line.

The mean $C^{18}O$ and ^{13}CO spectra over the full cube are shown in Figure 5.1. As expected, the $C^{18}O$ emission is weaker and noisier than that of ^{13}CO. The vertical dashed line denotes the $37\,kms^{-1}$ systemic velocity of SDC13, clearly indicating which portion of the emission belongs to SDC13. Five clearly distinct groups of emission are seen at different velocities, and given their asymmetry, each group is likely to contain multiple velocity components.

As an initial inspection, I separate each group and calculate their moments. This is not an ideal approach for spectra with multiple velocity components, but is a reasonable starting point. The integrated intensity of $C^{18}O(1\text{–}0)$ over each of the five identified velocity ranges is shown in the top row of Figure 5.2 (in the same order as the spectrum from left to right, and numbered 1 to 5). The $^{13}CO(1\text{–}0)$ maps are not included here, as they largely show the same features, and given the optically thick nature of $^{13}CO(1\text{–}0)$ it makes deriving its kinematics difficult. The intensity weighted velocity, and intensity weighted velocity dispersion is shown in the second and third rows respectively.

The morphologies of the integrated emission of the five regions are diverse. The fourth region for example appears more compact, whilst region 5 appears to have a hub-filament structure to it, with three prominent filament structures converging on a bright, centrally concentrated hub. From the moment one map of this hub candidate, this region corresponds directly to the secondary cloud identified by Peretto et al. (2014) in $N_2H^+(1\text{–}0)$ emission with a systemic velocity of $54\,\mathrm{kms}^{-1}$. With such a busy and rich environment, it is unclear which clouds are related to each other, and in particular, whether or not any of them have some influence in the formation and/or evolution of SDC13. As an initial investigation, we assessed whether there was any morphological correlation between any of these clouds to SDC13 (Figure 5.3). The only cloud that appears to somehow fit around SDC13 like a missing jigsaw piece is perhaps region 5, whose brightest regions of emission falls to the East of the North-East filament, with one of its filaments overlapping in projection with SDC13.

When looking more closely at the integrated emission of the SDC13 cloud (left panel of Figure 5.4), it is clear that the three largest filaments of SDC13 are well resolved. Just like with the GBT data shown in Chapter 4, the North filament is not resolved due to the large beam. A cavity in emission is clearly visible to the East of the North-East filament, and North of the South-East filament. Upon inspection, this clearly correlates very well to the position of the nearby radio-quiet HII region from the

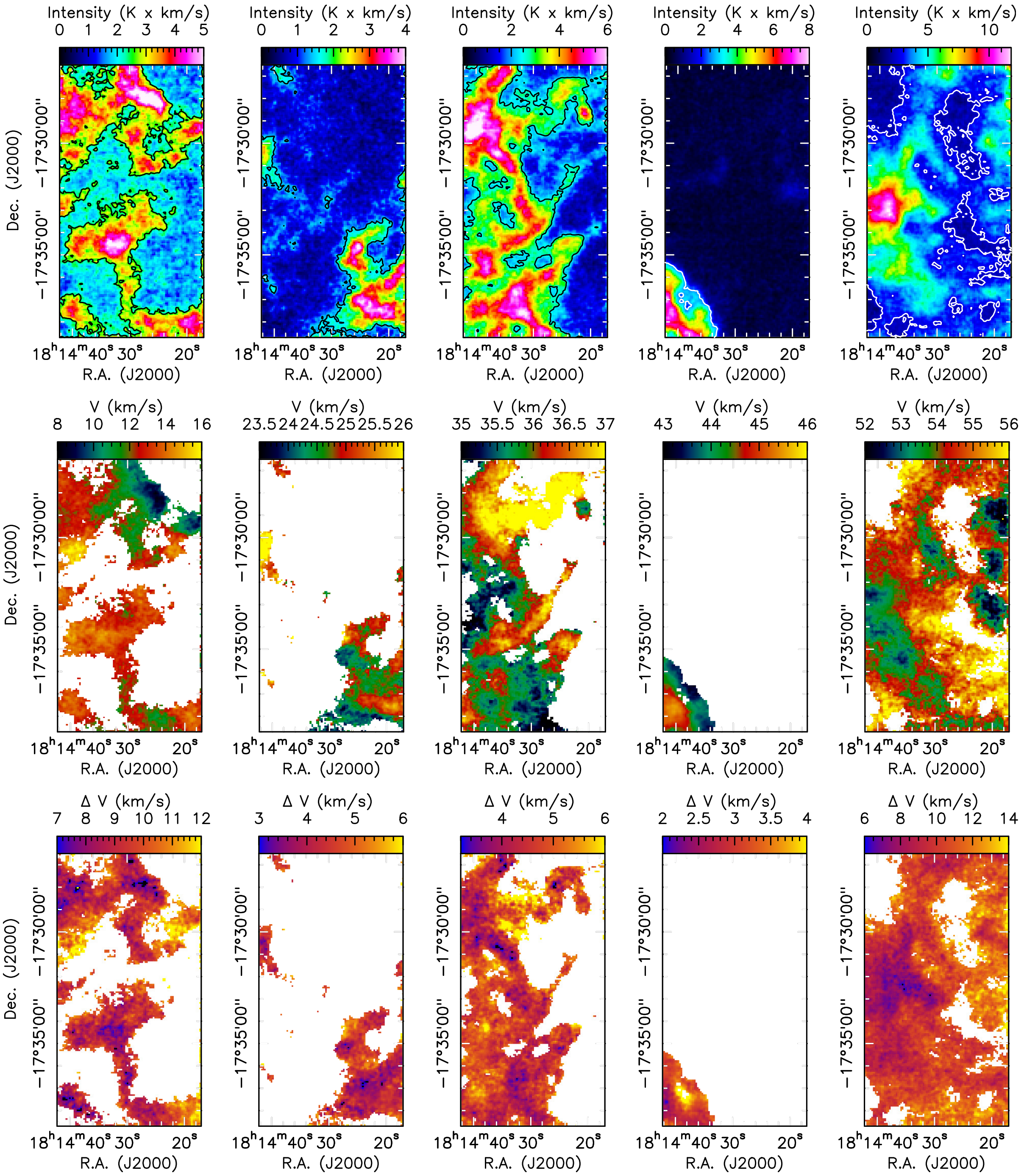

Figure 5.2 The C^{18}O(1–0) moment zero (top row), moment one (middle row) and moment two (bottom row) maps for the 5 groups of emission identified from the mean spectrum. Each column corresponds to the identified groups in chronological order, meaning, that from left to right, the integration intervals are as follows: 2–21kms^{-1}; 21–30kms^{-1}; 30–40kms^{-1}; 40–47kms^{-1}; 47–67kms^{-1}. In the text, the regions are referred to by their column number, defined as 1 to 5 from left to right. The outlying contour on the moment zero maps indicates the mask area applied to the moment one and moment two maps. These represent 5σ contours in all but the second column which was masked to 3σ as it is a weaker component of the emission (where $\sigma = 0.5\,$K is the RMS noise of an emission free polygon).

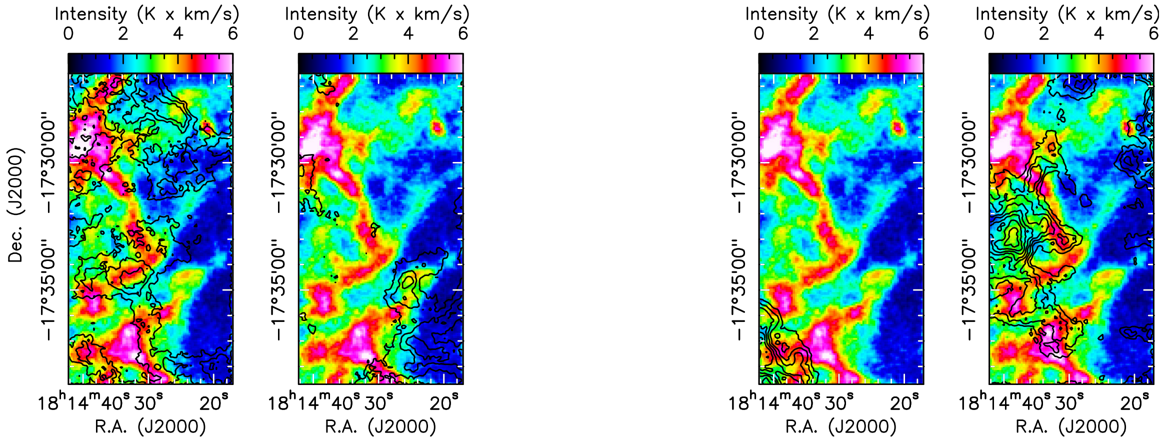

Figure 5.3 Each panel plots the intensity of the SDC13 cloud integrated between velocities of 30–40 kms^{-1}, overplotted in each panel by the integrated intensity contours of the other four groups of emission. The contours of the emission in each column correspond to the integrated intensity map of the same column in Figure 5.2.

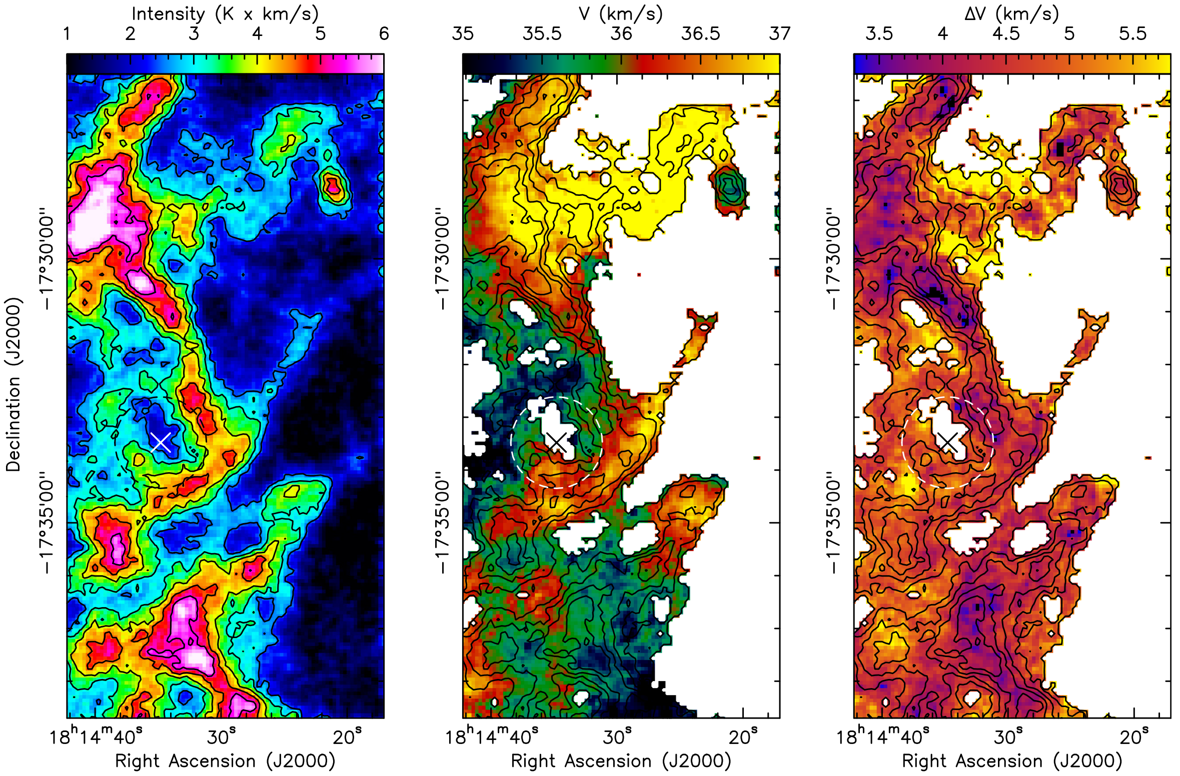

Figure 5.4 The moment one (left) and moment two (right) maps of the SDC13 cloud, integrated between 30–40kms^{-1}, of the C^{18}O(1–0) data. Overlaid contours are of the moment zero intensity, from 2.5 K×kms^{-1} to 5.3 K×kms^{-1} by 0.7 K×kms^{-1}. Black cross and white dashed circle marks the position and radius of the HII region respectively. Masks are applied to a 5σ level.

WISE catalogue (G013.170-00.097, Anderson et al. 2014). Overplotting the HII region radius of 26″, we find that it matches very well the ring of emission which surrounding the cavity, and overlaps with the bottom portion of the North-East filament, and the top portion of the South-East filament. In producing a three colour composite image of the $C^{18}O$(1–0) integrated intensity, hot dust emission traced by 70μm HIGAL and cold dust emission traced by 8μm Spitzer GLIMPSE (Figure 5.5) it is apparent that the cavity in gas is filled by dust. Furthermore, the position of the HII region appears to coincide with a peak in 8μm emission. From the NH_3 emission (Chapter 4), it was concluded that the most likely explanation for strong radial velocity gradients observed across those portions of the filaments was the compression caused by this HII region. This is all strong evidence to support this theory.

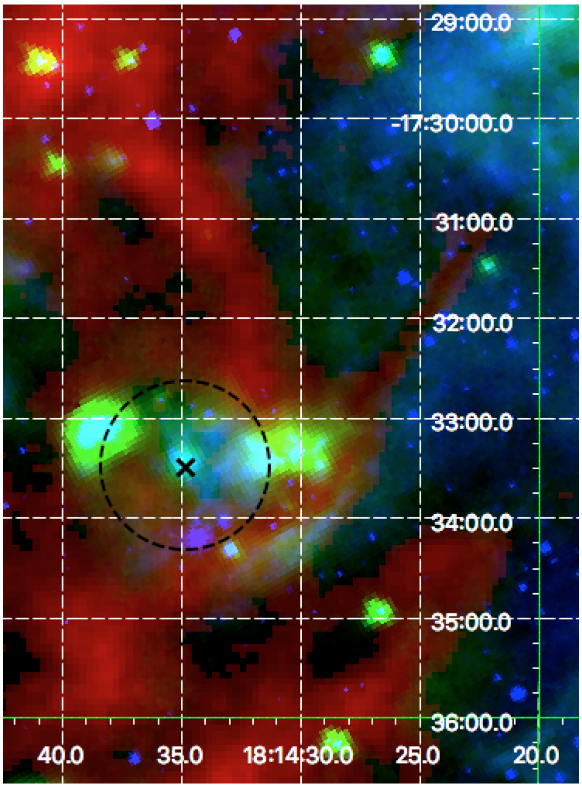

Figure 5.5 Three colour composite image, where R, G and B bands are the $C^{18}O$(1–0) integrated emission of SDC13, 70μm HIGAL (Molinari et al. 2010) and 8μm *Spitzer* GLIMPSE (Churchwell et al. 2009) bands respectively. The black cross and dashed circle marks the position and radius of the catalogued HII region (Anderson et al. 2014). The dust emission is seen to fill the $C^{18}O$ cavity, whilst the position appears to coincide with a bright Spitzer 8μm source.

The moment one kinematics of each of the regions are all rather different too, but all appear to have sharp transitions in velocity, particularly distinct in the northern portion of region 1. Looking at the velocity structure of the SDC13 cloud in more detail (Figure 5.4), it appears consistent with the NH_3 data (in Chapter 4), where the South-East and North-West filament appear red-shifted to the North-East filament. This is corroborated when taking the profiles of the velocity along the filament spines, where the large scale morphology observed in NH_3 is also observed in $C^{18}O$(1–0) (Figure 5.6). Gradients are seen along the filaments, including the secondary gradient along the top of the North-East filament identified by Peretto et al. (2014) in N_2H^+(1–0) (see Figure 3.2). Interestingly, to the North of SDC13, the velocity structure appears to follow exactly the intensity of the cloud. This is discussed in more detail in Section 5.2.3.

Interestingly, the moment two maps do all have one distinct common feature. The brightest emission in each region, and hence likely the highest column density gas, all appear to have the narrowest velocity widths locally, compared to the lower brightness, more diffuse regions which appear to have the widest velocity widths. This is shown in Figure 5.7, where the velocity width appears to narrow towards the centre of both the North-East and North-West filaments. It is suggested in literature that filaments represent subsonic, stagnation regions following the collision of supersonic turbulent flows (Padoan et al. 2001; Klessen et al. 2005; Federrath et al. 2016). With sub/transonic velocity dispersion, the SDC13 filaments were suggested in Chapter 4 to represent such regions. The consistency of the large scale structure of the $C^{18}O$(1–0) moment two map (Figure 5.4) with the small scale NH_3 data could be tantalising evidence pointing towards such a formation process. By nature a moment analysis blends multiple velocity components, hence no significance can be assigned to the values of the widths, however this trend may still prevail following robust line fitting. Whilst accounting for the vast difference in size scales being probed by the NH_3 interferometry data and the IRAM 30 m data, it appears that the large scale morphology of the velocity width profiles along the filaments (Figure 5.6) are consistent with each other. One clear departure exists however, where the velocity width towards the centre of the hub narrows in the C^{18}O(1–0), whilst it broadens in the NH$_3$(1,1) data. This could be an indication of the failings of the moment analysis. However, with the moment one centroid velocity profiles being consistent with the fitted NH$_3$ data, it is possible that this is instead an indication of the dense gas kinematics not prevailing in the more diffuse gas, as discussed in Chapter 4.

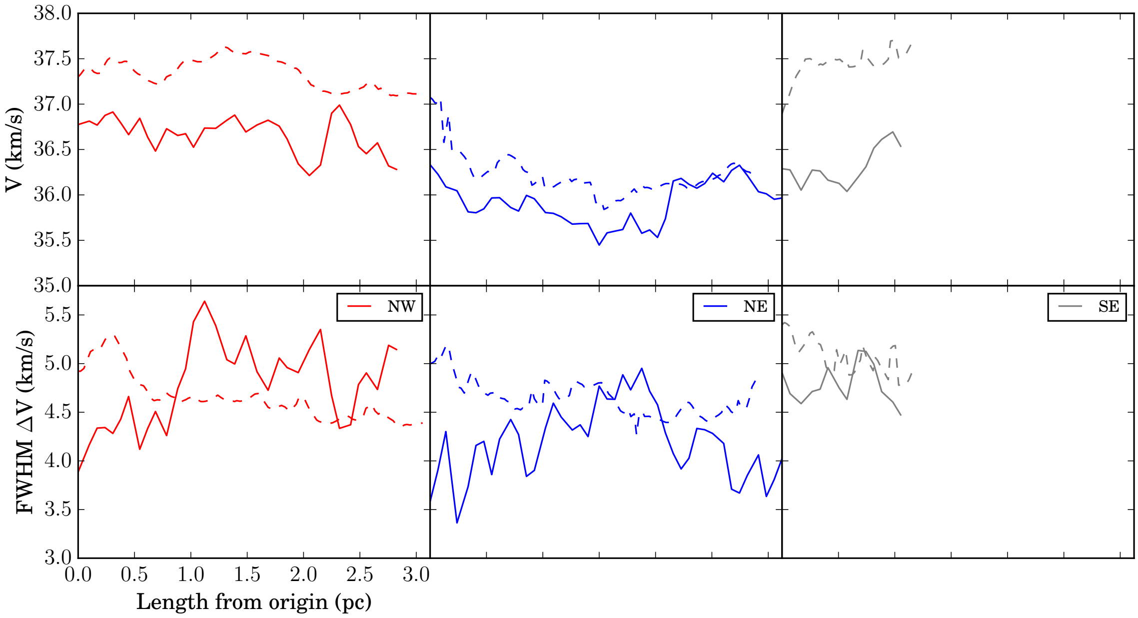

Figure 5.6 Longitudinal profiles of the C^{18}O(1–0) moment zero (first row), moment one (second row) and moment two (third row) maps along the SDC13 filament spines. Each column from left to right plots the North-West in red, the North-East in blue, and the South-East in grey. In each, the dashed line shows the NH$_3$ data from Chapter 4, with an offset of +4 applied to the velocity widths for clarity. The spines are identical to those extracted in the NH$_3$ analysis of Chapter 4, but have been regridded to the IRAM 30 m data. Differences in the spine lengths between the data sets originate from the regridding.

5.1.1 The presence of fibres

Recent observations of filamentary regions have shown that filaments themselves contain narrower, velocity-coherent sub-structures, called fibres (e.g. Hacar

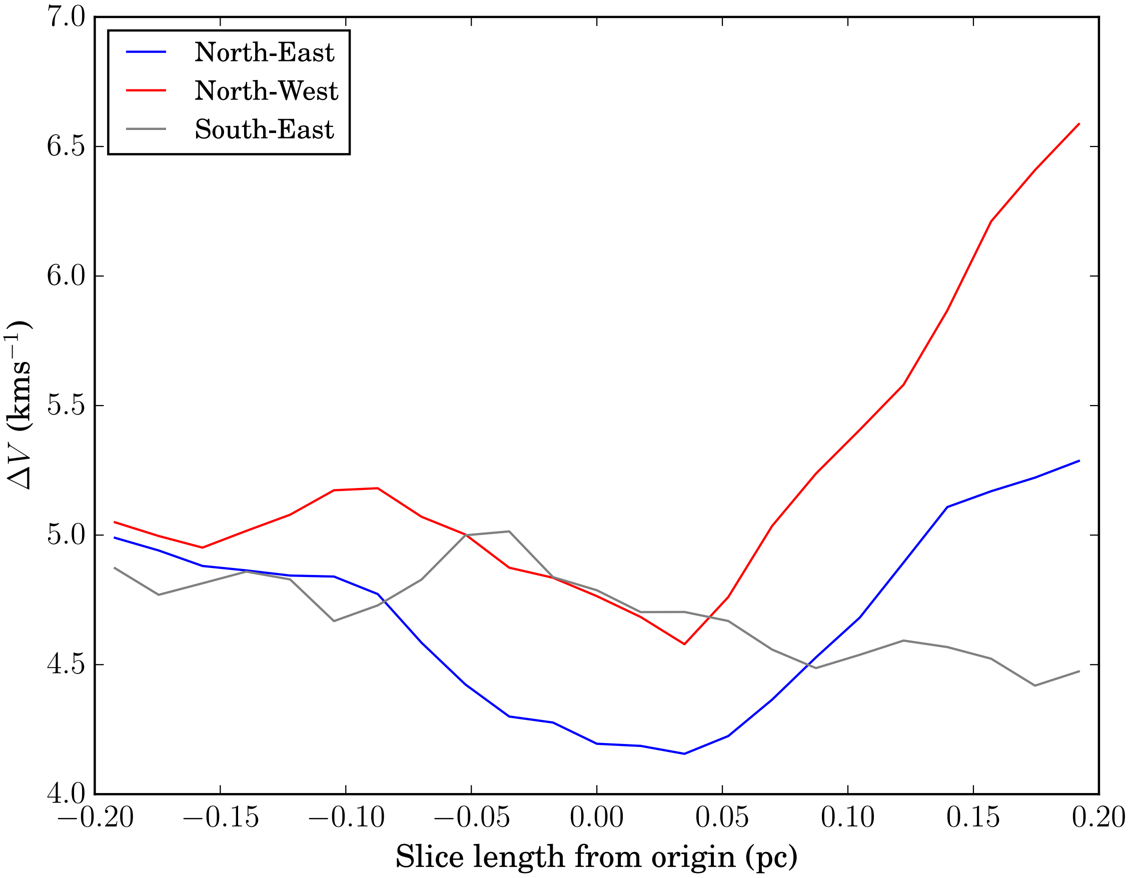

Figure 5.7 The mean profile of the velocity width across the North-East (blue), North-West (red) and South-East (grey) filaments, derived from moment analysis of the $C^{18}O(1–0)$. In both North-East and North-West filaments, the width appears to narrow towards the centre of the filament, whilst it broadens slightly towards the centre of the South-East filament. Uncertainties are equivalent to the spectral resolution of $0.13\,\mathrm{km\,s^{-1}}$.

et al. 2013; Henshaw et al. 2017). As mentioned in Chapter 1, they are thought to either fragment from the parent filament by turbulent motions due to gravity (Tafalla & Hacar 2015), or fragment in a turbulent ISM and then gathered into the larger filament structure by gravity (Smith et al. 2014). There is much debate as to whether these fibres are common features of the interstellar medium. Zamora-Avilés et al. (2017) conducted magnetohydrodynamic (MHD) simulations of a self-gravitating molecular cloud, finding that fibres are indeed prevalent, however only in the very densest regions of the cloud is a fibre identified in more than one projection. This suggests that even though fibres may be velocity-coherent, they may not be physically-coherent, and merely an effect of projection. This result is corroborated by Clarke et al. (in preparation), who find that fibres are prevalent in their synthetic observations of $C^{18}O(1\text{–}0)$, however a fibre found in position-position-velocity space is not always present in position-position-position space. This makes comparing and interpreting fibres found in simulations to those found in observations difficult indeed.

Longitudinal filament structure

As shown by previous works, fibres may be identified by extracting position-velocity slices from a spectral data cube. The schematic shown in Figure 5.10 taken from Hacar et al. (2013) shows what sort of features one could expect to see in such a diagram were fibres present in a filament. Outlined by the blue and red lines are two, clear, velocity-coherent structures that would themselves be peaks in emission. As an initial investigation into the presence of fibres in SDC13, position-velocity (PV) slices were taken along the spines of the North-East, North-West and South-East filaments of the $C^{18}O(1\text{–}0)$ and $^{13}CO(1\text{–}0)$ IRAM 30 m data (shown in Figures 5.8 and 5.9). These spines are re-gridded, identical copies of those extracted from the NH_3 data in Chapter 4.

It is clear from our position-velocity diagrams that both the North-West and North-East filaments look very velocity-coherent in themselves, meaning the high

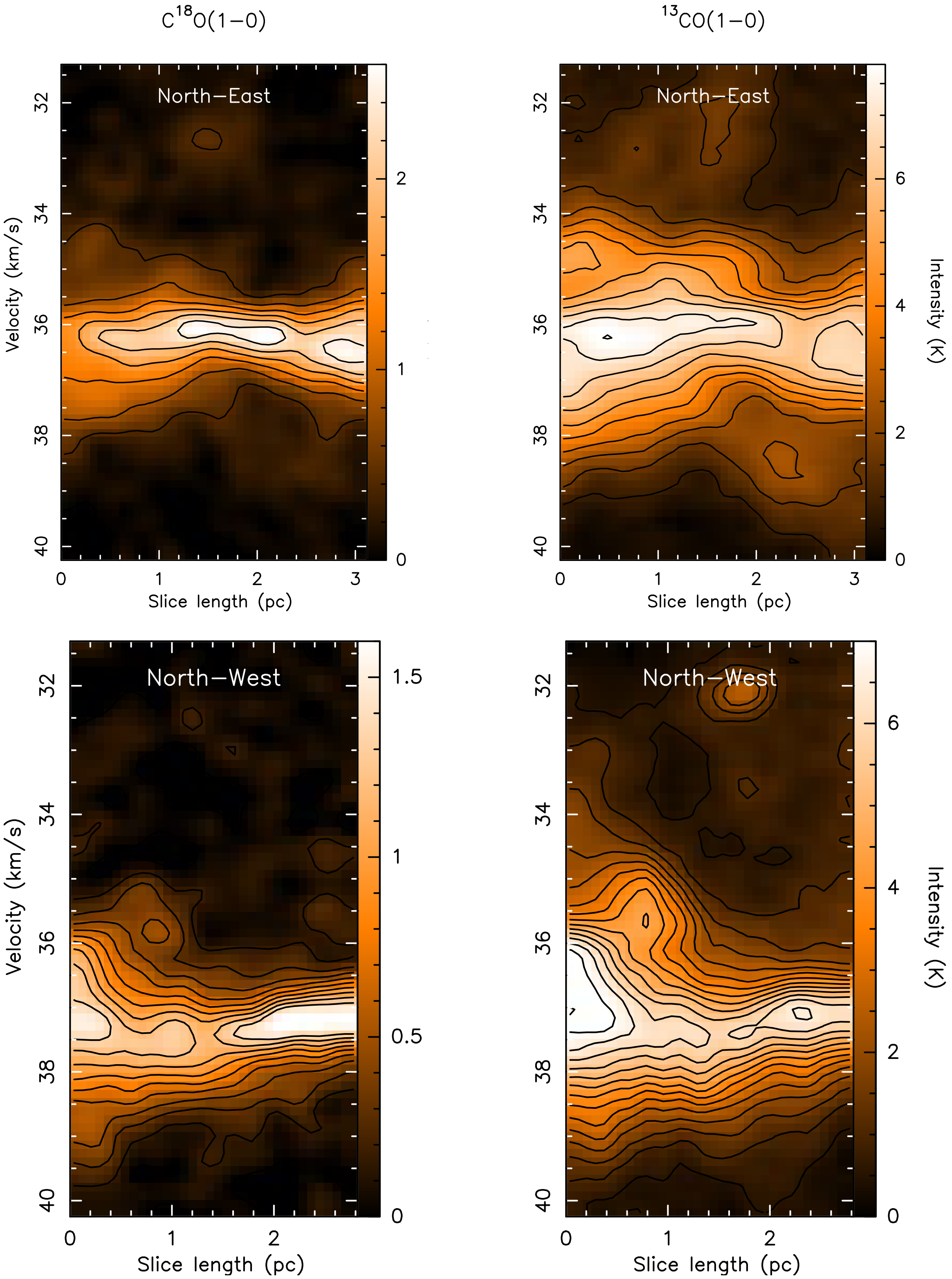

Figure 5.8 The position-velocity diagrams taken along the directions of the North-East filament spine (top row) and the North-West filament spine (bottom row) of the original C^{18}O(1–0) emission (left column) and the ^{13}CO(1–0) emission (right column). The C^{18}O and ^{13}CO data were spatially smoothed by a Gaussian kernel with a FWHM of 11″ and 8″ respectively, for visual purposes. The centre of the cloud is at a zero on the position axis.

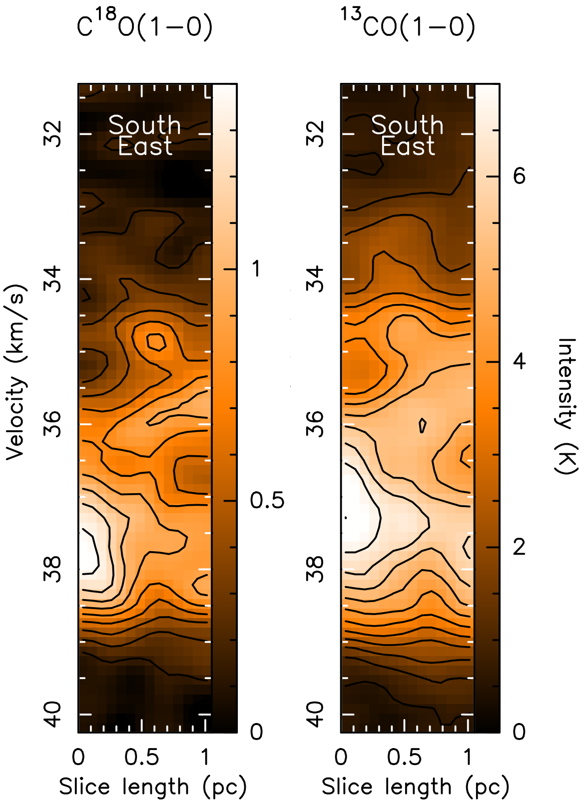

Figure 5.9 Same as Figure 5.8, but for the South-East filament.

intensity peaks are grouped together without peaking at multiple velocities. This strongly suggests that the filaments themselves are not constituted by fibres. With the spatial resolution of the data of 23.6″, we do not expect to spatially resolve fibres. However, the spectral resolution of 0.13 $\mathrm{km s^{-1}}$ should indeed be sufficient to resolve them in velocity space. The broad nature of the high intensity emission at slice lengths between 0–0.5 pc in the North-West filament can be attributed to the spine intersecting the hub region.

The PV diagram along the South-East filament (Figure 5.9) is a little more complex to interpret. The main body of the filament is seen centred at a velocity of $\sim$38 $\mathrm{km s^{-1}}$. A second peak in emission is centred at $\sim$35.8 $\mathrm{km s^{-1}}$. Although initially suggestive of perhaps a velocity-coherent fibre, this is rather most likely a signature of the effect of the nearby H ii region, whose radius overlaps with the filament at this location. These features are perhaps stronger in the South-East filament due to it

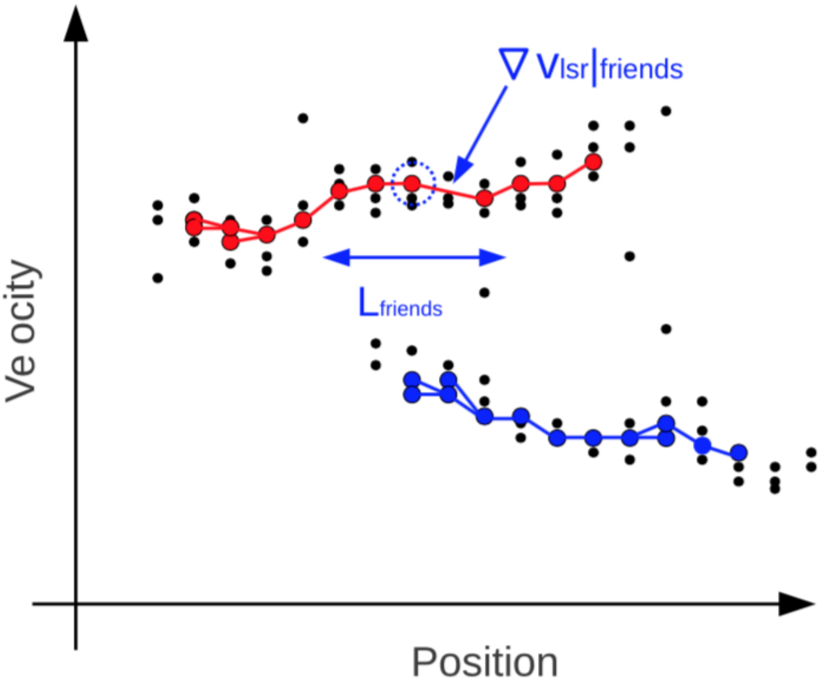

Figure 5.10 A schematic presented by Hacar et al. (2013) (their Figure 10) showing the features one would expect in a position-velocity diagram were fibres present. The red and blue lines outline the two separate velocity-coherent fibres.

being more impacted by the HII region, given that its radius overlaps marginally more with the South-East filament than the North-East.

Radial filament structure

The formation of filaments has been suggested to possibly be due to the accretion of more diffuse gas from the environment (e.g. Palmeirim et al. 2013). Studying the radial velocity structure of filaments may therefore reveal such inflows when such a scenario is true for a system. As such, the radial structure of the SDC13 filaments were investigated by taking slices across the filaments, at a 90° angle to each spinal pixel. Each slice is 0.38 pc long, and were interpolated using the Taylor expansion method (and as discussed in Chapter 4). Given that the HII region appears to be local to the bottom portion of the North-East filament, the top half and bottom half are separately considered to investigate if there are any discernible differences that may be caused by the HII region impact. These PV diagrams are shown in Figure 5.11, where

Table 5.1 The radial velocity gradients across the North-East filament, in kms^{-1}pc^{-1}.

	C^{18}O(1–0)	^{13}CO(1–0)
Top half	1.9	2.0
Bottom half	2.7	1.7

the top and bottom rows correspond to the top and bottom halves of the North-East filament, and the first and second columns correspond to the C^{18}O and ^{13}CO emission. To avoid contamination, regions of the spine in the bottom half of the filament that intersect the central hub were excluded. Radial velocity gradients were calculated across each filament half for each tracer, as listed in Table 5.1. The gradient measured across the top half of the filament are consistent with both tracers. In C^{18}O(1–0), the gradient is steeper in the bottom half by 0.8 kms^{-1}pc^{-1}. This is consistent with the 3.0 kms^{-1}pc^{-1} measured by the JVLA NH$_3$ data (see Chapter 4), where we concluded the most likely explanation for this steep gradient was the presence of the HII region causing compression of the filament. However, ^{13}CO(1–0) traces the gradient to be dramatically shallower in the bottom half compared to C^{18}O(1–0) emission, by an entire 1 kms^{-1}pc^{-1}. As listed in Table 1.1 in Chapter 1, all three molecules have critical densities of $\sim 2 \times 10^3$ cm^{-3} at 20 K, therefore should trace similar density regimes. However, ^{13}CO(1–0) is much more optically thick than both NH$_3$ and C^{18}O(1–0). The abundance of ^{13}CO and C^{18}O relative to ^{12}CO is 1/61 and 1/500 respectively (Wilson & Rood 1994). For these reasons, it takes more column for C^{18}O(1–0) to become optically thick than ^{13}CO(1–0). From the integrated intensity maps of Figure 5.4, the difference in emission between the bottom and top halves of the North-East filament appears to be 1.5 times at its most. This difference in emission may translate to the top half of the filament having less column, meaning ^{13}CO(1–0) may be more optically thick in the bottom of the filament, accounting for consistent gradients in the top half, whilst only measuring the gradient of the surface of the column density shell in the bottom.

Figure 5.12 shows the radial PV diagrams of the North-West and South-East

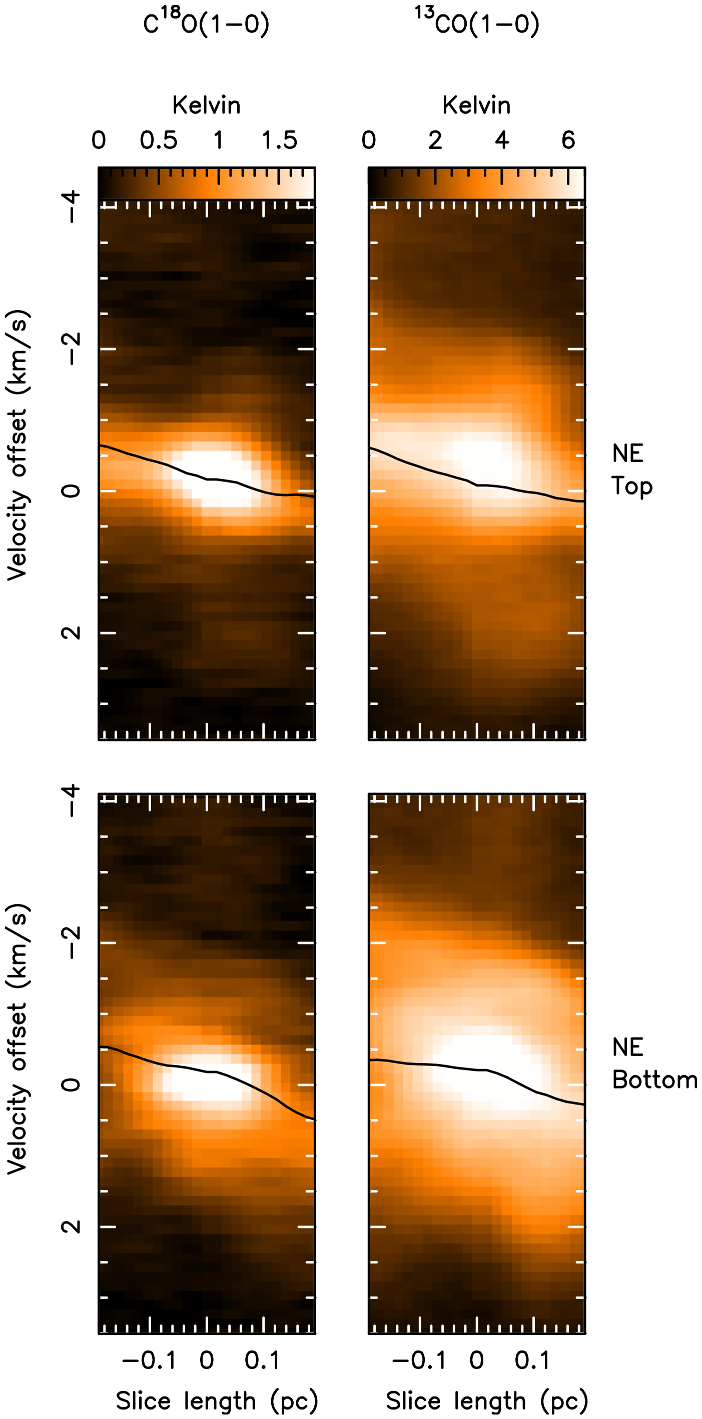

Figure 5.11 The mean radial position-velocity slices across the spines of the top half (top row) and bottom half (bottom row) of the North-East filaments in $C^{18}O$(1–0) emission (left column) and ^{13}CO(1–0) emission (right column). Regions of the spine that intersected the hub were excluded. The solid black line denotes the intensity-weighted average velocity at each position along the radial slice. The velocity of each of the radial slices was centred to the systemic cloud velocity of 37 $\mathrm{km s^{-1}}$ before taking the mean. The data was smoothed by a Gaussian kernel of 11.8″.

filaments. As the HII region appears local to the entire South-East, the mean profile was taken across the entire length. Such a split is not necessary in the North-West filament. There appears to be no radial velocity gradient across the central region of the North-West in neither tracer, and both appear to follow the exact same morphology. Interestingly there appears to be a gradient in velocity either side of the central regions of the filaments. This is a behaviour not seen in the North-East filament, which has a gradient across its entire width. Observations seems to suggest such gradients are also observed at the edges of the filaments in Orion B (Orkisz, Peretto et al. in preparation), and may be tentatively suggestive of accretion onto the filament. The South-East filament however appears far more complex. The first peak in emission is observed at $+1\,\mathrm{kms}^{-1}$ relative to the systemic cloud velocity of $37\mathrm{kms}^{-1}$, and corresponds to the main body of the South-East filament. The second peak in emission is observed at $-1\,\mathrm{kms}^{-1}$, and can be attributed and matched to the same ring of material surrounding the HII region that was identified in the PV diagram along the South-East filament (Figure 5.9). This double-peaked nature means evaluating a radial velocity gradient from such plots is difficult, given that the intensity-weighted mean velocity appears flat due to the two heavy weights in intensity.

This absence of fibres on the large scale is indeed interesting, but not entirely unexpected given that it was very clear from the small scale NH_3 interferometric data (see Chapter 4) that there was a single velocity component everywhere in the dense gas of SDC13. Whether or not the lack of fibres is due to effects of chemistry is unclear, as $C^{18}O$ is often frozen out onto dust grains at high densities of $\gtrsim 10^5\,\mathrm{cm}^3$ (e.g. Lippok et al. 2013). Tafalla & Hacar (2015) propose the *"fray and fragment"* scenario of fibre (and subsequently core) formation. Firstly, the parent filament is formed from the collision of large scale gas flows. With the dissipation of residual turbulence from such an interaction, the subsonic, velocity-coherent fibres are "frayed" from the parent filament. The fibres with enough line mass (called *"fertile"* fibres) then fragment into cores due to gravity. In the *"fragment and gather"* scenario proposed

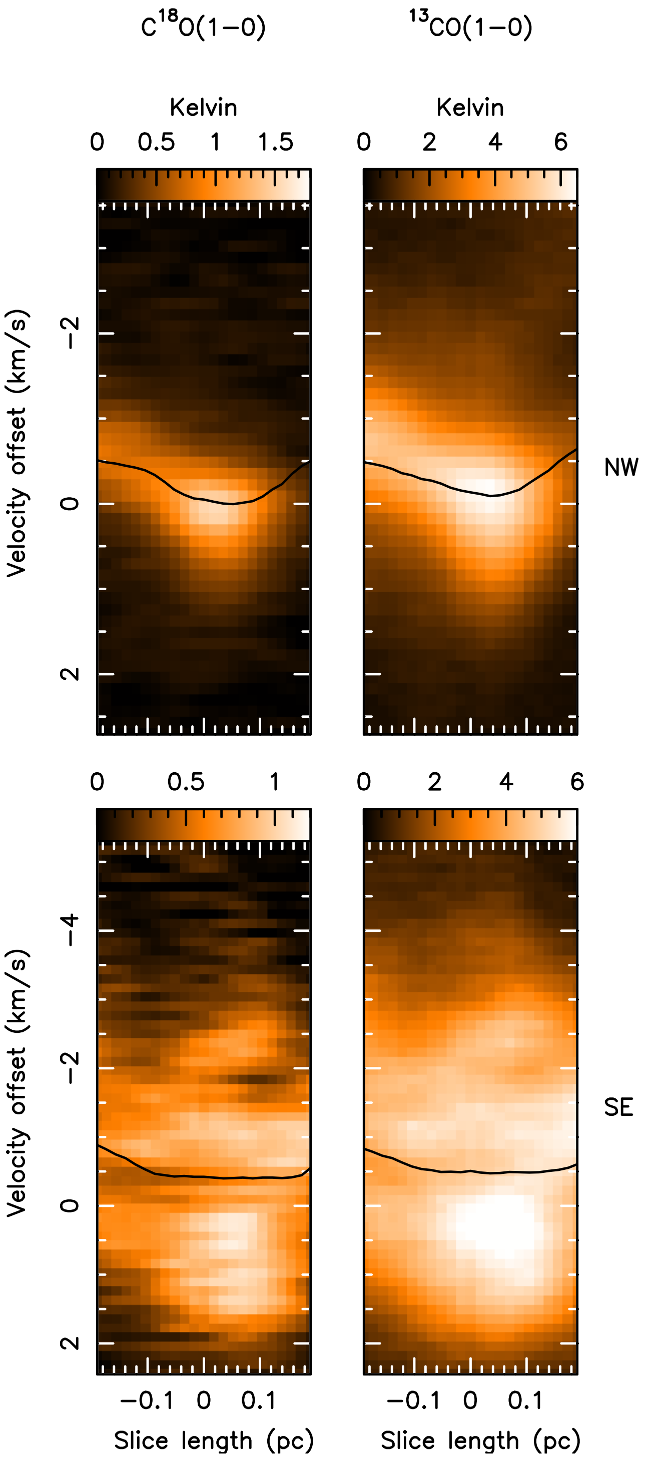

Figure 5.12 Caption as for Figure 5.11, however plots the North-West filament in the top row, and the South-East filament in the bottom row.

by Smith et al. (2016), fibres instead first form due to turbulent fragmentation in the initially turbulent cloud which is itself evolving due to gravity. These fibres are then swept up into a large scale filament by gravity. The common feature in both scenarios is that turbulence is required in the first instance. As already concluded from the dense NH_3 gas presented in Chapter 4, the filaments with their sub/transonic non-thermal motions is indicative of them being post-shock regions. Gravity as a result of the morphology of the hub itself becomes dominant in the evolution of the system, causing strong acceleration gradients, both fragmenting filaments and pulling gas towards the hub centre. I suggest that in this scenario, that gravity dominates the energy terms, preventing the necessary turbulent *fraying* of fibres. This suggests that fibres are surpressed in such hub-filament systems. This is currently speculation, and would require synthetic observations of hub-filament systems to test it.

5.2 LINE FITTING

When emission appears Gaussian in shape, conducting a moment analysis (such as that shown in Figure 5.2) is sufficient in studying the kinematics of the gas. However, when a spectrum is more complex, details such as multiple velocity components for example are inherently overlooked and blended. To recover such information, the fitting of every velocity component is essential. Unlike the line fitting conducted for the NH_3 emission in Chapter 4, neither $^{13}CO(1\text{–}0)$ nor $C^{18}O(1\text{–}0)$ contain hyperfine structure emission. However, from initial inspection of the data cubes (such as Figure 5.1), it is clear that there is an abundance of emission from a number of clouds in the vicinity in projection of SDC13. The busy nature of the environment makes fitting the emission tricky, as they undoubtedly require the fitting of multiple velocity components. As shown in Figure 5.3, it is unclear from initial inspection which clouds are associated to SDC13 and may have impacted the formation or kinematics, and which clouds are not at all associated. For this reason, we cannot exclude any of the emission, which adds to the complexity of the fitting.

A number of methods are available to fit spectral lines effectively, most notably the SCOUSE semi-automated fitting algorithm developed by Henshaw et al. (2016b). The extent of the emission is identified and split into boxes within which the spectra are spatially averaged. Fits are performed by hand on each of the averaged spectra, which are then used as prior guesses for the fits to all of the original, un-averaged spectra. This is an excellent method of performing such line fitting, however is time consuming to manually fit the spatially averaged spectra in the first instance, and then to check the fits in the final stage. A lot of subjectivity is also required in deciding how many components to fit to each spectrum in the first instance, which is not ideal for very complex spectra. For this reason, I proceed to do the line fitting using a fully-automated home-made code (Peretto et al. in preparation).

The code initially fits N number of Gaussian profiles to each individual spectrum, where N is defined by how many distinct peaks in emission are found across the whole bandwidth of the spectrum from taking the first derivative (as the derivative of a peak position should be zero). If the dispersion of the residual of the fit attempt to the original spectrum is larger or smaller than the RMS noise of the original spectrum (within a tolerance level of 30%), it is considered that the spectrum may have been fitted by either too many, or too few, Gaussian components. If this is the case, either fewer, or more, Gaussian profiles are included in the fit. This is iterated until the dispersion of the residual is brought back in line with the RMS noise of the original spectrum. To aid the fitting algorithm, the cube was spectrally smoothed by a boxcar of width 5 channels, whilst also smoothed spatially by a Gaussian of width 11.8″. A signal-to-noise limit of 5 was also set so as to limit noise features being identified as peaks in emission.

Examples of the model fits are shown in Figure 5.13. The iterative method of the fitting procedure has indeed ensured that the residual of the spectrum and the model fit does fall around the RMS noise of 0.16 K (evaluated from emission free areas). However, a large number of Gaussian components is required in some cases to achieve this. It is clear this is due to the asymmetric nature of many of the lines, which the code reproduces by fitting many Gaussian profiles. These asymmetries in themselves may be interesting features, and may be true velocity components that we cannot spatially resolve nor correlate to any meaningful structure with this high angular resolution data set. Significant features or not, it is clear that this fitting method may perhaps be prone to over-fitting a spectrum at times. The example fits shown in Figure 5.13 do indeed reproduce the emission very well, however the sheer number of components makes using the fits to study the kinematics of the gas difficult at this stage. Due to its complexity, the fitting of the emission is still a work-in-progress. Fitting the ^{13}CO(1–0) line is even trickier due to it having even more emission in the rich environment surrounding SDC13. As a result, the rest of this chapter only includes analysis of the C^{18}O(1–0) emission. An immediate objective of mine for the future is to realistically fit both lines, and more robustly analyse the centroid velocity and velocity width of the fits.

5.2.1 CLOUD EXTRACTION

As there are a number of clouds along the line-of-sight, this can cause confusion as to which clouds are associated to each other. To disentangle this, individual clouds are extracted using a friends-of-friends algorithm (Peretto et al. in preparation) which identifies any emission spatially close to each pixel, and within the width of the spectrum at that pixel in velocity space. Every cloud is then assigned an ID number, which allows it to be separated from the rest of the emission in position-position-velocity space. A pixel limit of 100 is set as a lower limit on the size of a structure considered a cloud. Cloud extraction in this way becomes more tricky if a spectrum has been fitted by too many velocity components, as pixels that have perhaps been over-fitted find themselves connected to regions of emission that are unrelated. This is why careful inspection of the spectra is required, and why caution is required in

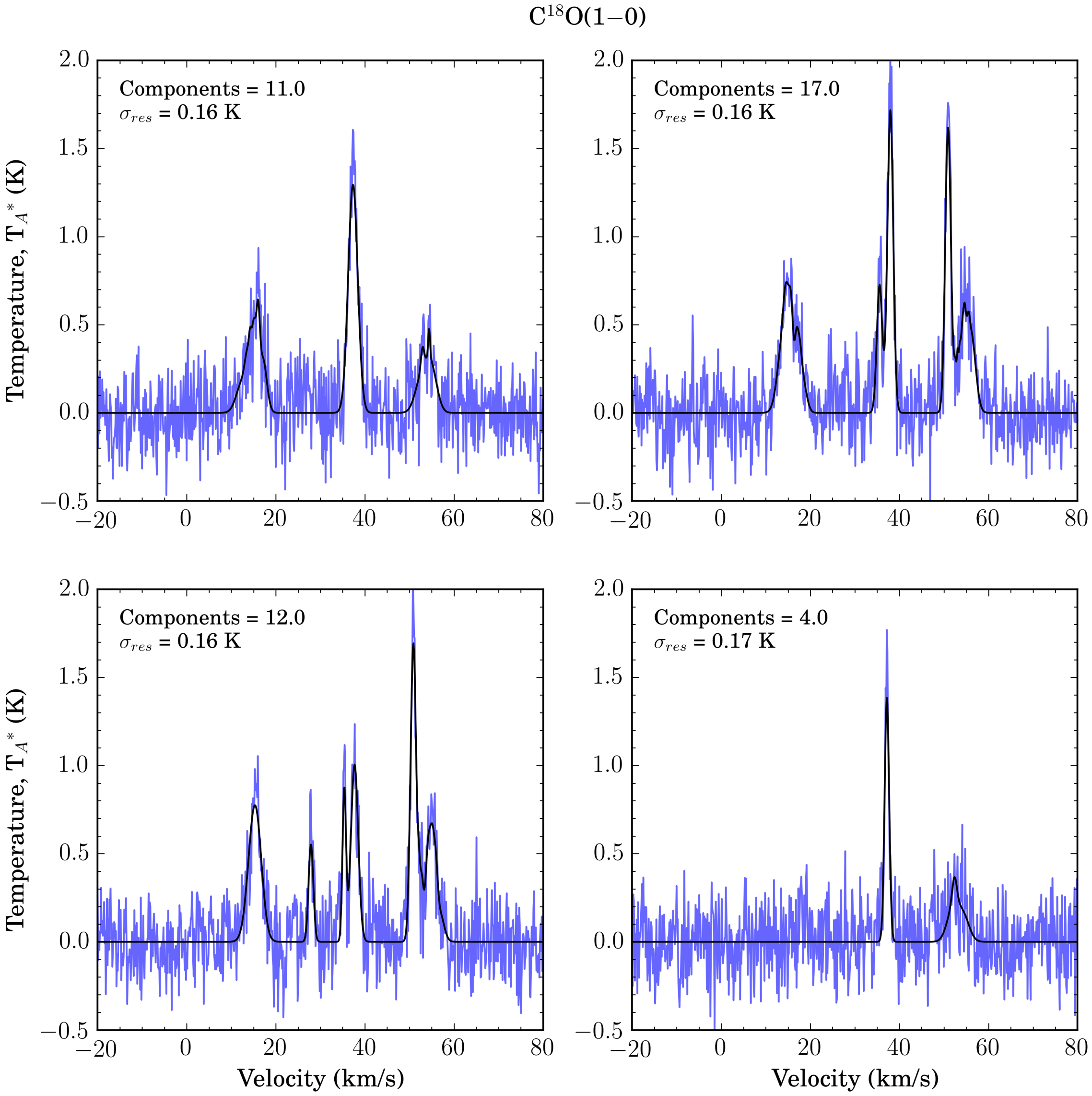

Figure 5.13 Examples of four C^{18}(1–0) spectra (in blue) and their model fits (in black). Printed in each panel is the standard deviation of the residual, and the number of Gaussian components used to produce the fit. The typical RMS noise of the cube is 0.16 K.

doing this at this stage.

In total, we identify 16 clouds, the integrated intensity maps of each are shown below in Figure 5.14. It is clear that in doing this, regions of emission that were bundled together initially from inspecting the mean spectra shown in Figure 5.1 are able to be separated from each other. One of the most striking examples of such a separation is clouds 29 and 32, both large and distinct clouds that could not previously be distinguished. Other examples include the separation of clouds 11 and 12, and of clouds 22 and 24.

Figure 5.15 shows the histogram of the model fit integrated intensity of cloud 15 with respect to the moment zero map evaluated over the entire velocity range of the central emission component in $C^{18}O(1\text{–}0)$. From this, the integrated intensity recovered from the model cube which is devoid of noise recovers 10% more emission than the moment zero map. The example fits to the emission shown in Figure 5.13 do indicate that the fits reproduce the emission well. This clearly shows loss of information when simply conducting a moment analysis, and demonstrates the need for correctly fitting the line emission. Some pixels that have recovered integrated intensity less than that in the moment analysis can be attributed to the number of pixels where the fit was poor, and where the emission was zero. Pixels with larger fitted integrated intensity can be attributed to low brightness wing emission that one loses in a noisy spectrum. This is expected to improve with more work in the very near future.

5.2.2 HII region impact

As concluded in Chapter 4, the most likely cause for the strong radial velocity gradients in the North-East and South-East filaments was the external influence of an active star formation region. It was found that the infrared bright emission within 1 pc proximity on the sky to SDC13 was associated to a HII region (Anderson et al. 2014). However, no kinematic nor flux information was available in the WISE catalog,

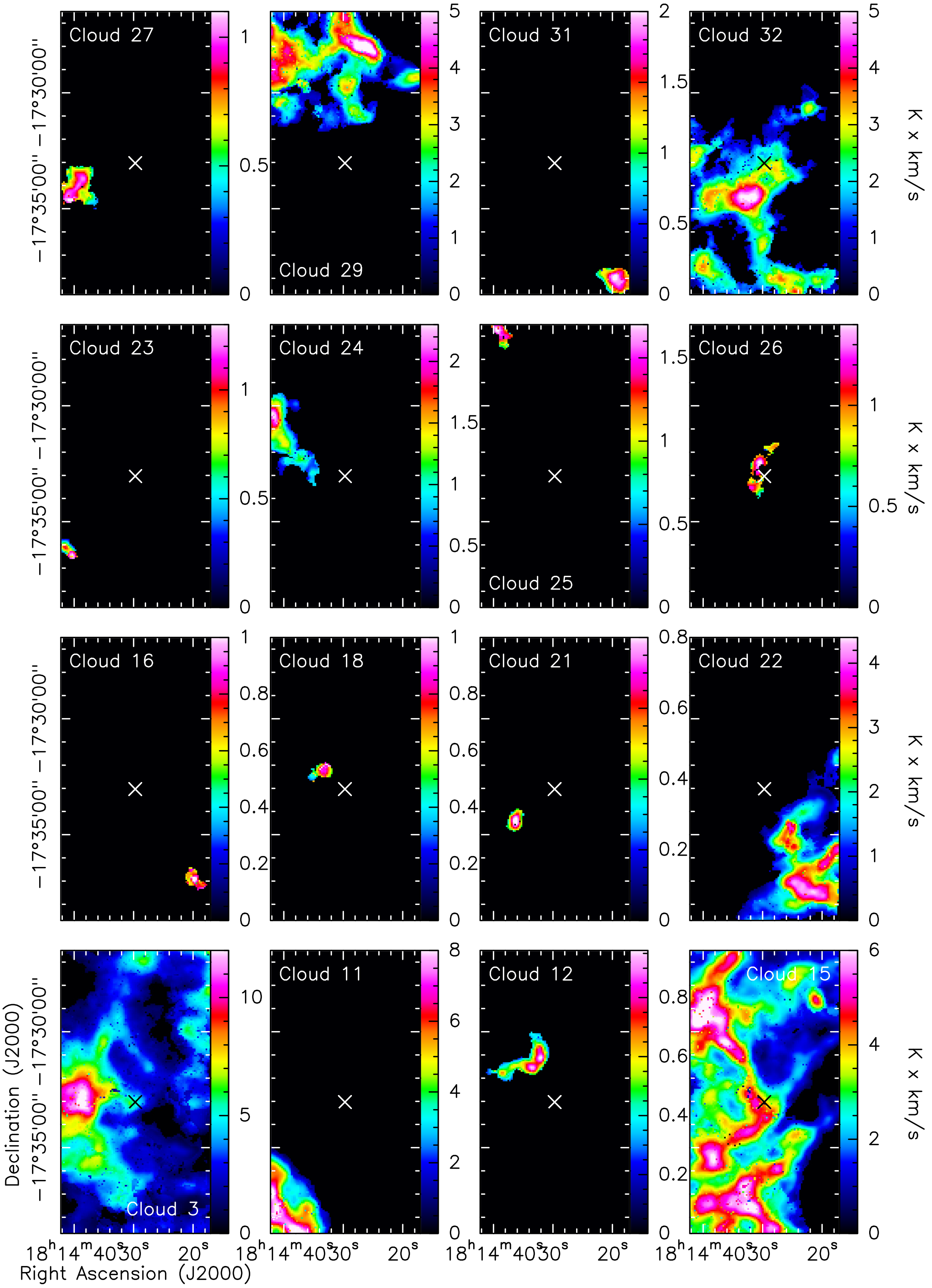

Figure 5.14 The model integrated intensity of $C^{18}O(1–0)$ emission in units of $K\times kms^{-1}$ of all 16 of the extracted velocity-distinct structures. The cross denotes the centre of the image. Cloud 15 clearly shows the typical shape of the SDC13 filaments.

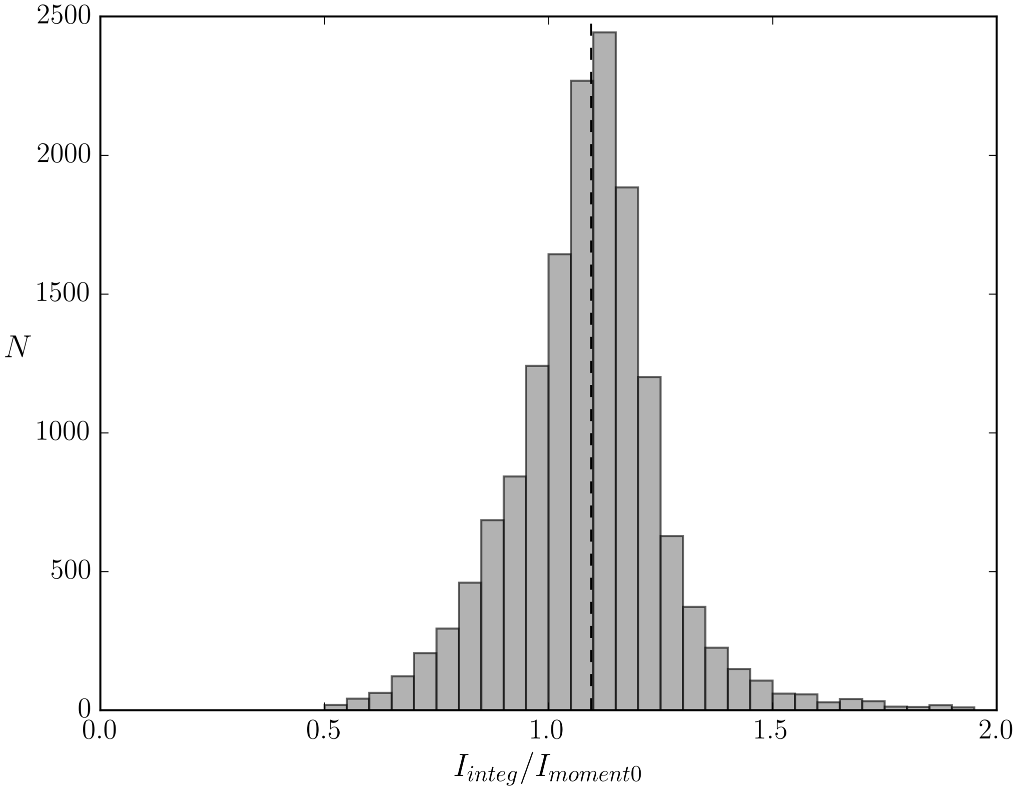

Figure 5.15 Histogram of the model fit integrated intensity of the extracted cloud 15 ,divided by the calculated moment zero of the entire central component of line emission in the original $C^{18}O(1\text{–}0)$ cube. Bins are 0.05 in size. The median value of 1.1 is marked by the vertical dashed line.

greatly limiting our ability to quantify its impact on the system. Some signs of its impact have already been noticed from the PV slices along the North-East and South-East filaments, and across the bottom half of the North-East filament.

Cloud 24 extracted using the friends-of-friends algorithm is an interesting cloud to consider in conjunction with the HII region. Looking at its integrated intensity, it falls exactly coincident with the position of the HII region, shown in Figure 5.16. This poses the question, is this a mere coincidence, or are the two objects linked? The spine of cloud 24 was identified by calculating the 2^{nd} derivative matrix for each pixel of the integrated intensity map i.e. the Hessian matrix, (e.g. Schisano et al. 2014, as described in Section 4.2.2 of Chapter 4). A PV slice was then constructed along this spine (shown in Figure 5.17). First impressions reveal that the cloud is certainly not an outflow emanating from the central HII region source. The nature of an outflow results in gas being accelerated to high velocities, manifesting as high velocity wings in molecular line emission. In this case, no wings are seen at all, as the emission appears very coherent in Figure 5.17.

Two distinct velocity gradients are observed. The steepest gradient of $0.9\,\mathrm{kms^{-1}pc^{-1}}$ is observed along the first quarter of the cloud, whilst the shallowest gradient of $0.5\,\mathrm{kms^{-1}pc^{-1}}$ is observed along the remaining three-quarters of the cloud. This change in the kinematics of the cloud at approximately 1.3 pc along it is interesting, and is coincident with the ring in emission seen surrounding the HII region. It is likely that the two sources are then indeed linked, with the HII affecting the southern part of the cloud in its expansion, but not yet the North. However, we already concluded previously that the impact of the HII region was the most likely explanation for the strong radial velocity gradients across the North-East and South-East filaments in $\mathrm{NH_3}$ emission.

Cloud 24 ranges in velocity between 24–28 $\mathrm{kms^{-1}}$, therefore it must have a different kinematic distance to SDC13 whose systemic velocity is $37\mathrm{kms^{-1}}$. Depending on how this compares to the kinematic distance of SDC13 determines whether or not

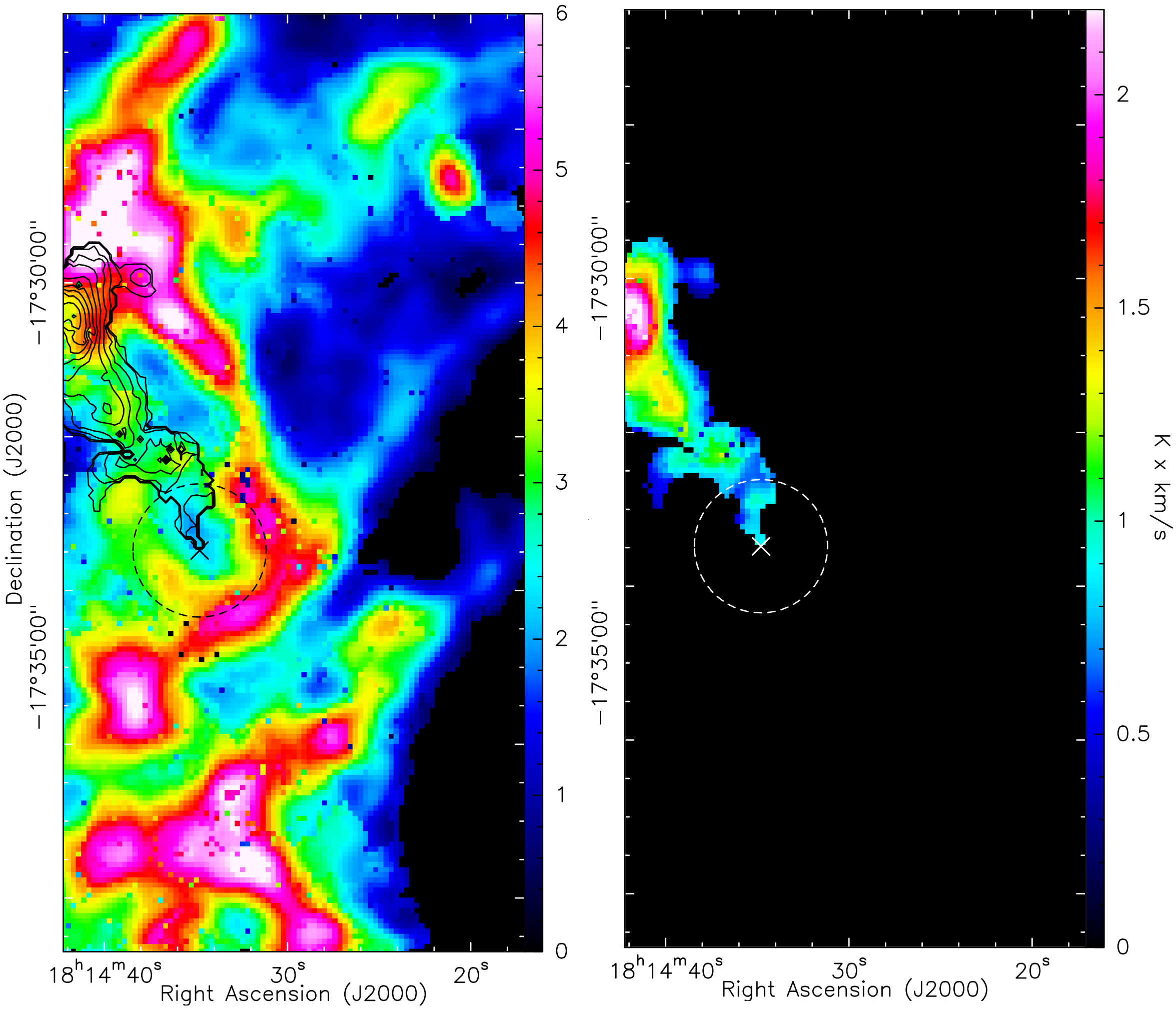

Figure 5.16 The integrated intensity of $C^{18}O(1–0)$ emission in units of K×km/s of the extracted cloud 15 (left) and cloud 24 (right). Overplotted on the left are the integrated intensity contours of cloud 24, in steps of 0.2 K×kms^{-1}, from 0.4 K×kms^{-1} to 2.4 K×kms^{-1}. A cross in both panels marks the position of the radio quiet HII region (G013.170-00.097 Anderson et al. 2014), with its catalogued radius of 26″ plotted by the dashed circle.

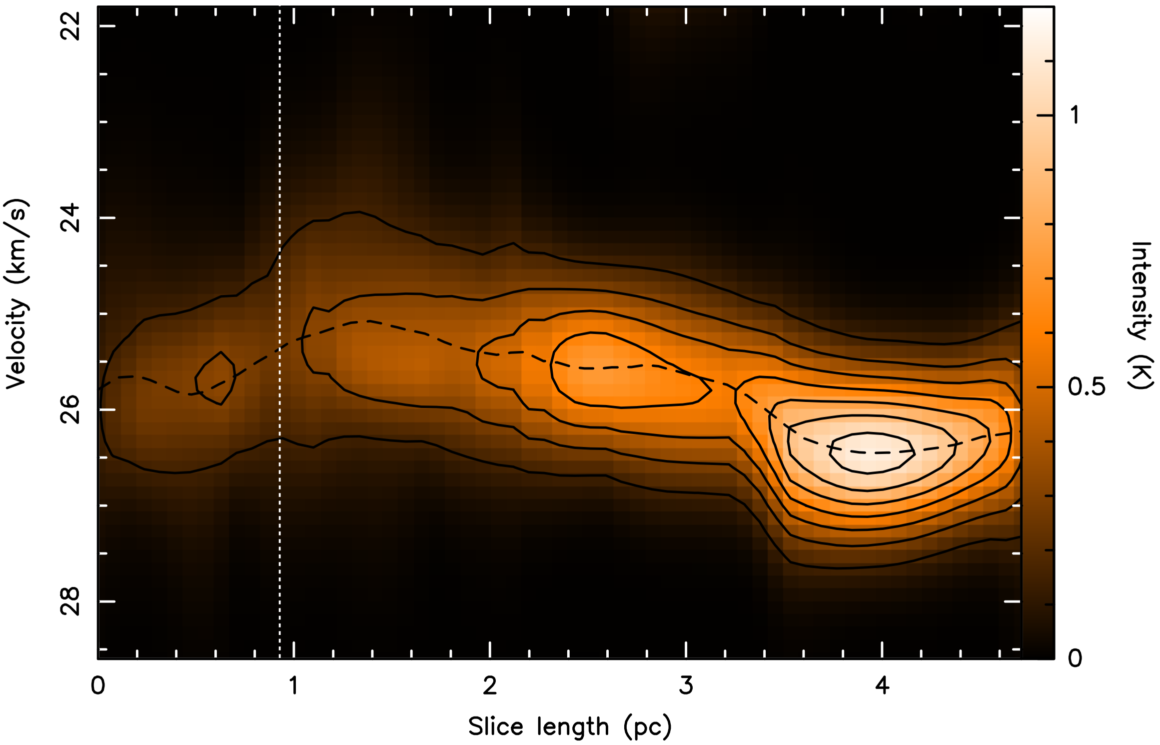

Figure 5.17 The position-velocity diagram along the identified spine through cloud 24 in the fitted $C^{18}O(1\text{-}0)$ cube. The data was spatially smoothed by a Gaussian of width 11.8″. The length of the spine is 4.71 pc, and the cloud covers a velocity range of $21.8 - 28.6$ km/s. Contours are placed in 0.15 K steps, from 0 to 1.2 K. The dashed black line plots the intensity weighted mean velocity. The vertical dashed white line plots the rough position of the HII region shell edge.

the HII region can affect both clouds simultaneously. Reid et al. (2016) use a Bayesian approach to calculate distances to galactic sources from their coordinates and velocity. The first distance estimate is done with respect to the spiral arms of the galaxy. The second is the kinematic distance, calculated based on the observed value of the target velocity with respect to what one would expect due to Galactic rotation. Sources with known parallax are also included in the calculation, where the probability of the source lying in the same GMC as the target cloud is estimated from their separation and relative velocities. Finally, the latitude (b) of an object is used as a measure of distance independent of the spiral arms. All methods are combined to give an overall PDF. A prior probability called P_{far} is set defining how likely it is that the source lies in the far side or near side of the spiral arms. A $\mathrm{P}_{far} = 0.5$ is set when such information is not available, and gives equal weight to both cases. Given the context of the source being infrared dark, and given its environment, it is a fair assumption that the cloud lies at the near distance, however I keep $\mathrm{P}_{far} = 0.5$. Taking the position of the peak intensity of cloud 24 at $l = 13.23°$, $b = -0.097°$ and $\mathrm{V} = 26.5\mathrm{kms}^{-1}$, the resulting probability density function of the distance is shown in Figure 5.18). The far distance is calculated to be $13.35 \pm 0.26\,\mathrm{kpc}$ (with a probability of 0.47), whilst the near distance (the most sensible given the context) is $2.88 \pm 0.29\,\mathrm{kpc}$ (with a probability of 0.4). The kinematic distance to SDC13 is $3.6 \pm 0.4\,\mathrm{kpc}$, therefore the near distance of cloud 24 is just compatible with it being a neighbour of SDC13. Given this corroboration, and given there is no kinematic information available for the HII region in the WISE catalogue, we speculate that the HII is indeed affecting the kinematics of both clouds simultaneously.

5.2.3 CENTROID VELOCITY STRUCTURES

One product of the fitting procedure is the best fit centroid velocity of each of the pixels of the map at each of the channels. This allows one to keep all of

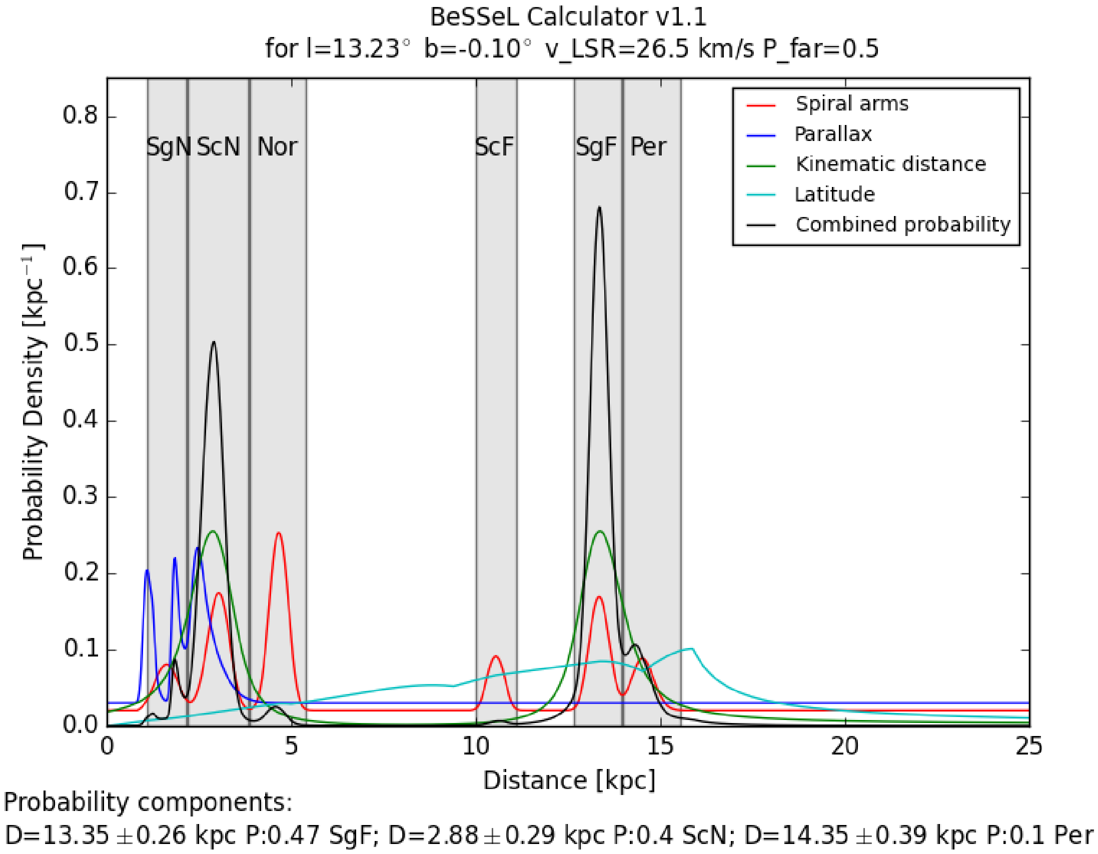

Figure 5.18 The kinematic distance to cloud 24, calculated to its coordinate of peak intensity ($l = 13.23°, b = -0.10°$), and a velocity of 26.5 $\mathrm{km s^{-1}}$ (Reid et al. 2016). The near distance of 2.88 ± 0.29 kpc is most plausible given the environment and context. The red line marks the positions of the spiral arms, green is the kinematic distance, blue is based off the distance to nearby parallax source on the sky, whilst cyan is based off the latitude (b) of the target.

the centroid velocity information that one loses when simply taking the intensity-weighted moment map. We constructed a cube where voxels with a signal-to-noise above the noise level were filled with the value of their own centroid velocity. This means that in any given channel, the only structures that are shown are those that are connected in velocity, effectively grouping the centroid velocities since the centroid velocity of a voxel will not be similar (if not the same) as the velocity of its channel. Viewing the data in such a simplified way reveals interesting features that one is not able to identify by eye when the cube is more information rich, for example when also displaying the intensity of emission. The channel map of a portion of the cube between velocities of 39.2–36.9 $\mathrm{kms^{-1}}$ is shown in Figure 5.19. At the top of the map, a connected velocity structure can be seen expanding outwards towards the centre of the map.

When comparing the location of these velocity structures to the integrated intensity (Figure 5.4), it becomes clear that they originate from the less bright, more diffuse gas to the North of the SDC13 cloud. Generally, diffuse gas can be said to be more impacted by turbulent motions than dense gas. Given this, perhaps these velocity "shells" are representative of the turbulence of the gas itself. One way to test this speculation would be conduct this analysis on synthetic images or simulations with a known turbulent field. Clark et al. (in prep) conducted magnetohydrodynamical (MHD) ^{13}CO(1–0) simulations using the AREPO moving-mesh code (Springel 2010). They collide two atomic clouds head-on with masses of $10^4 \mathrm{M_\odot}$, and radii of 19 pc. They are injected with a solenoidal turbulent velocity field of velocity dispersion 1 $\mathrm{kms^{-1}}$, and have relative velocities of 3.75 $\mathrm{kms^{-1}}$ to each other in the collision. The collision occurs along the magnetic field lines of strength 3μG. A plot of the mean column density along the line-of-sight is shown in Figure 5.20.

We use this simulation to make an initial investigation to see if such expanding velocity "shells" are seen in the turbulent simulation. The simulated position-position-velocity cube was spectrally and spatially smoothed to the resolution of the

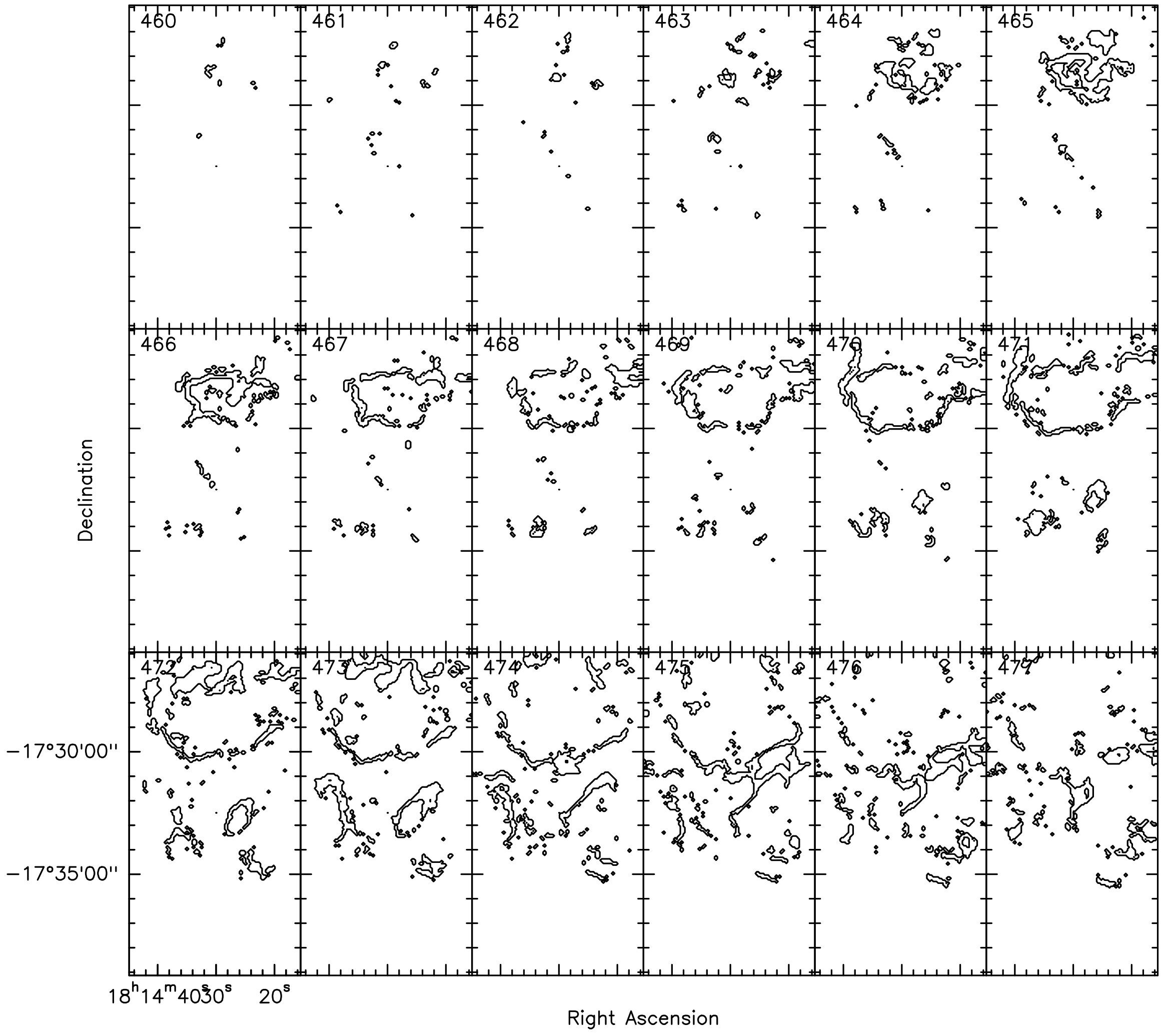

Figure 5.19 A channel map of the identified velocity structures, between the velocities of 39.2–36.9 kms^{-1} (with a difference of -0.13kms^{-1} between each panel) extracted from the line fitting of the C^{18}O(1–0) emission. Data below a declination of -17°34′00″ were masked for clarity given there were no organised structures.

IRAM 30 m data. In conducting the same line fitting, and centroid velocity analysis, first indications seem to suggest that some similar structures may indeed exist (see Figure 5.21). It is important to note that this is a first-look investigation. There are many factors yet to investigate, and this simulation has not been optimized for such a system as SDC13. The type of seeded turbulence may not be applicable for example, and this simulation includes a very high velocity collision, with a combined collision velocity of 7.5 kms^{-1}. Given this is a single snap-shot, investigation of other times during the collision is also needed. Therefore, whether or not these velocity "shells" are characteristic of the turbulence remains to be seen, however, this is a promising avenue of future work to pursue.

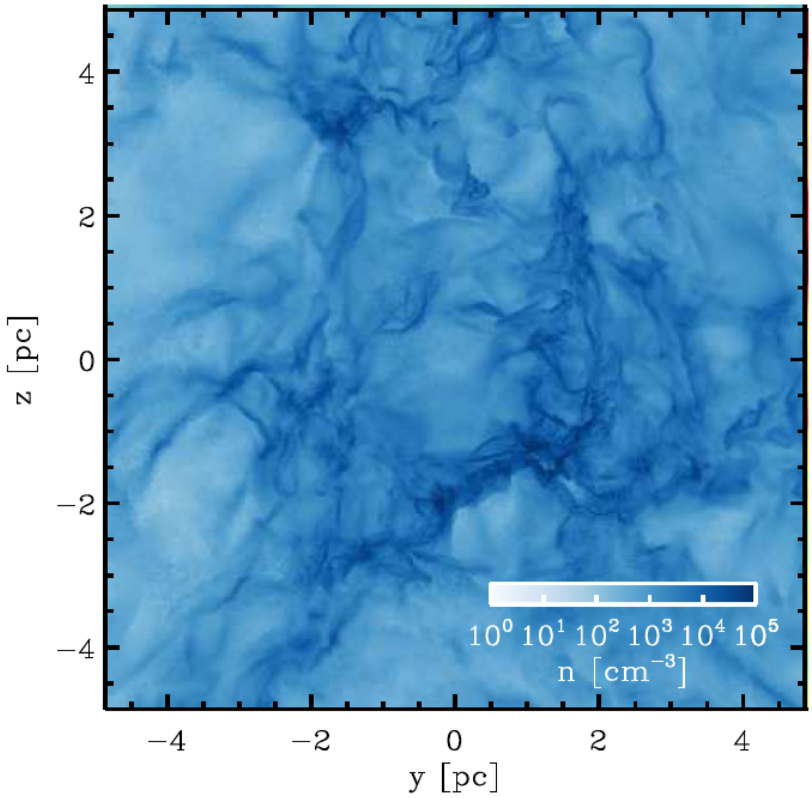

Figure 5.20 The mean density along the line-of-sight for the ^{13}CO(1–0) cloud-cloud collision simulation, weighted by mass (Clark et al. in preparation).

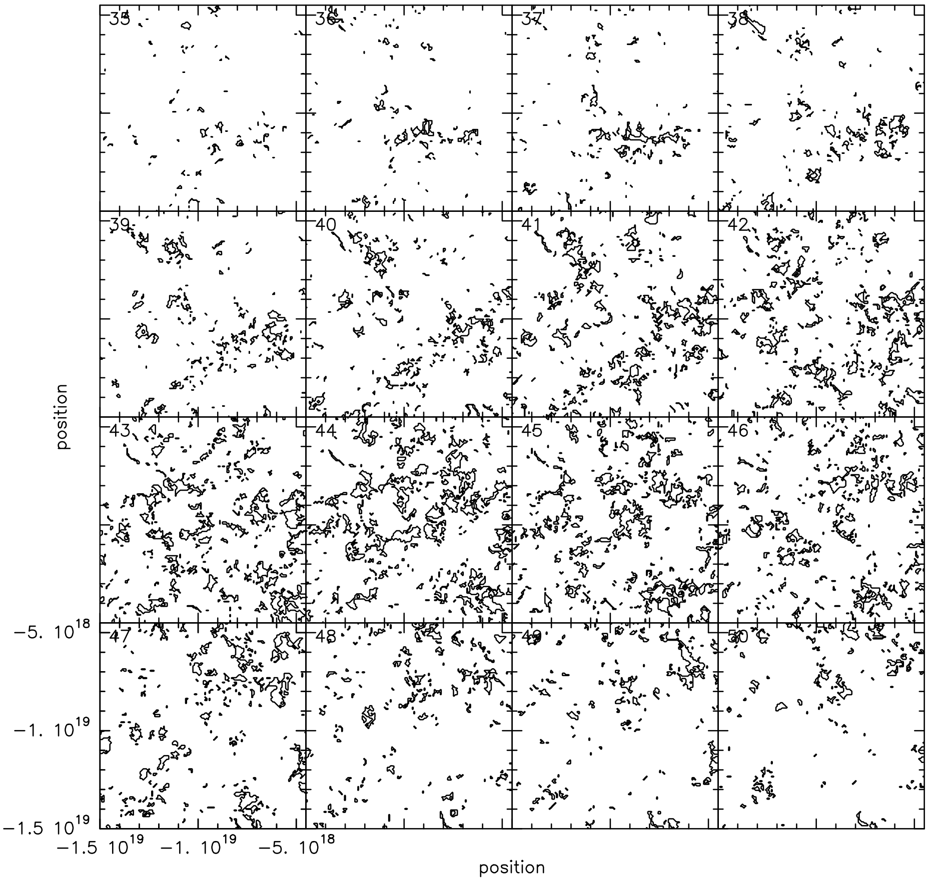

Figure 5.21 A preliminary channel map of the centroid velocity analysis conducted on the ^{13}CO(1–0) MHD simulations of Clark et al. (in preparation). Structures are shown across a range of ~ 2.1kms^{-1} in velocity. Structures only containing a single pixel were masked.

5.3 Summary and conclusions

I have conducted an initial analysis of $C^{18}O(1–0)$ and $^{13}CO(1–0)$ molecular line emission in SDC13, with the goal of understanding the formation of its hub-filaments. Fibres in particular have been suggested to represent a formation mechanism of filaments dominated by turbulence. After inspecting position-velocity slices along the filaments, velocity-coherent sub-filaments are not identified in the filaments. The spectral resolution of $0.13\,\mathrm{kms}^{-1}$ should indeed be sufficient for fibre detection were they present in the system. Works such as Tafalla & Hacar (2015) and Smith et al. (2016) suggest different fibre formation mechanisms, but turbulence is the essential first step in both scenarios. As concluded from the interferometric observations of NH_3 presented in Chapter 4, gravity due to the morphology of the hub itself is the dominant energy term in the SDC13 system, both fragmenting filaments and pulling gas towards the hub centre. In conjunction with this, it is suggested in this scenario that the formation of fibres in such a hub-filament system may be suppressed, hence their absence.

Conducting a moment analysis of the $C^{18}O(1–0)$ emission, the kinematics appear consistent with those of the denser NH_3 gas in Chapter 4, with the large scale morphology of the centroid line-of-sight prevailing. The velocity width of $C^{18}O(1–0)$ appears to narrow towards the centres of the SDC13 filaments themselves, again consistent with the conclusion that they are due to turbulence dissipation in post-shock structures. In contrast to the NH_3 data however, the velocity width narrows towards the centre of the hub instead of broadening. As mentioned in Chapter 4 when comparing the interferometric JVLA data to that of the GBT, it is possible that the dense gas kinematics does not prevail in the large scale, diffuse gas.

Fitting each of the individual velocity components of the $C^{18}O(1–0)$ emission recovers more emission than the moment analysis. Extracting the structures connected in velocity reveals the presence of concentric “shells” in the more diffuse cloud to the North of the SDC13 system. It is suggested that these may be characteristics of the turbulence of the gas. As an initial investigation, we performed the same line fitting analysis on an MHD turbulent cloud-cloud collision simulation by Clark et al. (in preparation). Even though the simulation is not tuned to the properties of SDC13, some similar structures may be present in the data. This is very much a work-in-progress, and will be at the centre of future work.

CHAPTER 6

SUMMARY OF THIS THESIS

In this chapter, I summarise the main conclusions of this work, and present avenues of future work that follow onwards from the work conducted in this thesis.

6.1 CONCLUSIONS

In this thesis, I have presented a detailed observational study of the SDC13 infrared dark cloud. Combining data from the Jansky Very Large Array and the Green Bank Telescope, I was able to probe the dense gas traced by $NH_3(1,1)$ and $NH_3(2,2)$ molecular line emission down to 0.07 pc spatial scales, suitable for studying the link between cores and filaments. Using $C^{18}O(1–0)$ and $^{13}CO(1–0)$ molecular line emission from the IRAM 30 m telescope, I probe the less dense gas of SDC13 and its surrounding environment down to 0.4 pc spatial scales, with the goal of constraining the formation of the filaments.

The dense NH_3 gas reveals that the filaments (with average line mass of $M_{line} \sim 264\,M_{\odot}pc^{-1}$) are all supercritical in nature, containing tens of gravitationally bound cores regularly spaced by 0.37 ± 0.16 pc along them. This is suggestive of gravitational instabilities along the filaments being the primary cause of their fragmentation. Following the hyperfine structure fitting of the emission, the filaments appear to be consistent with post-shock structures given their sub/transonic velocity dispersion. Furthermore, the velocity dispersion was found to be centrally peaked in two-thirds of the starless core population of the cloud in comparison with the surrounding filament. This is contrary to the decrease in velocity dispersion observed towards low-mass prestellar cores (termed the "transition to coherence") observed towards nearby prestellar cores and filaments (e.g. Pineda et al. 2010; Hacar et al. 2016, see Section 1.6.3). This opposite behaviour seen in SDC13 is suggested to be a direct result of the fragmentation process, converting gravitational potential energy into kinetic energy in the process. Using energy conservation arguments, I estimate that the gravitational to kinetic energy conversion efficiency in these cores is 40%, larger than theoretical values published in the literature. The velocity gradient is also seen to peak at the position of 63% of the cores, consistent with what one would expect during the early stages of filament fragmentation. Using a gas mass calculated from the derived H_2 column density from NH_3, the amplitude of the acceleration in SDC13 was computed. Due to symmetry effects, the acceleration at the filament spines are at a minimum. Interestingly, the largest acceleration gradients (which themselves represent accumulation points in matter) are observed at the hub-filament junctions, coinciding with the peak in velocity width towards the hub centre and the location of the most massive cores in the cloud. It is therefore suggested that gravity as a direct result of the hub-morphology itself shapes the evolution of the hub, fragmenting filaments and pulling gas towards the centre of the gravitational well. As a result, energy is converted into kinetic energy in both local (cores) and global (hub centre) potential well minima, generating more massive cores at the hub centre.

The NH_3 data also revealed a strong velocity gradient in the radial direction to the main axis of the North-East and South-East filaments. After investigation, gravity, shear and rotation were all excluded as possible explanations. Using the WISE catalog of HII region sources (Anderson et al. 2014), it was found that a radio-quiet HII region coincides with an infra-red bright patch within 1 pc proximity to

SDC13 on the sky. This was further investigated using the larger scale ^{13}CO(1–0) and C^{18}O(1–0) data, where a cavity in emission was found corresponding to the location of the HII region, consistent with the clearing of material, supporting the theory that the HII region may indeed be affecting the kinematics of SDC13.

Velocity-coherent sub-filaments called fibres in recent years have been suggested to represent a particular turbulence dominated mechanism of filament formation, either from the sweeping up of fibres that themselves formed due to turbulent fragmentation (Smith et al. 2016), or by turbulence dissipation within a larger scale filament that formed following shocks (Tafalla & Hacar 2015). After inspecting position-velocity slices of the C^{18}O(1–0) and ^{13}CO(1–0) emission along the filaments to investigate if such formation mechanisms may be true for SDC13, it is found that fibres to do not constitute the SDC13 filaments. In conjunction with the conclusions drawn from the NH$_3$ data, it is suggested that the dominance of gravity in the system as a direct result of the hub-morphology itself suppresses the formation of fibres, which in both observations and simulations are thought to be products of turbulence (Tafalla & Hacar 2015; Smith et al. 2016). There is much debate in the community on what exactly fibres represent, therefore it is also possible that the presence of fibres in Taurus (Tafalla & Hacar 2015) merely represents a unique scenario, and that fibres are not in fact common constituents of the ISM. Following the fitting of multiple velocity components of C^{18}O(1–0), the velocity dispersion is seen to decrease at the filament spines, consistent with them being post-shock structures. Coherent velocity structures resembling shells corresponding to a more diffuse cloud to the North of SDC13 are found to evolve with velocity. To investigate whether turbulence could produce such shells, I conducted the same analysis on an MHD, cloud-cloud collision simulation, post-processed using RADMC-3D to create ^{13}CO(1–0) synthetic observations (Clark et al. in prep). Initial analysis seems to suggest such shells may be present in the simulation, but this is certainly a work-in-progress at this stage. Whether such structures are indicative of the turbulent beginnings of SDC13 will be investigated in the near future.

The core accretion model of star formation is said to be a static process, with starless cores accreting slowly with time from a closed reservoir of material characterised in part by the ambipolar diffusion timescale. With competitive accretion said to be a fast process on the other hand, forming stars within a few free-fall times, Krumholz et al. (2005) show that an initially sub-virial state is essential to the theory in allowing for formation timescales within $\leq 1\,\mathrm{Myr}$. With the free-fall collapse time of SDC13 being 0.3 Myrs, the crossing time on the scale of filaments being 0.42 Myrs, and the time taken to assemble a critical filament due to accretion being 0.68 Myrs, this all points towards SDC13 being a dynamic rather than a static system. With the virial analysis of SDC13 in Section 4.3.5, it is shown that the large-scale parent cloud is indeed highly sub-virial, with cores also behaving sub-virially on the whole, whilst approaching unity. Combined, this points towards the dynamic competitive accretion theory of star formation. With starless cores being a direct prediction of the core accretion scenario, the starless state of the SDC13 cores will be investigated in a future ALMA study (as detailed in Section 6.2.1).

6.2 FUTURE WORK

As a result of the work presented in this thesis, I see three predominant topics of future work to be conducted in the near future to further our understanding of the SDC13 infrared dark cloud.

6.2.1 ARE SDC13'S STARLESS CORES REALLY STARLESS? AN ALMA STUDY

One of the key results of my PhD thesis is that the dense gas velocity dispersion evolves from transonic in the larger filament structure to being broadest and supersonic at the positions of two-thirds of apparently starless cores. This increase of turbulent support brings the average core virial ratio to ~ 1, making them more stable against further fragmentation. The masses of the cores range from $3.4\,\mathrm{M}_{\odot}$ to $162.8\,\mathrm{M}_{\odot}$ within a radius of ≤ 0.1 (see Table 4.1), making them ideal super-Jeans core candidates.

This behaviour observed in SDC13 is opposite to that seen in nearby, low-mass star formation regions where the velocity width narrows at the position of prestellar cores, interpreted as the dissipation of turbulence at that spatial scale (see Figure 1.8 Fuller & Myers 1992; Goodman et al. 1998; Caselli et al. 2002; Pineda et al. 2010, 2015). Transonic filaments and cores are expected to form in a turbulent ISM where supersonic shocks generate stagnation regions where turbulent energy is dissipated. SDC13 is a very dynamic region with a complex velocity structure. With mostly transonic filaments (as discussed in Section 4.3.4), the indication is that the filaments represent such post-shock regions. In this context, the velocity width broadening at the positions of the starless cores would then be purely generated by gravity, representing the accumulation of material from the surrounding filament into cores, converting gravitational potential energy into kinetic energy in this very dynamic process. This was discussed in Section 4.3.5, where an energy conversion efficiency of $\sim 40\%$ is calculated for the starless core population of SDC13. This value being much larger than theoretical published values of $\sim 5-10\%$ (e.g. Klessen & Hennebelle 2010; Heitsch 2013; Clarke et al. 2017) is suggestive of the important role that gravity-driven turbulence plays.

However, another possible explanation for this local broadening of velocity dispersion towards apparently starless cores could be the presence of low-mass protostellar sources deeply embedded in their centres. Even though we do not see any mid-infrared sources toward them, such protostars could be embedded enough to remain undetectable with both *Spitzer* and *Herschel*. These protostars could have associated outflows which disrupt the surrounding gas, contributing to a local increase in the velocity dispersion (Duarte-Cabral et al. 2012). On the other hand, one

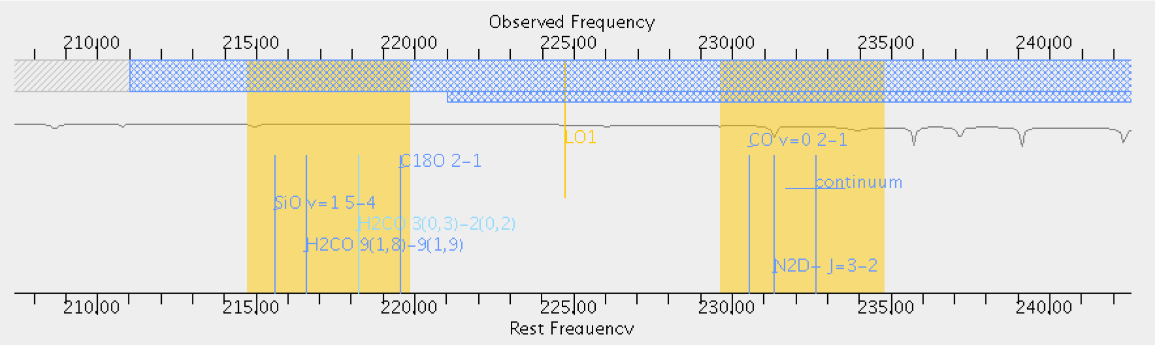

Figure 6.1 The spectral set-up of my Grade A ALMA Cycle 5 proposal. The bandwidth of the windows are shown in yellow whilst each of the molecular lines within the bandwidths are marked by vertical lines. The blue boxes denote the frequency band, whilst the grey line plots the atmospheric transmission.

could also imagine that the broadened velocity width could be due to unresolved core systems where the cores have already fragmented into smaller objects. In this case, the cores would no longer qualify as super-Jeans core candidates.

My ALMA Cycle 4 proposal (2016.1.01580.S) to settle this issue was awarded 8.9 hours of Band 6 time and ranked grade B, and was re-accepted in Cycle 5 as Grade A (2017.1.00351.S). The spectral set-up is shown in Figure 6.1, whilst the pointings are shown in Figure 6.2. The proposal had three primary immediate objectives. Firstly, ^{12}CO(2–1) and SiO(5–4) molecular emission has been shown to be a far more sensitive tracer of protostellar activity than mid-infrared emission (Hatchell et al. 2007) as they are shocked free from dust grains in the vicinity of the protostar. A sensitive search for outflows in the SDC13 cores will definitely confirm or rule out the presence of embedded protostars, and therefore the protostellar feedback origin of the increased velocity dispersion.

Secondly, the dense gas kinematics of the cores will be traced by C^{18}O(2–1) and N$_2$D$^+$(3–2) emission. If the origin of the increased velocity dispersion is due to the inflow of material from the filaments, we expect to resolve the region of increased velocity dispersion down to 1″. In the absence of outflows, this will be clear evidence that the large-scale kinematics of star-forming clouds directly impact the type of cores and stars that they are able to form.

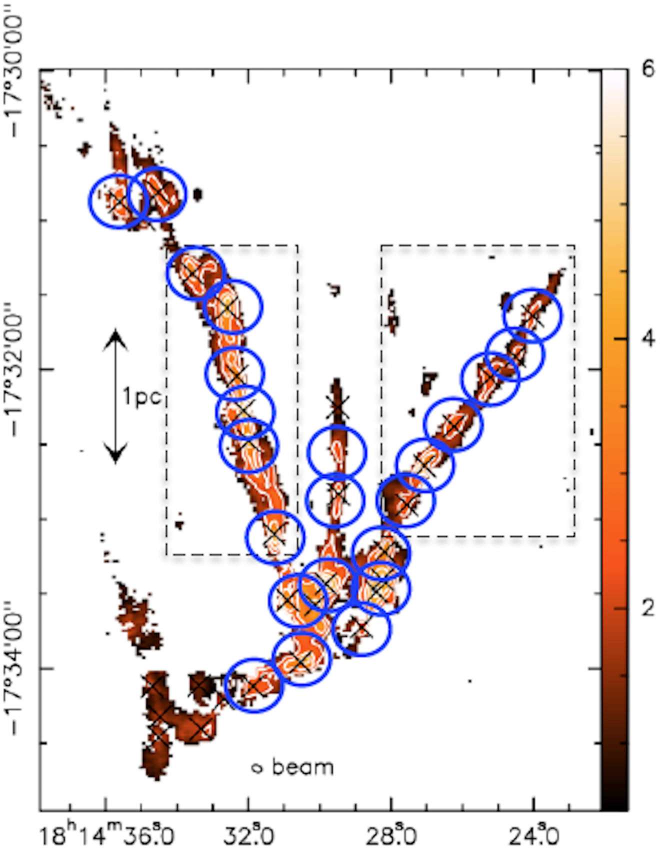

Figure 6.2 Each blue circle marks the position of a pointing in the ALMA Cycle 5 proposal. Each cross denotes the position of a core identified at the time of writing the proposal. The points are overplotted on the H_2 column density map derived from the JVLA–only data.

Thirdly, the cores will be resolved using 1.2 mm dust continuum emission. If the super-Jeans core candidates are sub-fragmented into clusters of Jeans mass sources, then deep dust continuum observations of the sources at $1''$ resolution will allow us to detect them. Combined with the gas kinematics information, we will be able to assess if the increased velocity dispersion observed in our JVLA data is the result of the dynamical interaction of the cores (via the measure of the core-core velocity dispersion).

The required configuration for the project (C40–2) is currently scheduled between May 5th and June 5th 2018, therefore I do not expect to receive the data until Autumn next year. In Cycle 4, one out of seven scheduling blocks were executed, with an average system temperature of 122.29 K and $\sigma = 12.43$ K. The minimum and maximum angular resolution achieved were $0.933''$ and $1.140''$, across a baseline range of 15–279 m.

6.2.2 DEPLETION OF NH_3 TOWARDS THE MM1 PROTOSTELLAR CORE

Nitrogen-bearing molecules are known to be excellent tracers of infrared dark clouds (with $n > 10^3\,\mathrm{cm^{-3}}$) as they do not get trapped onto dust grains unless the density exceeds $n \sim 10^6\,\mathrm{cm^{-3}}$. However, as discussed in Section 4.1.4 of Chapter 4, the abundance of NH_3 column density towards the MM1 core (strongly detected by 1.2 mm dust continuum emission Peretto et al. 2014) is lower than expected. The protostellar nature of MM1 points towards there being a destructive process of NH_3 affecting the abundance rather than depletion. This was crudely investigated in Section 4.1.4 by plotting the H_2 column density derived from 1.2 mm dust continuum emission from the MAMBO bolometer array on the IRAM 30m telescope (Peretto et al. 2014) against the NH_3 column density. However, to understand the nature of this depletion correctly, one needs to conduct chemical modelling. This was beyond the scope of this work, however, is a keen interest of mine going forward.

The abundance ratios of different molecules (such as Sulfur-bearing molecules for example, van der Tak et al. 2003; Viti et al. 2004; Li et al. 2015) can be used to estimate the age of a star-forming region, and are popularly termed *'chemical clocks'* as a result. Furthermore, the evolutionary state of a star-forming region can be evaluated if the molecules used have differential abundances that vary with time. Nitrogen-bearing molecules stay in the gas phase of the ISM for longer than the CO molecule (Bergin & Langer 1997). As the CO molecule disappears from the gas phase by freezing onto dust grains, deuteration of nitrogen-bearing molecules is able to occur, enhancing their abundance, happening at different rates for different species. For this reason, the abundance rates of nitrogen-bearing molecules are best for understanding evolutionary states of a star-forming region.

Studies have been conducted into the abundance ratios of nitrogen-bearing molecules in low mass star forming regions (e.g. Caselli et al. 2002; Hotzel et al. 2004; Friesen et al. 2010; Harju et al. 2017) and to a somewhat lesser extent in intermediate to high mass star forming regions (e.g. Palau et al. 2007; Busquet et al. 2011). The NH_3/N_2H^+ abundance ratio appears to differ greatly depending on the source under examination. Hotzel et al. (2004) observe two dense cores, both containing a YSO. They find an abundance ratio of 60–90 around the YSO region, which increases quite dramatically to 140–190 in the quiescent, starless region. This suggests an enhancement of the NH_3 abundance around the central portions of starless cores, a result also observed by Tafalla et al. (2002). For intermediate to high mass, the same trend is observed, showing that the two types of object are chemically distinguishable.

Such works lead to the question, how does the NH_3/N_2H^+ abundance behave in the MM1 protostellar and MM2 starless cores of SDC13. Peretto et al. (2014) already published work on N_2H^+(1–0) emission in SDC13 from the IRAM 30 m telescope. However, the data is not suitable for the above described analysis, as the data were taken as single pointings. Therefore, I plan to write a proposal to the Plateau de Bureau Interferometer (PdBI) asking for higher angular resolution N_2H^+ data to facilitate such a study. On the other hand, my ALMA Cycle 5 project described in Section 6.2.1 will observe N_2D^+(3–2) emission (the deuterated version of the N_2H^+ molecule) at the positions of the cores, therefore a similar study may be possible should the PdBI proposal not be successful.

6.2.3 THE MAGNETIC FIELD IN SDC13

The role played by magnetic fields in filament formation is a fevered topic of current star formation research. This can be studied through polarization studies, as dust grains are known to align their minor axis parallel to the magnetic field

(Lazarian & Hoang 2007). Recent observations of magnetic field alignment in filament structures have revealed alignment and anti-alignment with striations and filaments respectively (e.g. Palmeirim et al. 2013; Cox et al. 2016). These studies lead one to ask if striations are the funnels that accrete material onto filaments. Though such studies were conducted on *single* filaments, studies of the magnetic field in *hub-filament systems* however appears to be a gap in the market. As shown by Peretto et al. (2013), Peretto et al. (2014) and in this work, the converging nature of hub-filament systems is suggestive of the role played by gravity in shaping them. The global collapse of such clouds provides strong flows of gas towards the centre, fuelling the formation of super-Jeans cores. In such hub-filament systems, with distinct and organised velocity fields, it is important to study the B field morphologies hand-in-hand with the gas velocity fields. Do magnetic fields follow the flow of the gas velocity field, or is the converse the case, where the gas follows the magnetic field instead? Observations of SDC13 could shed light on this, given it contains both longitudinal and transverse velocity gradients with respect to the filament long axes. In singular filaments, works such as Seifried & Walch (2015) suggest that the B field morphology appears perpendicular to the main axis having been locked this way from the large flows of mass accretion at the formation of the filament. In hub-filament systems however, one may expect that the major influence of gravity in the shaping of the hub prevails and drags the B field with it along with the flow of gas.

I have begun a collaborative role on two proposals to the JCMT (*James Clerk Maxwell Telescope*), that proposed to use the POL-2 instrument to look at the dust polarization in infrared dark clouds. The second proposal was specifically aimed at observing SDC13, given its interesting velocity structure. This was awarded time, only 8% of the requested time having been observed at this point. An early reduction of the POL-2 data was done by Prof. Gary Fuller at the telescope site during observing, and is shown in Figure 6.3. Very interesting features begin to reveal themselves, however, given only 8% of the data has been observed, we do not yet give any weight

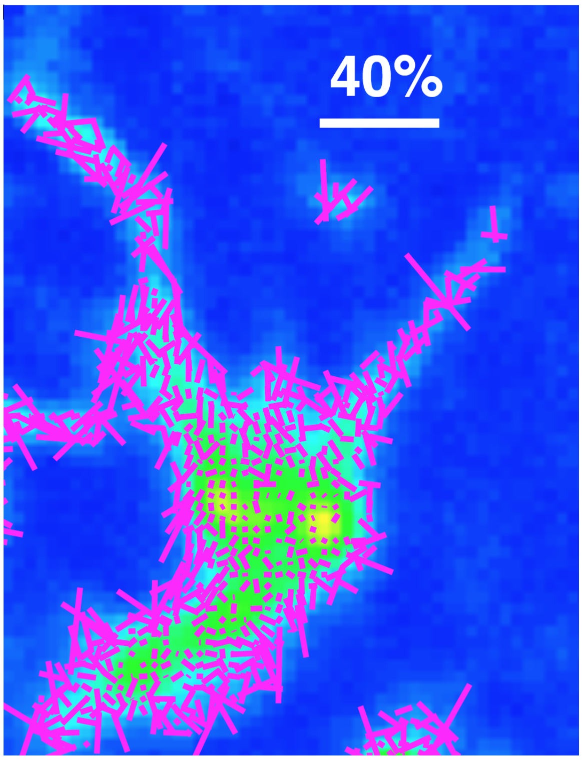

Figure 6.3 A preliminary polarization map of 3 hours on source time (8% of the full project) from pipeline reduction on-site (Koch et al. in preparation). Due to this preliminary nature, the polarization orientations and fractions are still uncertain, though is promising for high quality science once all data is observed.

to the polarization fraction of the plotted vectors. This map reveals it is promising that the final, fully observed data set will indeed detect SDC13 very well, allowing us to see if there are any differences in the magnetic field across the cloud, and if it follows the gas flows or not.

6.2.4 EXPANDING THE STUDY

The work presented in this thesis is a novel study of the SDC13 infrared dark cloud hub-filament system. One must expand this work to other clouds to see if the results hold in a wider range of infrared dark sources, or if such results are only inherent of hub-filament systems. Two such studies were devised for the last NRAO observing call for the JVLA and GBT in semester 2018B.

A neighbouring cloud to SDC13

The first proposal, (JVLA and GBT project codes: 18B-219, and 18B-220) focusses on a cloud to the North of SDC13 which appears to be an extension to SDC13. As discussed in Section 3.1.1, Peretto et al. (2014) find longitudinal velocity gradients along the filamentary arms of SDC13 as traced by N_2H^+(1–0) emission, indicating large scale longitudinal collapse of the system towards the gravitational potential well at the centre of the hub-filament system. Not only this, but they observe a secondary velocity gradient in the north of the North-East filament (shown in Figure 6.4) interpreted as a secondary collapse centre away from the hub centre. This secondary velocity gradient was also observed in both the ammonia kinematics (presented in Chapter 4) and the $C^{18}O$(1–0) emission (in Figure 6.5 and Chapter 5). With this in mind, when looking at the dust three-colour composite image (left panel of Figure 6.4), it is clear that this secondary collapse can be correlated to a neighbouring infrared dark cloud to the North of SDC13 (hereafter called SDC13-N). The suggested coupled nature of these two clouds makes the study of them both essential in the complete understanding of both their individual and mutual dynamics and evolution. This was the goal of this proposal, but also more fundamentally to see whether the results shown in SDC13 hold in the nearest infrared dark cloud possible to it in the Galaxy.

SDC13-N appears also very dark in the infrared, and appears to be *more pristine* and at an *earlier evolutionary stage* to SDC13 given its lack of infrared bright 70μm emission. The intensity of $C^{18}O$(1–0) emission at SDC13-N (Figure 6.5) also suggests that SDC13-N may be a more extreme version of SDC13, with a larger reservoir of mass. With this in mind, a direct, like-for-like comparative analysis between the more pristine SDC13-N and SDC13 would give insight into the global evolution of the entire region. The $C^{18}O$(1–0) kinematics (Figure 6.5) suggest velocity flows do prevail in SDC13-N, however given the optical thickness and likely depletion

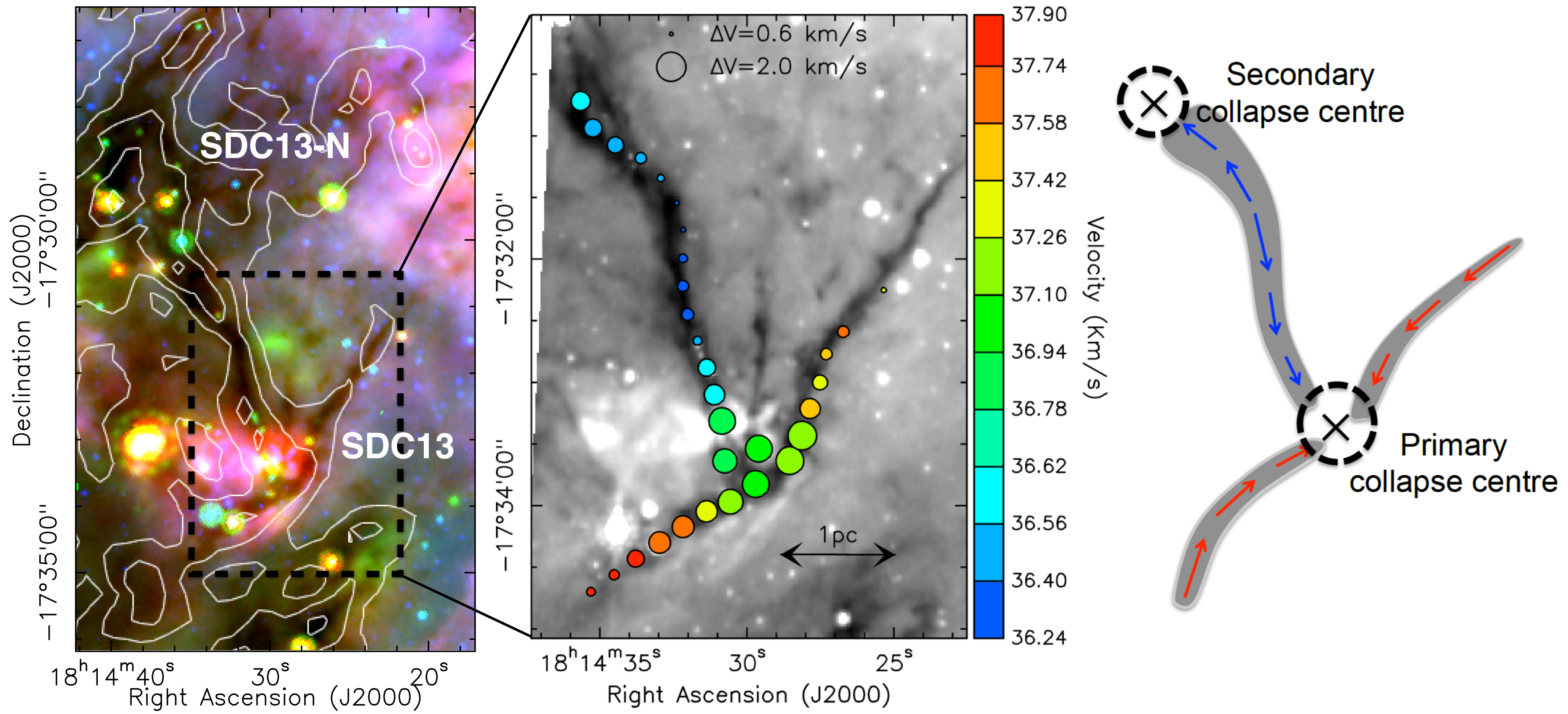

Figure 6.4 (left): Three colour composite image of the SDC13 and SDC13-N clouds (labelled), where R, G and B bands correspond to 70μm HIGAL, 24μm Spitzer MIPSGAL, and 8μm Spitzer GLIMPSE maps. Overlaid contours are of $C^{18}O(1\text{–}0)$ integrated emission from the IRAM 30 m telescope, in 1 K steps from 2.5 K to 8.5 K. (middle): Greyscale 8μm Spitzer GLIMPSE map, overplotted by $N_2H^+(1\text{–}0)$ pointings (Peretto et al. 2014) coloured by their velocity (following the colour bar to the right) and sized by the velocity width (following the scale on the top of the plot). Global collapse is observed (as depicted by the schematic on the left Peretto et al. 2014)), towards a primary and secondary collapse centre, suggested by global velocity gradients along the filaments corresponding to a broadening of the velocity width. SDC13-N connects to SDC13 at the secondary collapse centre.

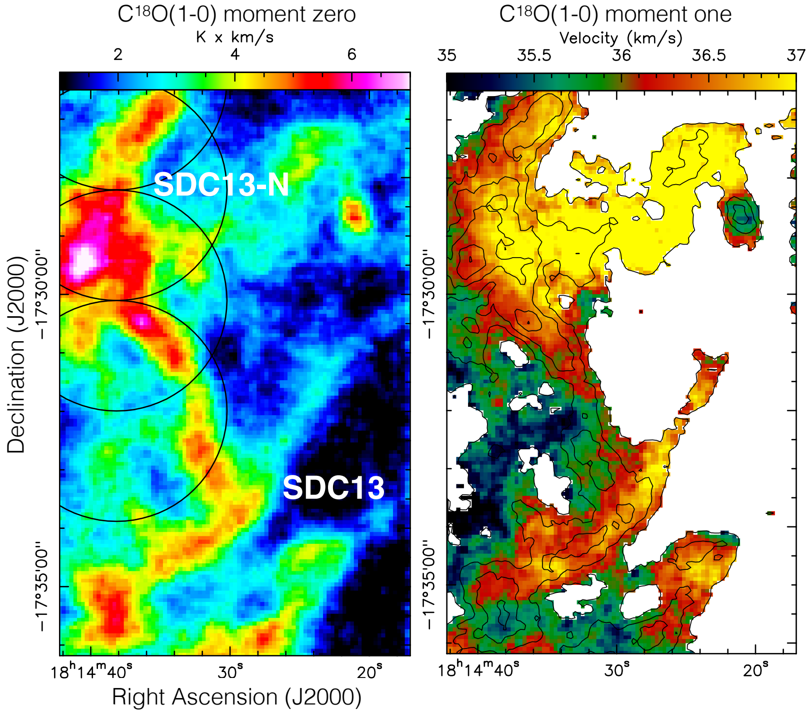

Figure 6.5 Moment zero integrated intensity map (left) of $C^{18}O(1–0)$ emission observed using the IRAM 30 m (Williams et al. in prep). Overplotted in black circles are the proposed four pointings, half-beam spaced mosaic of SDC13-N. Some very small overlap exists with the previous JVLA mosaic of SDC13 to ensure the resolving of the secondary collapse centre in the context of SDC13-N. Moment one velocity (right) of $C^{18}O(1–0)$ emission. A secondary velocity gradient is observed along the North-East filament of SDC13 towards SDC13-N.

is not reliable enough a tracer to study the kinematics in detail. As such, we proposed to observe SDC13-N using the JVLA to map the gas dynamics, and the core-scale fragmentation. We require ammonia to ensure that we compare a like-for-like gas density in SDC13 and SDC13-N. The three immediate objectives we will be able to test are:

1. Do we see a velocity gradient towards the centre of the SDC13-N hub, emanating from the secondary collapse centre in SDC13? Such a flow would confirm a complex gravitational interplay between the potential well minima of the two connected hubs. In fitting the hyperfine structure of NH_3, it will immediately be clear if this gas flow exists. Such a study is uniquely placed in revealing the interaction between the two neighbouring hub-filament systems.

2. Is there an increase of the dense gas velocity dispersion towards the hub centre of SDC13-N? As part of the dynamic gravity-dominated evolution of infrared dark hubs shown by our JVLA data on SDC13, the dense gas velocity width broadens at the hub centre as a direct result of the hub morphology. This will be tested from the hyperfine structure fitting of the NH_3 dense gas tracer.

3. Does HII region impact cause radial velocity gradients in SDC13-N? In our JVLA study of SDC13, the discounting of shear, rotation and gravity in causing the $3\,\mathrm{kms^{-1}pc^{-1}}$ gradient across the filaments led to the postulate that the nearby HII region was the most likely impact on the dense gas. If correct, then we should also see such an effect from the HII region that also neighbours SDC13-N, proving external effects can influence dense gas dynamics.

We proposed to observe perform a four half-beam spaced pointing mosaic to cover the full extent of SDC13-N using the C configuration, which provides enough angular resoltion ($\sim 1''$) to resolve the filamentary structure ($\sim 15''$ broad). We use the 1 GHz band, with one 8 MHz sub-band centred on the $NH_3(1,1)$ line, and one 4 MHz sub-band centred on the $NH_3(2,2)$ line. This is an improvement on the previous observations, given that the SDC13 spectral setup used to 4 MHz sub-bands centred on both NH_3(1,1) and NH_3(2,2), and as a result missed the final outer hyperfine satellite component of NH_3(1,1). In both sub-bands, a recirculation factor of 16 is used, with $n_{BIBP} = 2$ for the first sub-band, and $n_{BIBP} = 1$ for the second to achieve a channel width of 4 kHz ($\sim 0.05\,\mathrm{kms^{-1}}$) to be Hanning smoothed to $0.1\,\mathrm{kms^{-1}}$. To resolve SDC13-N to 5σ, and for direct comparison with the SDC13 data, we require an RMS noise of 3mJy/beam (~ 3.7 K) achieved by 80 mins on-source, equivalent to 40 mins per half-beam spaced pointing. This corresponds to 2.7 hours total on-source time, 5.3 hours including overheads. Zero-spacing was clearly required for the analysis of SDC13, therefore here we jointly proposed for the GBT observations too.

A sample of IRDCs

A study beyond SDC13 and its neighbours into a sample of a number of IRDCs is essential to further test if the revealed kinematics in SDC13 are also observed in other infrared dark clouds and hub-filament systems. An increase of the virial ratio from the larger scale cloud towards individual cores was observed in SDC13, corresponding to the broadening of the velocity width at two-thirds of starless core positions; a behaviour predicated in simulations as a result of the conversion of gravitational potential energy into kinetic energy during the global collapse of the cloud (e.g. Lee & Hennebelle 2016; Camacho et al. 2016). A sample of 27 IRDCs was chosen from the Peretto & Fuller (2009) catalog by Peretto et al. (2015)/Peretto et al. in prep to be observed in N_2H^+(1–0) and ^{13}CO(1–0) with the IRAM 30 m telescope. These 27 clouds lie within a kinematic distance range of 3–5 kpc and have a wide range of morphologies. Complimenting this 27″ resolution IRAM 30 m data with 46″ resolution from the GRS survey (Roman-Duval et al. 2010), the evolution of the virial ratio was studied from tens of parsec scales, down to sub-parsec scales by extracting structures using a dendrogram analysis (Peretto et al. in prep). As shown in Figure 6.6, virial ratios (α_{vir}) of typically 5 are observed at large structure radii indicating gravitationally unbound clouds where turbulent pressure dominates over gravity. This reduces smoothly with radius down to $\alpha_{vir} = 2$ where the gas becomes gravitationally bound. This further reduces until α_{vir} reaches a minimum at parsec scales, where α_{vir} proceeds to either flatten off or most notably increase at sub-parsec scales. This evolution of the virial ratio was interpreted as a transition from a turbulence dominated evolution on large scales to a gravity dominated evolution on smaller scales - a result that corroborates with our sub-parsec SDC13 data. However, the scales of individual cores is lacking from the Peretto et al in prep analysis, and is the motivation behind this JVLA proposal.

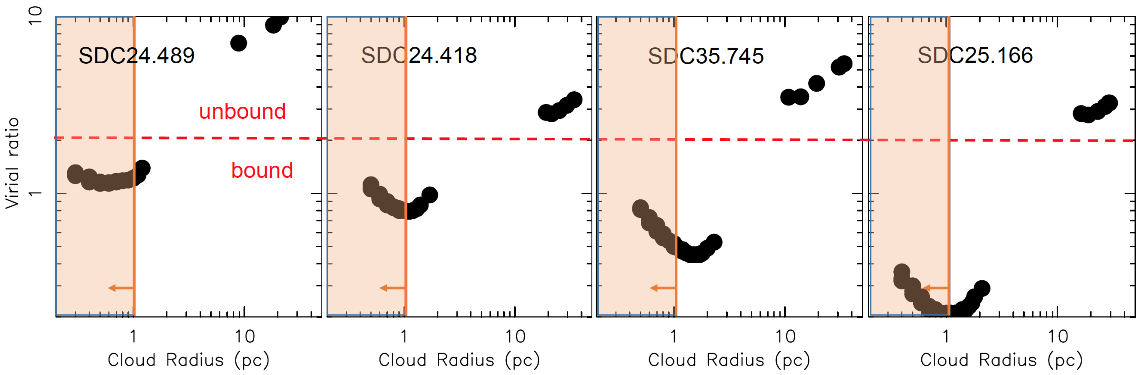

Figure 6.6 The evolution of the virial ratio of 4 IRDCs from the 27 IRDC sample (Peretto et al. in prep). The ^{13}CO(1–0) IRAM 30 m data correspond to large radii data points, whilst the low radii points correspond to the N_2H^+(1–0) data. The gap between the two scale regimes is due to the lack of optically thin tracer. This analysis was facilitated by use of a dendrogram analysis. The shaded region shows the scales at which the proposed VLA observations will probe.

We proposed the observation of a sub-sample of 9 IRDCs from these 27 clouds (JVLA project code: 18B-260). Proposing the observation of all 27 was not practical given the total time needed. Figure 6.7 shows that the full parameter space of the 27 IRDC sample is represented by our sub-sample. The proposal is aimed at calculating the virial ratio down to the scales of individual cores ($\sim$ 0.05 pc), and seeing whether the core-scale kinematics we observed in SDC13 is observed in the sample. Integrated intensity maps of the IRAM 30 m N_2H^+(1–0) emission for each of the 9 IRDCs are shown in Figure 6.8. A variety of morphologies are present, including elongated/filamentary clouds (e.g. SDC25.243 and SDC21.321), hub-filament systems (e.g. SDC18.888 and SDC28.333) and centrally concentrated clouds (e.g. SDC24.433). We proposed their observation using NH_3(1,1) and NH_3(2,2), making the results directly comparable with those of SDC13. We use the same spectral setup as outlined above in JVLA proposal 18B-219. We have not yet jointly proposed for GBT time, opting to instead wait and see which clouds are in most need of the zero-spacing data.

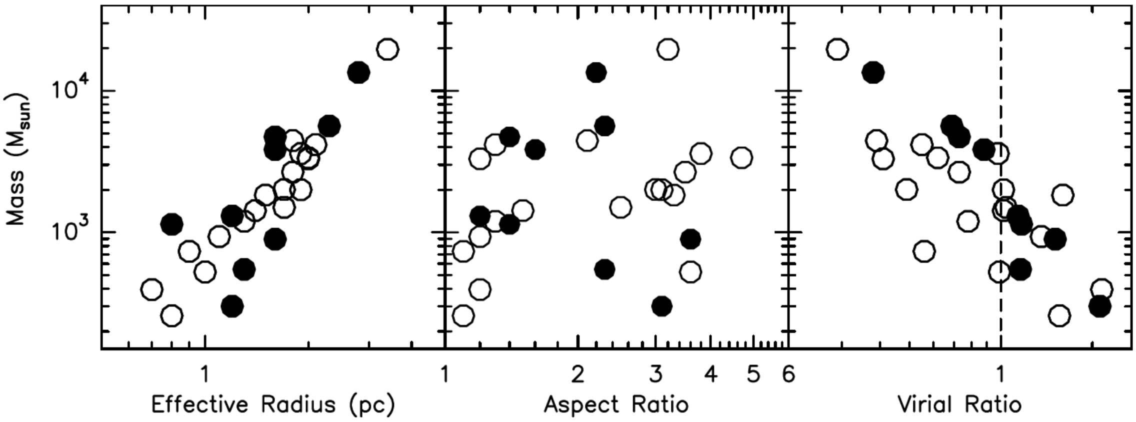

Figure 6.7 Each panel plots the mass against effective radius (left), aspect ratio (middle) and virial ratio (right) of each cloud. All circles represent those in the 27 IRDC sample of Peretto et al. in prep, whilst the black circles show the 9 IRDCs we chose to observe with the JVLA.

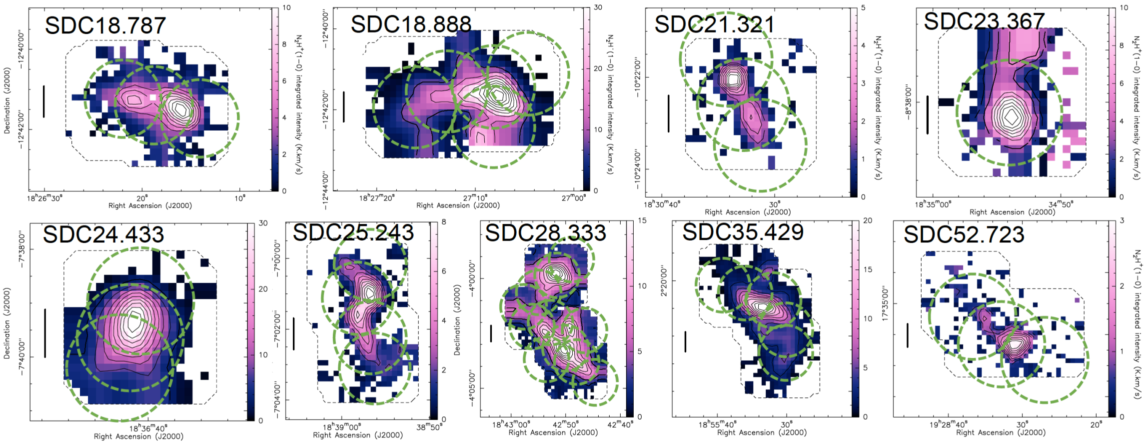

Figure 6.8 Each panel plots the N_2H^+(1–0) integrated intensity observed with the IRAM 30 m telescope (Peretto et al. in prep) of each of the 9 IRDCs we proposed to observe with the JVLA. The green circles represent the half-beam spaced pointings proposed. The sample exhibits a wide range of morphologies, from centrally concentrated, to hub-filament systems.

BIBLIOGRAPHY

Anderson, L. D., Bania, T. M., Balser, D. S., et al. 2014, ApJS, 212, 1

André, P., Men'shchikov, A., Bontemps, S., et al. 2010, A&A, 518, L102

André, P., Revéret, V., Könyves, V., et al. 2016, A&A, 592, A54

Andre, P., Ward-Thompson, D., & Barsony, M. 2000, Protostars and Planets IV, 59

Arzoumanian, D., André, P., Didelon, P., et al. 2011, A&A, 529, L6

Arzoumanian, D., André, P., Peretto, N., & Könyves, V. 2013, A&A, 553, A119

Avison, A. & George, S. J. 2013, European Journal of Physics, 34, 7

Avison, A., Peretto, N., Fuller, G. A., et al. 2015, A&A, 577, A30

Ballesteros-Paredes, J., Vázquez-Semadeni, E., Palau, A., & Klessen, R. S. 2017, arXiv:1710.07384

Barranco, J. A. & Goodman, A. A. 1998, ApJ, 504, 207

Barrett, A. H., Ho, P. T. P., & Myers, P. C. 1977, ApJL, 211, L39

Benson, P. J. & Myers, P. C. 1983, ApJ, 270, 589

Bergin, E. A. & Langer, W. D. 1997, ApJ, 486, 316

Bertoldi, F. & McKee, C. F. 1992, ApJ, 395, 140

Beuther, H., Ragan, S. E., Johnston, K., et al. 2015, A&A, 584, A67

Beuther, H., Sridharan, T. K., & Saito, M. 2005, ApJL, 634, L185

Beuther, H. & Steinacker, J. 2007, ApJL, 656, L85

Bonnell, I. A., Bate, M. R., Clarke, C. J., & Pringle, J. E. 2001, MNRAS, 323, 785

Bontemps, S., Motte, F., Csengeri, T., & Schneider, N. 2010, A&A, 524, A18

Breen, S. L., Ellingsen, S. P., Caswell, J. L., et al. 2012, MNRAS, 426, 2189

Burke, B. F. & Graham-Smith, F. 2014, An Introduction to Radio Astronomy

Busquet, G., Estalella, R., Zhang, Q., et al. 2011, A&A, 525, A141

Butler, M. J. & Tan, J. C. 2009, ApJ, 696, 484

Camacho, V., Vázquez-Semadeni, E., Ballesteros-Paredes, J., et al. 2016, ApJ, 833, 113

Carey, S. J., Noriega-Crespo, A., Mizuno, D. R., et al. 2009, PASP, 121, 76

Carter, M., Lazareff, B., Maier, D., et al. 2012, A&A, 538, A89

Caselli, P., Benson, P. J., Myers, P. C., & Tafalla, M. 2002, ApJ, 572, 238

Cheung, A. C., Rank, D. M., Townes, C. H., Thornton, D. D., & Welch, W. J. 1968, Phys. Rev. Lett., 21, 1701

Churchwell, E., Babler, B. L., Meade, M. R., et al. 2009, PASP, 121, 213

Clark, P. C. & Bonnell, I. A. 2004, MNRAS, 347, L36

Clark, P. C. & Bonnell, I. A. 2005, MNRAS, 361, 2

Clarke, S. D. & Whitworth, A. P. 2015, MNRAS, 449, 1819

Clarke, S. D., Whitworth, A. P., Duarte-Cabral, A., & Hubber, D. A. 2017, MNRAS, 468, 2489

Clarke, S. D., Whitworth, A. P., & Hubber, D. A. 2016, MNRAS, 458, 319

Cox, N. L. J., Arzoumanian, D., André, P., et al. 2016, A&A, 590, A110

Cyganowski, C. J., Brogan, C. L., Hunter, T. R., et al. 2014, ApJL, 796, L2

Dame, T. M., Hartmann, D., & Thaddeus, P. 2001, ApJ, 547, 792

Dame, T. M., Ungerechts, H., Cohen, R. S., et al. 1987, ApJ, 322, 706

Danby, G., Flower, D. R., Valiron, P., Schilke, P., & Walmsley, C. M. 1988, MNRAS, 235, 229

Dempsey, J. T., Thomas, H. S., & Currie, M. J. 2013, ApJS, 209, 8

Dirienzo, W. J., Brogan, C., Indebetouw, R., et al. 2015, ApJ, 150, 159

Dobbs, C. L., Burkert, A., & Pringle, J. E. 2011, MNRAS, 413, 2935

Dobbs, C. L., Pringle, J. E., & Duarte-Cabral, A. 2015, MNRAS, 446, 3608

Duarte-Cabral, A., Bontemps, S., Motte, F., et al. 2013, A&A, 558, A125

Duarte-Cabral, A., Chrysostomou, A., Peretto, N., et al. 2012, A&A, 543, A140

Duarte-Cabral, A. & Dobbs, C. L. 2017, ArXiv e-prints

Egan, M. P., Shipman, R. F., Price, S. D., et al. 1998, ApJL, 494, L199

Federrath, C., Rathborne, J. M., Longmore, S. N., et al. 2016, ApJ, 832, 143

Federrath, C., Roman-Duval, J., Klessen, R. S., Schmidt, W., & Mac Low, M.-M. 2010, A&A, 512, A81

Fernández-López, M., Arce, H. G., Looney, L., et al. 2014, ApJ, 790, L19

Fiege, J. D. & Pudritz, R. E. 2000, MNRAS, 311, 85

Friesen, R. K., Bourke, T. L., Di Francesco, J., Gutermuth, R., & Myers, P. C. 2016, ApJ, 833, 204

Friesen, R. K., Di Francesco, J., Myers, P. C., et al. 2010, ApJ, 718, 666

Fuller, G. A. & Myers, P. C. 1992, ApJ, 384, 523

Gatto, A., Walch, S., Naab, T., et al. 2017, MNRAS, 466, 1903

Girichidis, P., Federrath, C., Banerjee, R., & Klessen, R. S. 2011, MNRAS, 413, 2741

Girichidis, P., Walch, S., Naab, T., et al. 2016, MNRAS, 456, 3432

Glover, S. C. O. & Clark, P. C. 2012, MNRAS, 421, 116

Goldsmith, P. F. & Langer, W. D. 1999, ApJ, 517, 209

Gong, M. & Ostriker, E. C. 2015, ApJ, 806, 31

Goodman, A. A., Alves, J., Beaumont, C. N., et al. 2014, ApJ, 797, 53

Goodman, A. A., Barranco, J. A., Wilner, D. J., & Heyer, M. H. 1998, ApJ, 504, 223

Hacar, A., Kainulainen, J., Tafalla, M., Beuther, H., & Alves, J. 2016, A&A, 587, A97

Hacar, A. & Tafalla, M. 2011, A&A, 533, A34

Hacar, A., Tafalla, M., Kauffmann, J., & Kovács, A. 2013, A&A, 554, A55

Harju, J., Daniel, F., Sipilä, O., et al. 2017, A&A, 600, A61

Harju, J., Walmsley, C. M., & Wouterloot, J. G. A. 1993, A&AS, 98, 51

Hartmann, L., Ballesteros-Paredes, J., & Bergin, E. A. 2001, ApJ, 562, 852

Hatchell, J., Fuller, G. A., & Richer, J. S. 2007, A&A, 472, 187

Heitsch, F. 2013, ApJ, 769, 115

Hennebelle, P. 2013, A&A, 556, A153

Hennebelle, P., Banerjee, R., Vázquez-Semadeni, E., Klessen, R. S., & Audit, E. 2008, A&A, 486, L43

Henshaw, J. D., Caselli, P., Fontani, F., et al. 2016a, MNRAS, 463, 146

Henshaw, J. D., Jiménez-Serra, I., Longmore, S. N., et al. 2017, MNRAS, 464, L31

Henshaw, J. D., Longmore, S. N., Kruijssen, J. M. D., et al. 2016b, MNRAS, 457, 2675

Hill, A., Reynolds, R., Haffner, L., Wood, K., & Madsen, G. 2015, Highlights of Astronomy, 16, 574

Ho, P. T. P. & Townes, C. H. 1983, ARAA, 21, 239

Högbom, J. A. 1974, A&AS, 15, 417

Hotzel, S., Harju, J., & Walmsley, C. M. 2004, A&A, 415, 1065

Inutsuka, S.-i., Inoue, T., Iwasaki, K., & Hosokawa, T. 2015, A&A, 580, A49

Inutsuka, S.-I. & Miyama, S. M. 1992, ApJ, 388, 392

Jackson, J. M., Finn, S. C., Chambers, E. T., Rathborne, J. M., & Simon, R. 2010, ApJL, 719, L185

Jeans, J. H. 1928, Astronomy and cosmogony

Kainulainen, J., Hacar, A., Alves, J., et al. 2016, A&A, 586, A27

Keto, E. & Caselli, P. 2008, ApJ, 683, 238

Kirk, H., Myers, P. C., Bourke, T. L., et al. 2013, ApJ, 766, 115

Klessen, R. S., Ballesteros-Paredes, J., Vázquez-Semadeni, E., & Durán-Rojas, C. 2005, ApJ, 620, 786

Klessen, R. S. & Hennebelle, P. 2010, A&A, 520, A17

Kolmogorov, A. 1941, Akademiia Nauk SSSR Doklady, 30, 301

Könyves, V., André, P., Men'shchikov, A., et al. 2015, A&A, 584, A91

Krumholz, M. R., McKee, C. F., & Klein, R. I. 2005, Nature, 438, 332

Kukolich, S. G. 1967, Physical Review, 156, 83

Kurtz, S. 2005, in IAU Symposium, Vol. 231, Astrochemistry: Recent Successes and Current Challenges, ed. D. C. Lis, G. A. Blake, & E. Herbst, 47–56

Lazarian, A. & Hoang, T. 2007, ApJL, 669, L77

Lee, Y.-N. & Hennebelle, P. 2016, A&A, 591, A30

Li, D., Goldsmith, P. F., & Menten, K. 2003, ApJ, 587, 262

Li, J., Wang, J., Zhu, Q., Zhang, J., & Li, D. 2015, ApJ, 802, 40

Lippok, N., Launhardt, R., Semenov, D., et al. 2013, A&A, 560, A41

Liu, H. B., Ho, P. T. P., Wright, M. C. H., et al. 2013, ApJ, 770, 44

Lomax, O., Whitworth, A. P., & Cartwright, A. 2013, MNRAS, 436, 2680

Longmore, S. N., Bally, J., Testi, L., et al. 2013, MNRAS, 429, 987

Lu, X., Zhang, Q., Liu, H. B., Wang, J., & Gu, Q. 2014, ApJ, 790, 84

Mangum, J. G. & Shirley, Y. L. 2015, PASP, 127, 266

Maret, S., Faure, A., Scifoni, E., & Wiesenfeld, L. 2009, MNRAS, 399, 425

Marsh, K. A., Kirk, J. M., André, P., et al. 2016, MNRAS, 459, 342

Masters, J., Garwood, B., Langston, G., & Shelton, A. 2011, in Astronomical Society of the Pacific Conference Series, Vol. 442, Astronomical Data Analysis Software and Systems XX, ed. I. N. Evans, A. Accomazzi, D. J. Mink, & A. H. Rots, 127

McGuire, C., Fuller, G. A., Peretto, N., et al. 2016, A&A, 594, A118

McKee, C. F. & Ostriker, J. P. 1977, ApJ, 218, 148

McKee, C. F. & Tan, J. C. 2002, Nature, 416, 59

McKee, C. F. & Tan, J. C. 2003, ApJ, 585, 850

McMullin, J. P., Waters, B., Schiebel, D., Young, W., & Golap, K. 1992, (ASP Conf. Ser. 376), 127

Miyama, S. M., Nakamoto, T., Kikuchi, N., et al. 1994, The stability of circumstellar disks.

Miyama, S. M., Narita, S., & Hayashi, C. 1987, Progress of Theoretical Physics, 78, 1051

Molinari, S., Schisano, E., Elia, D., et al. 2016, A&A, 591, A149

Molinari, S., Swinyard, B., Bally, J., et al. 2010, PASP, 122, 314

Morgan, L. K., Moore, T. J. T., Allsopp, J., & Eden, D. J. 2013, MNRAS, 428, 1160

Motte, F., Andre, P., & Neri, R. 1998, A&A, 336, 150

Motte, F., Bontemps, S., Schilke, P., et al. 2007, A&A, 476, 1243

Myers, P. C. 1983, ApJ, 270, 105

Myers, P. C. 2009, ApJ, 700, 1609

Nishimura, A., Tokuda, K., Kimura, K., et al. 2015, ApJS, 216, 18

Ostriker, J. 1964, ApJ, 140, 1056

Padoan, P., Nordlund, Å., Rögnvaldsson, Ö. E., & Goodman, A. 2001, in Astronomical Society of the Pacific Conference Series, Vol. 243, From Darkness to Light: Origin and Evolution of Young Stellar Clusters, ed. T. Montmerle & P. André, 279

Palau, A., Estalella, R., Girart, J. M., et al. 2007, A&A, 465, 219

Palmeirim, P., André, P., Kirk, J., et al. 2013, A&A, 550, A38

Panopoulou, G. V., Psaradaki, I., Skalidis, R., Tassis, K., & Andrews, J. J. 2017, MNRAS, 466, 2529

Panopoulou, G. V., Tassis, K., Goldsmith, P. F., & Heyer, M. H. 2014, MNRAS, 444, 2507

Peñaloza, C. H., Clark, P. C., Glover, S. C. O., Shetty, R., & Klessen, R. S. 2017, MNRAS, 465, 2277

Perault, M., Omont, A., Simon, G., et al. 1996, A&A, 315, L165

Peretto, N., André, P., Könyves, V., et al. 2012, A&A, 541, A63

Peretto, N. & Fuller, G. A. 2009, A&A, 505, 405

Peretto, N., Fuller, G. A., André, P., et al. 2014, A&A, 561, A83

Peretto, N., Fuller, G. A., Duarte-Cabral, A., et al. 2013, A&A, 555, A112

Peretto, N., Fuller, G. A., Plume, R., et al. 2010, A&A, 518, L98

Peretto, N., Gaudel, M., Louvet, F., et al. 2015, in EAS Publications Series, Vol. 75, EAS Publications Series, 167–170

Peters, T., Naab, T., Walch, S., et al. 2017, MNRAS, 466, 3293

Pillai, T., Kauffmann, J., Wyrowski, F., et al. 2011, A&A, 530, A118

Pillai, T., Wyrowski, F., Carey, S. J., & Menten, K. M. 2006, A&A, 450, 569

Pineda, J. E., Goodman, A. A., Arce, H. G., et al. 2010, ApJL, 712, L116

Pineda, J. E., Offner, S. S. R., Parker, R. J., et al. 2015, Nature, 518, 213

Planck Collaboration, Abergel, A., Ade, P. A. R., et al. 2011, A&A, 536, A25

Polychroni, D., Schisano, E., Elia, D., et al. 2013, ApJL, 777, L33

Pon, A., Toalá, J. A., Johnstone, D., et al. 2012, ApJ, 756, 145

Purcell, C. R., Longmore, S. N., Walsh, A. J., et al. 2012, MNRAS, 426, 1972

Ragan, S. E., Bergin, E. A., & Wilner, D. 2011, ApJ, 736, 163

Ragan, S. E., Henning, T., Tackenberg, J., et al. 2014, A&A, 568, A73

Rathborne, J. M., Jackson, J. M., & Simon, R. 2006, ApJ, 641, 389

Recchi, S., Hacar, A., & Palestini, A. 2014, MNRAS, 444, 1775

Reid, M. J., Dame, T. M., Menten, K. M., & Brunthaler, A. 2016, ApJ, 823, 77

Rigby, A. J., Moore, T. J. T., Plume, R., et al. 2016, MNRAS, 456, 2885

Rohlfs, K. & Wilson, T. L. 2000, Tools of Radio Astronomy, 3rd edn. (Springer)

Roman-Duval, J., Jackson, J. M., Heyer, M., Rathborne, J., & Simon, R. 2010, ApJ, 723, 492

Rosolowsky, E. W., Pineda, J. E., Kauffmann, J., & Goodman, A. A. 2008, ApJ, 679, 1338

Rydbeck, O. E. H., Sume, A., Hjalmarson, A., et al. 1977, ApJL, 215, L35

Sakamoto, S., Hayashi, M., Hasegawa, T., Handa, T., & Oka, T. 1994, ApJ, 425, 641

Salji, C. J., Richer, J. S., Buckle, J. V., et al. 2015, MNRAS, 449, 1782

Sánchez-Monge, Á., Pandian, J. D., & Kurtz, S. 2011, ApJL, 739, L9

Sanhueza, P., Jackson, J. M., Zhang, Q., et al. 2017, ApJ, 841, 97

Schisano, E., Rygl, K. L. J., Molinari, S., et al. 2014, ApJ, 791, 27

Schneider, N., Csengeri, T., Hennemann, M., et al. 2012, A&A, 540, L11

Schneider, S. & Elmegreen, B. G. 1979, ApJS, 41, 87

Schöier, F. L., van der Tak, F. F. S., van Dishoeck, E. F., & Black, J. H. 2005, A&A, 432, 369

Seifried, D. & Walch, S. 2015, MNRAS, 452, 2410

Shu, F. H., Adams, F. C., & Lizano, S. 1987, ARAA, 25, 23

Simon, R., Rathborne, J. M., Shah, R. Y., Jackson, J. M., & Chambers, E. T. 2006, ApJ, 653, 1325

Smith, R. J., Glover, S. C. O., & Klessen, R. S. 2014, MNRAS, 445, 2900

Smith, R. J., Glover, S. C. O., Klessen, R. S., & Fuller, G. A. 2016, MNRAS, 455, 3640

Smith, R. J., Longmore, S., & Bonnell, I. 2009, MNRAS, 400, 1775

Springel, V. 2010, MNRAS, 401, 791

Stahler, S. W. & Palla, F. 2005, The Formation of Stars, 865

Tafalla, M. & Hacar, A. 2015, A&A, 574, A104

Tafalla, M., Myers, P. C., Caselli, P., & Walmsley, C. M. 2004, Ap&SS, 292, 347

Tafalla, M., Myers, P. C., Caselli, P., Walmsley, C. M., & Comito, C. 2002, ApJ, 569, 815

Takahashi, S., Ho, P. T. P., Teixeira, P. S., Zapata, L. A., & Su, Y.-N. 2013, ApJ, 763, 57

Teixeira, P. S., Takahashi, S., Zapata, L. A., & Ho, P. T. P. 2016, A&A, 587, A47

Thompson, A. R. 1989, in Astronomical Society of the Pacific Conference Series, Vol. 6, Synthesis Imaging in Radio Astronomy, ed. R. A. Perley, F. R. Schwab, & A. H. Bridle, 11

Thompson, A. R., Moran, J. M., & Swenson, Jr., G. W. 2017, Interferometry and Synthesis in Radio Astronomy, 3rd Edition

Toalá, J. A., Vázquez-Semadeni, E., & Gómez, G. C. 2012, ApJ, 744, 190

Townes, C. H. & Schawlow, A. L. 1955, Microwave Spectroscopy

Traficante, A., Fuller, G. A., Smith, R. J., et al. 2018, MNRAS, 473, 4975

Tremblin, P., Schneider, N., Minier, V., et al. 2014, A&A, 564, A106

Ungerechts, H., Winnewisser, G., & Walmsley, C. M. 1986, A&A, 157, 207

van der Tak, F. F. S., Boonman, A. M. S., Braakman, R., & van Dishoeck, E. F. 2003, A&A, 412, 133

Vázquez-Semadeni, E., Gómez, G. C., Jappsen, A.-K., Ballesteros-Paredes, J., & Klessen, R. S. 2009, ApJ, 707, 1023

Vázquez-Semadeni, E., González-Samaniego, A., & Colín, P. 2017, MNRAS, 467, 1313

Visser, R., van Dishoeck, E. F., & Black, J. H. 2009, A&A, 503, 323

Viti, S., Collings, M. P., Dever, J. W., McCoustra, M. R. S., & Williams, D. A. 2004, MNRAS, 354, 1141

Walch, S., Girichidis, P., Naab, T., et al. 2015, MNRAS, 454, 238

Walsh, A. J., Lo, N., Burton, M. G., et al. 2008, PASA, 25, 105

Wang, K., Testi, L., Burkert, A., et al. 2016, ApJS, 226, 9

Wang, K., Testi, L., Ginsburg, A., et al. 2015, MNRAS, 450, 4043

Wang, Y., Zhang, Q., Rathborne, J. M., Jackson, J., & Wu, Y. 2006, ApJL, 651, L125

Ward-Thompson, D. & Whitworth, A. P. 2015, An Introduction to Star Formation

Whitworth, A. P. 2016, MNRAS, 458, 1815

Whitworth, A. P. & Ward-Thompson, D. 2001, ApJ, 547, 317

Wilson, T. L. & Rood, R. 1994, ARA&A, 32, 191

Yang, B., Stancil, P. C., Balakrishnan, N., & Forrey, R. C. 2010, ApJ, 718, 1062

Zamora-Avilés, M., Ballesteros-Paredes, J., & Hartmann, L. W. 2017, MNRAS, 472, 647

Zhang, Q., Wang, Y., Pillai, T., & Rathborne, J. 2009, ApJ, 696, 268